

**UNCLASSIFIED**

---

**AD\_274 256**

*Reproduced  
by the*

**ARMED SERVICES TECHNICAL INFORMATION AGENCY  
ARLINGTON HALL STATION  
ARLINGTON 12, VIRGINIA**



---

**UNCLASSIFIED**

NOTICE: When government or other drawings, specifications or other data are used for any purpose other than in connection with a definitely related government procurement operation, the U. S. Government thereby incurs no responsibility, nor any obligation whatsoever; and the fact that the Government may have formulated, furnished, or in any way supplied the said drawings, specifications, or other data is not to be regarded by implication or otherwise as in any manner licensing the holder or any other person or corporation, or conveying any rights or permission to manufacture, use or sell any patented invention that may in any way be related thereto.

274 256

CAT. NO. 274 256  
AS AD NO.

# SOME EXPERIMENTS WITH NEW TYPES OF CROSSED FIELD ELECTRON GUNS

By  
Thomas A. Midford

Scientific Report No. 36  
Contract AF 19(604)-1930

The research reported in this document has been  
sponsored by the  
Electronics Research Directorate  
Air Force Cambridge Research Laboratories  
Office of Aerospace Research  
United States Air Force  
Bedford, Massachusetts

Reproduction in whole or part is permitted for  
any purpose of the United States Government

M. L. Report No. 885  
February 1962



*Microwave Laboratory*  
W. W. HANSEN LABORATORIES OF PHYSICS  
STANFORD UNIVERSITY  
STANFORD, CALIFORNIA

NOX

AFCRL-62-75

SOME EXPERIMENTS WITH NEW TYPES OF CROSSED FIELD ELECTRON GUNS

By  
Thomas A. Midford

Scientific Report No. 36  
Contract AF 19(604)-1930

The research reported in this document has been  
sponsored by the  
Electronics Research Directorate  
Air Force Cambridge Research Laboratories  
Office of Aerospace Research  
United States Air Force  
Bedford, Massachusetts

Reproduction in whole or part is permitted for  
any purpose of the United States Government

M.L. Report No. 885  
February 1962

Microwave Laboratory  
W. W. Hansen Laboratories of Physics  
Stanford University  
Stanford, California

AFCRL-62-75

SCIENTIFIC REPORT NO. 36

SOME EXPERIMENTS WITH NEW TYPES OF CROSSED FIELD ELECTRON GUNS

By

Thomas A. Midford

Electronics Research Directorate  
Air Force Cambridge Research Laboratories  
Office of Aerospace Research (USAF)  
Bedford, Massachusetts

CONTRACT AF 19(604)-1930

M. L. Report No. 885

February 1962

The research reported in this document has been sponsored by the Electronics Research Directorate of the Air Force Cambridge Research Laboratories, Office of Aerospace Research, UNITED STATES AIR FORCE, BEDFORD, MASSACHUSETTS. The publication of this report does not necessarily constitute approval by the Air Force of the findings or conclusions contained herein.

Microwave Laboratory  
W. W. Hansen Laboratories of Physics  
Stanford University  
Stanford, California

## ABSTRACT

The properties of two types of space-charge flow crossed-field electron guns are investigated. The first type is a form of short gun; the second one is a type of long gun in which the electron stream is accelerated adiabatically. Both guns are intended for use in M-type injected beam microwave devices in which, ideally, electron beams satisfy the conditions of laminar Brillouin flow. In practice, such beams have not been previously achieved.

Certain nonlaminar, more complex flow models which are supported in the same environment as Brillouin flow are discussed. From a survey of previous types of crossed-field guns, it was concluded that the beams from these guns were of this more complex type.

The analytic basis for the present guns was then developed; these guns are based upon the space-charge flow solution of the plane magnetron diode as first derived by Benham. The short gun was based on the exact form of this solution, while the long gun resulted from a simple approximation to this solution which was shown to be valid under certain initial conditions at the cathode. As these solutions are semi-infinite in extent and since the guns use only a finite portion of the flow, it was necessary, by means of an external system of electrodes, to synthesize the proper boundary conditions along the edges of the beam. The electrode system for both guns was obtained by means of a method of analytic continuation due to Kirstein and Lomax. The guns obtained in this manner are convergent, and have the advantage that the current density at the cathode and hence the total current emitted from the gun can be predicted.

Examples of both types of guns were designed and built. In regard to emission characteristics, both guns behaved substantially as predicted by the theory. Experimental values of the total emitted current, as a function of gun voltage and magnetic field, were found to be in very good agreement with approximate analytic expressions which were derived for these relationships. The short gun produced a beam which was seemingly a good approximation to planar Brillouin flow and moreover, a beam relatively free of the characteristic crossed-field instabilities. The beam from the long gun, however, was found to be unstable under certain conditions. The results of additional experiments with the beam from

this gun indicated that this instability, as evidenced by the collection of current by a negatively biased sole electrode, was the result of growth along the beam of a disturbance originating near the cathode and which was probably related to the formation of a potential minimum associated with space-charge limited emission. Furthermore, the rate of growth along the beam was found to scale with  $\lambda_c$ , the beam cyclotron wavelength, and moreover, became relatively small for sufficiently large values of  $\lambda_c$ . On the basis of these observations it is possible to account for stability of the beam from the short gun and, more generally, to relate the dc properties of the crossed-field beam to its stability.

#### ACKNOWLEDGEMENTS

I wish to express my thanks to Professor Gordon S. Kino for his guidance and interest throughout the course of this work.

I would also like to thank Professor Marvin Chodorow for reading the manuscript.

I would further like to express my appreciation to Messrs. P. Lee and F. Bicker for their assistance in fabricating and assembling the experimental tube.

My thanks are also due to Messrs. A. Braun and L. Nigro and to the staff of the Reports Office for their assistance in preparing the manuscript.



# TABLE OF CONTENTS

	Page
Abstract . . . . .	iii
Acknowledgement . . . . .	v
I. Introduction. . . . .	1
II. The steady-state crossed-field electron flow. . . . .	5
A. Introduction. . . . .	5
B. Crossed field flow with rectilinear boundaries. . . . .	7
1. The single trajectory models. . . . .	7
2. Miller's hydrodynamical analysis. . . . .	14
C. Waters' paraxial work . . . . .	16
D. Undulating beams resulting from improper injection optics. . . . .	19
E. The design of crossed-field guns. . . . .	24
III. Previous crossed-field gun designs. . . . .	27
A. Introduction. . . . .	27
B. The short gun . . . . .	29
C. The long gun. . . . .	32
D. The shielded gun. . . . .	38
IV. The analytical design of crossed-field guns . . . . .	41
A. Introduction. . . . .	41
B. The space-charge flow solutions and their use as a basis for convergent crossed-field guns . . . . .	42
C. The method for obtaining the electrodes necessary to produce a finite beam . . . . .	49
1. The electrode system for the short gun. . . . .	50
2. The electrode system for the long gun . . . . .	53
D. Assumptions and approximations inherent in the gun design method . . . . .	54
V. Experimental studies of the short and long guns . . . . .	57
A. Introduction. . . . .	57
B. The beam tester . . . . .	57
C. The experimental short gun. . . . .	67
1. Design considerations . . . . .	67
2. Mechanical design of the short gun. . . . .	72
3. Experiments with the short gun. . . . .	75

	Page
a. Measurement of cathode current as a function of the gun parameters . . . . .	75
b. Transmission measurements . . . . .	79
c. Photographs of the beam . . . . .	85
D. The experimental long gun . . . . .	93
1. Design considerations . . . . .	93
2. Mechanical design of the long gun . . . . .	97
3. Experiments with the long gun . . . . .	97
a. Measurement of cathode current as a function of the gun parameters . . . . .	102
b. Measurement of the cutoff characteristics of the long gun. . . . .	103
c. Cathode bias measurements . . . . .	109
d. Transmission measurements . . . . .	111
d-i. Gross characteristics of the sole and circuit current . . . . .	111
d-ii. The total sole current as a function of the cathode current for space-charge- limited conditions at the cathode . . . . .	119
d-iii. The effect of temperature-limiting the cathode on the magnitude of the sole current . . . . .	119
d-iv. Total sole current as a function of the scaling parameter in the drift function .	124
d-v. The distribution of the sole current along the length of the sole. . . . .	131
d-vi. Temperature of the electrons collected by the sole . . . . .	140
e. Visual observations . . . . .	145
f. Miscellaneous experiments . . . . .	150
i. Adiabatic acceleration in the drift region. . . . .	151
ii. Reduction of the gun transit angle. . . . .	153

	Page
VI. Conclusions and recommendations for further work . . . . .	157
A. Conclusions and recommendations regarding the guns . . .	157
B. Conclusions and recommendations regarding crossed-field instabilities. . . . .	158
Appendices	
A. A dc small-signal field analysis of a thin undulating crossed-field beam . . . . .	161
B. Approximate expressions for cathode current as a function of anode potential and magnetic field. . . . .	167
C. A method for improving the longitudinal homogeneity of the experimental magnet. . . . .	171
D. Amplification and attenuation of dc cyclotron waves by means of a periodic perturbation in a transverse electric field. . . . .	174
References. . . . .	185

# LIST OF FIGURES

	Page
1.1 Basic configurations of non-reentrant linear beam crossed-field microwave devices. . . . .	2
2.1 External configuration of some types of flow supported by crossed-fields. . . . .	6
2.2 Geometry for crossed-field flow with rectilinear boundaries.	8
2.3 Single trajectory beam . . . . .	12
2.4 Nonparallel flow as predicted by paraxial theory . . . . .	18
2.5 Beam undulations resulting from errors in the injection optics . . . . .	20
3.1 Various types of cycloidal motion executed by electrons in crossed uniform electric and magnetic fields . . . . .	28
3.2 Typical short gun geometry . . . . .	30
3.3 Short gun trajectories calculated by Miller and Larson . . .	33
3.4 Some possible long gun configurations. . . . .	34
3.5 The adiabatic long gun . . . . .	36
3.6 Shielded gun geometry. . . . .	39
4.1 The normalized trajectory and variation in normalized potential along it for Case 1. . . . .	47
4.2 Geometry of the space-charge flow crossed-field guns . . . .	48
4.3 Family of equipotentials for the short gun . . . . .	52
4.4 Family of equipotenitals for the long gun. . . . .	55
5.1 Optics of the crossed-field beam tester. . . . .	58
5.2 The segmented sole structure . . . . .	60
5.3 Beam tester. . . . .	62
5.4 Photograph of the beam tester. . . . .	63
5.5 Photograph of the magnet and vacuum envelope . . . . .	65
5.6 Arrangement for viewing the beam . . . . .	66
5.7 Electrode configuration for the experimental short gun . . .	68
5.8 Effect of tilting the gun on the exit angles . . . . .	69
5.9 Mechanical details of the short gun. . . . .	73
5.10 Photographs of the short gun . . . . .	74
5.11 Short gun characteristic . . . . .	77
5.12 Short gun characteristic for constant $\phi_A/B_0^2$ . . . . .	78
5.13 Geometry for the short gun transmission measurements . . . .	80

	Page
5.14 Circuit current as a function of circuit voltage for various values of sole voltage. . . . .	82
5.15 Sole currents for the conditions of Fig. 5.14 . . . . .	83
5.16 Normalized circuit current as a function of anode voltage .	84
5.17 Cathode and circuit currents as a function of the cathode bias potential. . . . .	86
5.18 Photographs of the beam from the short gun. . . . .	88
5.19 The beam in the gun region showing the theoretical edge trajectories. . . . .	92
5.20 Electrode configuration of the experimental long gun. . . .	94
5.21 Mechanical details of the long gun. . . . .	98
5.22 Photographs of the short gun. . . . .	99
5.23 Long gun characteristic . . . . .	104
5.24 Long gun characteristic with $\phi_A/B_0^2$ held constant. . . . .	105
5.25 Long gun cutoff characteristics . . . . .	107
5.26 Short gun cutoff data obtained by Anderson. . . . .	108
5.27 Cathode current and transmission as a function of cathode bias voltage. . . . .	110
5.28 Geometry for the long gun transmission measurements . . . .	112
5.29 Gross sole current characteristics. . . . .	114
5.30 Gross circuit current characteristics . . . . .	115
5.31 Gross sole current characteristics for various sole potentials. . . . .	116
5.32 Gross sole current characteristics of Miller. . . . .	118
5.33 Sole current as a function of cathode current, with the cathode space-charge limited. . . . .	120
5.34 Effect of temperature limiting on the gross sole current. .	122
5.35 Comparison of normalized sole current as a function of cathode current for temperature and space-charge limiting at the cathode. . . . .	123
5.36 Normalized sole current as a function of the drift region scaling parameter for constant $\phi_s$ . . . . .	127
5.37 Normalized sole current as a function of the drift region scaling parameter for scaled $\phi_s$ . . . . .	128

	Page
5.38 Normalized sole current as a function of the drift region scaling parameter for $\phi_s = \text{constant}$ , showing the effect of temperature limiting. . . . .	129
5.39 Normalized sole current as a function of the drift region scaling parameter for scaled $\phi_s$ , showing the effect of temperature limiting . . . . .	130
5.40 Normalized sole current distribution for various sole potentials . . . . .	134
5.41 Sole current distribution for various values of the drift region scaling parameter . . . . .	135
5.42 Normalized sole current distribution for various degrees of temperature-limiting. . . . .	136
5.43 Trochotron sole current distribution obtained by Åström. . .	139
5.44 Sole current intercepted by segments 1, 2, 3 and 5 as a function of their potential. . . . .	141
5.45 Sole current intercepted by segments 2, 3, and 5 as a function of their potential. . . . .	142
5.46 Total sole current as a function of sole potential for the continuous sole. . . . .	144
5.47 Increase in beam thickness as a function of the distance from the gun exit plane. . . . .	147
5.48 Photographs of the beam from the long gun. . . . .	148
5.49 Photographs of the beam from the long gun, showing the effect of varying the drift region scaling parameter . . .	149
5.50 Electrode configuration for extending the long gun . . . .	152
5.51 Geometry of the modified long gun. . . . .	154
A.1 Geometry for the thin beam analysis. . . . .	162
B.1 Geometry for the calculation of the emission relations . .	168
C.1 Geometry of the magnet pole pieces. . . . .	172
C.2 Variation in $B_0$ as a function of longitudinal position with and without the pole piece shims. . . . .	173
D.1 Geometry of the segmented sole and the slotted sole. . . .	175
D.2 Photographs illustrating amplification and damping of dc cyclotron undulations by means of periodic perturbations in the transverse electric field . . . . .	177

	Page
D.3    Comparison of normalized sole current as a function of the scaling parameter for the smooth and slotted sole plates. . . . .	179
D.4    Geometries for the paraxial analysis. . . . .	180

# LIST OF SYMBOLS

$\alpha$	Term defined by Eq. (A.18).
$\beta$	The dc propagation constant of the beam.
$\beta_e$	Term defined by Eq. (A.18).
$\beta_p$	The beam plasma propagation constant.
$\Delta$	The distance between the sole and focusing electrode at the gun exit plane.
$\delta$	The beam thickness.
$\epsilon_0$	The permittivity of free space.
$\eta$	The charge to mass ratio of the electron $\eta < 0$ .
$\theta$	The angle between the potential gradient and an incremental distance along an electron trajectory.
$\lambda_c$	The beam cyclotron wavelength $\lambda_c = 2\pi v_0/\omega_c$ .
$\rho_0$	The charge density in the beam.
$\sigma_0$	The surface charge density.
$\phi$	The beam potential.
$\phi_0$	The potential associated with the normal component of thermal velocities at the cathode.
$\phi^+, \phi^-$	The potentials above and below the beam, respectively.
$\phi_A$	The potential of the gun-accelerating anode in volts.
$\phi_c$	The cathode potential in volts.
$\phi_{co}$	The collector potential in volts.
$\phi_{ct}$	The circuit potential in volts.
$\phi_s$	The sole potential in volts.
$\Phi$	Normalized potential $\Phi = -(\epsilon_0^2 \omega_c^4 / \eta J y^2) \phi$ .
$\psi$	The angle of incidence of the beam or a trajectory with respect to the sole plane.
$\omega_c$	The radian cyclotron frequency of the beam $\omega_c = -\eta B_0$ .
$\omega_p$	The radian beam plasma frequency $\omega_p^2 = \eta \rho_0 / \epsilon_0$ .
A, B, C, D	Space-charge parameters defined by Eq. (A.8).
a	The cathode-anode spacing of the French short gun; also the half width of the sole slots.
$B_0$	The uniform dc magnetic field.
b	The distance from the center of the cathode to the gun exit plane.



c	The coordinate specifying the location of the sole.
d	The sole-circuit spacing.
$E_0$	The uniform dc electric field.
$E_{0y}$	The transverse dc electric field.
$G$	Geometrical quantities appearing in the emission equations for the short gun, $G = S\epsilon_0\eta^2/2\pi^2$ , $H = S(\eta/\pi h)$ .
$H$	
h	The spacing between the anode and focusing electrode at the gun exit plane.
$I_A$	The current collected by the gun anode.
$I_c$	The total cathode current.
$I_{co}$	The collector current.
$I_{ct}$	The current collected by the circuit.
$I_s$	The current collected by the sole.
$J_y$	The current density at the cathode.
$J_y^+$ , $J_y^-$	Current densities associated with the two components of double streaming nonlaminar flow.
j	The square root of -1.
L	The normalized cathode length $L = \epsilon_0\omega_c^3/\eta J_y(l)$ .
l	The length of the cathode.
M	Geometrical constant appearing in the long gun emission equation $M = S\epsilon_0/2bh^2$ .
m	The mass of the electron.
$P_x$	The x-component of generalized momentum.
r	The radius of cyclotron gyration.
S	The area of the cathode.
s	Arc length measured along a trajectory.
t	The time in seconds.
u	The normalized time or transit angle $u = \omega_c t$ .
$u_b$	The transit angle at the gun exit plane.
$v$	The velocity at a particular point in the beam.
$v_1$	The velocity of injection into a region of uniform crossed-fields.
$v_0$	The average beam velocity equal in magnitude to $E_0/B_0$ for a single electron.
W	The complex potential function in the u v plane.

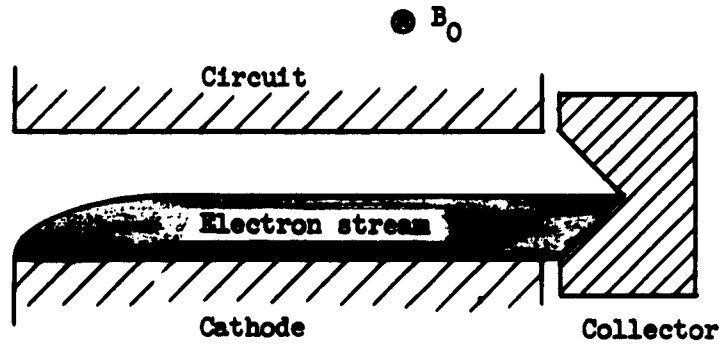
- w The width of the beam; also the complex variable  $u + jv$  .
- X Normalized distance  $X = (\epsilon_0 \omega_c^3 / \eta J_y) x$  .
- x The distance measured parallel to the plane of the cathode or sole.
- $x_0$  The x-coordinate at time  $t = 0$  or the unperturbed value of  $x$  .
- Y Normalized distance  $Y = (\epsilon_0 \omega_c^3 / \eta J_y) y$  .
- y Distance measured perpendicular to the plane of the cathode or sole.
- $y_0$  The y-coordinate at time  $t = 0$  , the unperturbed value of  $y$  or the distance of the beam above the sole.
- Z Complex normalized parameter  $Z = X + jY$  .
- z The distance measured parallel to the magnetic field.
- 0 In general, subscript 0 indicates an initial or stationary value, while subscript 1 indicates a first order perturbation. As usual, time differentiation  $d/dt( )$  is indicated by  $(\dot{\phantom{x}})$  .

## I. INTRODUCTION

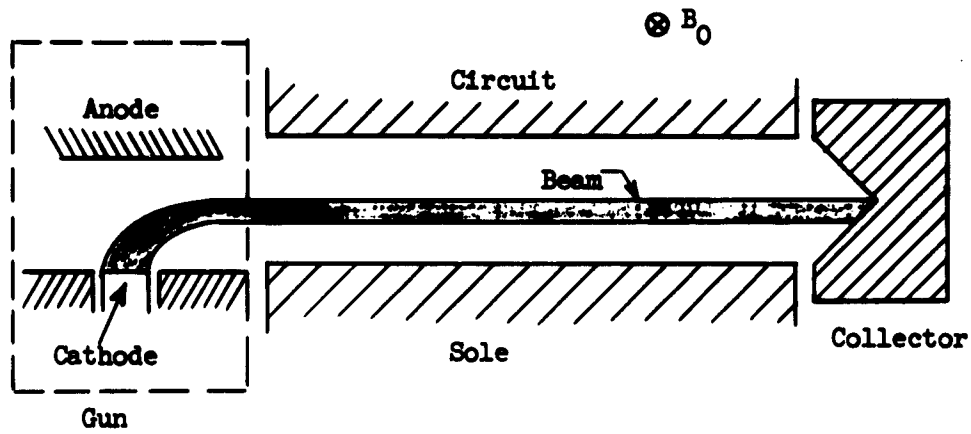
In recent years interest has increased in the class of microwave devices employing electron streams which move through mutually perpendicular electric and magnetic fields. Historically, the first and probably the most important of these devices was the magnetron oscillator. More recently, a series of backward and forward wave oscillators and amplifiers employing linear non-reentrant crossed-field electron streams have been proposed and studied. These devices are usually of two types where either: (1) the beam is emitted from a continuous cathode, or (2) the beam is focused and injected into the interaction region by means of a suitable gun structure. This distinction is illustrated in Fig. 1.1. This paper is concerned with an experimental study of some new types of guns for the latter configuration, frequently designated as the M-type injected beam device.

The new guns which have been investigated are based upon space-charge flow solutions first obtained for the plane magnetron by Benham,<sup>1</sup> Brillouin<sup>2</sup> and others a number of years ago. The gun design technique is similar to that for the Pierce gun in that an infinite space-charge flow is simulated by a finite, convergent portion of this flow and an external system of electrodes which synthesize the proper boundary conditions on the edges of this convergent flow. The electrode shapes have been found using a method due to Kirstein<sup>3</sup> and Lomax.<sup>4</sup> Two types of guns which are similar to the "short" and "long" guns of the French have been obtained by this method. Both guns are convergent, the short gun having a convergence of order ten while in principle the long gun is capable of considerably greater convergence. Both guns are designed to operate in a uniform dc magnetic field, and as they are based on space-charge flow solutions, the total current as a function of gun voltage and magnetic field may be specified analytically.

While the primary purpose of this paper is to present the results of a detailed experimental study of both of these types of guns, a number of related topics will be considered, either for the sake of completeness or to present experimental results not directly concerned with the two guns but which are relevant to general problems of crossed-field optics.



a. Continuous cathode



b. Injected beam

FIG. 1.1--Basic configurations of nonre-entrant linear beam crossed-field microwave devices.

The nature of the steady-state electron beam under uniform  $\omega$ -type crossed-fields is considered in Chapter II. Following in Chapter III is a discussion of earlier forms of crossed-field guns. The theory of the new guns is presented in Chapter IV and is followed by a discussion of the experiments in the following chapter. A discussion of the results of the experiments and recommendations for further work is given in Chapter VI.

## II. THE STEADY-STATE CROSSED-FIELD ELECTRON FLOW

### A. INTRODUCTION

Most field analyses of M-type crossed-field devices assume a beam whose unperturbed state is represented as planar Brillouin flow, or at least as a simple modification of this model.<sup>5,6</sup> In practice, such a beam is seldom, if ever, realized. In this chapter we shall consider the well known properties of Brillouin flow and a number of nonlaminar models given in the literature. These latter types of flow, which may exist under the same external crossed-field conditions as those which support a beam in Brillouin flow, are characterized by curvilinear trajectories and probably represent a more realistic description of actual beams than does the Brillouin flow model. In addition we shall consider the nature of the resultant flow if Brillouin or near Brillouin beams are subjected to sudden changes in the external crossed-field environment. Such a beam might result from potential or field discontinuities between the gun and interaction region either as a result of poor design or in practice from varying the dc circuit voltage for tuning purposes.

The types of flow which we shall consider may be described physically in terms of the macroscopic nature of the flow on its boundaries. The three types of flow which are of interest are shown in Fig. 2.1. The first of these, the sheet beam with rectilinear boundaries (Fig. 2.1a), will be discussed in terms of (1) the so called "single trajectory model" which originates from the theory of the plane magnetron diode<sup>1,2,7</sup> and (2) the hydrodynamical analysis as given by Miller.<sup>8</sup> In both of these cases planar Brillouin flow will be seen to be a special case of a more complex flow with curvilinear trajectories. Figure 2.1b illustrates the second form of flow to be discussed which is characterized by rippling boundaries and a periodically varying thickness. This type of beam has been analyzed by paraxial methods by Waters.<sup>9</sup> In the case of the third type (Fig. 2.1c) the beam as a whole describes an undulatory path in space. A small signal analysis under dc conditions for the thin beam case of c is given in Appendix A. In the case of both b and c the spatial periodicity of the flow is given approximately by  $\lambda_c = 2\pi v_0 / \omega_c$ , where  $v_0$  is the average dc velocity of the flow.



a. Rectilinear boundaries



b. Undulating boundaries and periodically varying thickness



c. Undulating beam

FIG. 2.1--External configuration of some types of flow supported by crossed fields.

Having surveyed these various forms of crossed-field flow, we shall then mention the requirements to be satisfied by suitable guns in terms of (1) potential effectiveness in producing a beam approximating as closely as possible Brillouin flow as well as (2) certain other practical considerations or the characteristics of particular devices.

Throughout the discussion a number of assumptions will be made, and for convenience they are listed as follows:

1. All quantities are invariant to change in position in a direction parallel to the uniform magnetic field. Thus the geometry is two dimensional.
2. Only dc effects will be considered.
3. All relativistic effects will be ignored.
4. With the exception of some of the discussion of the flow illustrated in Fig. 2.1c, fields due to the image charges of the beam in the sole and circuit electrodes will be ignored.
5. The effect of thermal velocities will be ignored.

#### B. CROSSED FIELD FLOW WITH RECTILINEAR BOUNDARIES

The geometry which we shall consider is shown in Fig. 2.2. The magnetic field is directed into the plane of the diagram along the negative z axis. Since only dc phenomena are of interest, the slow wave circuit, which is usually at a positive potential with respect to the sole, is considered to be a smooth conducting plane.

This form of flow may be analyzed, either from the "Lagrangian" or "Eulerian" points of view. The latter will be discussed in the section describing the hydrodynamical analysis of Miller. In the former case, after making some simplifying assumptions, it is possible to integrate the equations of motion and obtain the electronic trajectories within the beam. We shall now consider the details of this procedure.

##### 1. The Single Trajectory Models.

In the geometry of Fig. 2.2, the components of the Lorentz equation

$$\frac{dv}{dt} = \eta(\underline{E}_0 + \underline{v} \times \underline{B}_0) \quad (2.1)$$



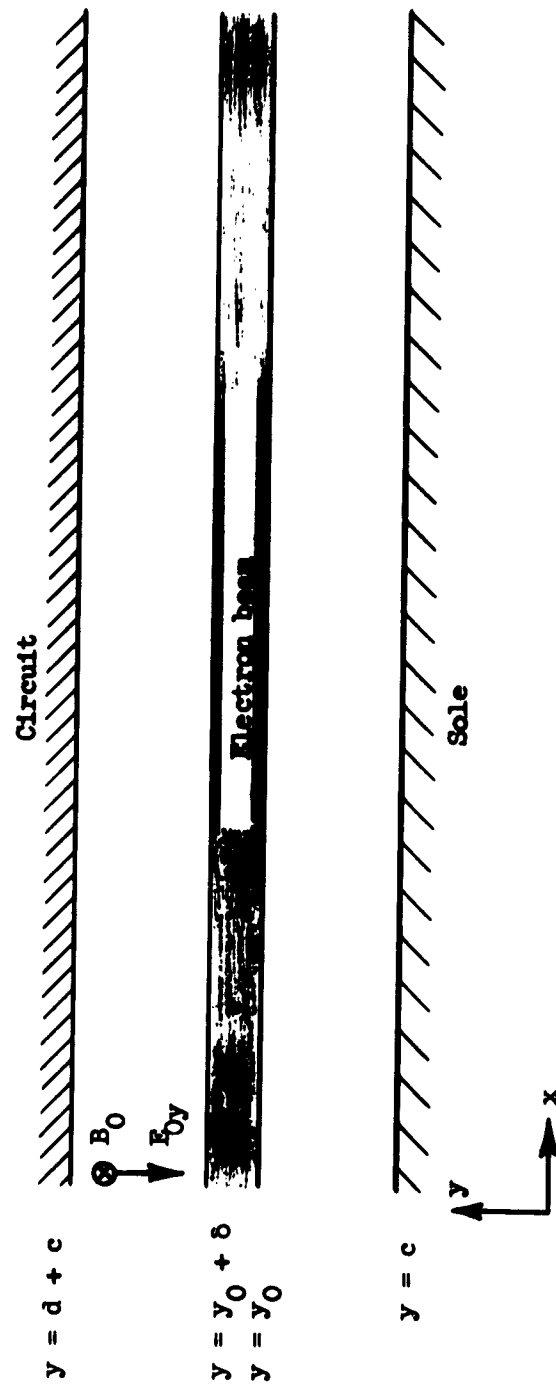


FIG. 2.2--Geometry for crossed-field flow with rectilinear boundaries.

become

$$\ddot{y} + \omega_c \dot{x} = \eta E_{Oy} \quad (2.2a)$$

$$\ddot{x} - \omega_c \dot{y} = 0 \quad , \quad (2.2b)$$

where  $E_{Oy}$  is the total transverse field including space-charge forces. All boundary conditions are considered to be uniform in the x-direction, thus  $E_{Ox} = 0$ . A description of electron motion, including the effects of space charge, for the case where neither potential nor charge density are functions of  $x$ , is then given by solving Eqs. (2.2) along with Poisson's equation

$$\frac{dE_{Oy}}{dy} = \frac{\rho_0}{\epsilon_0} \quad (2.3)$$

and the continuity equation

$$\frac{d}{dy} (\rho_0 \dot{y}) = 0 \quad , \quad (2.4)$$

where  $\rho_0$  is volume charge density in the beam. If, in addition, the flow originates at a unipotential cathode, conservation of energy requires that

$$\frac{1}{2}(\dot{x}^2 + \dot{y}^2) + \eta \phi = 0 \quad , \quad (2.5)$$

where  $\phi$  is the beam potential measured with respect to the cathode, and  $E_{Oy} = -\partial\phi/\partial y$ .

The nature of the solution of these equations depends upon further simplifying assumptions regarding the form of the electron trajectories.

#### a. Brillouin Flow

In this case the flow is laminar, and all electrons are assumed to move along parallel paths with  $\ddot{y} = \dot{y} = 0$ . As a result of space charge,  $\dot{x}$  becomes a function of  $y$  which we will denote as  $v(y)$ . By differentiating Eq. (2.5) with respect to  $y$  and combining with Eq. (2.2a), we find that

$$\frac{\partial v(y)}{\partial y} = \omega_c \quad . \quad (2.6)$$

Equations (2.6), (2.5) and (2.3) then imply that the charge density within the beam is constant and given by

$$\rho_0 = \frac{\epsilon_0 \omega_c^2}{\eta} ; \quad (2.7)$$

hence it follows that

$$\omega_p^2 = \frac{\eta \rho_0}{\epsilon_0} = \omega_c^2 . \quad (2.8)$$

Thus, in the absence of ions, the space-charge density in this type of beam is entirely controlled by the magnetic field, a condition first noted by Brillouin.<sup>10</sup>

A slightly more general form of laminar flow has been discussed by Gould.<sup>5</sup> Thus if Eq. (2.2a) (with  $\dot{y} = \ddot{y} = 0$  as before) is combined with Eq. (2.3) we obtain for the velocity gradient across the beam

$$\frac{\partial v(y)}{\partial y} = \frac{\eta \rho_0}{\epsilon_0 \omega_c} = \frac{\omega_p^2}{\omega_c} . \quad (2.9)$$

Equation (2.5) has not been used in the derivation of this expression. Consequently, if  $\omega_p \neq \omega_c$ , the implication is that all electrons in the beam need not have the same total energy,<sup>(1)</sup> and that  $\rho_0$  and hence  $\omega_p$  may not be constant across the beam. Hereafter in referring to "Brillouin" or "planar" flow, we shall be speaking of the monoenergetic beam characterized by Eqs. (2.6) and (2.8).

The properties of the laminar beam from an equipotential cathode are largely determined by the boundary conditions of the interaction region. If the magnetic field, the sole and circuit voltages, and the sole-current spacing are specified, only one degree of freedom, the beam thickness, or equivalently, the total beam current per unit width, remains. This follows as a result of the postulate of linear trajectories and because the magnetic field determines the charge density. The linear superposition of the field due to space charge and that supplied by the

---

<sup>(1)</sup> This would be the case for a beam in the presence of rf fields.

external electrodes, when divided by the magnetic field, then uniquely determine the velocity at any point in the beam.

b. Nonlaminar Single Trajectory Model

We define a "single trajectory" beam as one in which all electron trajectories are congruent in the geometric sense. Thus the Brillouin beam may be considered as the simplest type of single trajectory flow.

We now consider a more complex form of flow which is nonlaminar and which consists of a manifold of congruent periodic trajectories uniformly distributed in the direction of flow as shown in Fig. 2.3a. The motion is double streaming, with electrons moving between the beam boundaries which are envelopes of the trajectory turning points. On the boundaries the space-charge density is infinite. The beam is composed of two classes of electrons, one with  $\dot{y} > 0$  the other with  $\dot{y} < 0$ . The total net current associated with the transverse motion of these two classes of electrons must be zero and at any point  $|\dot{y}|$  must be the same for each class. Moreover, the trajectories must be symmetrical about the turning points.

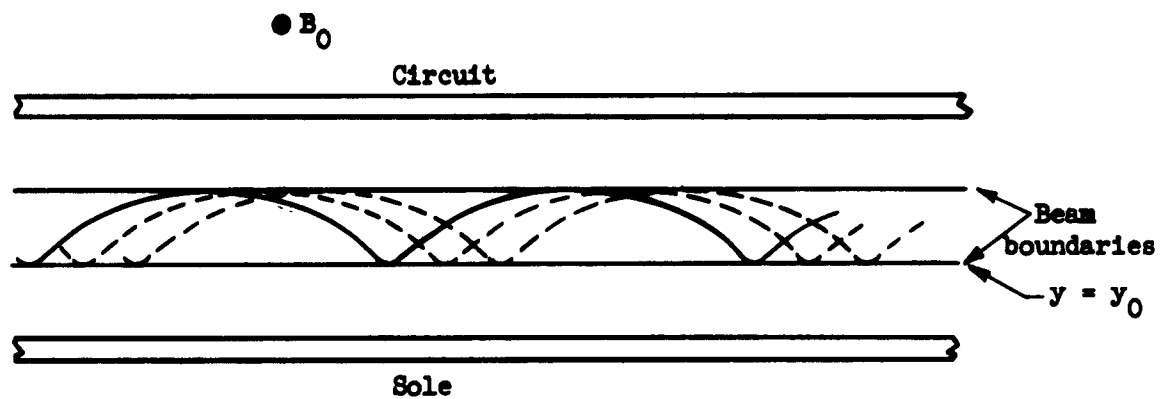
By means of an analysis essentially the same as for the plane magnetron,<sup>2,7</sup> we may obtain the equations of the trajectories. We define a transverse current density  $J_y$  such that

$$J_y = \rho_0 \dot{y} = 2 |J_y^+| = 2 |J_y^-| , \quad (2.10)$$

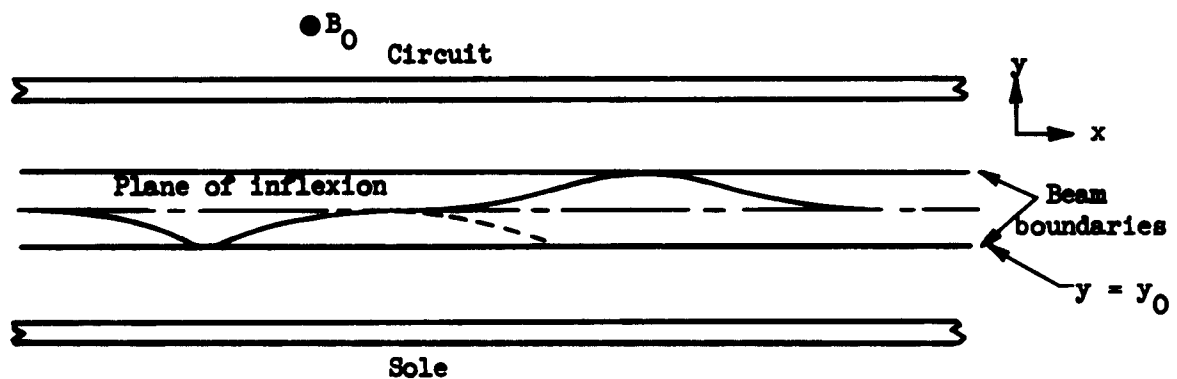
where  $J_y^+$  and  $J_y^-$  are the current densities associated with the two components of the double streaming flow. We further assume that the beam originates, with zero velocity, from a cathode which does not intercept magnetic flux. Under these conditions it can be shown that the curl of the generalized momentum  $m\mathbf{v} - e\mathbf{A}$  (where  $\mathbf{A}$  is the magnetic vector potential) must vanish everywhere in the beam. It follows that  $m[\dot{x} - \omega_c(y - y_0)]$  which we define as  $p_x$ , is a constant of the motion, equal for all electrons in the beam.

We consider a single trajectory such that at time  $t = 0$  the electron following this trajectory is on the lower edge of the beam at  $y = y_0$ . As the electric field has only a  $y$  component we may write

$$\frac{dE_{Oy}}{dt} = \frac{\rho_0}{\epsilon_0} \dot{y} = \frac{J_y}{\epsilon_0} ; \quad (2.11)$$



a. Nonstriated



b. Striated with one internal striation

FIG. 2.3--Single trajectory beam.

hence

$$E_{Oy} = \frac{J_Y}{\epsilon_0} t + E_{Oy}^- , \quad (2.12)$$

where  $E_{Oy}^-$  is the transverse electric field at the lower edge of the beam. By substituting this expression into Eq. (2.2a) and integrating, noting that at the turning points  $\dot{y} = 0$ , we obtain

$$y - y_0 = \left( \frac{\eta E_{Oy}^-}{\omega_c^2} - \frac{p_x}{\omega_c m} \right) (1 - \cos \omega_c t) + \frac{\eta J_Y}{\epsilon_0 \omega_c^3} (\omega_c t - \sin \omega_c t) . \quad (2.13)$$

Substituting Eq. (2.13) into Eq. (2.2b) and integrating, results in the other trajectory equation

$$\begin{aligned} x - x_0 = & \left( \frac{\eta E_{Oy}^-}{\omega_c^2} - \frac{p_x}{\omega_c m} \right) (\omega_c t - \sin \omega_c t) + \frac{\eta J_Y}{\epsilon_0 \omega_c^3} \left( \frac{(\omega_c t)^2}{2} + \cos \omega_c t - 1 \right) \\ & + \frac{p_x}{\omega_c m} (\omega_c t) . \end{aligned} \quad (2.14)$$

Here  $y_0$  and  $x_0$  are the coordinates of the electron at the lower edge of the beam at  $t = 0$ .

We note from Eq. (2.13) that  $\dot{y}$  and  $\ddot{y}$  vanish when  $\omega_c t$  assumes even integral multiple values of  $\pi$  if and only if

$$\left( \frac{\eta E_{Oy}^-}{\omega_c^2} - \frac{p_x}{\omega_c m} \right) = 0 . \quad (2.15)$$

This requirement is equivalent to specifying that the net acceleration experienced by an electron at the lower edge of the beam is zero. If this condition is satisfied, the beam becomes "striated" (see Fig. 2.3b) with internal planes of inflection which have infinite charge density as do the beam boundaries. At the values of  $y$  corresponding to these striations,  $\dot{y}$  and  $\ddot{y}$  are both zero so that the transverse motion may reverse its direction, that is,  $\dot{y}$  may undergo a change in sign.

Consequently, the double streaming may occur between striations as well as between the actual beam boundaries.

Adequate discussions of these striations and the associated double streaming effects have been given in conjunction with the theory of the plane magnetron.<sup>2,7</sup> The principal distinction between the case of the magnetron and beam which we have discussed is the nature of the boundary conditions at the lower edge of the space charge. Thus in the case of the magnetron, this boundary is at the cathode, and ignoring thermal velocity effects, the vanishing of  $E_{Oy}$  here is a necessary condition for striations, while for the beam the more general statement of Eq. (2.15) must be true.

Externally, the striated beam is indistinguishable from a Brillouin flow beam since for a given longitudinal current per width in the  $z$  direction, the striated beam has the same thickness, the same position relative to the sole and circuit, and the same potential and fields on its boundaries as does the planar beam. Indeed, the planar beam may be considered as the limiting case of an infinite number of striations.

If Eq. (2.15) does not hold, the beam is less compact and has a lower charge density than striated or laminar flow. In effect, such a flow has an extra degree of freedom associated with the value of the parameter in Eq. (2.15). In practice, it is thought that the various forms of the long gun (Chapter III) produce beams which approximate the nonstriated single trajectory model. To the knowledge of the author, neither the planar nor striated forms have been realized experimentally by previous workers.

## 2. Miller's Hydrodynamical Analysis

Miller<sup>8</sup> has considered the nonlaminar M-type of crossed-field beam from a somewhat different point of view. The single trajectory model is an application of the "Lagrangian formulation" of beam dynamics, in that electrons are considered as definite particles whose orbits are obtained explicitly as functions of the time. Miller adopts the hydrodynamical or "Eulerian" approach to take account of nonlaminar flow. Motion of the space-charge stream is described in terms of the local average velocity, the local average space-charge density, and a velocity distribution function which is a function of the phase space coordinates. It is assumed

that all particles within a given volume element of the stream must have equal speeds, but not necessarily equal velocities, thus permitting individual electron trajectories to cross. The distribution function then gives a measure of the angular spread in velocity direction about the average value in a given volume element in the stream.

The Lorentz equation in this hydrodynamic formalism is written as follows:

$$\frac{d\mathbf{v}_0}{dt} + \frac{\nabla \cdot (\rho_0 \tilde{\mathbf{P}})}{\rho_0} = \eta(\mathbf{E}_0 + \mathbf{v}_0 \times \mathbf{B}_0) \quad (2.16)$$

Here  $\mathbf{v}_0$  and  $\rho_0$  are the local average values of velocity and charge density. Coulomb forces are included in the electric field intensity  $\mathbf{E}_0$ . The term  $\tilde{\mathbf{P}}$  is an antisymmetric tensor completely analogous to the hydrodynamic pressure tensor. The components of  $\tilde{\mathbf{P}}$  are then of the form

$$P_{1j} = \frac{1}{\rho_0} \int u_1 u_j F d\mathbf{u} = \widehat{u_{1j}} \quad (2.17)$$

The subscripted  $u$ 's are the components in an orthogonal coordinate system of the vector  $\mathbf{u} = \mathbf{v} - \mathbf{v}_0$ , where  $\mathbf{v}$  ranges over all possible velocity directions. The distribution function  $F(\mathbf{v}, \mathbf{r})$  is defined such that

$$\int F d\mathbf{v} = \rho_0 \quad (2.18)$$

and hence

$$\mathbf{v}_0 = \frac{1}{\rho_0} \int F \mathbf{v} d\mathbf{v} \quad (2.19)$$

In the case of laminar flow,  $F$  becomes a  $\delta$  function, and  $u$  and hence all  $P_{1j}$  are identically zero.

This hydrodynamical formalism is used to analyze a nonlaminar M-type flow. Externally, this flow model is the same as that of the preceding sections in that the stream boundaries are rectilinear. In addition, the following assumptions are made. (Refer to Fig. 2.2.)



(1) The average stream velocity is assumed to have only an x component  $v_{Ox}$  and furthermore is assumed to be a linear function of y of the form  $v_{Ox} = \Omega y$ , where  $\Omega$  is a constant determined by the internal nature of the stream.

(2) The charge density  $\rho_0$  is assumed to be uniform across the stream, and the average stream motion is assumed to be invariant in x and z.

Under these assumptions all elements of  $\tilde{P}$  in the stream, except  $\sqrt{u_x^2}$  and  $\sqrt{u_y^2}$  are zero. From Eq. (2.16), Poisson's equation and the conservation of energy, the magnitudes of these two quantities are obtained as a function of the stream parameters and the local position in the stream. While the detailed nature of the nonlinear trajectories is not specified, the quantity  $\sqrt{u_x^2} + \sqrt{u_y^2}/v_{Ox}^2$  is considered to be a direct measure of the nonlaminarity of the flow.

The significant results of the analysis may be stated qualitatively as follows:

(1) For a given beam geometry and external environment,  $\sqrt{u_x^2} + \sqrt{u_y^2}/v_{Ox}^2$  increases with decreasing charge density  $\rho_0$ .

(2) For a given charge density and external environment, this same nonlaminarity parameter is larger for thick streams  $[y_0/(y_0 + \delta) \ll 1]$  than for thin streams  $[y_0/(y_0 + \delta) \approx 1]$ .

(3) Under all conditions,  $dv_{Ox}/dy \geq \omega_c$ , the equality being true only in the case of Brillouin flow.

It may be noted that (1) is in general agreement with the results of the other nonlaminar analysis given in this chapter. Conclusion (2) is interpreted by the author to imply that, for thick streams, nonlaminar perturbations from the average stream motion may be large and hence that such average motion is a poor description of the true situation. For thin streams, however, the author concludes that since the perturbed quantities are relatively small, this model, based on the motion of an average stream, is a realistic one.

### C. WATERS' PARAXIAL WORK

In a general paraxial analysis of crossed-field sheet beams, Waters<sup>9</sup> has considered a model, based on small amplitude departures from the Brillouin flow conditions, which is characterized by periodically undulating boundaries. This analysis assumes the nature of the central

"ray axis" to be specified in advance. The flow then consists of small extensions on either side of the ray axis. Furthermore, angles between the trajectories of edge electrons and the ray axis are assumed to be small. Under these restrictions a paraxial ray equation relating beam thickness to path length along the ray axis is derived. This equation is

$$2\phi\xi'' + \phi'\xi' + \xi(4K^2\phi + \phi'' + 2KB_0v - \eta B_0^2) = \pm \frac{|I_0|}{2\epsilon_0 w \sqrt{-2\eta\phi}} \quad , \quad (2.20)$$

where

$s$  = arc length, measured from any convenient point on the ray axis

$\phi$  = beam potential as function of arc length on the ray axis

$\xi$  = beam thickness as a function of arc length

$K$  = curvature of the ray axis as a function of arc length

$v$  = beam velocity

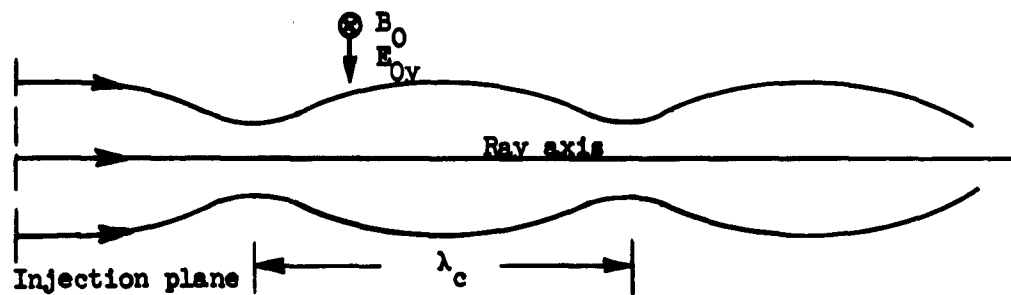
$w$  = beam width, a constant

$I_0$  = total beam current

' denotes differentiation with respect to  $s$ .

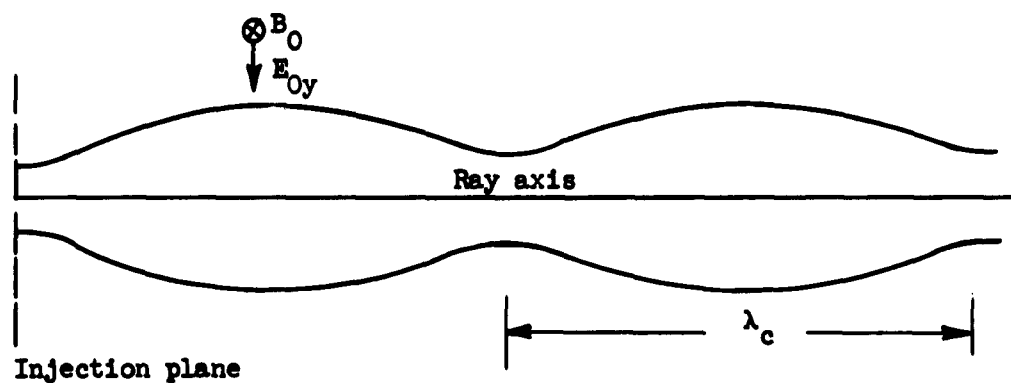
The solutions of Eq. (2.20) are examined by Waters for a number of specific geometries and boundary conditions. For M-type geometry where the ray axis is linear, necessary conditions for an unrippled beam ( $\xi$  = constant) are found to be: (1) the flow must be parallel to the ray axis at the plane of injection and (2) the total current, velocity and beam thickness must be related such that  $\omega_c = \omega_p$ . If these conditions are not fulfilled, the paraxial analysis predicts boundary rippling with a period corresponding to the cyclotron wavelength  $\lambda_c$ . In the cases where the current is too small or too large, the rippling beam is found to have an average thickness for which  $\omega_c = \omega_p$ . The various possible flows are illustrated in Fig. 2.4.

Waters' analysis also provides quantitative information about the magnitude of departure from Brillouin flow. In particular, a necessary condition was found so that crossing of the ray axis would not occur. This criterion is that  $\omega_p^2/\omega_c^2 \geq \frac{1}{2}$ . It is interesting to compare this result with the conclusion which Miller draws from his nonlaminar model. Miller's analysis predicts that the maximum degree of nonlaminarity which



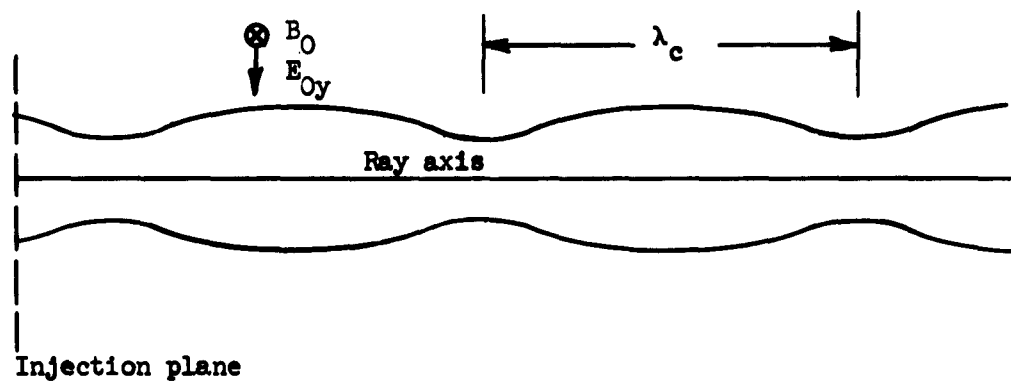
a. Current too small

$$\omega_p^2 < \omega_c^2$$



b. Current too large

$$\omega_p^2 > \omega_c^2$$



c. Nonparallel flow at injection plane

FIG. 2.4--Nonparallel flow as predicted by paraxial theory.

can occur in a beam of given dimensions is proportional to a term  $(1 - \omega_p^2/\Omega^2)$  where  $\Omega \geq \omega_c$ , the equality occurring for regular Brillouin flow. Thus, in spite of the quite different nature of the two models, they both predict the severest nonlaminarities for small values of the ratio  $\omega_p/\omega_c$ .

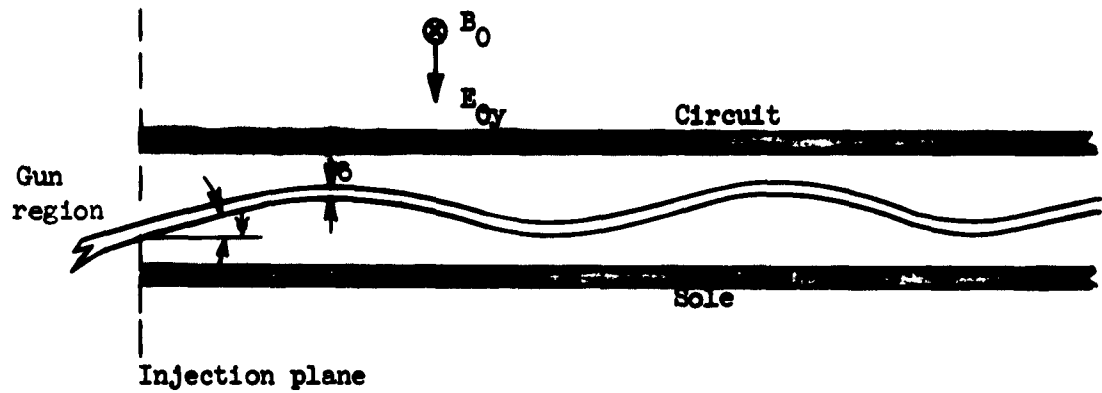
#### D. UNDULATING BEAMS RESULTING FROM IMPROPER INJECTION OPTICS

In the preceding sections we have considered examples of nonlaminar flow which may exist in the same environment as the planar flow. Each of the models considered is intrinsically nonlaminar, that is, they are characterized by crossing trajectories and for the most part by lower charge densities than that required by the Brillouin condition [Eq. (2.8)].

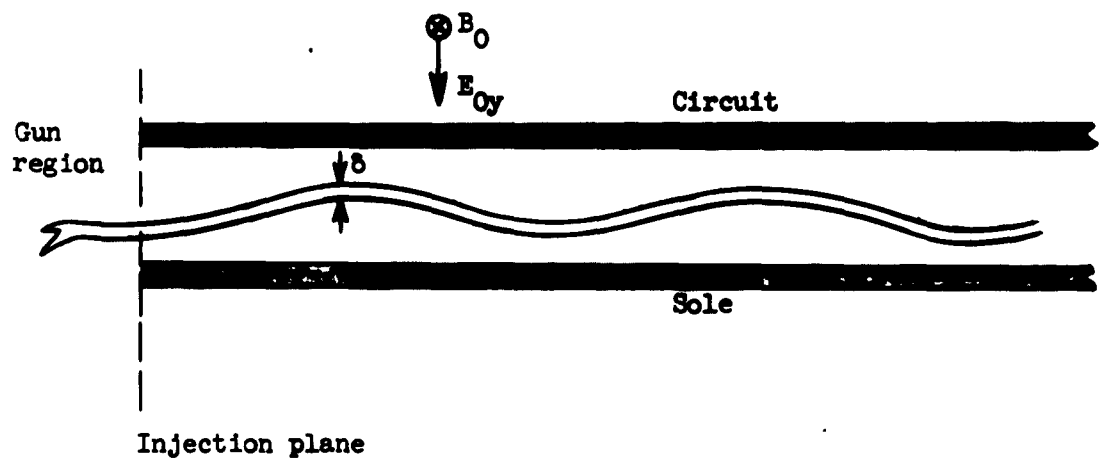
We now consider another form of perturbed Brillouin flow. It may be assumed in practice that intrinsically nonlaminar beams are the result of inadequate gun optics. But even assuming a gun which is capable of accelerating and focusing a beam so that at the gun exit the beam fulfills the Brillouin conditions, certain matching conditions at the gun exit plane must be satisfied if Brillouin flow is to be achieved in the interaction region. Thus, if at the plane of injection a discontinuity in the external fields or potential exists, or if the beam is injected nonparallel to the plane of the sole, the beam will not be planar in the interaction region. The typical behavior of beams under the influence of errors in injection optics is shown in Fig. 2.5. In Fig. 2.5a the beam is injected nonparallel to the sole plane and in Fig. 2.5b a discontinuity in  $E_{Oy}$  exists at the gun exit.

In this section we shall consider the nature of a well defined beam (which may or may not satisfy the Brillouin conditions) which is injected into the interaction region under the influence of such errors in injection optics. It should perhaps be pointed out that, in the course of some of the experimental work, observations were made which tended to indicate that undulating beams of this type might be subject to dc instabilities. More details will be given in a later section of this work (Chapter V), but it may be noted here that the experimental results have provided the motivation for work which is described in this section.

In the absence of space-charge effects the motion of a charged particle in a region of uniform crossed fields is well known. In



- a. Beam is injected nonparallel to planes of circuit and sole



- b. Discontinuity in electric field between gun and interaction region

FIG. 2.5--Beam undulations resulting from errors in the injection optics.

particular, if the particle is injected into the uniform field region with velocity whose magnitude is  $E_0/B_0$  and a direction normal to both  $\underline{E}_0$  and  $\underline{B}_0$ , the resulting trajectory is linear. If the injection conditions are only slightly different from those for the linear trajectory, the motion is approximately sinusoidal with a periodic length  $\lambda_c$ . The motion of a thin beam<sup>(2)</sup> injected under such conditions might be expected to be similar, although in the case of Brillouin or near-Brillouin beams, space-charge forces may well be of sufficient magnitude to substantially alter the motion of the beam.

Little attention has been given to this problem in the literature. Waters<sup>9</sup> has shown on the basis of his paraxial theory that the focusing properties of crossed-fields hold even though the ray axis is sinusoidal. Thus on the basis of dc considerations, one would expect the beam thickness  $\delta$  to be constant or at worst, periodic, as the undulating beam drifts through the interaction region. Pierce<sup>11</sup> has predicted that no dc instabilities of the sort observed with cylindrical hollow crossed-field beams should be found in the case of planar beams. On this basis the magnitude of the undulations would presumably be a constant which is determined by the entrance conditions and uniform fields in the drift region.

In an attempt to gain further insight into the nature of such undulating beams, a dc small-signal field analysis including space-charge effects has been made for the case of a thin beam. The details are found in Appendix A. A significant difference exists between this analysis and those discussed in conjunction with other nonlaminar models in this chapter. All of the previous nonlaminar models specify only that a uniform static dc electric field is to exist in the region of the flow; however they do not consider the precise configuration of external electrodes which supply this field. The analysis in Appendix A takes into account not only the space-charge forces due to the beam itself, but, since impedances above and below the beam are matched to the circuit and sole electrodes, also the forces due to the images of the beam in these electrodes. As a result, the fields acting on the beam depend upon the relative spacing of the sole and circuit and on the position of the beam with respect to these electrodes.

<sup>(2)</sup> We shall assume the inequality  $\delta \ll \lambda_c$  to be the criterion for a thin beam.

We shall state the results of this analysis here. In the absence of space-charge effects, for a thin rippling beam whose parameters are assumed to vary longitudinally as  $e^{-j\beta x}$ , and in the absence of space-charge, we find as expected that

$$\beta = \pm \beta_c ; \quad (2.21)$$

however, when the effects of space charge are included, we obtain

$$\beta = \pm \alpha \beta_c - \beta_q , \quad (2.22)$$

where  $\alpha$  and  $\beta_q$  are real numerical factors which depend on the geometry, the charge density of the beam, and  $\beta_c$ .<sup>(3)</sup> These results have been calculated to first order in the quantity  $\beta_p^2/\beta_c$ , which is a small quantity in the thin beam approximation. Since  $\beta_q$  and  $|\alpha - 1|$  are also of first order in this quantity, the perturbing effect of the space-charge on the values of  $\beta$  is also small.<sup>(4)</sup>

The effects of the beam images in the sole and circuit become quite evident if we examine the constants appearing in Eq. (2.22) under some limiting or special geometries. Thus if the sole and circuit are spaced quite closely together in comparison to the beam wavelength so that  $\beta d \ll 1$ , we find that  $\beta_q = 0$  and

$$\beta \approx \pm \beta_c \left( 1 - \frac{\beta_p^2}{2\beta_c^2} \right)^{\frac{1}{2}} . \quad (2.23)$$

Under these conditions the fields acting on the beam due to the beam images in the sole and circuit become much stronger than is the case for larger values of  $d$ , and as a result the total space-charge effects may become quite large. Now if the beam is located midway between the sole

---

<sup>(3)</sup> Refer to Eq. (A.18) in Appendix A for the definition of these quantities.

<sup>(4)</sup> See an exception in the discussion of Eq. (2.14).

and circuit and if the inequality leading to Eq. (2.14) does not hold, we may show that

$$\beta \approx \pm \beta_c - \frac{\beta_q^2}{2 \sinh \beta_c d}, \quad (2.24)$$

and in the limit of large sole-circuit spacing such that  $\beta_c d \gg 1$ , we see that the propagation constant assumes the values given by Eq. (2.21) which were obtained by neglecting space-charge effects. An index of the space-charge perturbation is given by the magnitude of the quantity  $\beta_p^2 / \sinh \beta_c d$  as compared to  $\beta_c$ . For a Brillouin beam of 50 mm with

$$w = 1.1 \text{ in.}$$

$$(\phi_{ct} - \phi_s) = 500 \text{ v}$$

$$B_0 = 600 \text{ gauss}$$

$$d = .100 \text{ in.},$$

we find that

$$\frac{\beta_p^2}{\sinh \beta_c d} = 3.31 \times 10^1 \text{ m}^{-1} \text{ while } \beta_c = 1.62 \times 10^3 \text{ m}^{-1}.$$

Apart from these geometrical effects, the significant result of this analysis is that under no condition is any part of the propagation constant imaginary; hence the dc cyclotron motion which characterizes the motion of the beam as a whole is not subject to growth or decay in space, and as a result such a beam should not exhibit dc transverse cyclotron instabilities. Thus, in this respect our results are in agreement with those of Pierce.

In the case that  $\beta_q$  is nonzero so that the two values of the propagation constant given by Eq. (2.22) are unequal in magnitude, there exists the possibility of a beating phenomenon between the two solutions, assuming that both "waves" are excited. We thus might expect a periodic variation in the amplitude of the cyclotron undulation. Such a variation would then have a periodic length of order of magnitude  $\beta_c / \beta_p^2 \lambda_c$ , or for the beams which have been investigated experimentally, about 10-100 times  $\lambda_c$ . This phenomenon has not been observed experimentally



and the analysis has not therefore been carried further to the point of examining the effects of conditions at the entrance plane.

It may be noted here that growth and decay of the cyclotron undulations existing on a thin beam can occur if the externally applied transverse electric field is nonuniform and periodic. This effect has been strikingly observed experimentally and will be discussed later in this work (see Appendix D).

In concluding this discussion of non-Brillouin crossed-field flow, it should be emphasized that while for purposes of description and analysis the models have been treated individually, an actual beam produced experimentally might well exhibit the characteristics of more than one of the models. As a result, the complete description of such a beam would of necessity become somewhat more complex, although in the case of some of the models, the nonlaminar beams have been considered as first order perturbations from the laminar flow, and hence in principle these effects could be combined linearly in a more detailed analysis.

#### E. THE DESIGN OF CROSSED FIELD GUNS

In the previous sections we have considered the nature of some forms of steady-state space-charge flow which may exist in M-type uniform crossed fields. Little attention has been given to the means of launching such beams and to the effects that deficiencies in a particular gun structure might have on the nature of a beam after it has been injected into the interaction region. Instabilities usually associated with such crossed-field beams, which are evidenced by sole current<sup>8,12,13</sup> and excessive noise,<sup>14</sup> have not been considered, although these may well be related to the dc state of the beam.

It is tempting to assume, although perhaps not with complete justification, that these instabilities are in some way related to, or at least are characteristic of, nonlaminar beams. In this respect, a type of multistream amplification might be a contributing factor. In any event, one could obtain a considerable amount of insight into the problem if it were possible to produce and identify planar Brillouin flow experimentally. As will be seen in the following chapter, earlier guns have not even approximately produced such beams, and it is from this point that the present work proceeds.

A crossed-field gun which is to establish Brillouin flow must accelerate and focus electrons from a cathode in such a manner that at the injection plane of the interaction region the beam boundaries are each parallel to the plane of the sole. If, as is usually the case, the cathode is a unipotential one, Eqs. (2.6) and (2.8) must also apply. At the exit plane of the gun, the potentials supplied by external electrodes must be continuous and the average speed of the beam at injection must be equal to  $E_0/B_0$  in the interaction region. These latter conditions, insofar as dc beam optics are concerned, may be closely satisfied by the correct location of, and the dc potentials applied to, the sole and circuit, and thus place no serious limitations on the gun.

The practical limitations of presently available cathode materials and the relatively high current densities required in the beam make a convergent gun very desirable. Whether the gun is to be operated temperature-or space-charge-limited is at present very much open to question. While in certain respects the space-charge-limited mode is more stable, particularly in terms of short-term cathode poisoning and emission "slumps," there is a considerable amount of evidence to indicate that the inherent crossed-field instabilities are related to space-charge-limitation at the cathode. This question will be discussed in somewhat greater detail in Chapter V.

A further characteristic of guns which are to be utilized in certain types of devices, particularly in the case of oscillators, is often desirable. Backward wave oscillators are tuned by varying the beam drift velocity which in turn is accomplished by adjusting the voltage on the circuit. Hence the emission current of guns used in these devices should be relatively insensitive to changes in circuit voltage.

### III. PREVIOUS CROSSED-FIELD GUN DESIGNS

#### A. INTRODUCTION

Previous to the work under discussion, electron guns for M-type crossed-field devices have usually been of one of the types referred to under the general classification of "short" or "long" guns. In the case of both of these forms, the entire gun is located in the same uniform dc magnetic field as the rest of the tube, and hence the electron ballistics within the gun are dependent on magnetic as well as electrostatic and space-charge forces. Moreover, space-charge forces have usually been ignored in the design of these two types of guns. A third type of gun which has received some attention makes use of a convergent "Pierce gun" in a shielded region free from dc magnetic field. The beam from such a gun is then injected into the rf interaction area through a transition region in which the magnetic field is gradually increased from zero to the value desired in the interaction region. In the following sections we shall consider each of these three types of guns, particularly in terms of their effectiveness in producing a beam characterized by regular laminar flow.

Neglecting space-charge effects, the two-dimensional motion of an electron in the M-type geometry may be quite generally described by the equations<sup>15</sup>

$$\omega_c = - \eta B_0 \quad (3.1a)$$

$$\underline{v}_0 = \frac{\underline{E}_0 \times \underline{B}_0}{B_0^2} \quad (3.1b)$$

$$\omega_c^2 r^2 = (\underline{v}_1 - \underline{v}_0)^2 \quad (3.1c)$$

Here  $\underline{v}_1$  represents the velocity with which the electron is injected into the uniform crossed-field region. The motion is that generated by a point on the circumference of a circle of radius  $r$  rotating with angular velocity  $\omega_c$  whose center is moving with constant velocity  $\underline{v}_0$ . The four possible types of cycloidal motion are shown in Fig. 3.1 in order of decreasing magnitude of  $r$  and increasing  $v_1$ . In Fig. 3.1a,

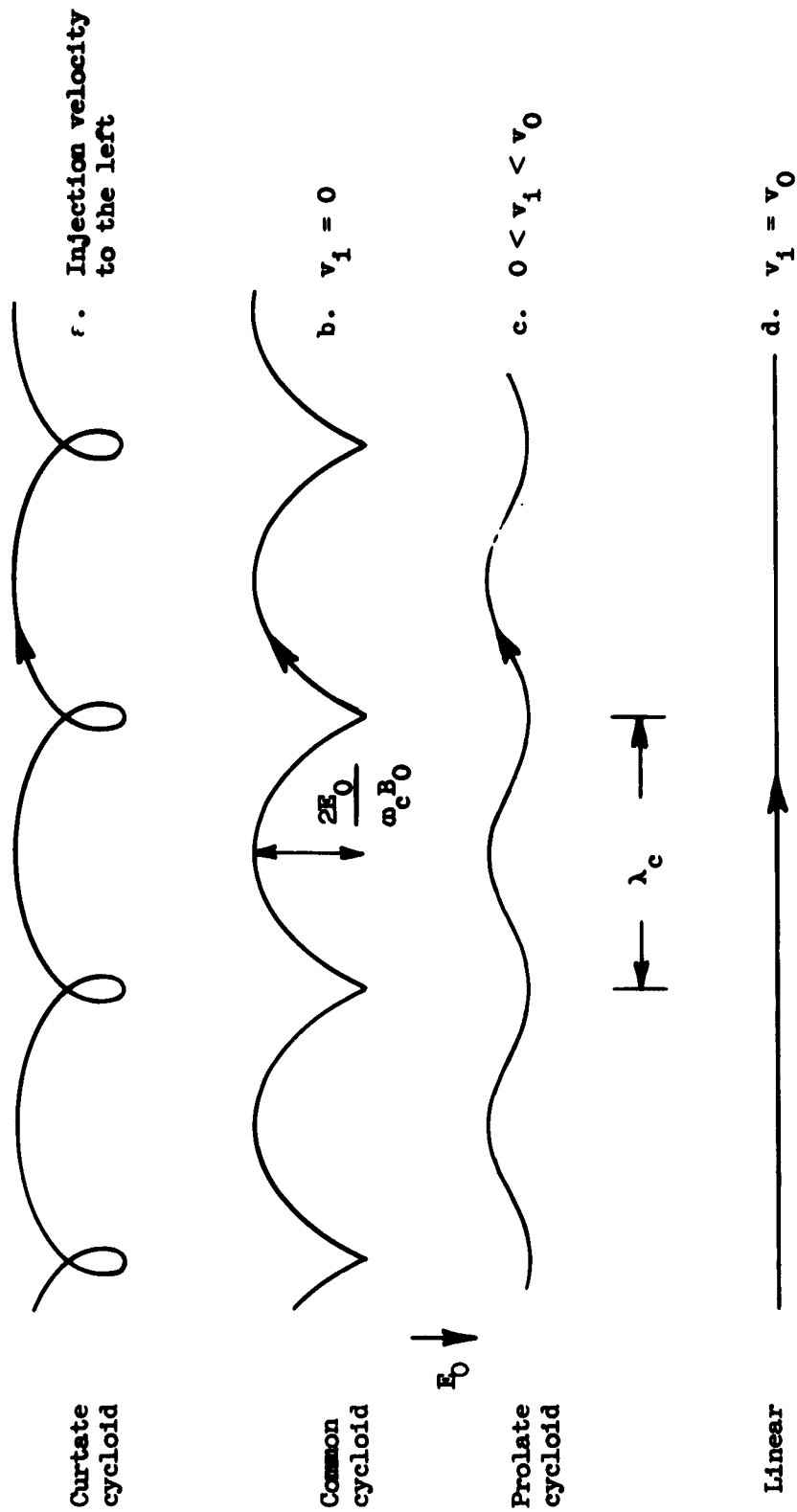


FIG. 3.1.--Various types of cycloidal motion executed by electrons in crossed uniform electric and magnetic fields. Magnetic field is perpendicular to plane of the figure. Arrows indicate direction of electron motion.

we have  $r > v_0/\omega_c$ , implying a negative injection velocity; in 3.1b we have  $v_1 = 0$ ; in 3.1c  $0 < v_1 < v_0$  -- in this case for sufficiently small  $r$  the motion is approximately sinusoidal; in 3.1d  $v_1 - v_0 = 0$  and the motion is linear. As  $v_1$  is further increased the classes of motion repeat in the reverse sequence. In each case the spatial periodicity of the motion is the cyclotron wavelength  $\lambda_c$ .

Now any type of simple gun structure which is immersed in a magnetic field,  $B_0$ , will usually be characterized by having cycloidal electron trajectories like that in Fig. 3.1b, at least to the approximation of negligible thermal velocities at the cathode and ignoring the effects of space-charge. But since it is desired that after the beam leaves the gun it be characterized by linear trajectories as in Fig. 3.1d, a suitable gun must be capable of transforming the cycloidal trajectories into linear motion at the point of injection into the interaction region. If this transition is accomplished in a distance less than one cyclotron wavelength, the gun is usually referred to as a "short" gun, while if several or many cyclotron wavelengths are needed, the gun is designated as a "long" gun.

#### B. THE SHORT GUN

The geometry for a common form of short gun is shown in Fig. 3.2. Neglecting space charge and thermal velocities at the cathode, the trajectory of an electron from the cathode is a common cycloid as in Fig. 2.1b.<sup>(5)</sup> At the top of the cycloid, moreover, the electron velocity is  $2E_0/B_0$  and is perpendicular to both  $E_0$  and  $B_0$ . At this point the electric field is abruptly increased by a factor of two by adjusting both the position and potentials of the sole and circuit elements correctly. Under these conditions electrons from a single point on the cathode would be injected into the interaction region with exactly the proper  $v_1$

---

<sup>(5)</sup> On the basis of paraxial theory, Waters<sup>9</sup> has shown that in the presence of space-charge forces the trajectories are not cycloidal near the cathode.

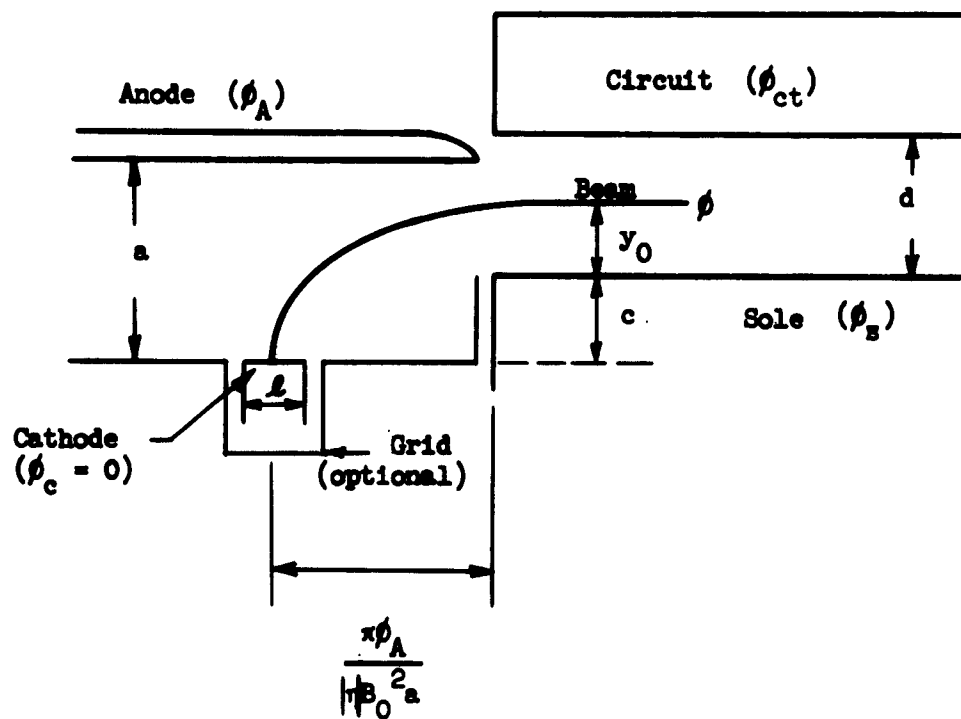


FIG. 3.2--Typical short gun geometry.

for linear flow. For such electrons the following relations must hold:

$$\frac{2\phi_A}{a} = \frac{(\phi_{ct} - \phi_s)}{d}, \quad (3.2a)$$

which expresses the above-mentioned field discontinuity at the gun exit,

$$(y_0 + c) \frac{\phi_A}{a} = (\phi_{ct} - \phi_s) \frac{y_0}{d}, \quad (3.2b)$$

which implies potential continuity along the beam

$$\phi = \phi_A \frac{(c + y_0)}{a}, \quad (3.2c)$$

which insures conservation of energy, and

$$c + y_0 = \frac{2\phi_A}{|\eta B_0|^2 a}, \quad (3.2d)$$

which specifies the half-cycloidal nature of the gun trajectories. For definitions of the symbols, refer to Fig. 3.2.

For a given beam voltage  $\phi$  and  $B_0$  the other voltages and the dimensions of the system are related by these equations. The beam voltage may be varied without changing the shape of the trajectory by varying all other voltages proportionally, provided that at the same time  $B_0$  is varied as the square root of the voltage. It should be noted further that in practice the gun anode is placed just above the position grazing the top of the cycloid in order to achieve maximum perveance. In addition a negative grid, the so called "Wehnelt" electrode, may be located as shown in Fig. 3.2 to supply an extra degree of freedom in adjusting the transition region field and as a means of shielding the cathode from effects of tuning the circuit voltage.

While the above considerations may be reasonably valid for a single electron trajectory from a cathode of very small length  $\ell$ , certain difficulties arise when  $\ell$  is not small. Ignoring space-charge forces,

the edge trajectories from a cathode of finite length would be expected to cross near the exit of the gun. Thus, not only is the practical convergence of such a gun limited, but in addition, the beam could be expected to be nonlaminar and exhibit crossing trajectories in the interaction region away from the gun.<sup>(6)</sup> In practice it appears that due to space-charge forces the crossover problem may not be so severe. Figure 3.3 shows the edge trajectories from a cathode of finite width for a short gun geometry as given by Miller and Larson.<sup>16</sup> These trajectories were obtained by using an analog trajectory tracer. Figure 3.3a shows the trajectories obtained neglecting space-charge, while Fig. 3.3b shows the same edge trajectories when an approximate computation of space-charge effects was included in the calculation. The convergence of the latter gun is seen to be quite limited, although trajectory crossing is not apparent. In practice it may be supposed that a space-charge-limited short gun is characterized by both trajectory crossing and unwanted space-charge spreading.<sup>(7)</sup>

In spite of these difficulties the short gun has been widely used both in commercial crossed-field tubes and in various types of experimental crossed-field devices.<sup>8,18,19</sup>

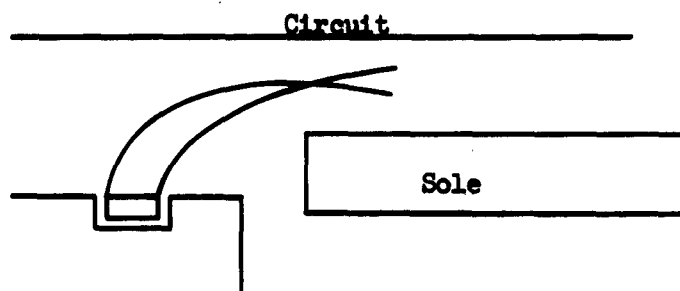
### C. THE LONG GUN

Figure 3.4 shows a number of possible idealized long gun geometries for thin beams as given by Wightman.<sup>19</sup> The guns in 3.4a and 3.4b utilize a periodic variation in transverse electric field as a means of damping the cyclotron undulations on the beam. The periodicity in  $E_0$  for these two cases is  $\lambda_c/2$ . Figures 3.4c and 3.4d illustrate a second form, characterized by a monotonically increasing transverse electric field  $E_0$ , the variation occurring discontinuously in intervals of  $\lambda_c$ . It is quite clear from these four illustrations that guns of these types, depending upon periodic and discontinuous jumps in  $E_0$  (and hence  $v_0$ )

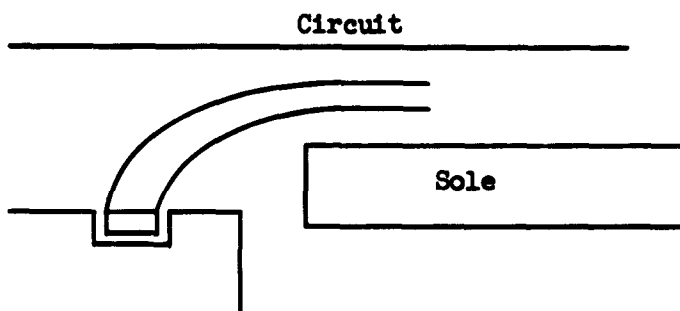
<sup>(6)</sup> French workers<sup>17</sup> have reported that larger cathodes tend to increase beam thickness and decrease the useful beam efficiency by increasing the velocity spread. A maximum value of the ratio  $l/a$  of 2 to 5 is reported.

<sup>(7)</sup> See sketches of crossed-field beams in geometries similar to the short gun observed by gaseous discharge techniques and reported by Van Duzer,<sup>20</sup> page 96.





a. Without space charge



b. Including space charge

FIG. 3.3--Short gun trajectories calculated by Miller and Larson.

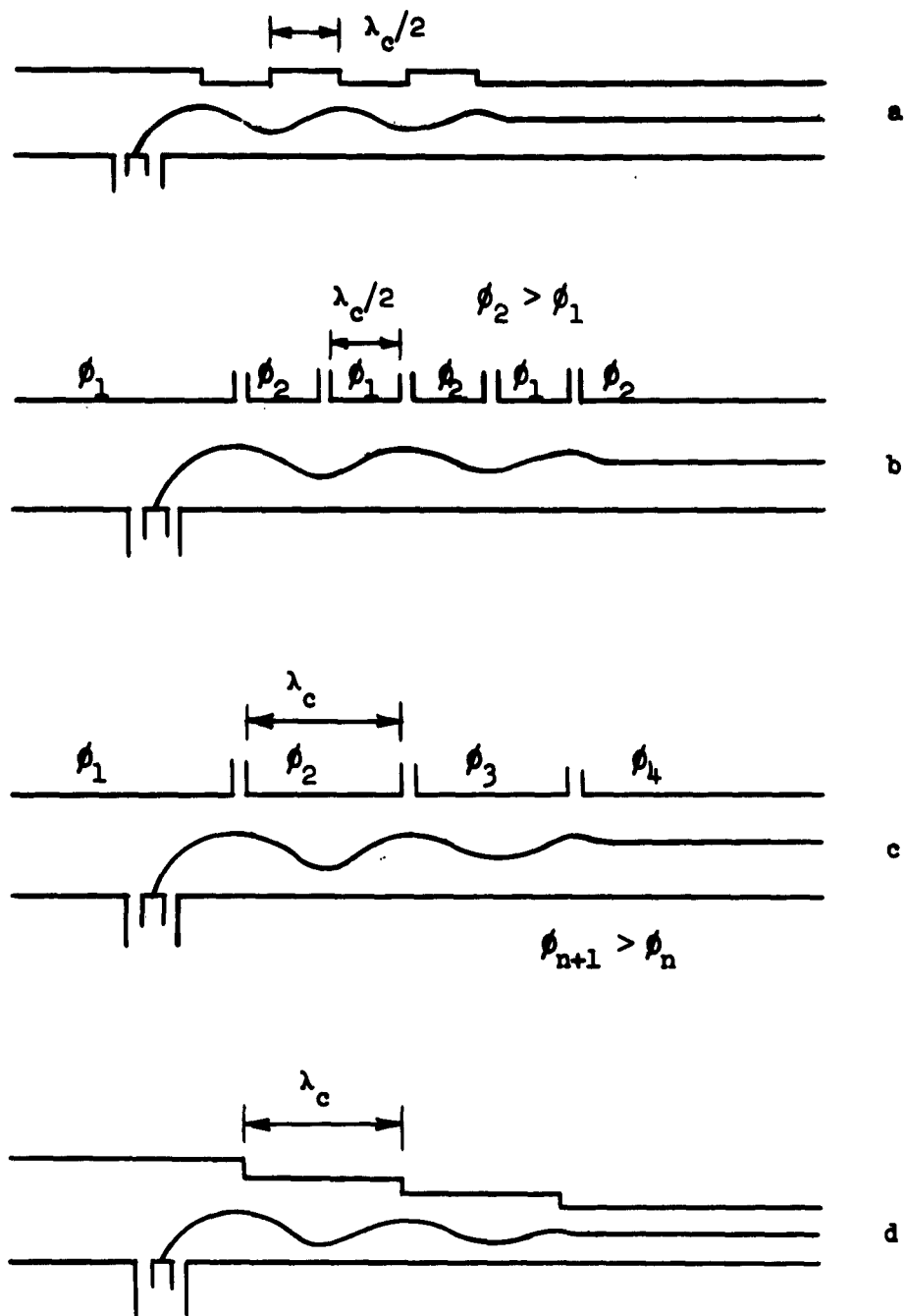


FIG. 3.4--Some possible long gun configurations. (After Wightman)

a,b .Attenuation of cyclotron waves by periodic transverse electric field

c,d Monotonic increase of transverse electric field

are only feasible for thin beams from short cathodes.

A useful modification of the form shown in Fig. 3.4d is found in the adiabatic gun illustrated in Fig. 3.5.<sup>15</sup> In this case  $E_0$  is increased continuously, but slowly over the length of the gun. The term "long gun" is usually in reference to this form.

The adiabatic gun is based on an application of Ehrenfest's principle of adiabatic invariance. For the dynamical system composed of an electron under M-type crossed-field conditions and ignoring space-charge effects, it can be shown that the quantity  $\omega_c r^2$  is invariant under changes in external fields, provided that these changes take place in a period  $\tau$  such that  $\tau \gg 2\pi/\omega_c$ . Equivalently, one may consider variations in time to be brought about by the drift velocity of an electron carrying it through a region where the fields have a spatial dependency. In this case adiabatic invariance requires that any spatial variation in fields be small in the distance traveled by an electron during the time  $\tau$ . Using the invariance condition in conjunction with the trajectory Eqs. (2.1a), (2.1b), (2.1c) in both the cathode region and in the interaction region, relationships which determine the beam thickness in the interaction region are obtained:

$$\frac{y_{\max}}{d} = \frac{1}{4} \left( \frac{B_c}{B_1} \right)^2 (1 + f)^2 \quad (3.3a)$$

$$\frac{y_{\min}}{d} = \frac{1}{4} \left( \frac{B_c}{B_1} \right)^2 (1 - f)^2 \quad (3.3b)$$

$$2 \frac{r_1}{d} = \left( \frac{B_c}{B_1} \right)^2 f \quad (3.3c)$$

$$f = \left( \frac{E_0}{E_1} \right) (B_1/B_0)^{3/2} = \frac{E_0}{E_1} \quad \text{for uniform B} \quad (3.3d)$$

$$B_c = \left( \frac{(2E_1)}{r_1 d} \right)^{1/2} \quad (3.3e)$$

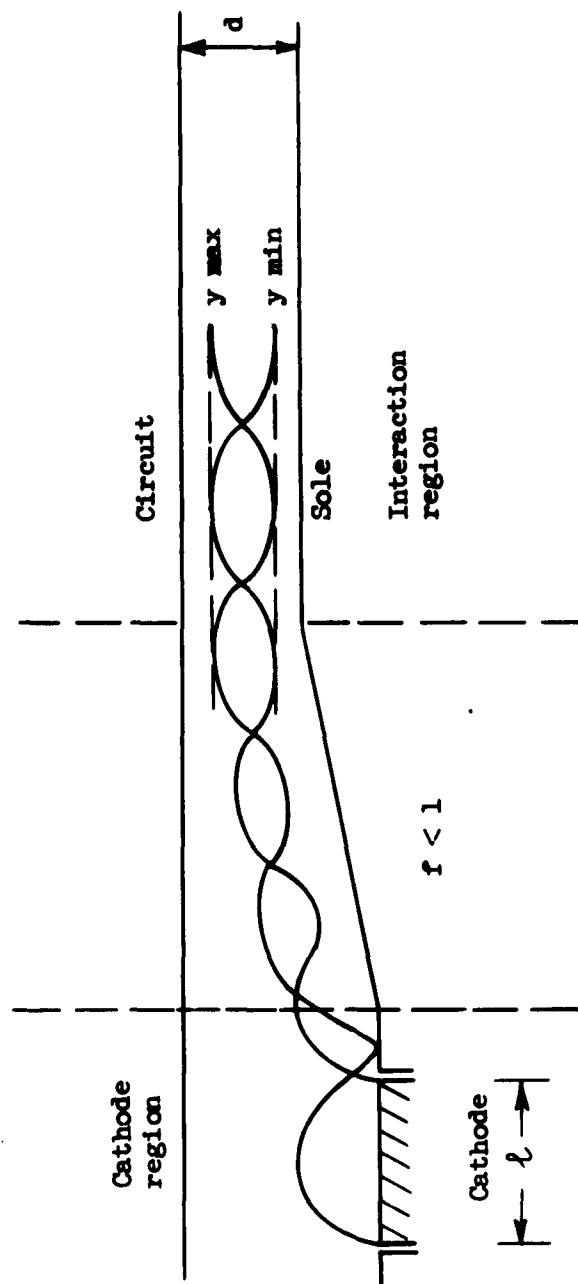


FIG. 3.5--The adiabatic long gun.

Here the subscript 0 refers to quantities in the cathode region and the subscript 1 refers to quantities in the interaction region. For the case of  $f = 1$  the motion (again ignoring thermal effects at the cathode) is that shown in Fig. 3.1b. For  $f < 1$ ,  $|y_{\max} - y_{\min}|$  in the interaction region is less than would be the case for parallel electrodes in a uniform field, thus resulting in an increase in beam compactness with no restrictions on  $l$ ; however, as shown, the beam in the interaction region would be expected to be completely nonlaminar with all trajectories crossing all others. However, under certain conditions a beam with linear trajectories might in principle be realized: For if  $r_0 = 0$  in the cathode region, the invariance of  $\omega_c^2 r$  implies  $r_1 = 0$  for nonzero magnetic fields. But in the cathode region, we have

$$r_0^2 = \frac{1}{\omega_c^2} (v_1 - v_0)^2 \quad (3.4)$$

Now if  $E_0$ , and hence  $v_0$ , and in addition  $v_1$  are zero at the surface of the cathode, then  $r_0$  is also zero. But, ignoring thermal velocity effects, these conditions are fulfilled at the surface of a space-charge-limited cathode. Subject only to the condition that space charge and hence electric field should vary adiabatically,<sup>(8)</sup> electronic trajectories should be smooth streamlines in the gun region and linear in the interaction region.

A form of the adiabatic long gun was first proposed by Guenard and Huber.<sup>13</sup> They describe its use in an experimental crossed field device for studying excessive sole current and the diotron effect. More recently Bartram and Pease<sup>21</sup> have proposed the so-called "Ramp Gun." This form of the adiabatic gun which includes the effect of space charge uses a series of overlapping electrodes or ramps, fixed at different potentials to achieve the adiabatic variation in electric field.

It should be noted that no restriction has been placed upon the precise nature of the varying fields between the cathode region and the interaction region. The only requirement is that of adiabatic variation. It may be further noted that in one specific geometry, characterized by a

---

<sup>(8)</sup> These conditions may well not be valid very near the cathode where the beam potential varies as the four-thirds power of path length measured from the cathode.

uniform  $B_0$  and a varying  $E$  produced by hyperbolic electrodes, it is possible, neglecting space-charge effects, to obtain the electronic trajectories directly.<sup>22</sup> The results are found to be in agreement with adiabatic theory, provided that  $E$  is made to vary sufficiently slowly.

#### D. THE SHIELDED GUN

The discussion of the final form of crossed-field gun to be considered in this chapter, the so-called shielded gun, is based primarily on the work of Hoch and Watkins.<sup>23</sup> The geometry of the gun is shown in Fig. 3.6. Here a convergent Pierce type gun forms a strip beam of electrons in a region completely free of magnetic field. In the fringing region, the variation in  $B_{Oz}$ , along the center axis of the beam, was determined analytically and the transition electrodes shaped so as to provide a constant ratio of  $E_{Oy}/B_{Oz}$  along the same center axis of the beam. The behavior, in the fringing region, of a beam of finite thickness, i.e., a beam whose edge trajectories are displaced from the stable center axis, was investigated analytically. The analysis took account of space-charge effects. The results indicated that in the transition region a finite beam would be characterized by undulatory rather than linear boundaries and by periodically varying beam thickness with a spatial periodicity of approximately  $\lambda_c$ . Experimentally, only limited success was obtained with the gun and focusing system.

However, the principal difficulties seemed to lie with the shielded gun rather than in the fringing region; for it was found that 20 to 30 per cent of the total cathode current was intercepted by the focusing anodes in the gun, while as much as 95 per cent of the current which entered the crossed-field region could be focused to the collector. In view of the undulating nature of the beam boundaries in the transition region, the beam would certainly be expected to be nonlaminar in the interaction region, although probably less nonlaminar than a beam from the general form of the adiabatic gun. Thus while in principle the shielded gun could provide a focusing system with a convergence of perhaps ten to one, in its present form it exhibits a number of disadvantages, not the least among these, in the opinion of the author, being its relatively high degree of complexity.

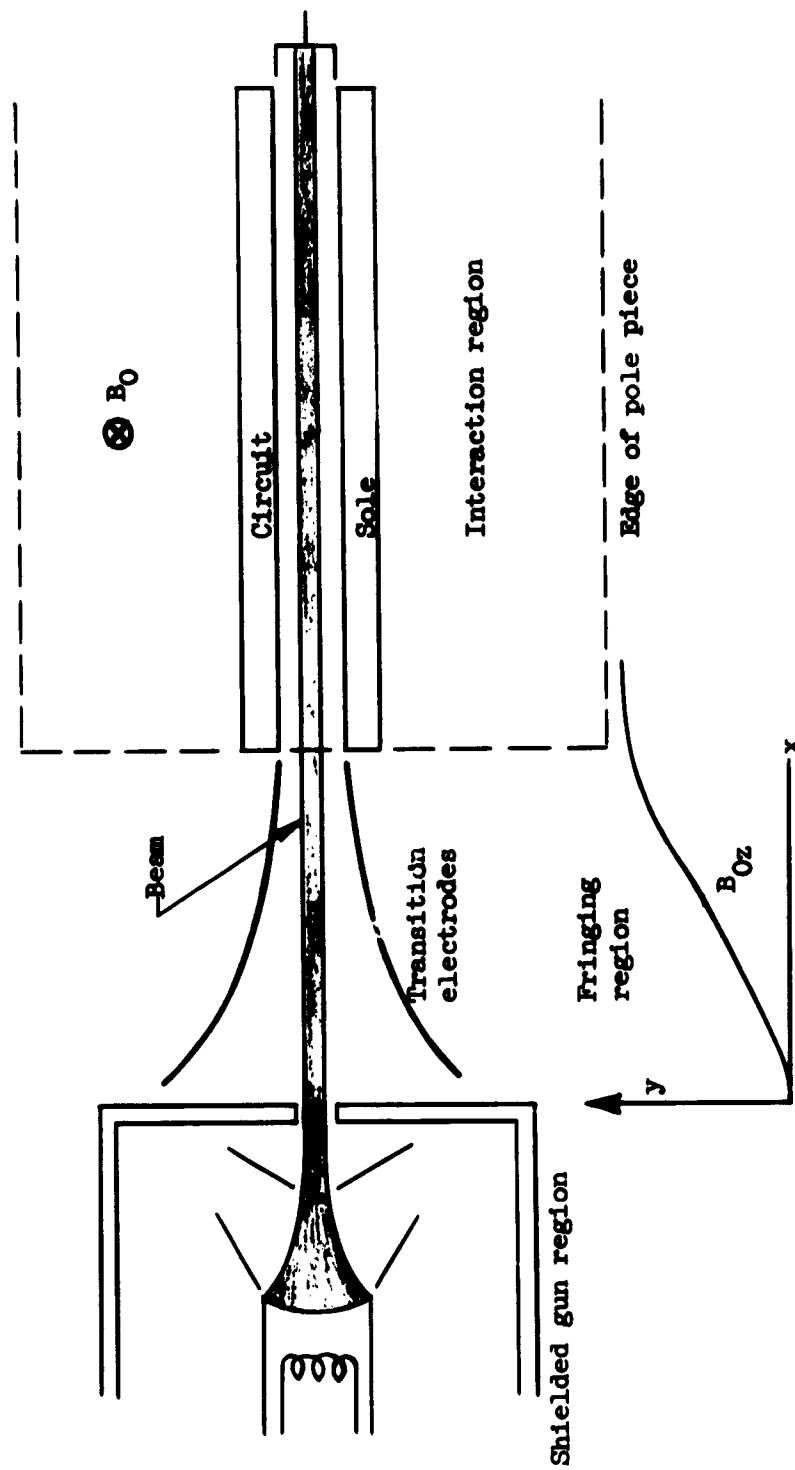


FIG. 3.6--Shielded gun geometry.

A possible advantage of the shielded gun over the nonshielded types should be mentioned. Since the cathode region is free of magnetic field, instabilities resulting from magnetic effects at the potential minimum should be absent. It is thought (see Chapter V) that such instabilities, if indeed they exist, are related to the excessive sole current usually observed in M-type crossed-field devices. The relatively high transmission through the region of uniform crossed fields achieved with the experimental shielded gun indicates small values of sole current, although no direct measurements of sole current were reported. Experimentally, the possibility of increased beam stability resulting from a shielded cathode is still open to question.

In summary, a number of possible schemes for M-type crossed-field guns have been presented. All of these guns have been studied experimentally, and one form, the short gun, has been used extensively in devices. All of these guns, moreover, represent only an approximation to the fundamental problem of producing a convergent space-charge flow in a crossed field. Practical guns have been limited to convergences of the order of unity, and the resulting beams have most certainly been nonlaminar.



#### IV. THE ANALYTICAL DESIGN OF CROSSED-FIELD GUNS

##### A. INTRODUCTION

In this chapter we shall describe a general method for the analytical design of two new forms of crossed-field guns. These guns are based upon the space-charge flow solutions for the linear magnetron first obtained by Benham,<sup>1</sup> Brillouin,<sup>2</sup> Slater,<sup>7</sup> and others. Certain portions of this flow are suitable for convergent crossed-field guns. As the space-charge solutions are obtained for a semi-infinite geometry, in using a finite portion of the flow as the basis for an electron gun, it is then necessary, by means of external electrodes, to synthesize the correct potentials and fields along the boundaries of the finite flow. This technique of designing crossed-field guns is the same as that used by Pierce<sup>24,25</sup> in designing electron guns based upon the well known space-charge flow solutions of Langmuir. As is the case with certain forms of the Pierce gun, a method of analytic continuation in the complex plane is used to obtain the proper external electrode system for the crossed-field gun. However, for the present guns these analytic methods are employed for a beam with curvilinear boundaries. Previously it has been necessary to use various analog methods, such as the electrolytic tank, in obtaining a suitable electrode system for such a beam.<sup>24,25</sup>

We shall describe two types of gun, recently proposed by Kino,<sup>26,27</sup> which are based upon such design methods. The first is similar to the French "short gun" in that the trajectories, in the region of acceleration, are approximately half-cycloidal. The second gun, essentially a type of "long gun," is based upon an approximation to the exact space-charge solution, which will be shown to be valid under certain conditions. Both of these guns have been studied quite extensively experimentally. The results of these experiments are given in Chapter V.

Both of these guns exhibit a number of obvious advantages over previous guns. Since they are based on a space-charge flow solution, the current density at the cathode and hence the total emitted current as a function of the magnetic field and the voltages on the external electrodes may be calculated. Both guns are convergent. While the short gun is limited by geometrical considerations to an area convergence of about ten

to one, the long gun is in principle capable of much greater convergence, the principal limitation on its convergence being the effect of thermal velocities at the cathode and instabilities in the flow. Moreover, both of these guns, insofar as the types of flow on which they are based are actually established, should produce beams with noncrossing and nearly parallel trajectories at the exit plane.

In the present chapter we begin by reviewing the space-charge flow solutions on which these guns are based, followed by a discussion of the method for obtaining the electrode shapes. Finally, we shall consider the approximations and the assumptions made in the design of these guns.

#### B. THE SPACE-CHARGE FLOW SOLUTIONS AND THEIR USE AS A BASIS FOR CONVERGENT CROSSED-FIELD GUNS

The space-charge flow solution which we consider is quite similar to that given for the electron motion in the single trajectory beam discussed in Chapter II. Two significant differences do exist however: (1) the solution on which the gun is based does not permit double streaming, and (2) the boundary conditions at the lower edge of the space-charge sheath, which in the case of the gun solution is at the cathode, are different in the two cases. Otherwise, the analyses for the beam and gun solutions are completely parallel. We now consider the details.

Consider a coordinate system with an infinite cathode in the plane  $y = 0$ . There is a uniform magnetic field  $B_0$  in the negative  $z$ -direction. We shall assume that all motion is confined to planes perpendicular to the  $z$  axis; hence, we shall treat the problem as two-dimensional. The resulting electron flow solution is then obtained for  $E_{Ox} = 0$  and is characterized by having all trajectories congruent. Furthermore, current density, charge density and velocity at any point in the flow are independent of the  $x$  coordinate.

The equations of motion for an electron in this system are

$$\ddot{x} = \omega_c \dot{y} \quad (4.1a)$$

$$\dot{y} = \eta E_{Oy} - \omega_c \dot{x} \quad (4.1b)$$

Since  $E_{Ox} = 0$ , we may write

$$\frac{dE_{Oy}}{dy} = \frac{\rho_0}{\epsilon_0} \quad (4.2)$$

The charge and current densities in the flow are related by the expression

$$J_y = \rho_0 \dot{y} \quad (4.3)$$

where  $J_y$  is the current density at the cathode. We note that since the present analysis is assumed to be single-streaming, it follows that  $\dot{y} \geq 0$  and that  $J_y$  is equivalent to  $J_y^+$  which was defined earlier in Chapter II.

By combining Eqs. (4.2) and (4.3), we find that

$$\frac{dE_{Oy}}{dt} = \frac{J_y}{\epsilon_0} \quad (4.4)$$

If we assume that at  $t = 0$  an electron is at the space-charge limited cathode where  $E_{Oy} = 0$ , we may integrate Eq. (4.4) to obtain the field  $E_{Oy}$  as a function of the transit time along the trajectory of such an electron. The result is

$$E_{Oy} = \frac{J_y}{\epsilon_0} t \quad (4.5)$$

With this expression for the transverse field, we may integrate Eqs. (4.1) subject to the initial conditions  $\dot{x} = \dot{y} = 0$ ,  $x = x_0$  and  $\dot{y} = \dot{y}_0$  at  $t = 0$ . The resulting parametric trajectory equations, expressed in terms of the transit time, are then

$$y = \frac{\eta J_y}{\epsilon_0 \omega_c^3} (\omega_c t - \sin \omega_c t) + \frac{\dot{y}_0}{\omega_c} \sin \omega_c t \quad (4.6)$$

and

$$x = x_0 + \frac{\eta J y}{\epsilon_0 \omega_c^3} \left[ \frac{(\omega_c t)^2}{2} + \cos \omega_c t - 1 \right] + \frac{\dot{y}_0}{\omega_c} (1 - \cos \omega_c t) . \quad (4.7)$$

We may also compute the potential at any point on an electron trajectory as a function of the transit time by evaluating the integral

$$\phi = - \int_0^y E_{Oy} dy = - \int_0^t E_{Oy} \dot{y} dt ,$$

which yields the result

$$\begin{aligned} \phi = & - \frac{\eta J y^2}{\epsilon_0^2 \omega_c^4} \left[ 1 - \cos \omega_c t + \frac{(\omega_c t)^2}{2} - \omega_c t \sin \omega_c t \right] \\ & + \frac{J y \dot{y}_0}{\epsilon_0 \omega_c^2} \left[ \omega_c t \sin \omega_c t + \cos \omega_c t - 1 \right] . \end{aligned} \quad (4.8)$$

For convenience, we define a set of normalized parameters  $X$ ,  $Y$ ,  $u$ ,  $\phi$  as follows:

$$x = \frac{\eta J y}{\epsilon_0 \omega_c^3} X , \quad (4.9a)$$

$$y = \frac{\eta J y}{\epsilon_0 \omega_c^3} Y , \quad (4.9b)$$

$$\omega_c t = u , \quad (4.9c)$$

$$\phi = \frac{-\eta J y^2}{\epsilon_0^2 \omega_c^4} \phi . \quad (4.9d)$$

We shall consider the parametric equations for the trajectories and potential [Eqs. (4.6), (4.7), (4.8)] for two different values of  $\dot{y}_0$  :

1. Case 1:  $\dot{y}_0 = 0$

In this case the parametric equations for the trajectories may be written in the normalized form as

$$X = X_0 + \frac{u^2}{2} + \cos u - 1 , \quad (4.10)$$

$$Y = u - \sin u , \quad (4.11)$$

while the expression for the potential becomes

$$\phi = \frac{u^2}{2} - u \sin u + 1 - \cos u . \quad (4.12)$$

The normalized form for the electric field is then

$$-\frac{\partial \phi}{\partial Y} = u . \quad (4.13)$$

2. Case 2:  $\dot{y}_0 = \eta J_y / \epsilon_0 \omega_c^2$

In this case, the solutions become very much simplified. The normalized trajectory equations are

$$X = X_0 + \frac{u^2}{2} , \quad (4.14)$$

$$Y = u , \quad (4.15)$$

and the expression for the potential is

$$\phi = \frac{u^2}{2} \quad (4.16)$$

$$-\frac{\partial \phi}{\partial Y} = u . \quad (4.17)$$

The trajectories are thus simple parabolas of the form

$$Y^2 = 2(X - X_0) . \quad (4.18)$$

We shall now consider these two solutions in more detail, and in particular we shall show that solution 1 may be used as the basis of a space-charge flow short gun, while solution 2 may be used in the design of a type of long gun, which is capable of very great convergence.

First, it is useful to examine the conditions under which each of these solutions might be applicable, considering the effects of thermal velocities at the cathode. Neglecting thermal transverse velocities, solution 2 assumes that electrons leave the cathode with an energy  $\phi_0$  which is given by

$$\phi_0 = \frac{\eta J_y^2}{2\epsilon_0^2 \omega_c^4} \quad (4.19)$$

A criterion for the validity of solution 1 is then that the thermal potential at the cathode (approximately .1 volt at normal operating temperature) be much less than  $\phi_0$ , while if these two quantities are approximately equal, we would expect the much simpler solution 2 to be applicable. We note that  $\phi_0$  is determined only by the magnetic field and the current density at the cathode. In practice, the conditions for the validity of both solutions are easily attainable. For example, for  $B_0 = 140$  gauss and  $J_y = 50$  ma/cm<sup>2</sup>,  $\phi_0$  is approximately 7 volts; for  $B_0 = 800$  gauss and  $J_y = 200$  ma/cm<sup>2</sup>,  $\phi_0$  has a value of .1 volt.

In Fig. 4.1, the normalized trajectory for solution 1 from the point  $X_0 = 0$ ,  $Y_0 = 0$  is plotted. All other trajectories are then given by a displacement in  $X$ . In this same figure, the variation in potential along this trajectory is also plotted. We note that points on the trajectory where  $u$  is an even integral multiple of  $2\pi$  are points of inflection, so that at these points  $dY/dX = d^2Y/dX^2 = 0$ . Thus, at certain values of  $y$ , virtual cathodes exist, and at such planes electrons could in principle undergo a reversal in sign of  $\dot{y}$  and hence could return toward the cathode. However, this fact does not pose any problem since only a small portion of the flow is to be used as the basis for a gun, and in particular, the trajectories in the gun will have a total transit angle  $u$  of approximately  $2\pi$ .

The general method by which these solutions may be used to produce finite, convergent beams, suitable for electron guns, is shown in Fig. 4.2.

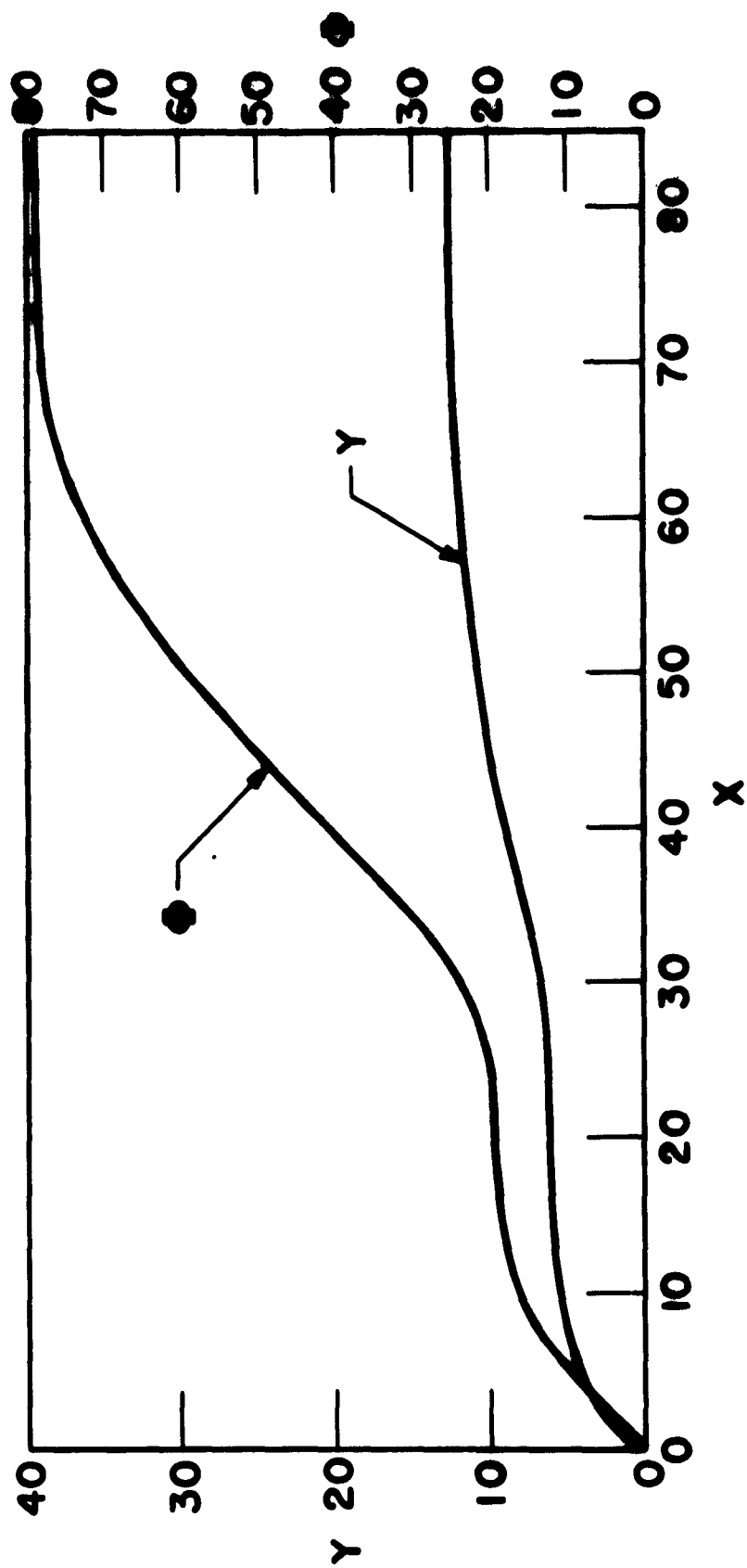
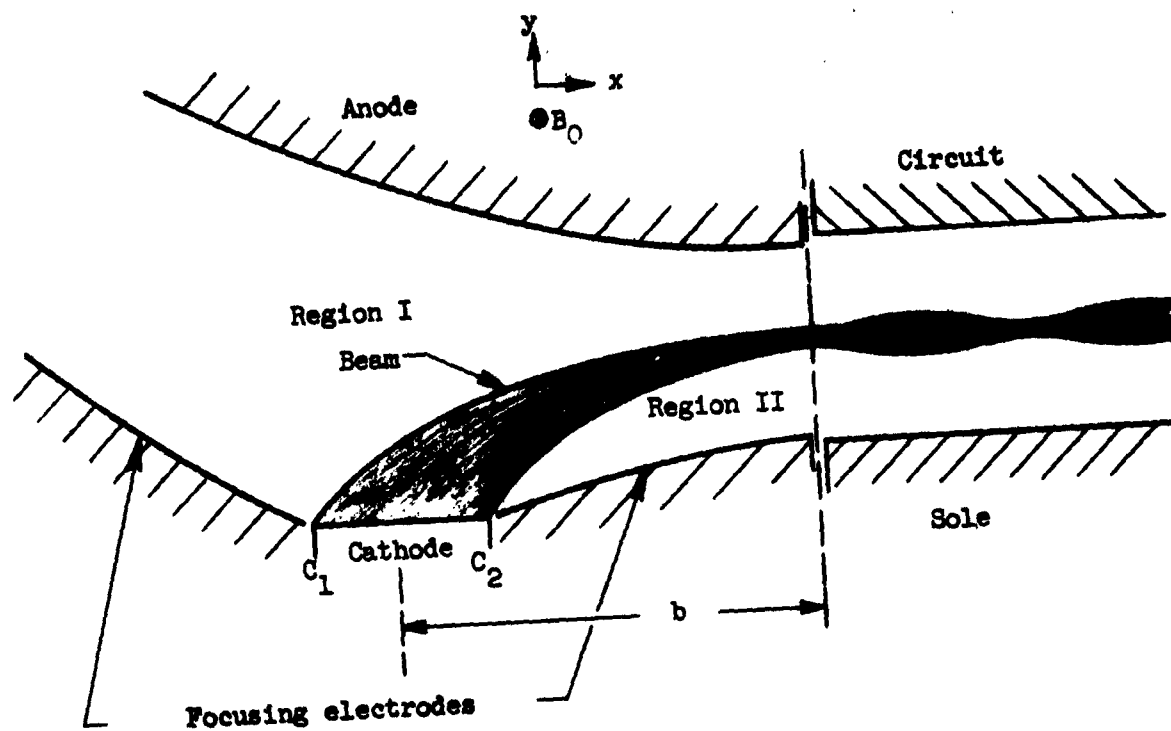
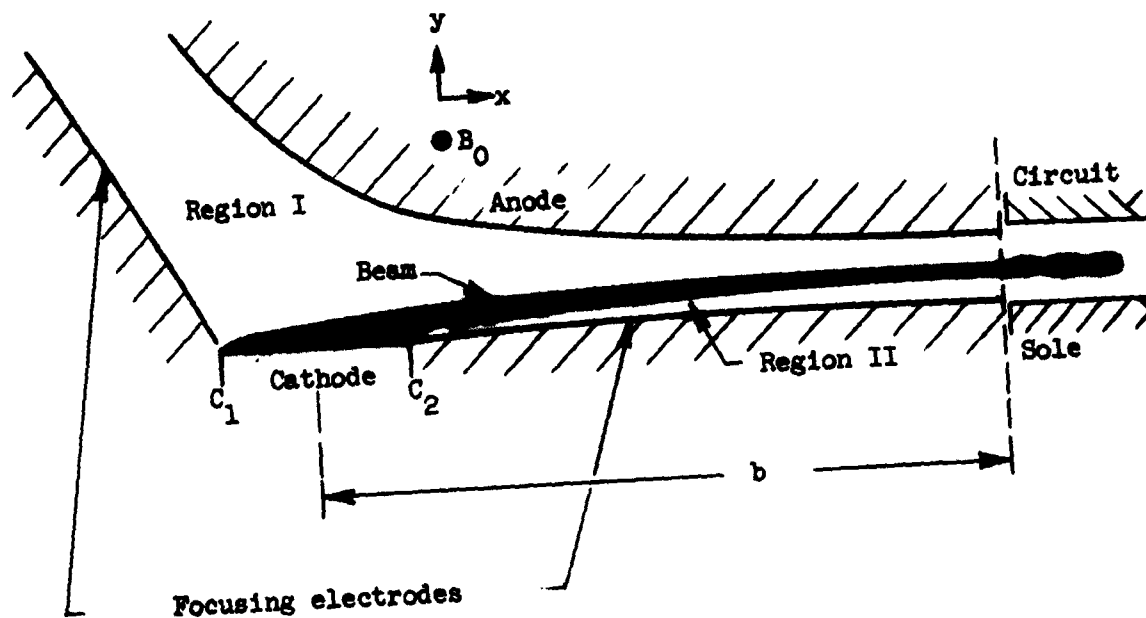


FIG. 4.1--The normalized trajectory and variation in normalized potential along it for Case 1.



a. Short gun geometry



b. Long gun geometry

FIG. 4.2--Geometry of the space-charge flow crossed-field guns.



Figure 4.2a illustrates a possible short gun, while in Fig. 4.2b the geometry for the long gun is shown. In either case the trajectories from the two ends of the cathode  $C_1$  and  $C_2$  are seen to converge toward each other. The convergence, defined as the length of the cathode  $C_1 C_2$  divided by the thickness of the beam at the exit plane, in the case of the long gun, increases monotonically with the distance  $b$  of the exit plane from the cathode. The convergence of the short gun behaves similarly, as long as the exit plane does not lie much beyond the point  $u = 2\pi$  on the trajectory from  $C_1$ . Beyond this point the edge trajectories diverge, and converge again at the next inflection point  $u = 4\pi$ , this process continuing at each subsequent inflection point. We shall discuss later the possibility of extending the gun trajectories beyond the first point of inflection.

As shown in Fig. 4.2, the guns are abruptly terminated at the exit plane. In each type of gun the edge trajectories are not exactly parallel at the exit plane; hence, we would not expect a perfectly laminar beam in the interaction region. We shall return to this question in more detail later, but we may note here that we would expect that any non-laminarities resulting from such abrupt termination should be of small magnitude, particularly in the case of the long gun where the beam at the exit plane almost satisfies the conditions for Brillouin flow.

In order to achieve the finite flow necessary for these guns, an electrode system is necessary to supply the proper values of electric field and potential along the bounding trajectories. Thus, in reference to Fig. 4.2, the anode and focusing electrode from the rear of the cathode at  $C_1$  must supply a potential which satisfies Laplace's equation in region I, and which, to a good approximation, provides the specified variation of potential and field along the trajectory from  $C_1$ . Similarly, the focusing electrode originating at the front of the cathode must provide the same variation in field and potential (as a function of path length from the cathode) for the trajectory from  $C_2$ . We shall now show how the shape of these electrodes may be obtained analytically.

#### C. THE METHOD FOR OBTAINING THE ELECTRODES NECESSARY TO PRODUCE A FINITE BEAM

The electrode systems for both the short and long guns have been

obtained by a method of complex variables due to Kirstein,<sup>3</sup> and derived independently by Lomax.<sup>4</sup> We shall summarize the method and the results of these calculations in the following section.

### 1. The Electrode System for the Short Gun

Following Kirstein, we write the normalized trajectory equations for the short gun in complex form:

$$Z = X - X_0 + jY = \frac{u^2}{2} + e^{-ju} + ju - 1 \quad (4.20)$$

We next generalize the parameter  $u$  by substituting for it the complex parameter  $w = u + jv$ . Equation (4.20) then becomes

$$Z = \frac{w^2}{2} + e^{-jw} + jw - 1 \quad (4.21)$$

This expression provides a conformal transformation between the  $w$  plane and the  $Z$  plane, and we note that the real axis  $v = 0$  of the  $w$  plane corresponds to the beam trajectory in the  $Z$  plane. From the known potential along the  $u$  axis of the  $w$  plane, Kirstein finds, by means of analytic continuation, the potential at any other point in the  $w$  plane (excluding regions of singularity). He then determines the potential at any point in the  $z$  plane by means of the transformation of Eq. (4.21).

Following Kirstein, we define two functions on the trajectory:

$$\phi_u(u) = |\nabla\phi| \cos\theta \frac{ds}{du} \quad (4.22)$$

$$\phi_v(u) = |\nabla\phi| \sin\theta \frac{ds}{du} \quad (4.23)$$

where  $ds$  is the incremental distance moved along the trajectory when  $u$  changes to  $u + du$  and  $\theta$  is the angle between  $\nabla\phi$  and  $ds$ . Now if  $dY/dX = \tan\psi$  so that  $\sin\psi = dY/ds$  and  $\cos\psi = dX/ds$ , we see that since  $\nabla\phi$  has only a  $Y$  component, that  $\theta = \pi/2 - \psi$ . Using the normalized form of the trajectory and potential Eqs. (4.10), (4.11) and (4.12), we find that

$$\phi_u(u) = u(1 - \cos u) \quad (4.24)$$

$$\phi_v(u) = u(u - \sin u) \quad (4.25)$$

Kirstein shows that along the trajectory  $\phi$  is given by the real part of the function  $W(u, 0)$  where

$$W(u, 0) = \int_0^u \phi_u(u') - j\phi_v(u') du' , \quad (4.26)$$

and that  $\phi$  is given elsewhere in the  $w$  plane by the real part of  $W(u, v)$  where

$$W(u, v) = \int_0^w \phi_u(w') - j\phi_v(w') dw' ; \quad (4.27)$$

hence,

$$W = \frac{w^2}{2} - \frac{jw^3}{3} - jw e^{-jw} - e^{-jw} + 1 . \quad (4.28)$$

Finally it can be shown that for an equipotential,  $\phi = \text{constant}$  in the  $w$  plane, which may be written as

$$v = V(u) , \quad (4.29)$$

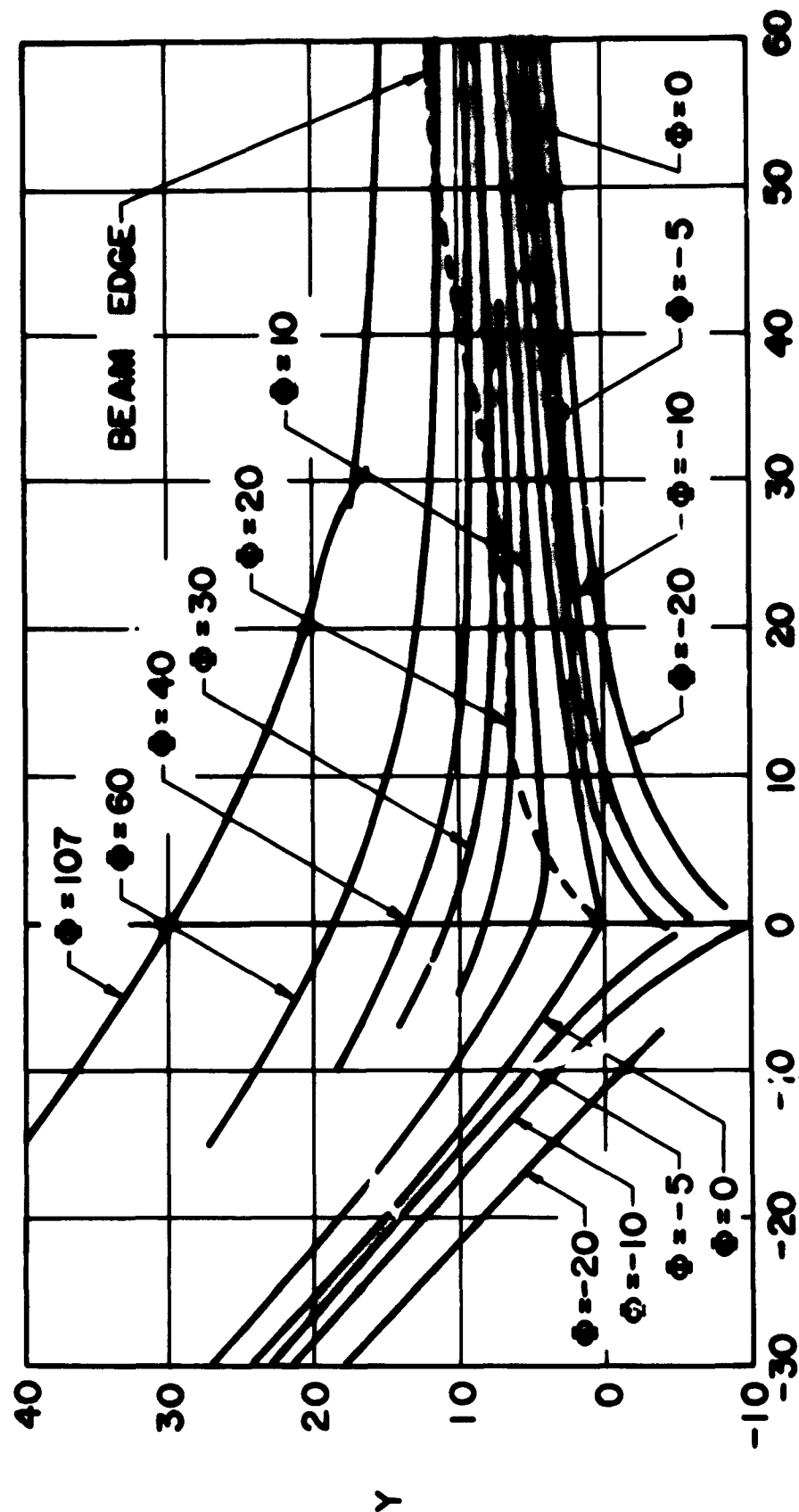
that the differential equation

$$\frac{dv}{du} = \frac{\text{Re}\left(\frac{dW}{dw}\right)}{\text{Im}\left(\frac{dW}{dw}\right)} \quad (4.30)$$

must hold. The equipotentials in the  $w$  plane and hence in the  $z$  plane are then obtained by evaluating the transformation given by Eq. (4.21) along the contour in the  $w$  plane defined by Eq. (4.30) which contains  $W$  as given by Eq. (4.28).

Kirstein has performed these calculations numerically on a computer.<sup>(9)</sup> The results are shown graphically in Fig. 4.3. These curves show contours of the electrodes which, if raised to the indicated value of normalized potential, will insure the proper variation of potential and field along the edge trajectory of the beam. In practice, the beam is defined by two such trajectories displaced by a distance equal to the normalized cathode length  $L$ , so that in Region I (see Fig. 4.2) above the beam

<sup>(9)</sup> The curves given in Kirstein's paper are incorrect, due to a numerical computation error.



X

FIG. 4.3--Family of equipotentials for the short gun.

those solutions corresponding to  $v > 0$  are valid; while in Region II beneath the beam, the solutions with  $v < 0$  are valid.

As a result of the multivalued nature of the transformation between the  $w$  plane and the  $z$  plane, it can be shown that additional electrodes at other potentials will be necessary if the beam trajectories are to be carried much beyond the point  $u = 2\pi$ . In general, for each point of inflection on the gun trajectory, an additional electrode must be added. An additional restriction on the choice of electrodes which may be used with this gun should be mentioned. If the method of analytic continuation is carried to a region where the potential is too high, two electrodes of different potential may appear to cross each other. This phenomenon also results from the multivalued nature of Eq. (4.21). Physically it is then necessary to use electrodes which are sufficiently close to the beam to achieve the prescribed potential variation along the beam and electrodes which are too far removed can not give this variation. In the range of normalized potentials shown in Fig. 4.3, this effect does not occur, and in general it does not provide a serious difficulty in short gun designs.

## 2. The Electrode System for the Long Gun

We proceed exactly as in the case of the short gun. Writing the normalized trajectory equations in complex form as

$$Z = (X - X_0) + jY = \frac{u^2}{2} + ju, \quad (4.31)$$

which becomes

$$Z = \frac{w^2}{2} + jw \quad (4.32)$$

in terms of the complex parameter  $w = u + jv$ . Furthermore we find that

$$X - X_0 = \frac{u^2}{2} - \frac{v^2}{2} - v, \quad (4.33)$$

and

$$Y = u(1 + v). \quad (4.34)$$

The expressions for  $\phi_u(u)$  and  $\phi_v(u)$  are simply

$$\phi_u(u) = u \quad , \quad (4.35)$$

$$\phi_v(u) = u^2 \quad , \quad (4.36)$$

and we obtain

$$W = \left( \frac{u^2}{2} - \frac{v^2}{2} + u^2v - \frac{v^3}{3} \right) + j \left( uv - \frac{u^3}{3} + uv^2 \right) \quad . \quad (4.37)$$

Now since at any point on the normalized equipotential  $\phi$  we have  $\phi = \text{Re } W$ , we may write

$$u^2 = \frac{2\phi + v^2(1 + \frac{2}{3}v)}{1 + 2v} \quad . \quad (4.38)$$

From Eqs. (4.33), (4.34), and (4.38), the electrode shape corresponding to a given value of  $\phi$  may be obtained by a simple computation. Figure 4.4 shows a family of such curves. We note that since the transformation given by Eq. (4.31) involves no multivalued functions, no restrictions are placed either on the choice of electrode potentials, or on the length of the gun trajectory. Thus, guns of this type may have  $u \gg 1$  at the exit and hence should be capable of very large convergences.

#### D. ASSUMPTIONS AND APPROXIMATIONS INHERENT IN THE GUN DESIGN METHOD

In concluding this chapter, it is pertinent to review the assumptions and approximations which are implied and the effects which have not been considered in the methods of crossed-field gun design described in this chapter. We list these as follows.

1. Possible lens effects at the exit plane have not been considered. It should, however, be possible to minimize such effects by the proper choice of sole and circuit voltage.

2. The analysis has been entirely in terms of a two-dimensional model. Effects such as space-charge spreading in the z-direction parallel to the magnetic field have been ignored. This problem will be considered again in Chapter V in conjunction with the experiments.

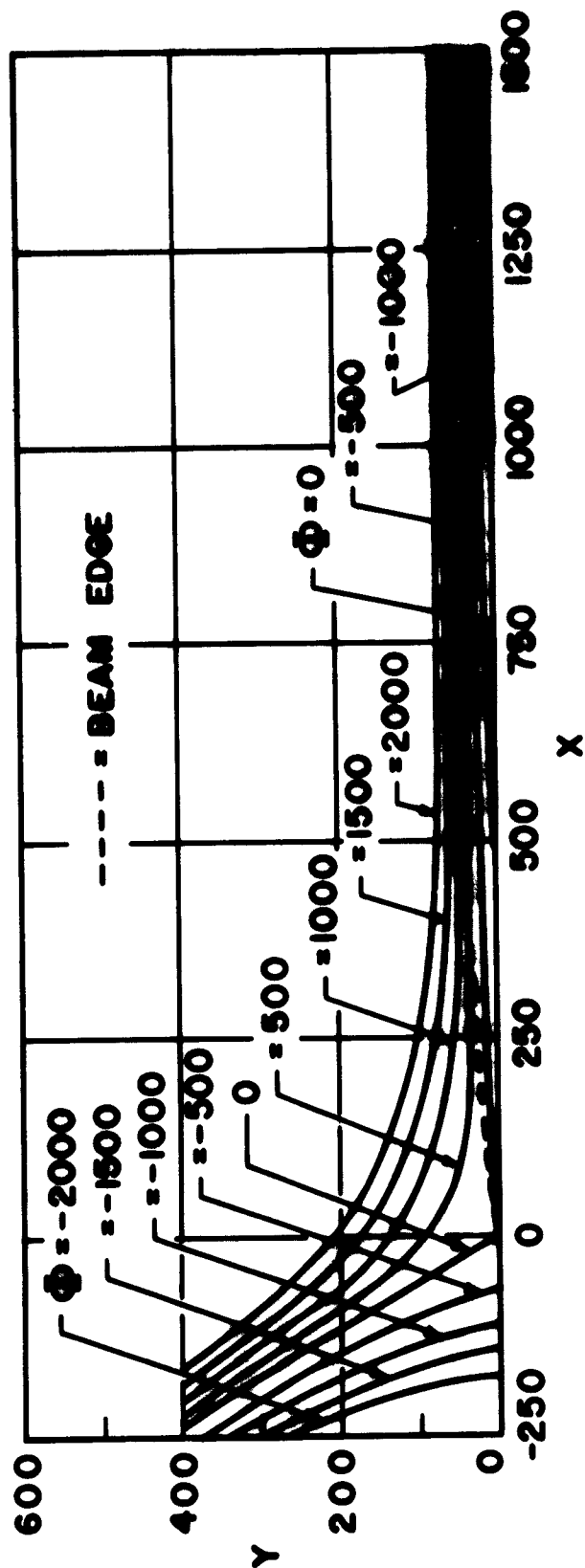


FIG. 4.4--Family of equipotentials for the long gun.

3. Some of the effects of thermal velocities at the cathode have been ignored. In the case of the short gun, all such effects are probably negligible. For the long gun, however, as a result of both the Maxwellian distribution in  $\dot{y}_0$ , which we have assumed to be a constant for all electrons, as well as thermal transverse velocities  $\dot{x}_0$ , which we have ignored entirely, we would expect an actual beam to be somewhat more complex than the simple analytical model. In particular, we should expect that the parabolic trajectories obtained in the analysis would actually consist of small amplitude cyclotron undulations about the parabolic paths. As a result, the convergence of such a gun would be less than calculated on the basis of the simple flow model.

4. All rf instabilities, and in particular, rf growth of thermal fluctuations at the cathode, have not been considered.

We consider some of these points again in Chapter VI. We adopted the point of view that only through a series of comprehensive experiments with both types of guns can the validity of these approximations and the significance of those effects not considered be determined. These experiments comprise the principal subject of the present work.



## V. EXPERIMENTAL STUDIES OF THE SHORT AND LONG GUNS

### A. INTRODUCTION

Having reviewed the space-charge flow solutions and shown how suitable electrode configurations may be obtained, subject to certain restrictions and approximations, we next describe the experimental studies which have been made of examples of each of the two types of guns.

The basic experimental approach which we have adopted is to simulate the dc environment of a typical M-type device. Thus the beam which is produced by the gun under investigation is injected into a drift region of uniform dc crossed fields. The behavior of the beam in this region is then a good indication of the quality of the gun and exit plane optics. In addition, if the parameters of the gun system are held fixed or are scaled, it is possible, by varying the conditions in the drift region, to study the characteristics of the uniform flow. The experiments performed with both guns are then of two general types: (1) experiments dealing with the intrinsic nature of the gun, such as measurement of cathode current as a function of the other gun parameters and (2) experiments dealing with the nature of the beam after leaving the gun, for example, the measurement of the fraction of the total beam current collected by the drift region electrodes as a function of conditions both in the drift region and in the gun.

We shall begin this chapter by describing the optics and the general details of the experimental beam tester. The remaining portions of the chapter deal with a description of the experimental guns and a discussion of the experiments and results for each gun.

### B. THE BEAM TESTER

The electrode configuration of the beam tester is shown in Fig. 5.1. With the exception of certain changes in electrode spacers, this same experimental arrangement was used in testing both the long and short guns. The gun illustrated in Fig. 5.1 is the short gun.

The beam tester was designed so as to be as flexible as possible and so as to facilitate adjustments in the optics as easily as possible. Thus the experiments were performed in a continuously pumped demountable vacuum system, eliminating the need for conventional processing, while

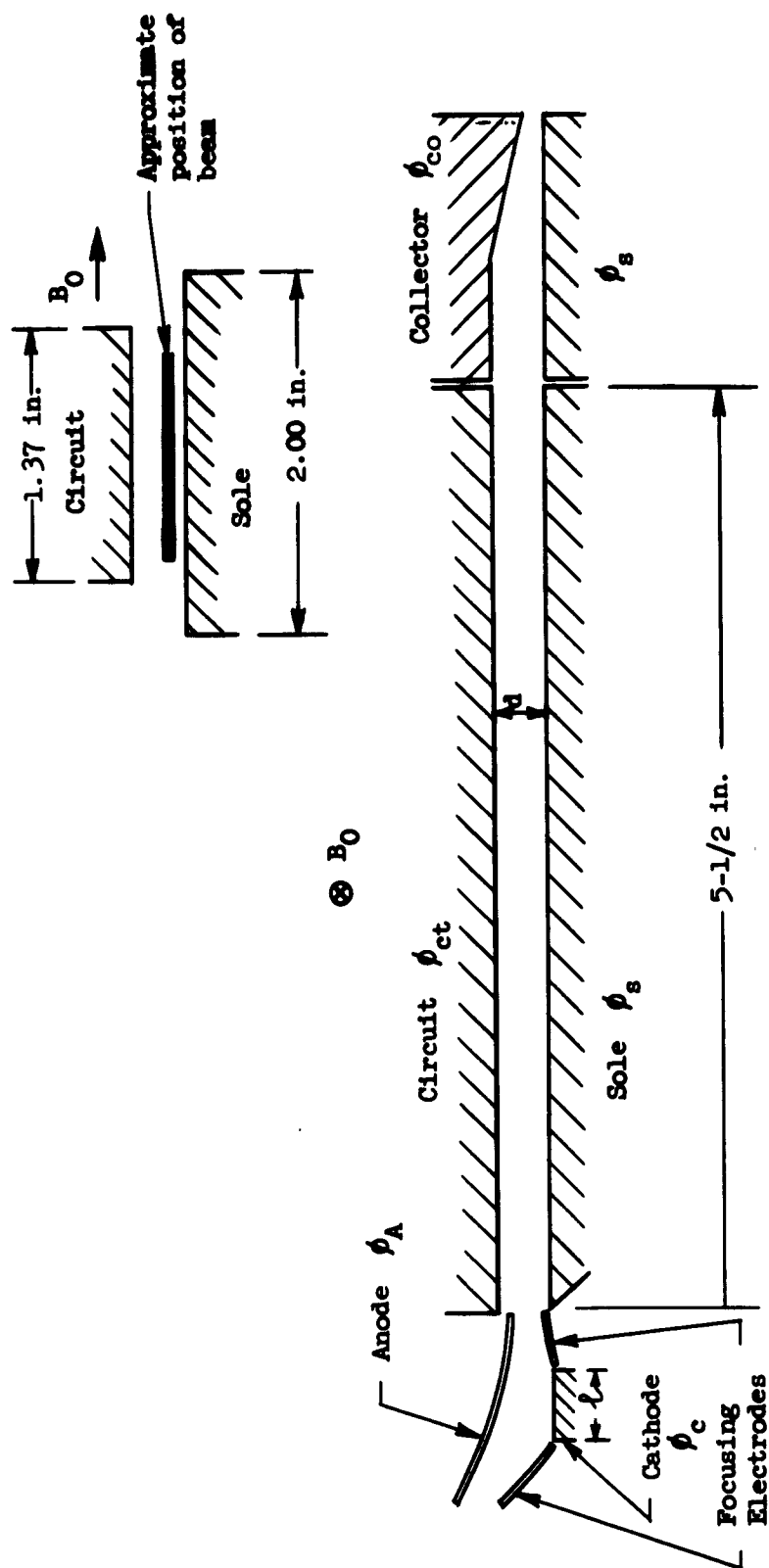


FIG. 5.1--Optics of the crossed-field beam tester.

at the same time providing maximum accessibility to the focusing structures. The lifetime of the oxide cathodes which were used proved to be somewhat limited under these experimental conditions, but through the use of extended interface cathodes and by designing the gun structure to permit the changing of cathodes with a minimum of effort, this problem did not seriously hinder the experiments. To effect minor geometry changes or to make simple repairs we used, with good success, a technique described by Haas and Jensen<sup>28</sup> for keeping the cathode warm during the "let down" period.

Since the short and long gun structures are slightly different in detail, we shall discuss each of them separately later in this chapter. A few remarks regarding the remainder of the beam tester structure will be made here.

The length of the uniform drift region bounded by the sole and circuit electrodes is about 5-1/2 in., a distance equal to a minimum of about 4, and as many as 50 cyclotron wavelengths of the beam. These electrodes, made of 1/8 in. stainless steel plate, are mechanically supported and insulated by means of commercial vacuum feed-through seals in such a manner that the sole-circuit spacing  $d$  may be easily adjusted. (see detail A., Fig. 5.3). The surfaces of the sole and circuit facing the beam are roughened by means of chemical etching in order to reduce the secondary emission.

The beam tester, as originally conceived, was designed with provisions for measuring the sole current distribution as a function of the distance along the drift region. Thus, in addition to a continuous sole plate, an interchangeable segmented structure was also constructed. This assembly, shown slightly modified in Fig. 5.2, consists of 20 copper segments 1/4 in. in length mounted on two sapphire rods and separated by mica spacers. As shown in the photograph, some of the space have been removed so that only 7 rather than 20 insulated segments result. The entire structure is supported from below by a series of insulated pins which protrude into the underside of every fourth segment. In order to achieve an adequate degree of surface flatness, the structure was first assembled without spacers on tungsten rods of the same diameter as the sapphire rods, and the entire surface milled flat. Using this

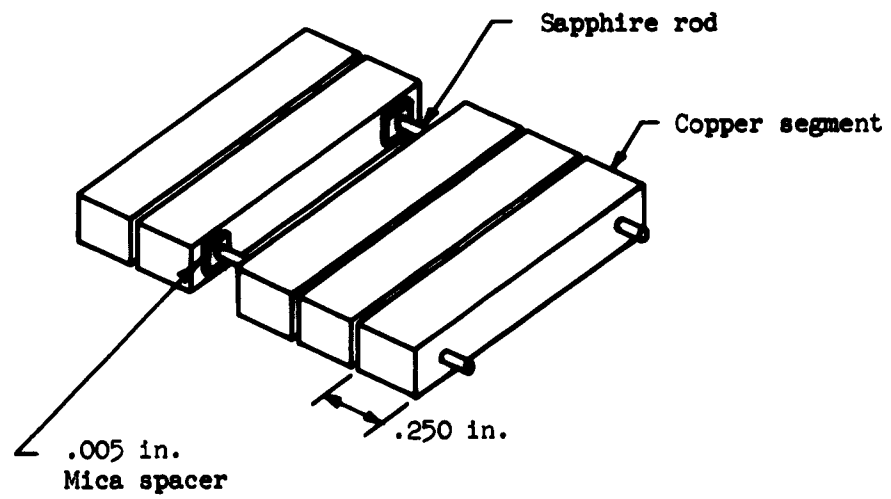


FIG. 5.2--The segmented sole structure.

technique, the variation in height along the sole is only about .002 in.

As shown in Fig. 5.1 the sole and circuit electrodes are not of the same width,<sup>(10)</sup> the sole being some 30 per cent wider than the positive circuit. The net result of this configuration is to provide fringing fields near the edges of the beam which tend to prevent lateral beam spreading in the direction of the magnetic field  $B_0$ . Throughout the course of the experiments, during which  $d$  was varied from .050 in. to .215 in., under most conditions no significant beam spreading was evidenced. Indeed, burn outlines on the collector indicated a beam width in this area only about 10 per cent greater than the width of the cathode. Previous workers have found it necessary to place confining negative electrodes along the edges of the beam, or to distort the dc magnetic field, in order to provide lateral confinement. During the course of our experiments it was noted that the severest lateral spreading seemed to occur when the beam was defocused and badly scalloped, while in the case of a rectilinear beam, lateral confinement, probably resulting from the electrode configuration mentioned above, appeared to be quite adequate.

The water cooled copper collector shown in Fig. 5.3 is of a type commonly used in crossed-field devices. In the tapered region the beam is accelerated, as a result of the increased transverse electric field, to a potential equal to that of the collector. The collector was designed as shown with a nontapered region directly adjacent to the circuit electrode so as to better isolate the sole-circuit space from undesirable effects of the collector, such as fringing fields and secondary electrons. The portion of the sole extending beneath the collector, while electrically isolated from the remainder of the sole, was usually maintained at sole potential. The narrow slot between the collector and the circuit provides a convenient means of estimating the width of the beam at pressures ( $> 5 \times 10^{-6}$  torr) where the beam is visible as a result of radiation from collision-excited gas molecules.

The entire electron optical system, with supporting members, and electrical and water connections, is mounted on a circular flange as shown in Figs. 5.3 and 5.4. This flange is attached by means of an O

---

<sup>(10)</sup> In all cases "width" shall refer to a dimension parallel to the  $z$  axis and the magnetic field.



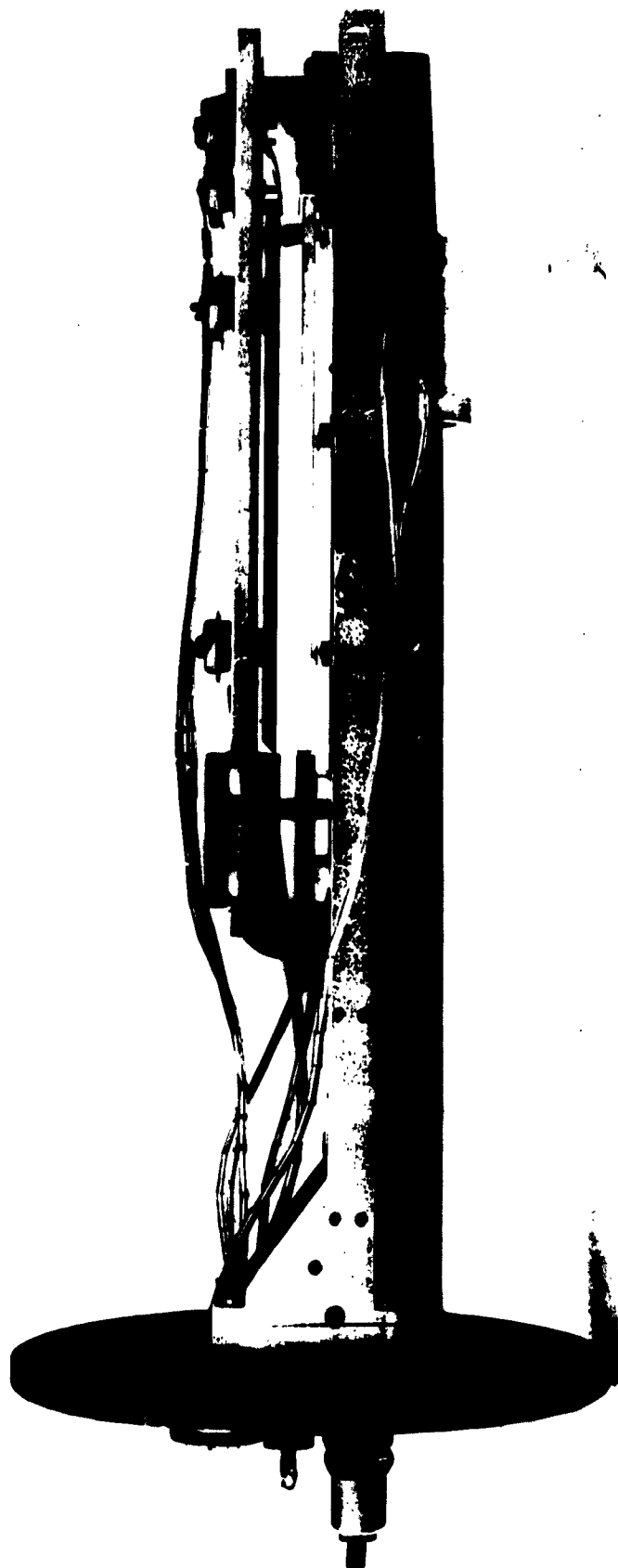


FIG. 5.4--Photograph of the beam tester.

ring seal to the open end of a length of 3-inch Pyrex glass pipe which provides the vacuum envelope and visual access to the beam. The system is pumped with a conventional oil diffusion pump with a liquid nitrogen trap. A valve between the pump and the experimental area of the system enables the pumping speed and hence the pressure in the working area to be accurately controlled. With the exception of the visual and photographic data which were taken at somewhat higher pressures, the experiments were all performed at pressures of  $5 \times 10^{-7}$  torr or lower.

The dc magnetic field was supplied by an external electromagnet with rectangular pole pieces measuring 4 in.  $\times$  14 in. The magnet produced a maximum field of about 1300 gauss across a gap of 4.0 in. The homogeneity of the field in the gap was improved by a simple method of shimming described in Appendix C. This technique yielded a field homogeneous to 1 per cent over the region occupied by the beam in the gun and drift space. Measurements of magnetic field strength were made using a rotating-coil gaussmeter. By means of the tube shown in Fig. 5.3, it was possible to insert the probe of the gaussmeter into the magnet gap with the entire structure in position and thus to measure the magnetic field with the beam tester in operation. This arrangement was found to be particularly useful at low values of  $B_0$  ( $< 200$  gauss) where hysteresis effects could result in errors of 5-10 per cent in field measurements based on precalibration of  $B_0$  as a function of magnet current. Since the probe is actually about 1-1/2 in. below the position of the beam, as a result of fringing effects it is necessary to calibrate in advance the relationship between the transverse magnetic fields at the two locations. By means of this technique, measurements of magnetic field in the region occupied by the beam were accurate to within about 3 per cent.

Figure 5.5 shows a photograph of the magnet and the vacuum envelope of the beam tester. Since the area occupied by the beam is not visible when the magnet pole pieces are in position, a long strip mirror extending from the gun to the end of the collector is placed at a  $45^\circ$  angle to the sole, as shown in Fig. 5.6. With this arrangement an edge view of the beam could be seen and easily photographed from the top of the apparatus.



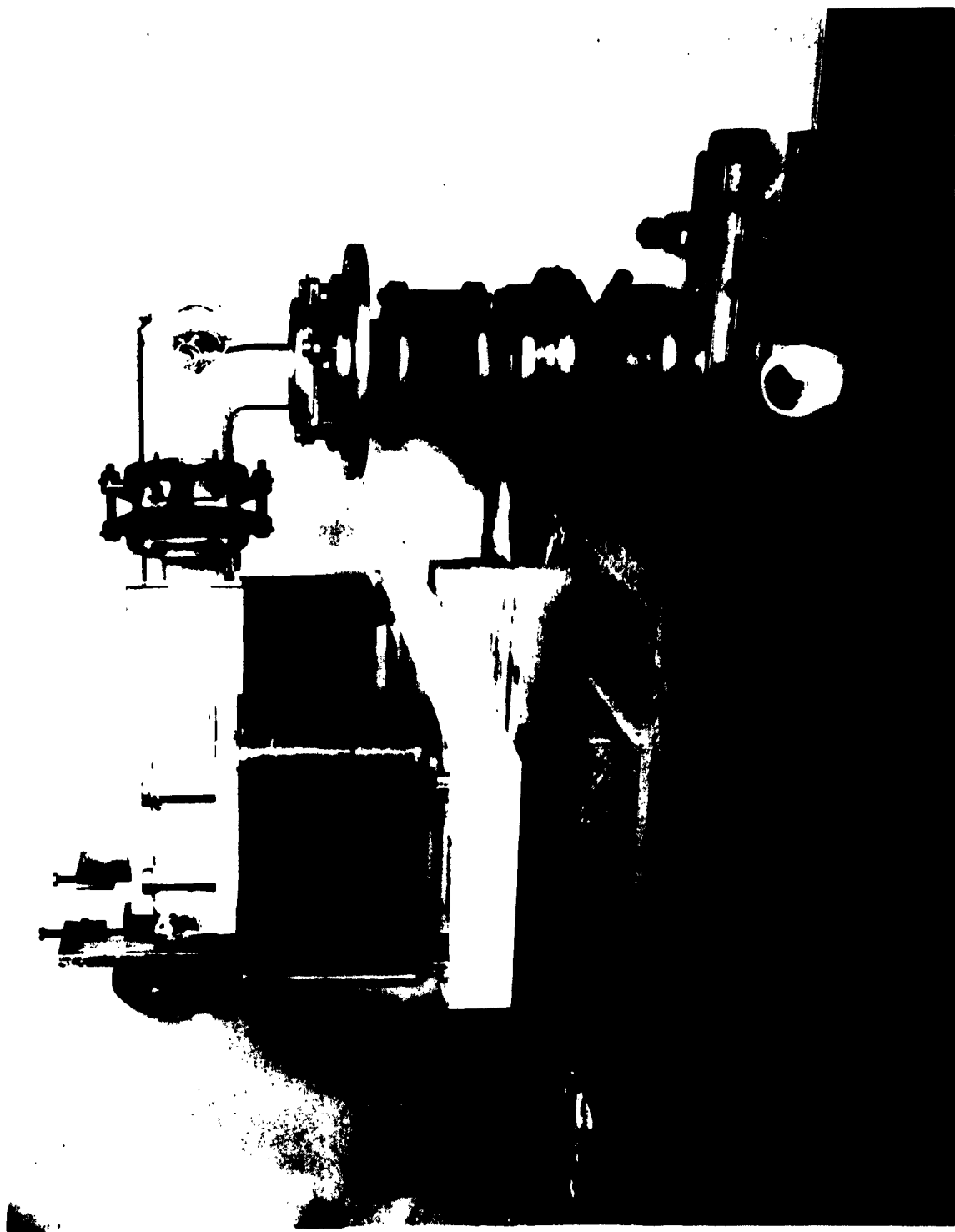


FIG. 5.5--Photograph of the magnet and vacuum envelope.

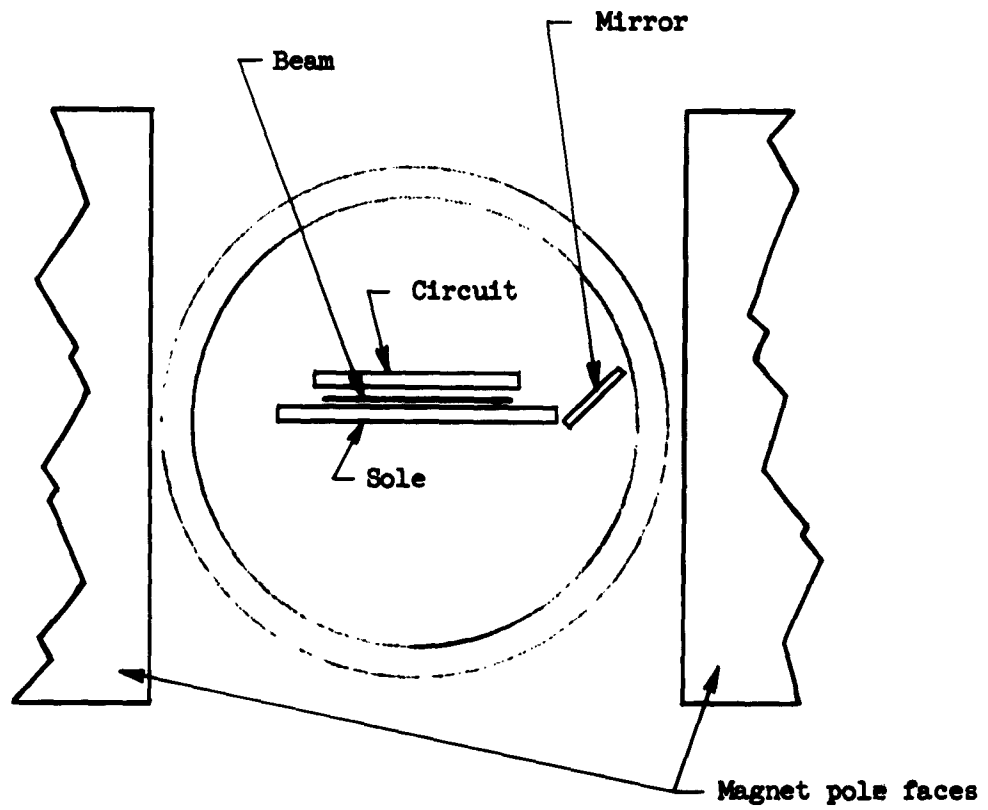


FIG. 5.6--Arrangement for viewing the beam.

### C. THE EXPERIMENTAL SHORT GUN

#### 1. Design Considerations

The electrode configuration for the short gun, is shown in Fig. 5.7. The focusing electrodes correspond to the normalized equipotential  $\phi = 0$  while the anode is a portion of the normalized equipotential  $\phi = 37.5$ . The normalized cathode length,  $L$ , is 12 and the exit or "cutoff" plane is at a normalized distance  $X = 24$  on the trajectory from the rear of the cathode. The values of  $u$  at the exit plane on the upper and lower edge trajectories are then 6.96 and 5.03, respectively. At the exit plane we see that the normalized beam thickness is about .4 and thus the gun should have an area convergence of approximately 30, although for reasons discussed below we would not expect such a high convergence to be attained in practice.

It should be noted that the nature of the trajectories places an upper limit on the value of  $L$  which may be used. This follows from the requirement that the trajectories be approximately parallel at the exit plane. In order to compare the performance of this gun with that of the conventional French short gun, which has a very limited convergence, we have purposely chosen a fairly long cathode, although the exit angles are not excessively large. From the normalized trajectory equations we may easily show that the slope  $\partial Y / \partial X = \tan \psi$  at any point on the trajectory is given in terms of  $u$  by

$$\tan \psi = \frac{1 - \cos u}{u - \sin u} \quad (5.1)$$

At the position of the exit plane shown in Fig. 5.7 the values of  $\psi$  for the upper and lower trajectories are found to be 2.08 degrees and 6.57 degrees, respectively. Thus to optimize the injection conditions for the beam as a whole, it would seem reasonable to tilt the entire gun structure through an angle of about 4 degrees (see Fig. 5.8). This was done during the course of the experiments. As a result, improvement in transmission was noted under certain conditions; however, it can not be stated conclusively that the optics were substantially improved as a result of this change.

The remainder of the design procedure consisted in evaluating the normalization parameters appearing in Eq. (4.9). Thus if we specify the

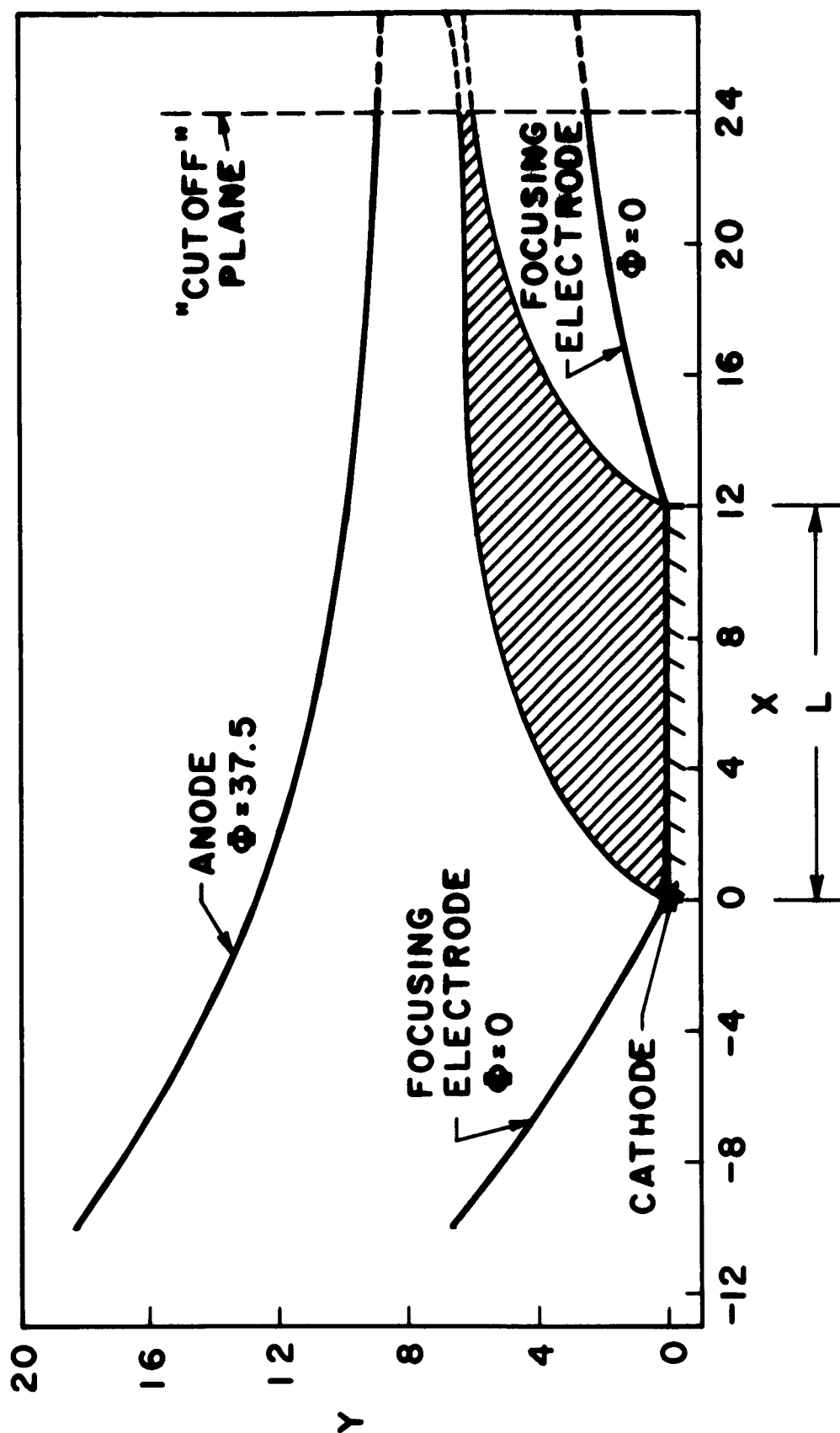


FIG. 5.7--Electrode configuration for the experimental short gun.  
Ordinate and abscissa scaled in normalized units.

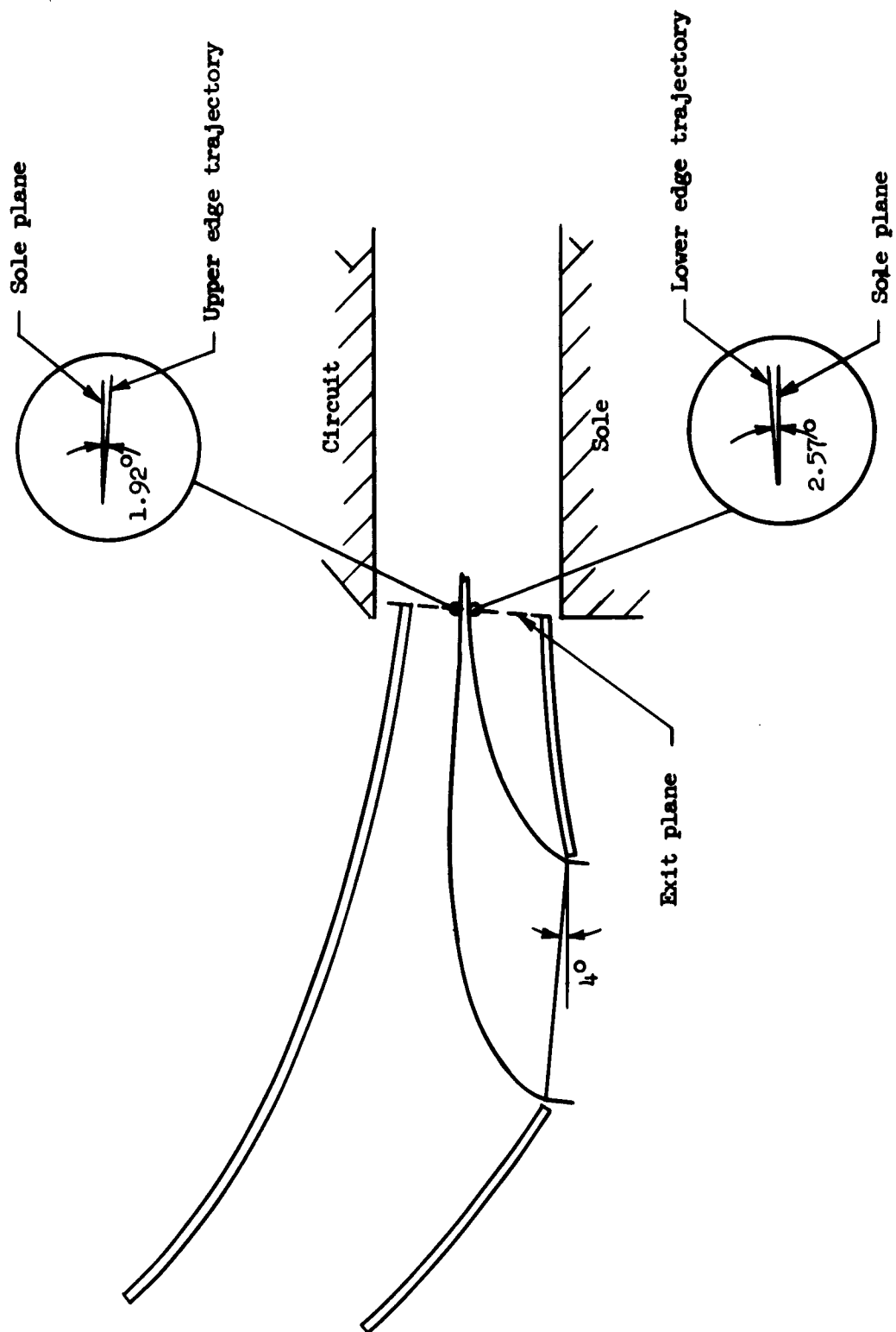


FIG. 5.8--Effect of tilting the gun on the exit angles.

total beam current per unit width, which is equal to  $J_y \ell$ , and since we have fixed  $L$ ,  $J_y$  is also determined for a given value of magnetic field.<sup>(11)</sup> The actual dimensions and potentials corresponding to the normalized values are then computed. We summarize the results of these calculations in terms of the design parameters given in Table I. We note that under these conditions, the initial potential  $\phi_0 = \eta J_y^2 / 2\epsilon_0^2 \omega_c^4$  has a magnitude of 7.2 volts, a quantity much larger than the potential of the thermal electrons at the cathode.

The exit conditions require further comment. For Brillouin flow it is required that both the plasma frequency and velocity gradient across the beam should be equal to  $\omega_c$ . We see from Table I that neither of these conditions is satisfied, although the most serious error is the high value of  $\omega_p$  at the exit. If the exit plane were to be moved closer to the cathode, the beam plasma frequency at the exit plane would be decreased, but simultaneously the exit angle of the lower edge trajectory would be increased radically. Thus if the cutoff plane is at the point  $u = 2\pi$  on the top trajectory, with all other conditions as given in Table I, we find that while the upper edge trajectory leaves the gun parallel to the cathode, and  $\omega_p$  at the exit plane is reduced to  $3.53 \times 10^9 \text{ sec}^{-1}$ , the exit angle for the lower edge trajectory is almost 15 degrees. In the early course of these experiments, a gun with this geometry was constructed and tested and was found to give inferior results in terms of transmission and visual appearance of the beam, in comparison to the gun with the extended cutoff plane. We shall consider the exit plane conditions later in discussing photographs of the beam; suffice it to say here that in practice it appears that the beam is somewhat thicker near the exit plane than predicted by the theory; hence  $\omega_p$  is not as large as the value given in Table I. The best results are obtained then with optics where the edge trajectory exit angles are small and approximately equal.

Unless otherwise noted, all of the data which we present were obtained with the gun whose design is based upon the geometry of Fig. 5.7 and the parameters given in Table I.

---

<sup>(11)</sup> We may note that  $J_y$  and  $B_0$  are not independent, and in fact the choice of one of these quantities immediately determines the other, a condition we should expect for "nonchaotic" space-charge flow in a magnetic field.

TABLE I

## A. DESIGN PARAMETERS FOR THE EXPERIMENTAL SHORT GUN

total beam current $I_c$	105 ma
beam width	1.1 in.
current density at the cathode $J_y$	48.8 ma/cm <sup>2</sup>
dc magnetic field $B_0$	140 gauss
linear normalization factor $\eta J_y / \epsilon_0 \omega_c^3$	.0254 in./normalized unit
potential normalization factor $\eta J_y^2 / \epsilon_0^2 \omega_c^4$	14.4 volts/unit of normalized potential
anode potential $\phi_A$	540 volts
perveance	$7.98 \times 10^{-6}$
beam thickness $\delta$ at the exit plane	.010 in.

## B. EXIT CONDITIONS

upper edge trajectory at the exit plane	potential	274 volts
	exit angle	6.57 degrees
lower edge trajectory at the exit plane	potential	249 volts
	exit angle	2.08 degrees
average velocity at exit	$9.61 \times 10^6$ m/sec	
velocity gradient across the beam at exit	$1.85 \times 10^9$ sec <sup>-1</sup>	
plasma frequency of the beam at exit $\omega_p$	$5.41 \times 10^9$ sec <sup>-1</sup>	
cyclotron frequency $\omega_c$	$2.46 \times 10^9$ sec <sup>-1</sup>	

## 2. Mechanical Design of the Short Gun

Since one of the principal purposes of the experiments was to verify the theoretical design of these guns, certain requirements were placed on a suitable experimental gun which might not otherwise be necessary for a gun whose sole purpose is to "produce a beam." One such requirement which influenced the design of the experimental guns is the need for a uniform temperature over the cathode emitting surface, to insure that the entire cathode is actually space-charge-limited. In addition, it is necessary that the emitting surface be accurately aligned with respect to the other focusing elements at operating temperature. Finally, since the experiments were performed under less than ideal vacuum conditions, it is necessary that the cathode be rugged and not easily susceptible to poisoning or, alternatively, be easily replaceable.

The important mechanical details of the gun structure are shown in Fig. 5.9. Photographs of the assemblies and some of the parts are illustrated in Fig. 5.10.

The rectangular cathode button, which is in the form of a shallow box, is electroformed from nickel. The double bifilar heater is of tungsten wire and is sprayed with an insulating coating of alumina. The cathode surface is of the extended interface type, formed by sintering nickel powder to the base metal of the cathode. This procedure results in an improved bond between the oxide coating material and the nickel substrate and in general a more rugged cathode than if the coating is applied directly to the smooth base metal.

The entire cathode assembly, consisting of the cathode button, heater and heat shields, is keyed into position in the channeled cathode block by ten sapphire rods. These rods provide insulation as well as mechanical alignment, and since the cathode button only touches them at one short line of tangency, heat losses are quite small. The rods are positioned so that they are all in contact with the cathode button at operating temperature, thus insuring accurate alignment of the button. The single constraint not supplied by the system of rods is provided by a spring loaded screw, which passes through an insulated sleeve in the bottom of the cathode block, and which attaches to a nut welded to the underside of the cathode. This screw also provides a convenient electrical connection to the cathode.



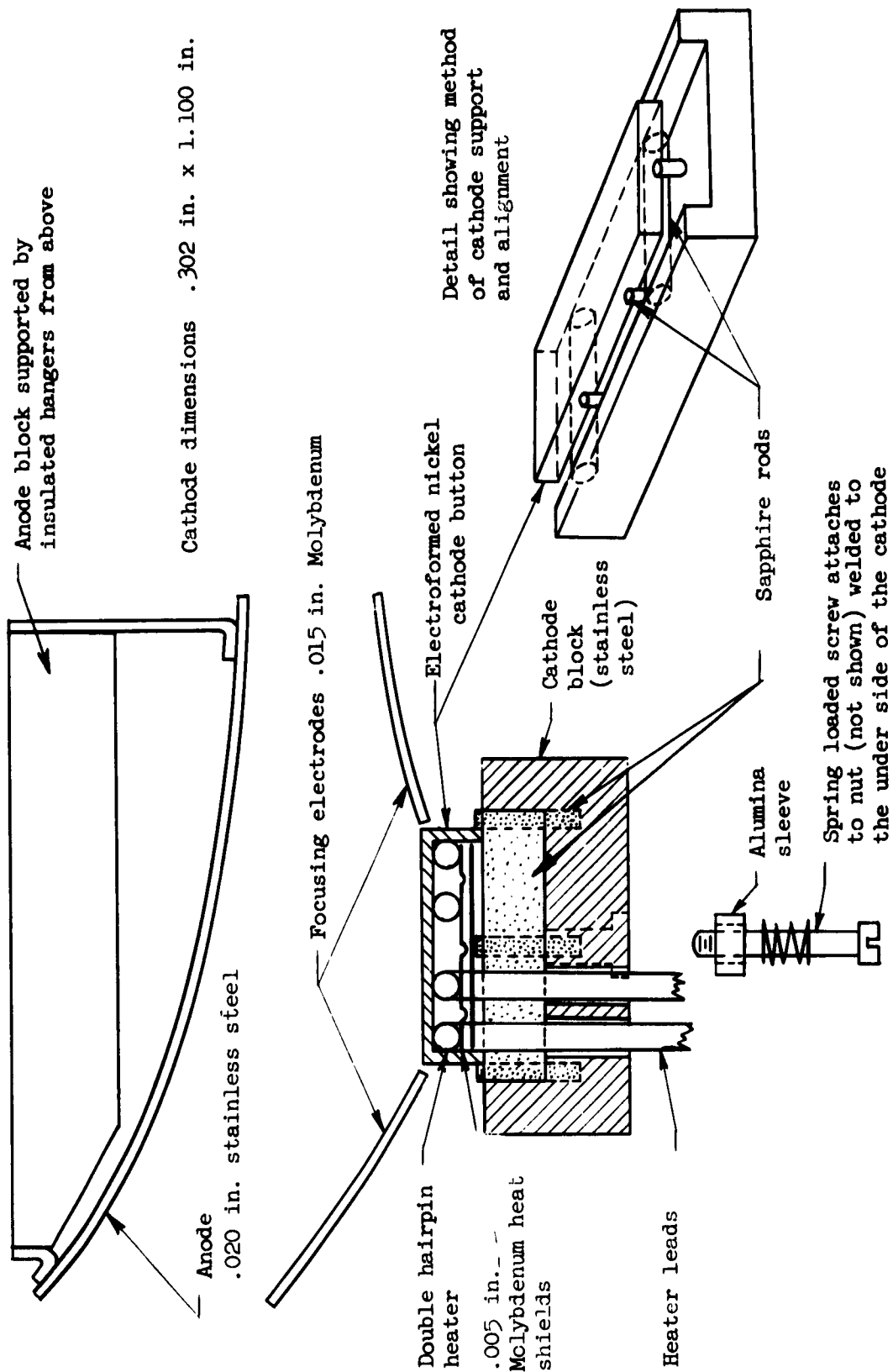
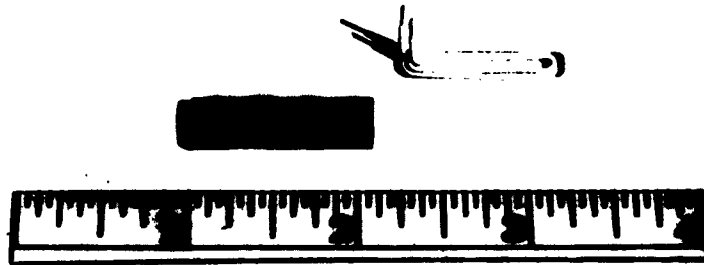
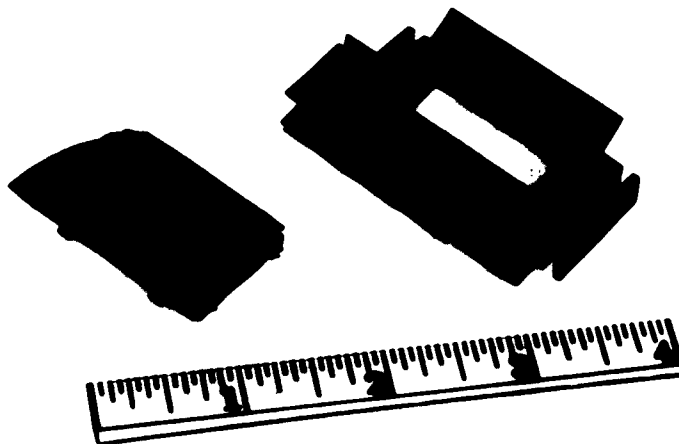


FIG. 5.9--Mechanical details of the short gun.



a. Short gun cathode and heater.



b. Short gun cathode and anode assemblies.

FIG. 5.10--Photographs of the short gun.

The cathode block was clamped into a mounting fixture (not shown in Fig. 5.9) which in turn supports the focusing electrodes. These were formed from a single piece of sheet metal as is the anode. The shaping and alignment of these electrodes is accomplished by means of a jig and as they are thermally isolated from the hot cathode, the amount of thermal misalignment is kept at a minimum.

This type of cathode assembly is found to have a very uniform temperature over the emitting surface. Thus at 850°C the temperature variation over the uncoated cathode surface is only about 10°C, as measured by an optical pyrometer.

Originally, confining electrodes were placed at the sides of the cathode to prevent lateral spreading of the beam. These electrodes consisted of "Pierce electrodes" inclined at 45 degrees, with respect to the cathode. During the early course of the experiments these electrodes were removed, with little or no apparent effect on the beam optics, in order to be better able to view the profile of the convergent beam in the gun.

It should be noted that the mechanical design of the short gun as we have described it is the result of a certain amount of trial and error which was necessary to achieve the desired results. Most of the experience acquired during this process was put to very good use in the subsequent design of the long gun, and as a result few mechanical and structural difficulties were encountered during this latter stage of the work.

### 3. Experiments with the Short Gun<sup>(12)</sup>

#### a. Measurement of Cathode Current as a Function of the Gun Parameters.

In Appendix B approximate expressions relating the total gun current,  $I_c$ , voltage applied to the anode,  $\phi_A$ , and the magnetic field,  $B_0$ , are derived for both guns. For the short gun, the expression is of the form

$$I_c = - G B_0^3 + H B_0 \phi_A, \quad (5.2)$$

---

<sup>(12)</sup> All of the short gun measurements were made under space-charge limited conditions at the cathode.

where  $G$  and  $H$  are geometrical constants. Since the derivation of this expression is based on a small perturbation of the gun transit angle,  $u$ , from the exact design conditions, it is not valid for large departures of either  $B$  or  $\phi_A$  from the design values. In the range of validity however, we see that for constant  $B_0$ , the current should vary linearly with anode voltage, while for constant  $\phi_A$ , the current should decrease with increasing  $B_0$ .

In Fig. 5.11 measured values of cathode current as a function of  $\phi_A$  for a number of values of  $B_0$  are shown.<sup>(13)</sup> The solid lines are obtained from Eq. (5.2) where the values of the constants are those given in Appendix B. The exact design points for the different values of magnetic field are also shown. We see that for each value of magnetic field the experimental points are in excellent agreement with the theory, except for values of anode voltage significantly below the design points, where the measured currents all lie above the theoretical curves. This we should expect in view of the approximations used in deriving Eq. (5.2). Physically, at these low values of anode voltage, the actual electron trajectories are significantly altered from the design trajectories, and hence the variation in the transit angle may not be treated as a small perturbation.

Now if the gun trajectories are maintained constant by keeping the scaling parameter  $\phi_A/B_0^2$  fixed at approximately the design value, Eq. (5.2) implies that  $I_c \propto \phi_A^{3/2}$  as is the case for any space-charge limited gun. In Fig. 5.12 this behavior is shown. Experimental values of  $I_c$  are plotted on a two-thirds power scale as a function of  $\phi_A$  for two values of the scaling parameter greater and less than the design value. The solid curves are computed from Eq. (5.2). In this case the gun transit angle is fixed and we should expect all of the experimental points to be on a straight line. We see that for most points, agreement of experimental values with the theory is within 5 per cent.

The type of data which is presented in Figs. 5.11 and 5.12 was taken on a number of occasions after reassembly of the gun for repairs or other

<sup>(13)</sup> During these measurements, conditions in the drift region were adjusted for optimum transmission, and it should be noted that the gun current was found to be completely insensitive to variations in sole and circuit voltages.

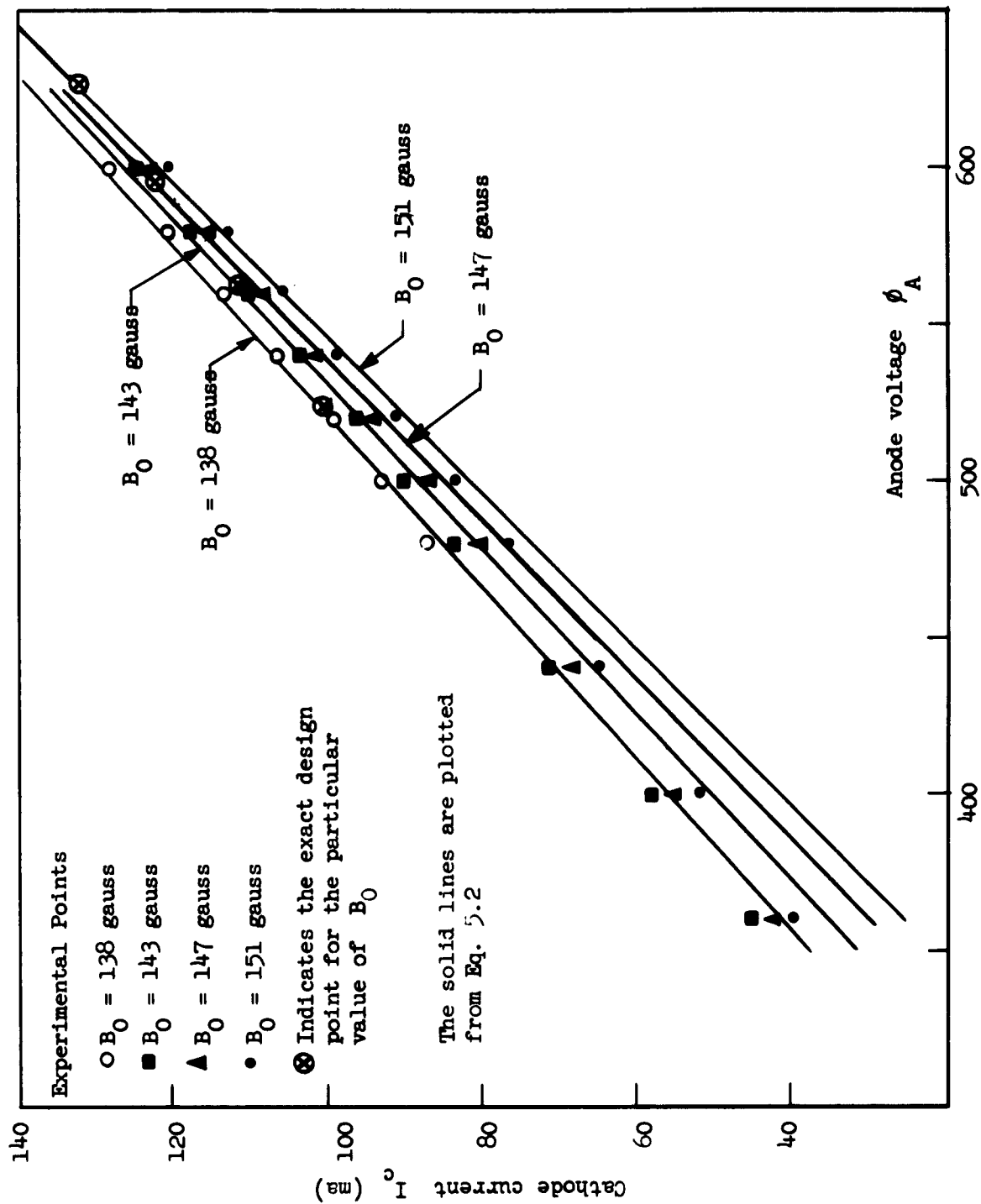


FIG. 5.11--Short gun characteristic.

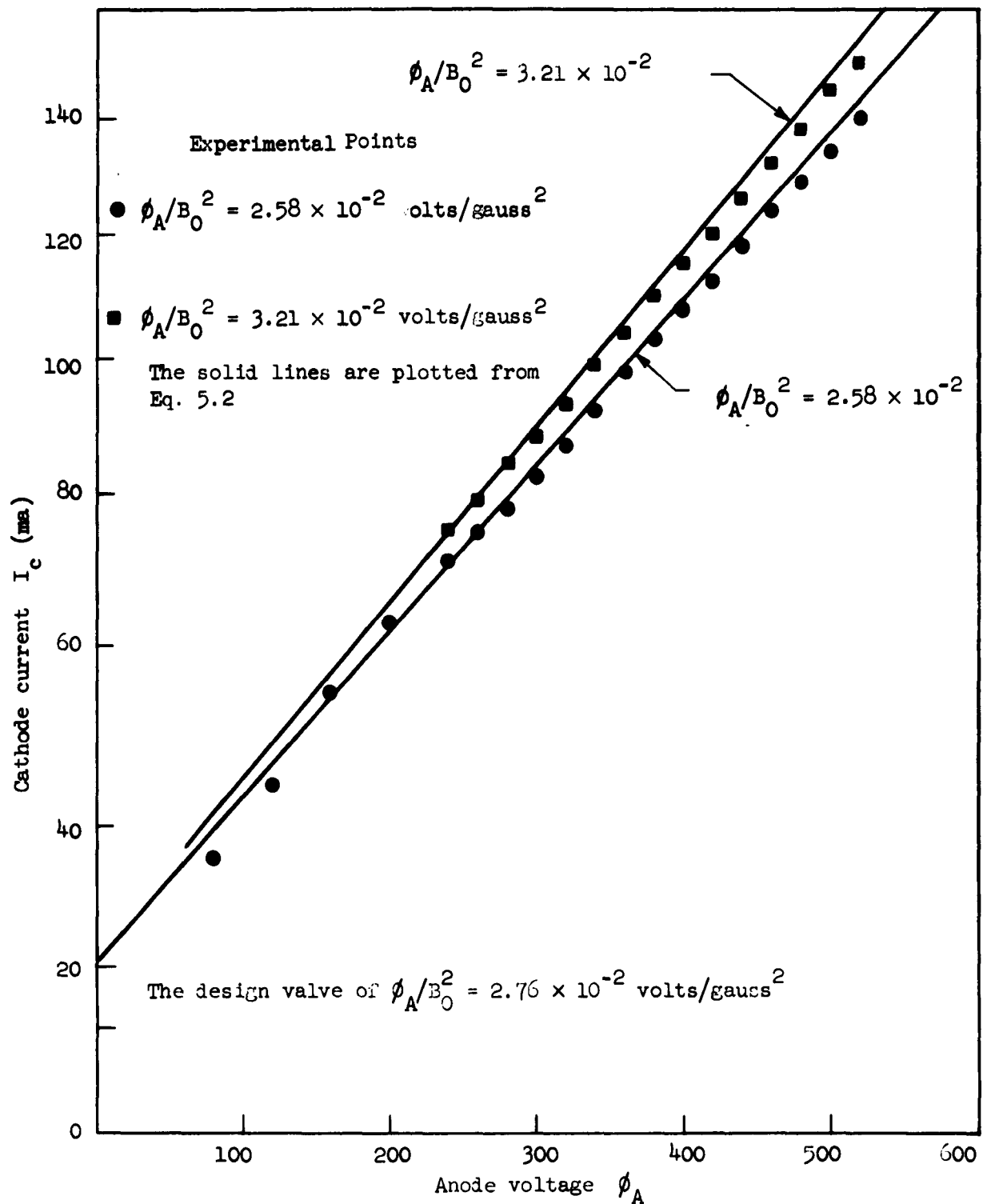


FIG. 5.12--Short gun characteristic for constant  $\phi_A/B_0^2$ .

reasons and such data was found to be reproducible in most cases to an accuracy of 5 per cent. Such variation undoubtedly resulted from errors in alignment and possibly imperfections in the emitting surface of the cathode. Since errors in the measurement of the magnetic field and the voltages and currents were on the order of 2 to 3 per cent, we concluded that the discrepancy between theory and experiment could well result from experimental error.

It may be noted that, with the gun operating at design conditions, no measurable current was drawn by the gun anode. It was found necessary to raise the anode voltage about 20 per cent above design value in order for this electrode to draw current, and for further increase in  $\phi_A$ , such current was found to increase very rapidly.<sup>(14)</sup> These observations would tend to indicate a very well defined beam in the gun region. This conclusion is supported by the visual appearance of the beam as seen in the various photographs. (see Fig. 5.19).

b. Transmission Measurements.

These measurements consisted in determining the amount of beam current collected by the drift region electrodes: (1) as a function of the circuit and sole potentials with the gun parameters fixed at, or near, design conditions, and (2) as a function of conditions in the gun with the sole and circuit voltages held constant. During all of these measurements the geometry of the gun in relation to the drift region electrodes was as shown in Fig. 5.13.

Before considering the detailed results, some general comments regarding the transmission characteristics are in order. Under all circumstances, in order to achieve maximum transmission, it was found necessary to increase the electric field intensity in the drift region, over the value existing at the exit plane of the gun. This phenomenon is probably a consequence of the high charge density at the gun exit, a result of the gun's excessive convergence mentioned above. Furthermore, for all conditions under which it was possible to support a stable beam in the drift region, very low sole currents, usually much less than 1 per cent of the total beam current were observed. Furthermore, the sole

---

<sup>(14)</sup> See section D-3b of this chapter.

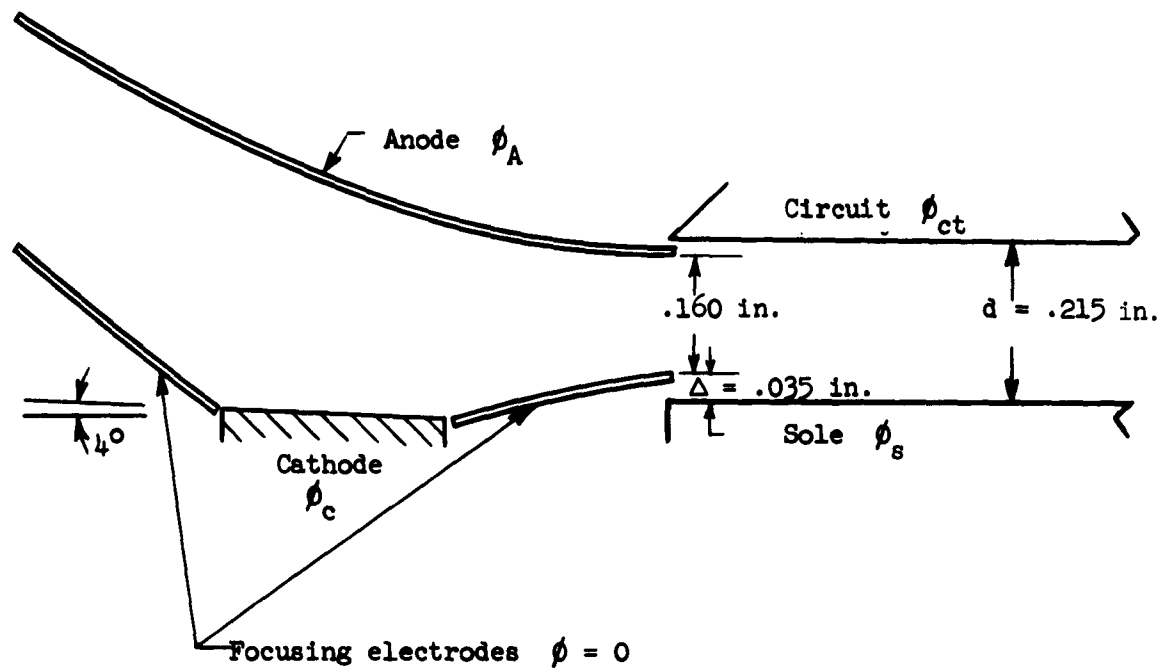


FIG. 5.13--Geometry for the short gun transmission measurements.



current under these conditions was always found to be negative,<sup>(15)</sup> even when the sole was made positive with respect to the cathode. It is thought that this negative sole current was a result of positive ion current to the sole and possibly of secondary emission effects. In support of the former, it was noted that the magnitude of this negative current was pressure-dependent, and was found to increase with increasing pressure.

(i). Transmission characteristics as a function of the drift region electrode potentials. With the gun at approximately the design conditions, currents to the circuit, sole and collector were measured as a function of the circuit potential for a number of values of sole potential. In Fig. 5.14 the current intercepted by the circuit is plotted as a function of circuit voltage for both positive and negative sole voltage. Figure 5.15 shows the negative sole currents corresponding to the data of the preceding figure. We see that, under optimum conditions, transmissions of about 98 per cent are achieved, even for positive sole voltages, over a range of approximately 200 volts, or 20 per cent, variation in  $\phi_{ct}$ .

The extreme left ends of both sets of these curves, corresponding to lower values of  $\phi_{ct}$  and markedly increased circuit and sole currents, represent areas of relative beam instability since both circuit current and negative sole current tended to fluctuate and were not reproducible in this region. For values of  $\phi_{ct}$  giving approximate field continuity between the gun and drift region, rather poor transmission was noted with 10 to 20 per cent of the total beam current going to the circuit. Under these conditions the magnitude of the negative sole current was also somewhat larger, although generally not exceeding 1-2 ma. On the other end of the transmission curves, where  $\phi_{ct}$  is greater than the range of voltage for minimum interception, no evidence of instability was seen; in this range, we see from the data that the current intercepted by the circuit slowly increases with increasing circuit voltage. However, the sole current is seen to reach a minimum value of less than 25  $\mu$ a.

(ii). Transmission as a function of gun potential. Figure 5.16 shows the circuit current, normalized to the total cathode current, as

<sup>(15)</sup> We define negative current in this case to be opposite in polarity to the collector current.

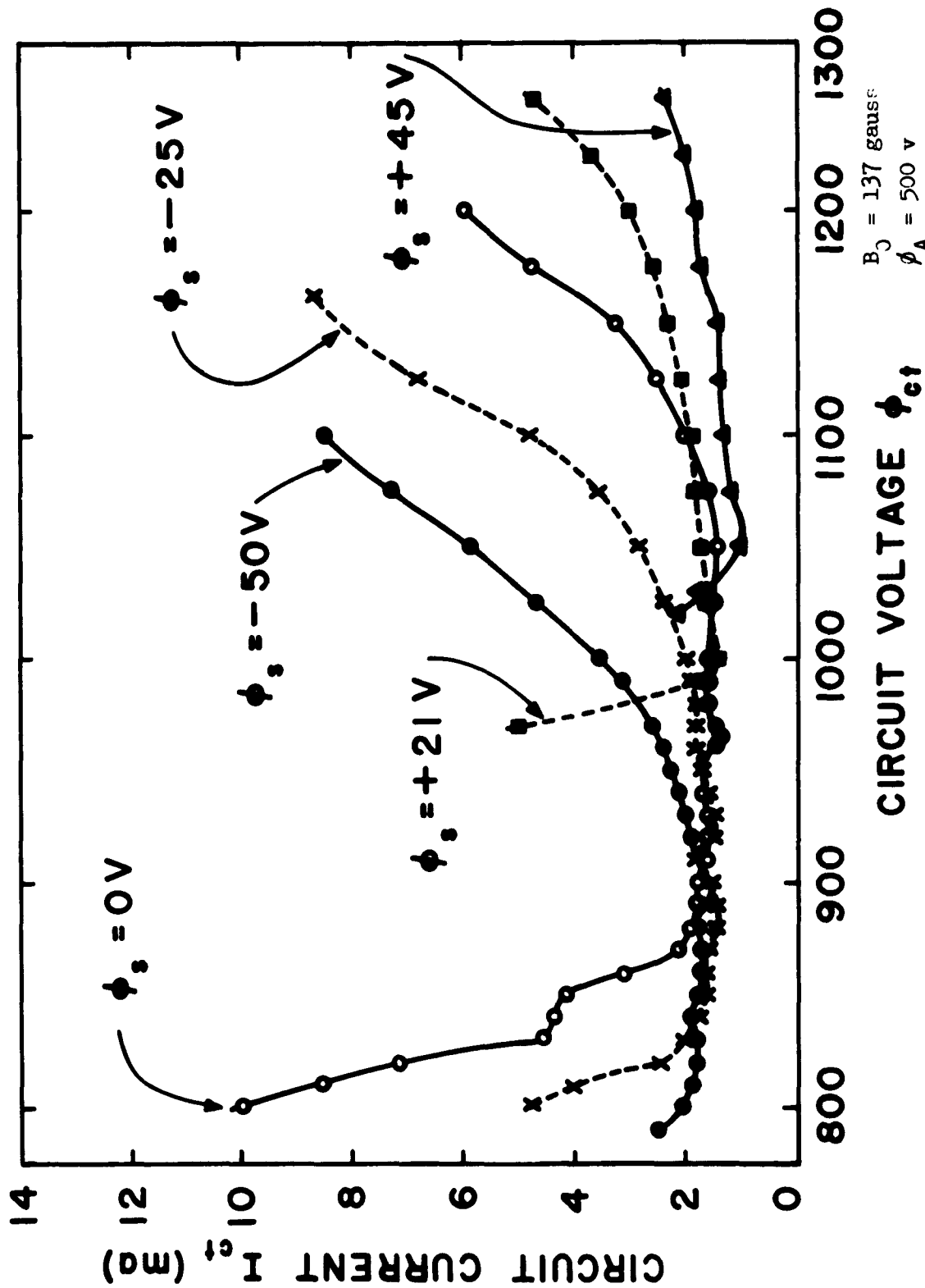


FIG. 5.14--Circuit current as a function of circuit voltage for various values of sole voltage.

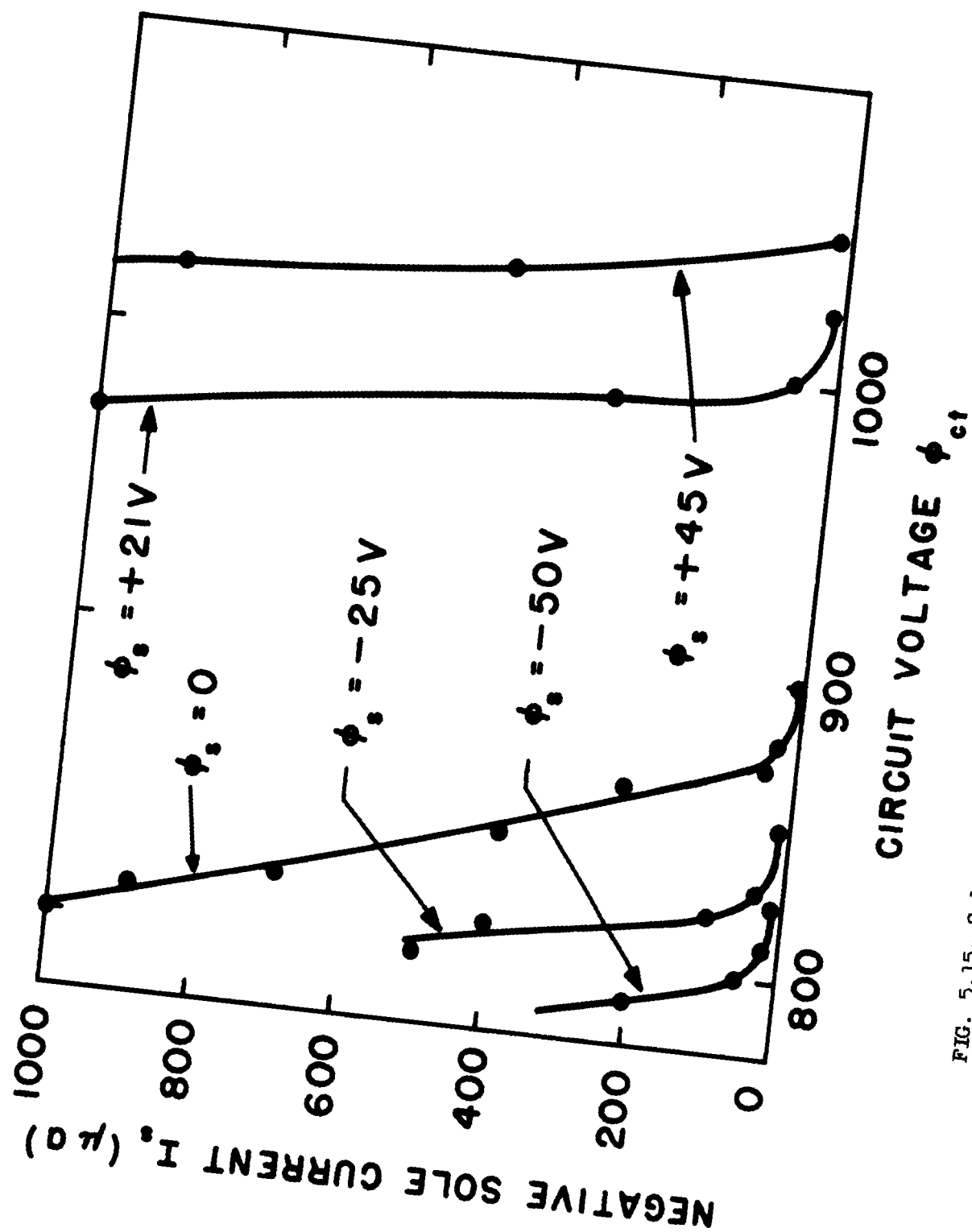
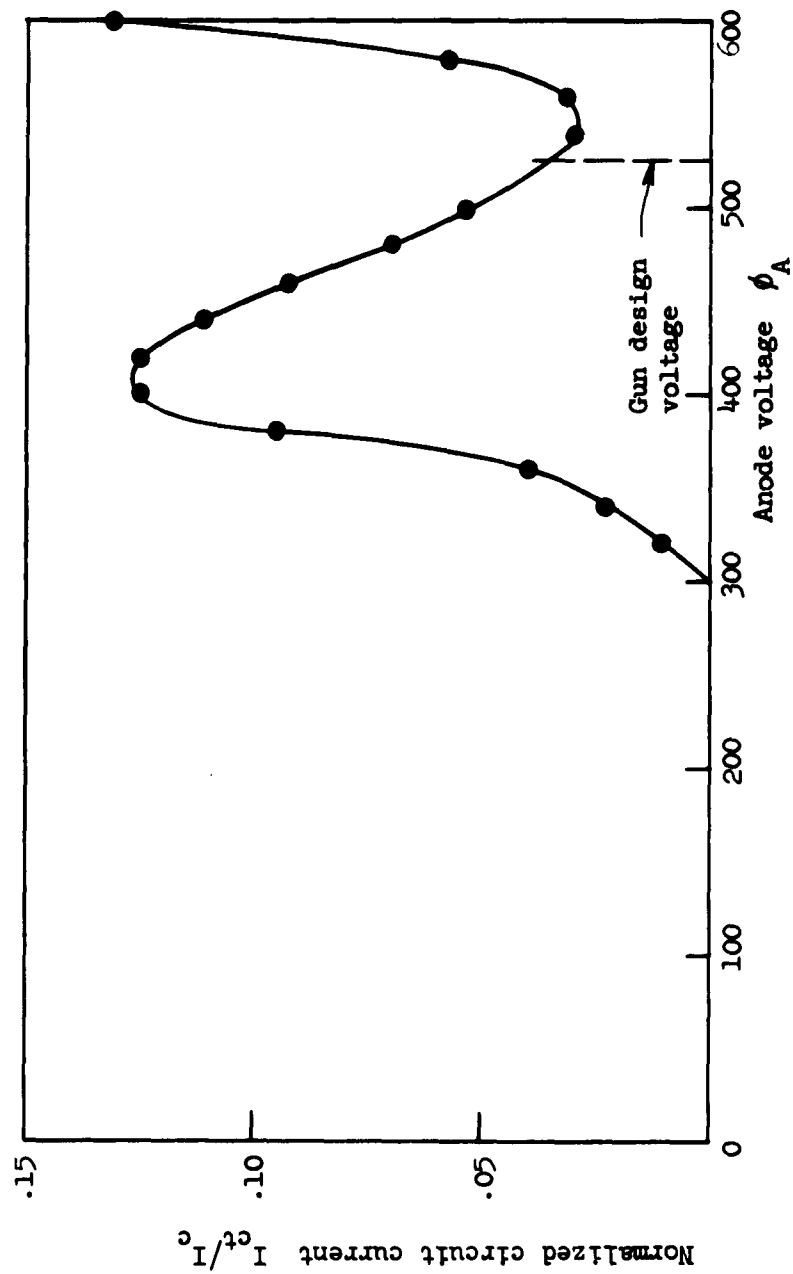


FIG. 5.15--Sole currents for the conditions of Fig. 5.14.



$B_0 = 138$  gauss

$\phi_{ct} = 975$  volts

$\phi_s = -45$  volts

FIG. 5.16--Normalized circuit current as a function of anode voltage.

a function of the gun anode voltage. For all points shown, current to the sole is less than 100  $\mu$ a and is negative. The significant result of this measurement is that a sharp minimum in current intercepted by the circuit is located very near the exact design voltage for the gun. The principal effect on the transmission of varying  $\phi_A$  from the design value is to cause the beam to enter the drift region nonparallel to the sole-circuit planes. The net result is a rippling beam and increased current collection by the second anode.

(iii). Cathode current and transmission as a function of cathode bias voltage. Normally the cathode was kept at the same potential as the focusing electrodes which are grounded. The cathode was, however, electrically isolated from ground. When the cathode was biased slightly positive or negative with respect to the beam focusing electrodes, the effect was to change the cathode current without changing appreciably the shape or the transmission characteristics of the beam (see Fig. 5.18f). Moreover, the variation of cathode current with cathode bias voltage, for small bias voltage, was found to be reasonably linear. Cathode current and circuit current as a function of cathode bias voltage are shown in Fig. 5.17. The values of circuit current are included as a general indication of the effect of such biasing on overall beam characteristics. It was noted that while this type of biasing would provide an easy method of current modulating the beam, it was not possible, by biasing the cathode sufficiently positive, to cut off the beam entirely. Moreover, after reducing the cathode current more than about 35 per cent by this means, it was found that noticeable current was collected by the gun anode.

#### c. Photographs of the Beam

At pressures of approximately  $10^{-5}$  torr, it is possible to observe the approximate geometry of the beam by means of the weak ionization and excitation induced by the beam. Estimates of the accuracy of this technique as applied to the M-type geometry have been made,<sup>19</sup> and both the effect of the ion fields and the errors due to the combination of the drift velocity and the finite relaxation time of the collision-excited molecules have been found to be negligible. The former result is in agreement with our observations, since no significant change,

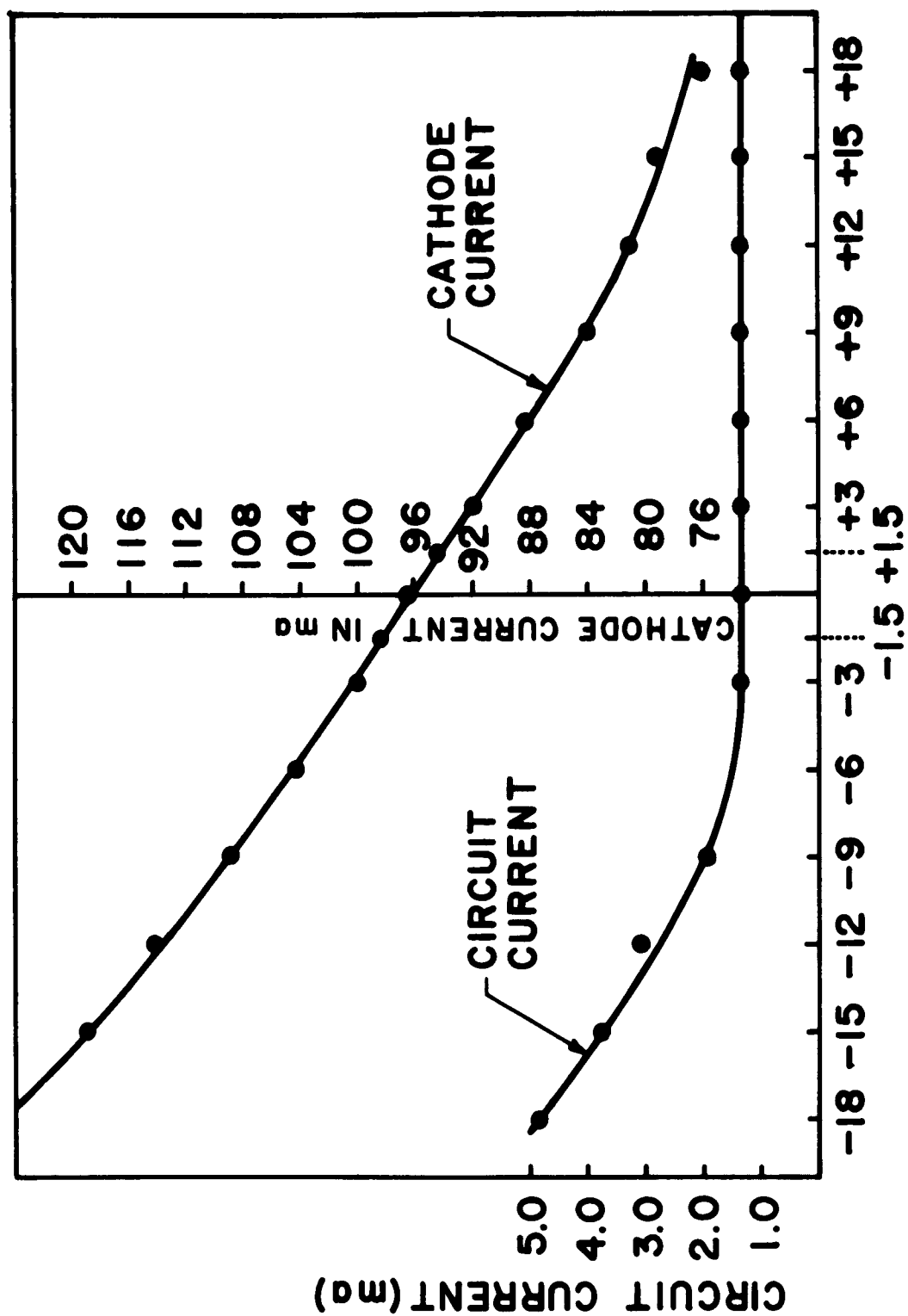


FIG. 5.17--Cathode and circuit currents as a function of the cathode bias potential.

either in total beam current or transmission was noted in making a change of pressure from  $5 \times 10^{-7}$  to  $10^{-5}$  torr, except in the case of partially poisoned cathodes where the higher pressure tended to restore the lagging emission.

In the case of the short gun, the pressure was raised by introducing hydrogen into the system by means of a titanium hydride generator of the type used in hydrogen thyratrons. By this means, reasonably accurate pressure control could be achieved by adjusting the power to the generator heater, while maintaining full pumping speed. This procedure, however, was found to be somewhat damaging to the cathode, probably as a result of the poisoning effects of the hydrogen, and in the later experiments with the long gun the hydrogen system was removed and increased beam viewing pressures provided by decreasing the pumping speed. It is felt that this latter procedure caused less cathode damage than the former.

Visual observations of the beam profile were made in two ways. By using a vernier telescope, it was possible to see any fine details which might escape detection with the naked eye as well as to measure the beam thickness. In addition numerous photographs of the beam under varied gun and drift region conditions were taken.

Figure 5.18 shows a series of representative photographs of the beam in the gun and drift region. These prints were made from color transparencies taken with high-speed Ektachrome color reversal film. The printing paper was selected so as to have a very hard response to blue, the color of the beam, and a much softer response to yellow and red. As a result the effective cathode glare was reduced and a sharp profile of the convergent beam in the gun was obtained.

Figure 5.18a is intended to represent an example of a reasonably straight, well-focused beam. From the photograph, recalling that the length of the cathode is .3 in., we see that the thickness of the beam in the drift region, well away from the gun exit plane, is about .040 to .045 inches. The effective convergence of the gun is then about 7:1. For a beam current of 114 ma, with a beam drift velocity equal to  $E_0/B_0$  in the drift region, and an assumed beam width of 1.1 in., the ideal Brillouin thickness is .036 in.; thus the ratio of the measured beam thickness to that of the corresponding Brillouin beam is about 1.2 .



(a)

$$\phi_A = 560v \quad I_c = 11.4ma$$

$$\phi_{ct} = 1050v \quad I_{ct} = 1.8ma$$

$$\phi_s = -45v \quad B_0 = 140 \text{ gauss}$$



(b)

All parameters are as in  
(a) except

$$\phi_{ct} = 1150v$$

$$I_{ct} = 4.0ma$$



(c)

All parameters are as in  
(a) except

$$\phi_{ct} = 950v \quad I_{ct} = 2.6ma$$

FIG. 5.18--Photographs of the beam from the short gun.



(d)

$$\begin{aligned}\phi_A &= 545v & I_c &= 112ma \\ \phi_{ct} &= 1100v & I_{ct} &= 2.4ma \\ \phi_s &= 0 & B_0 &= 140 \text{ gauss}\end{aligned}$$

(e)

$$\begin{aligned}\phi_A &= 560v & I_c &= 114ma \\ \phi_{ct} &= 1175v & I_{ct} &= 1.8ma \\ \phi_s &= 90v & B_0 &= 140 \text{ gauss}\end{aligned}$$

(f)

Cathode biased + 45v with respect  
to the focusing electrodes  $I_{ct} = .5ma$

$$\begin{aligned}\phi_A &= 500v & I_c &= 52ma \\ \phi_s &= 0 & \phi_{ct} &= 960v & I_A &= 1.0ma\end{aligned}$$

Fig. 5.18--(con't).

The gun is then seemingly successful in launching a beam approximating planar Brillouin flow, at least in its gross features.

Several comments should be made regarding this conclusion. In order to achieve the optimum focusing shown in the photograph, it was necessary to abruptly accelerate the beam at the gun exit. Thus on the basis of the gun design, the average beam velocity at exit, for the conditions of the photograph, is approximately  $1 \times 10^7$  m/sec while  $E_0/B_0$  in the drift region is  $1.53 \times 10^7$  m/sec. Note additionally that while the average beam thickness in the drift region is only slightly greater than that for a Brillouin beam, some evidence of instability and departure from Brillouin flow is seen. In all of the beam photographs, we note that the lower edge of the beam is not uniformly well defined. At periodic intervals along the beam, relatively thin laminar sections appear to separate from the main portion of the beam and diverge toward the sole.<sup>(16)</sup> This effect is more pronounced under less ideal focusing conditions than those of Fig. 5.15a, but is clearly seen in the extreme right end of all of the beam photographs in Fig. 5.18. This phenomenon appears at periodic intervals of approximately  $\lambda_c$  along the beam. It is thought that these "tails" probably are the envelopes of a relatively small class of electron trajectories which are undulating across the beam as a whole. These excessively perturbed trajectories are probably a result of the sudden acceleration experienced by the beam at the gun exit plane and are most likely a periodic repetition of the beam spreading which occurs in this area.

It should be noted that under no conditions was any visual evidence of rf growth, such as a continual increase in beam thickness, seen in the drift region. This observation is in general agreement with the absence of measurable sole current.

The remainder of the beam photographs are intended to show the general behavior of the beam under less ideal focusing conditions than those of Fig. 5.15a.

Figures 5.18 b and c show the effect of increasing and decreasing

---

<sup>(16)</sup> It is definitely believed that this phenomenon is not related to hollow beam instability. We have shown in Appendix A, in agreement with the earlier results of Pierce, that such dc instabilities should not exist for planar crossed-field beams.

the circuit voltage in comparison to the value in the first photograph. We see that  $\phi_c$  may be varied 20 per cent without greatly affecting the shape of the beam, a result in agreement with the transmission data shown in Fig. 5.14.

Figures 5.18 d and e show the beam with the sole potential zero and + 45 volts, respectively. As the sole voltage is increased, the effect is to increase the potential discontinuity at the exit plane. We see that, as a consequence, the beam becomes somewhat less compact and in the case of positive  $\phi_s$ , undulates noticeably. Again, it should be emphasized that even under such conditions as these no significant sole current was measured.

Figure 5.18 f shows the geometry of the beam with the cathode biased + 45 volts with respect to the focusing electrodes. The beam current is approximately half that measured with no bias voltage. From the photograph, which indicates the extent of the cathode emitting surface, it appears that most of the current is drawn from the center of the cathode, with little current coming from the edges near the focusing electrodes. The shape of the resultant beam is then similar to that of a beam from a shorter cathode. It is thought that the normal components of the biasing field, which is certainly the strongest on the portions of the cathode surface nearest the focusing electrodes, effectively "cutoff" these areas, yet that the potentials do not vary sufficiently from the exact values to greatly alter the shape of the remaining portion of the beam coming from the center of the cathode.

Figure 5.19 shows an enlargement of the beam in the gun region. The points outline the edge trajectories of the theoretical beam which is traced to the approximate position of the exit plane. The black rectangular area near the cathode is an obstruction between the camera and the end of the cathode which is seen in all of the photographs. We see that the shape of the experimental beam is in good agreement with the theory, except near the exit plane, where the beam spreads and is considerably thicker than predicted. We note in addition what appears to be a slight deficiency in emission from the rear of the cathode.

On the basis of these photographs we concluded that the gun focuses the beam substantially as predicted by the theory, except near the exit



FIG. 5.19--The beam in the gun region  
showing the theoretical edge  
trajectories.

plane where spreading occurs, and consequently the high space-charge densities, predicted by the flow equations, are not achieved in practice. By accelerating the beam at the exit, an apparent tendency towards instability and beam breakup is overcome, and a reasonable approximation to Brillouin flow is achieved. In practice it may well be desirable to provide such additional acceleration somewhat more gradually than has been done in these experiments. Thus a short transition region might be placed between the gun and the drift region to accelerate the beam to the drift region velocity. It is also possible that the same result might be achieved by modifying the gun electrodes near the exit plane so as to raise the gun exit velocity without greatly altering the form of the beam. However, in view of the success achieved with the simple gun as we have described it, these possibilities have not been pursued further.

#### D. THE EXPERIMENTAL LONG GUN

##### 1. Design Considerations

The electrode configuration for the long gun which we have studied is shown in Fig. 5.20. The focusing electrodes correspond to the normalized equipotential  $\Phi = 0$  while the anode is a portion of the equipotential  $\Phi = 2000$ . The normalized cathode length,  $L$ , is 130, and the cutoff plane is at  $X = 1000$  on the upper edge trajectory. At the exit plane, the values of  $u$  on the upper and lower edge trajectories are 44.7 and 41.7, respectively; thus the average transit angle in the gun is roughly about  $14\pi$ . The beam thickness at exit is 3.0 normalized units, and thus on the basis of dc theory, the gun would be expected to have an area convergence of 43.4.

We may show, as in Eq.(5.1), that the slope  $dY/dX$  at any point on the long gun trajectories is given in terms of  $u$  simply by

$$\frac{dY}{dX} = \tan \psi = \frac{1}{u} , \quad (5.3)$$

a monotonically decreasing function of  $u$ . The exit angles of the upper and lower edge trajectories are then found to be 1.28 degrees and 1.37 degrees, respectively. In view of these small values, the gun was not tilted in an effort to minimize the injection angles, as was done with the short gun.

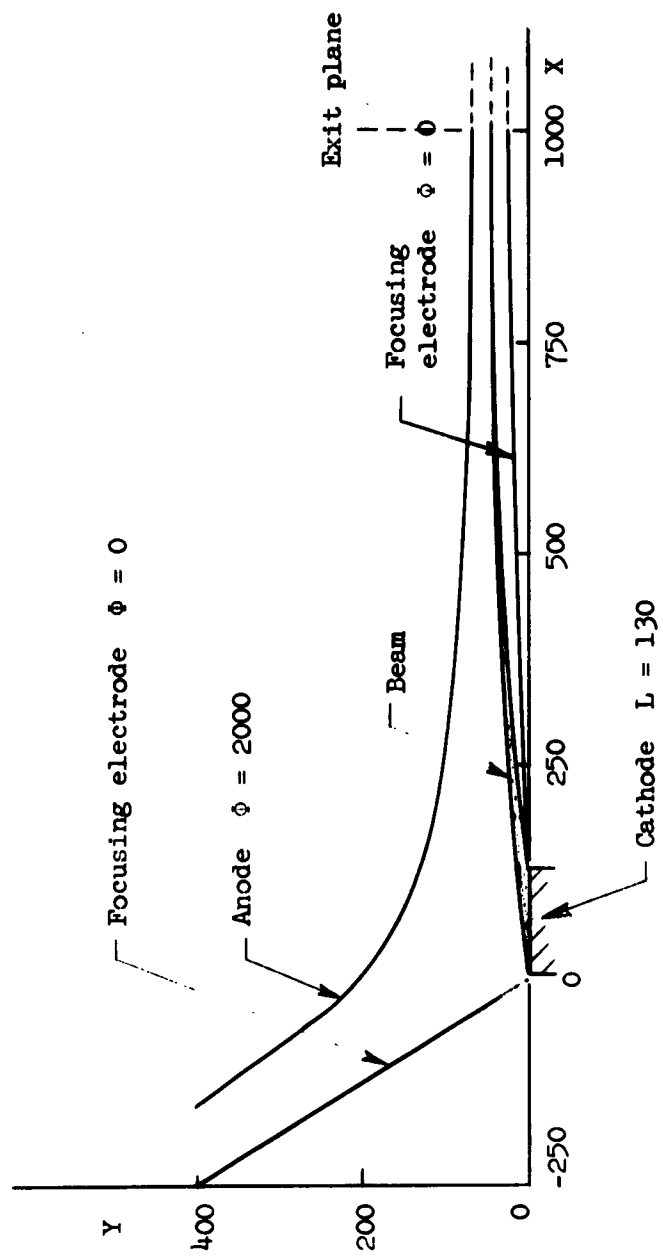


FIG. 5.20--Electrode configuration of the experimental long gun.

The remainder of the design parameters are evaluated exactly as before. The results are summarized in Table II. We see that at the exit, the beam, on the basis of the gun theory, almost exactly satisfies the Brillouin conditions. This we should expect, since it can be shown very simply from the flow equations that at any point in the beam sufficiently far from a finite length cathode, the Brillouin conditions are satisfied to a high degree of accuracy. Thus, in principle, insofar as it is possible to establish the flow, the long gun would seem to provide the ultimate solution to the problem of producing Brillouin flow. However, we shall see that experimentally there are difficulties, and the theory is overoptimistic, primarily because of the appearance of rf instabilities in the gun flow.

For the design parameters given in Table II. the quantity  $\phi_0$ , the initial potential at the cathode, has a value of .114 volts. At a cathode temperature of  $900^\circ\text{C}$ ,  $kT = .101$  electron volts, so that at the cathode the conditions for the validity of the simple flow solution are approximately satisfied. We may also note that by scaling the gun parameters, that is, by varying the anode potential  $\phi_A$  and  $B_0$  such that  $\phi_A/B_0^2$  is constant at the design value of  $7.10 \times 10^{-4}$  v/gauss<sup>2</sup>, it is possible to vary  $\phi_0$  so that its value ranges well above and below the value of the thermal potential. Thus for  $B_0 = 1000$  gauss and 400 gauss, the corresponding values of  $\phi_0$  are .178 volts and .0285 volts, respectively. The effect of this form of scaling on the beam has been examined experimentally and will be discussed later.

It should be pointed out that we have purposely chosen a rather short cathode, primarily for very practical reasons, the principal one being the necessity for limiting the beam current because of collector cooling problems. The ability to be able to carry out the type of scaling measurements discussed in the previous paragraph, and the magnetic field which is available, essentially determines the choice of  $J_y$ . Hence, the restriction on total current dictates the choice of the cathode length. It should be emphasized that, in principle, much greater convergence, current and perveance are available from this type of gun through the use of a longer cathode.

TABLE II

## A. Design Parameters for the Experimental Long Gun

total beam current $I_c$	104 ma
beam width	1.1 in.
current density at the cathode $J_y$	200 ma/cm <sup>2</sup>
dc magnetic field $B_0$	800 gauss
linear normalization factor $\eta J_y / \epsilon_0 \omega_c^3$	.000559 inches/normalized unit
potential normalization factor $\eta J_y^2 / \epsilon_0^2 \omega_c^4$	.227 volts/unit of normalized potential
anode potential $\phi_A$	454 volts
perveance	$10.8 \times 10^{-6}$

## B. Exit Conditions

beam thickness $\delta$ at the exit plane	.00168 in.
upper edge trajectory at the exit plane; potential	227 volts
exit angle	1.28 degrees
lower edge trajectory at the exit plane; potential	197 volts
exit angle	1.37 degrees
average velocity at exit	$8.63 \times 10^6$ m/sec
velocity gradient across the beam at exit:	$1.46 \times 10^{10}$ sec <sup>-1</sup>
beam plasma frequency at exit $\omega_p$	$1.42 \times 10^{10}$ sec <sup>-1</sup>
cyclotron frequency $\omega_c$	$1.41 \times 10^{10}$ sec <sup>-1</sup>



## 2. Mechanical Design of the Long Gun

The details of the experimental long gun are shown in Fig. 5.21. In many respects this structure is similar to the short gun discussed earlier. While the cathode emitting surface is physically smaller than that of the short gun, the same type of cathode and heater assembly, as well as the means of aligning this structure with respect to the focusing electrodes, has been employed with equally good success in this later gun.

The curved surfaces of the anode and focusing electrodes were machined from solid stock. The anode curvature was approximated by two straight lines and two circular arcs of different radii. With solid electrodes of this type, the alignment problem was reduced to one of aligning plane, rather than curved surfaces. The alignment was therefore simpler, and more accurate than for the earlier gun.

The cathode surface was prepared in a somewhat different fashion from the earlier gun. In this case, a fine nickel mesh (250 meshes per in., wire diameter .0016 in.) was bonded to the surface of the cathode button under pressure in a hydrogen atmosphere at 950°C. The chief advantage of this technique over the nickel powder method was a greater uniformity in the thickness of the applied matrix material.

As shown in Fig. 5.21, confining Pierce electrodes inclined at 45 degrees to the cathode plane are situated at each side of the cathode. Since these electrodes obscure only a very small portion of the beam close to the cathode, they do not provide a serious hindrance to beam viewing.

Photographs of the gun and some of its component parts are shown in Fig. 5.22. It should be noted that, as the result of a later experiment, the electrodes as shown in the photographs have been modified (see section 3f of this chapter). The cutoff plane has in effect been moved much closer to the cathode by removing a portion of the anode and the forward focusing electrode. All other details are as originally constructed.

## 3. Experiments with the Long Gun

As was the case for the earlier gun, the experiments which were performed with the long gun were generally of two types: (1) experiments

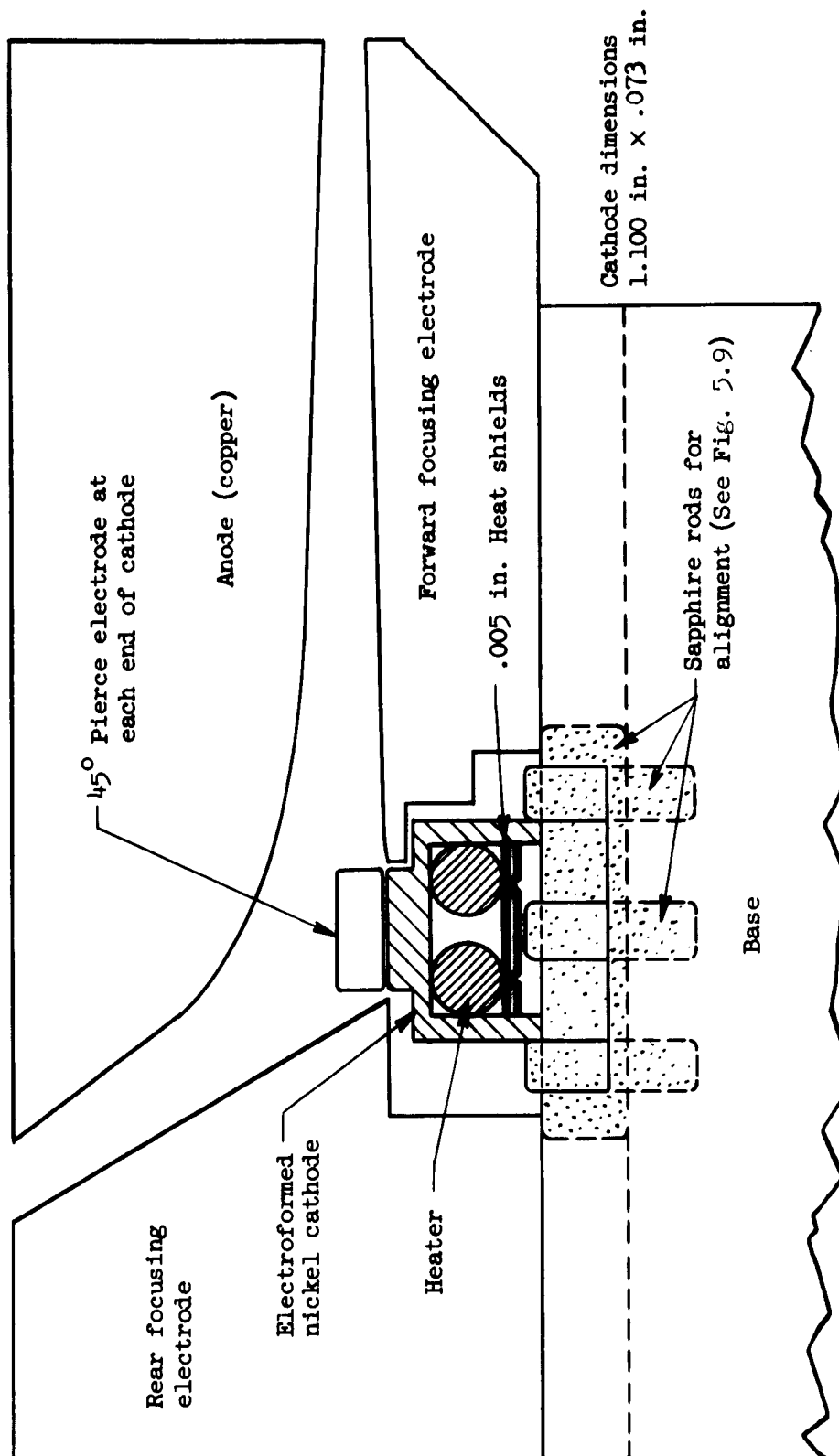
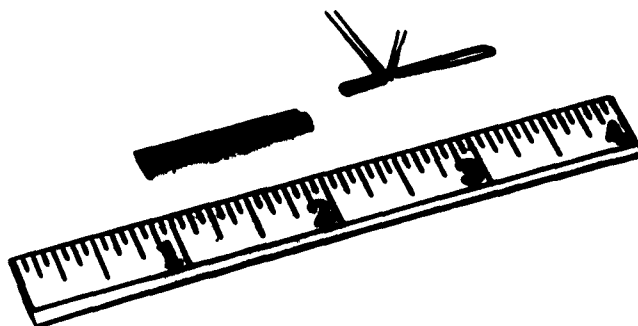


FIG. 5.21--Mechanical details of the long gun.



a. Short gun cathode and anode assemblies.



b. Short gun cathode and heater.

FIG. 5.22--Photographs of the short gun.

dealing only with the gun and with the beam in the gun region (sections a, b and c) and (ii) transmission measurements dealing with the nature of the beam in the drift region (section d) as a function of both the gun and drift region parameters. In addition, visual observations of the beam are described in section e, while two additional experiments involving basic changes in the long gun optics are discussed in section f.

The object of the first group of experiments (i), like similar ones performed with the short gun, was to verify the dc theory of the long gun. Thus, these measurements consisted primarily of obtaining cathode current as a function of anode potential and magnetic field over a wide range of these parameters (section a). In addition to these measurements, the cutoff characteristics of the gun, i.e., current collected by the accelerating anode as a function of magnetic field, were obtained (section b). Such data is of interest since the absence of an abrupt cutoff of anode current is characteristic of an unstable beam, that is, a beam containing excess energy electrons. Finally, the effects of biasing the focusing electrodes with respect to the cathode were investigated (section c) in an experiment much like an earlier one performed with the short gun.

The second series of experiments (ii) was much more extensive than was the similar group of measurements made with the earlier gun, primarily because of the appearance of beam instabilities as evidenced by the collection of current by the sole. Such current was noted even with this electrode biased many volts negative with respect to the cathode. As mentioned earlier, this phenomenon has been observed in almost all previous crossed-field experiments. The mechanism responsible for such sole current as well as the excessive amounts of noise usually measured in crossed-field beams is not at present understood. Some evidence (including that from the present work) indicates that these phenomena are related to diocotron or slipping-stream amplification<sup>6,29,30</sup> in the beam and to some form of instability originating very close to the cathode which appears to depend on whether the cathode is space-charge or temperature limited.<sup>18</sup> In the long gun transmission measurements, we have attempted to gain as much information as possible as to precisely which aspects of the beam or its external environment are important in

determining the magnitude of the sole current, and consequently, how it may be possible to overcome this instability.

For the most part, the transmission experiments consisted in measuring the magnitude and other properties of the sole current as a function of certain parameters characteristic of the gun, the drift region, or the beam itself. With the exception of certain of the early experiments (see for example, section d-1), the circuit was sufficiently far removed from the beam so that little measurable circuit current was observed under most experimental conditions. In addition to measuring the total sole current intercepted by the continuous sole, in some cases measurements were made of the sole current distribution as a function of the distance from the gun exit plane. These results were obtained by using the segmented sole structure. In addition, some attempts, by using Langmuir probe techniques,<sup>32</sup> were made to measure the temperature of the electrons collected at the sole. These measurements consisted of obtaining negative sole current as a function of the negative sole potential for both the continuous sole and for the individual sections of the segmented sole. A semilogarithmic plot of such data, if linear, may be related to the electron temperature  $T$ , since for a Maxwellian energy distribution of the sole current electrons the slope of such a curve is  $e/kT$ . In many cases, experimental curves of this sort (including ours) are found not to have a constant slope, so an accurate evaluation of temperature is not possible. Moreover, such experiments are subject to rather large errors, as a result of secondary emission effects at the sole. The results obtained are therefore somewhat suspect, and do not represent a very accurate description of the true energy distribution. We have included such measurements only as a means of obtaining a rough comparison of the energy spread in the beam under various conditions and at different locations in the drift region.

Section d-1 describes investigations of the transmission of the beam through the drift region as a function of the externally applied fields, these fields being continuous between the gun and drift region. The data are found to be scalable in terms of the quantity  $(\phi_{ct} - \phi_s)/B_0^2$ , which we shall hereafter refer to as the drift region scaling parameter. In section d-11 the observed dependency of the sole current on the total

beam current when the cathode is space-charge limited is described, while in section d-iii the reduction in the magnitude of the total sole current brought about by temperature-limiting the cathode is presented.

In sections d-iv through d-vi we describe a series of measurements related entirely to conditions in the drift region. During these experiments the gun parameters were kept at or near the design values, except when the cathode current was reduced from the design value by temperature limiting. In section d-iv, the observed dependency of the sole current on the value of the drift region scaling parameter is discussed. In these experiments potential and field discontinuities existed at the gun exit plane. It is found that the sole current becomes very small for sufficiently large values of the scaling parameter. In section d-v we consider the distribution of sole current as a function of the distance from the gun exit plane, the experimental observations having been carried out for various conditions in the drift region, and for both space-charge and temperature limited conditions at the cathode. In section d-vi the measurements of sole current temperature are described, and particular note is made of the observed dependency of these measurements on the value of the scaling parameter.

Like the short gun, described earlier, the long gun was normally operated space-charge limited. However, some of the measurements, particularly those pertaining to the beam instabilities, were made under both space charge and temperature-limited conditions. In the following sections, these data are given simultaneously for purposes of comparison. However, unless specifically noted, the measurements were made under space-charge limited conditions.

a. Measurement of Cathode Current as a Function of the Gun Parameters.

We show in Appendix B for the long gun that the cathode current, anode voltage and magnetic field should vary approximately according to the relation

$$I_c = M \phi_A^2 / B_0, \quad (5.4)$$

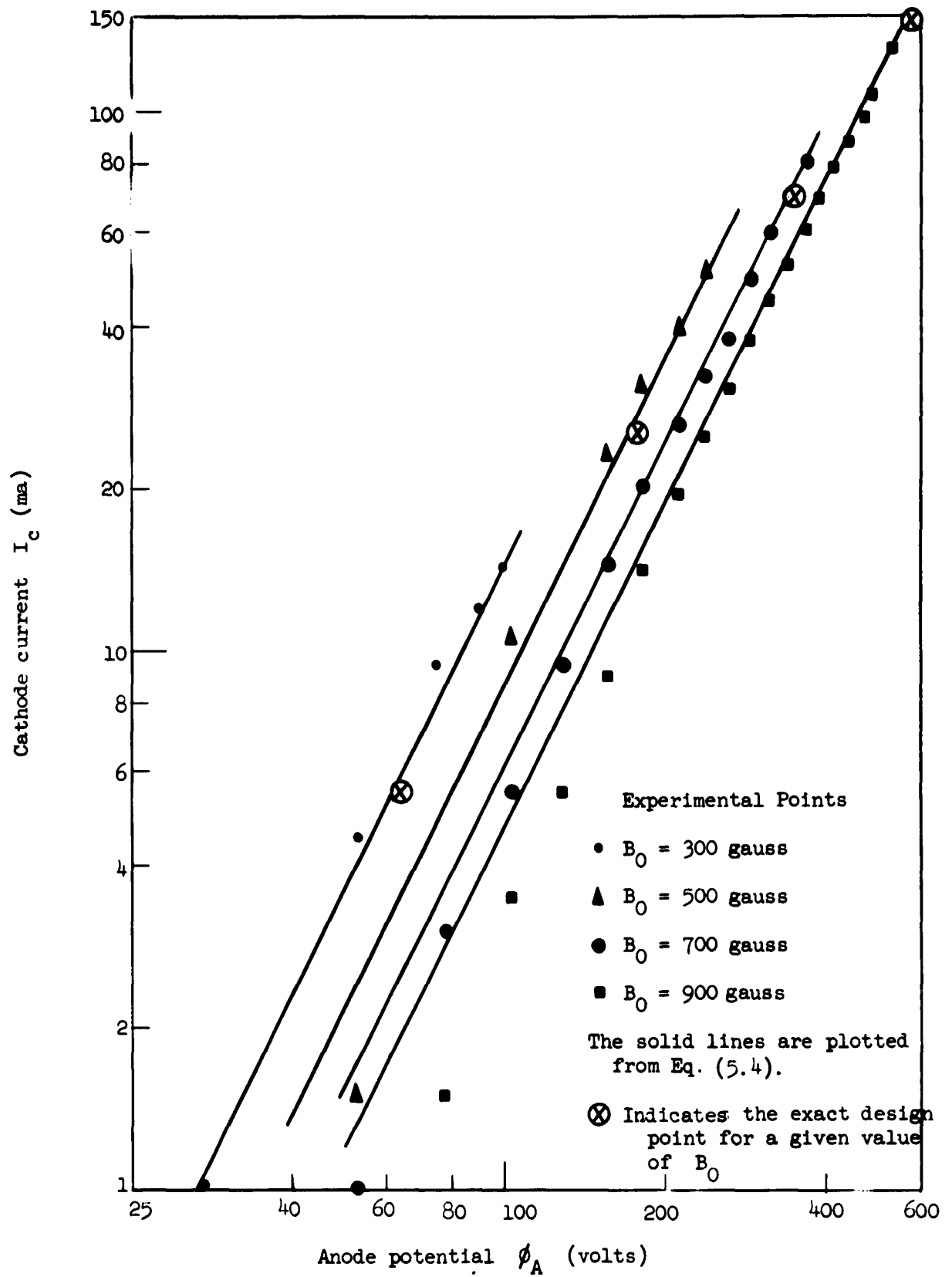
where  $M$  is a constant dependent on geometry.<sup>(17)</sup> Since the derivation of this equation is not based upon a perturbation approximation in  $u$ , as was the corresponding expression for the short gun, it does not have such a limited range of validity, and in particular, it should hold over a range of anode voltages widely different from the design value. However, as a result of such variation on  $\phi_A$ , the gun transit angle, and hence the shape of the trajectories, do change. If  $\phi_A$  and  $B_0$  are varied so that  $\phi_A/B_0^2$ , and hence the shape of the trajectories remain unchanged, the current varies as  $\phi_A^{3/2}$ , as we should expect for a normal space-charge limited gun.

Figure 5.23 shows the values of  $I_c$  which were measured experimentally as a function of  $\phi_A$  for four different values of  $B_0$ . The solid curves are plotted from Eq. (5.4) with the constant  $M$  as evaluated in Appendix B. In addition, the exact design points ( $\phi_A/B_0^2 = 7.10 \times 10^{-4}$  v/gauss<sup>2</sup>) are shown for each value of  $B_0$ . The experimental results are seen to be in good agreement with the theory, except for values of  $\phi_A$  and  $I_c$  very much below the design points where the experimental values of current are smaller than predicted by theory. Figure 5.24 shows the experimental values of  $I_c$  for two different constant values of  $\phi_A/B_0^2$ , larger and smaller than the exact design value. The experimental points are plotted on a two-thirds power scale as before. The solid curves are plotted from Eq. (5.4) for the two experimental values of  $\phi_A/B_0^2$  as well as the exact design value of this quantity. Again, the experimental points are seen to be in good agreement with the theory. The same remarks, which were made earlier for the short gun on experimental error and reproducibility of this type of measurements, also apply to these results.

b. Measurement of the Cutoff Characteristics of the Long Gun. The object of this experiment was to determine how well defined the beam was at the gun exit. The measurement consisted of determining the fraction of the cathode current drawn by the accelerating anode as a

---

<sup>(17)</sup> The difference in the form of Eq. (5.4) and the corresponding expression for the short gun [Eq. (5.2)] should be noted. Previous workers<sup>8,18</sup> have found experimentally that the cathode current of simpler guns of both the long and short types varies approximately as the ratio of the anode voltage squared over the magnetic field; thus the form of Eq. (5.4) is not unexpected.



5.23--Long gun characteristic.



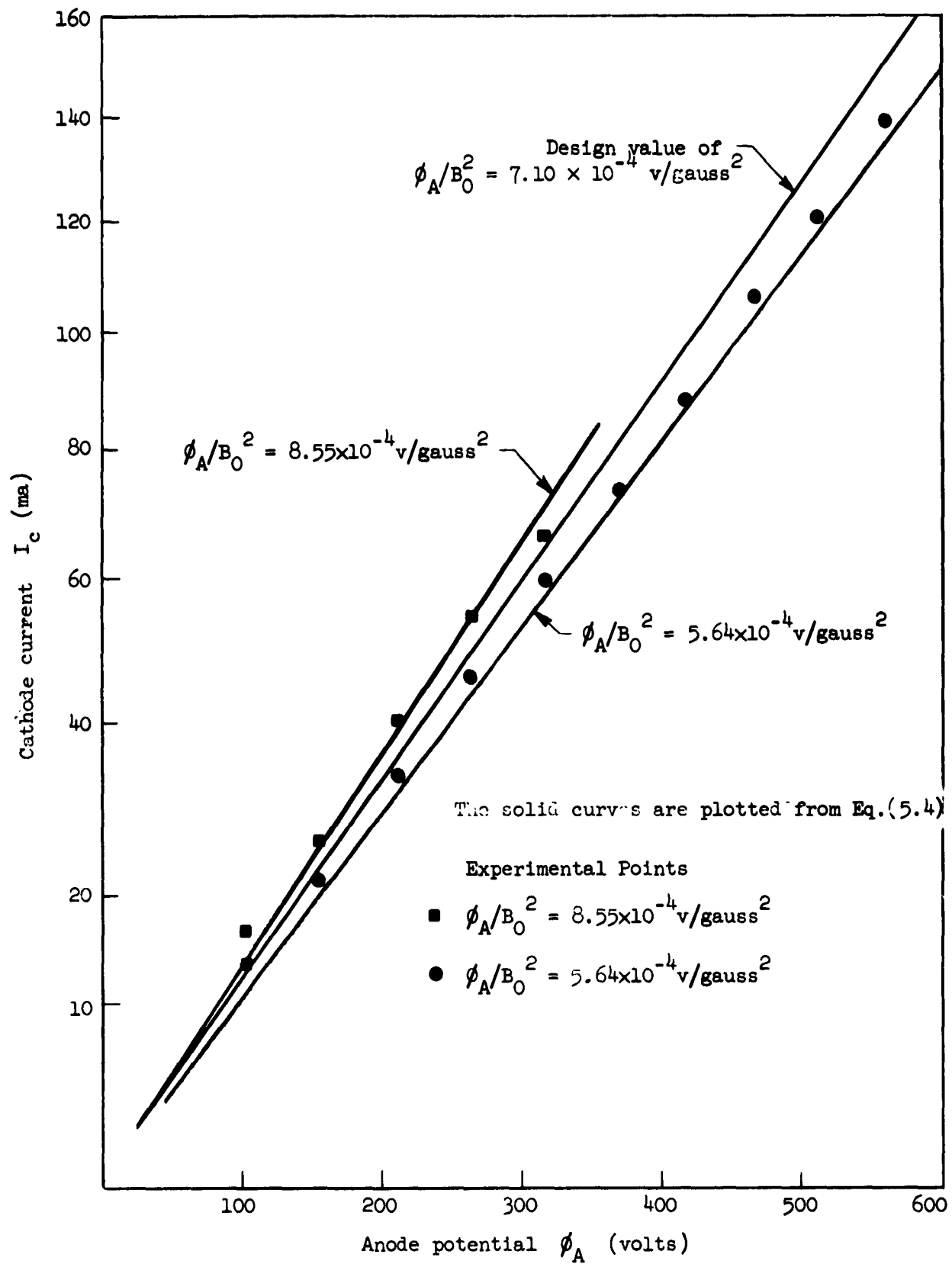


FIG. 5.24--Long gun characteristic with  $\phi_A/B_0^2$  held constant.

function of the magnetic field strength. The results are shown in Fig. 5.25. The ratio of the anode current  $I_A$ , normalized to the cathode current, is shown as a function of magnetic field which is normalized to the design value of  $B_0$  for  $\phi_A = 114$  volts. Data are shown for both space-charge and temperature limited conditions at the cathode. In the latter case the heater power was reduced so that  $I_c$  reached exactly half of its space-charge limited value. We see that at the design value of  $B_0$ , the normalized anode current is reduced from unity to a factor of roughly  $5 \times 10^{-3}$  and that this reduction occurs over a range of from 50 to 100 per cent of the design magnetic field. In addition, the space-charge limited points are seen to always fall below the corresponding temperature-limited values. We may compare these results with those of Anderson,<sup>31</sup> who has made similar measurements on a short gun, similar to ours, which was recently incorporated into an M-type backward wave amplifier. Anderson's data are shown in Fig. 5.26. Normalized anode current is shown as a function of the magnetic field also normalized to the design value. From his data we see that the rate of reduction of  $I_A$  is more rapid than for our results. For Anderson's gun, normalized anode current obtained under space-charge limited conditions always is greater than its temperature-limited values. In addition, the normalized anode current reaches a plateau well below the cathode current; this plateau is at a much lower level in the temperature-limited case. In our measurements with the long gun, no such plateau was observed even with a normalized anode current as low as  $10^{-5}$ .

We suggest that the behavior observed with Anderson's gun is actually a result of secondary electrons which are formed when a portion of the beam strikes the front focusing electrode near the exit plane. As a result of the decreased separation between the focusing electrode and anode in this region, the critical magnetic field<sup>(18)</sup> is about 1.5 times the design field for the gun, and hence secondaries from the focusing electrode could strike the anode. The only difficulty with this explanation is that on the basis of this simple argument, the same phenomena should be observed for the long gun for, as in Anderson's case, the critical magnetic field near the exit plane is larger than the design field.

---

<sup>(18)</sup>For a definition of this quantity, see section d.

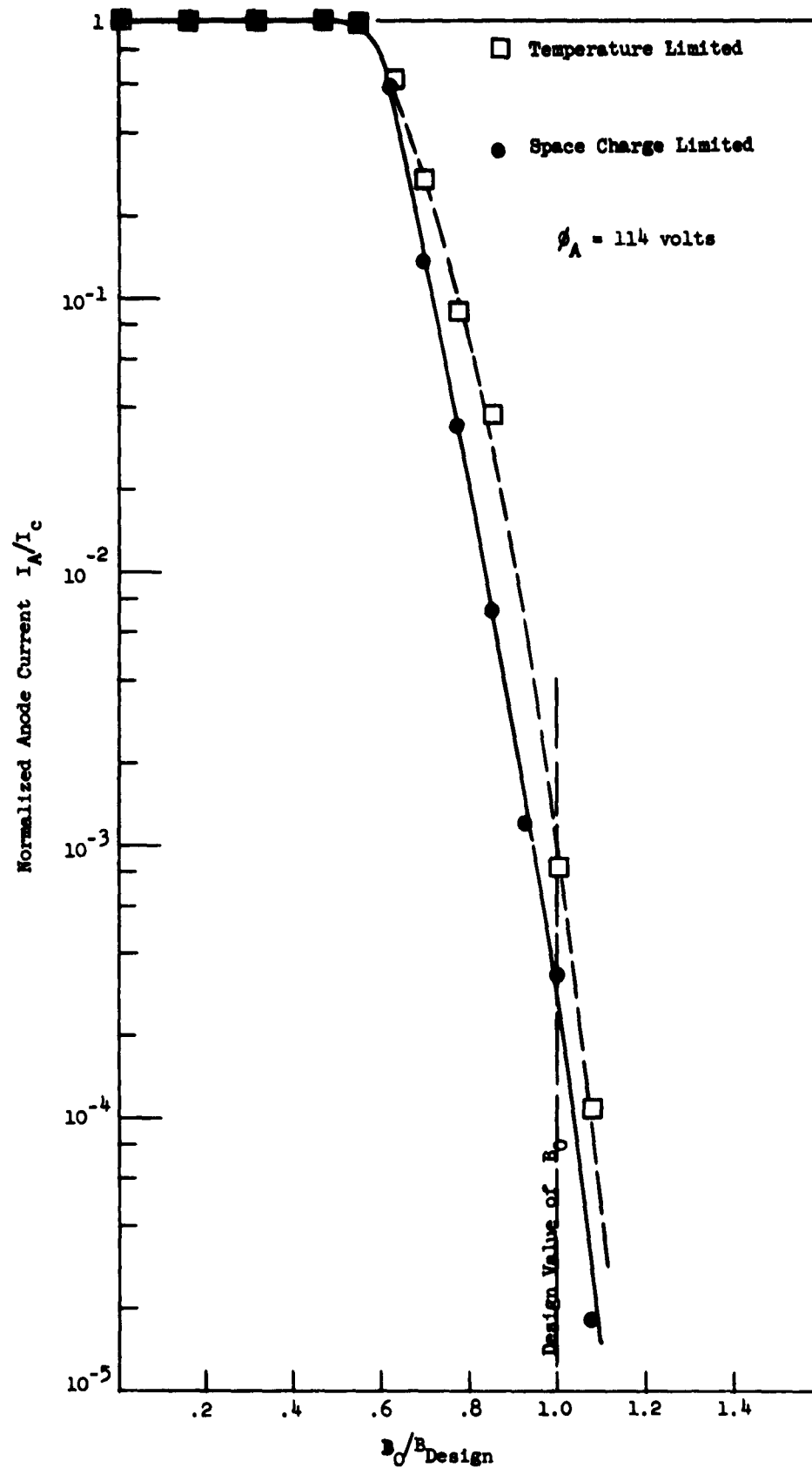


FIG. 5.25--Long gun cutoff characteristics.

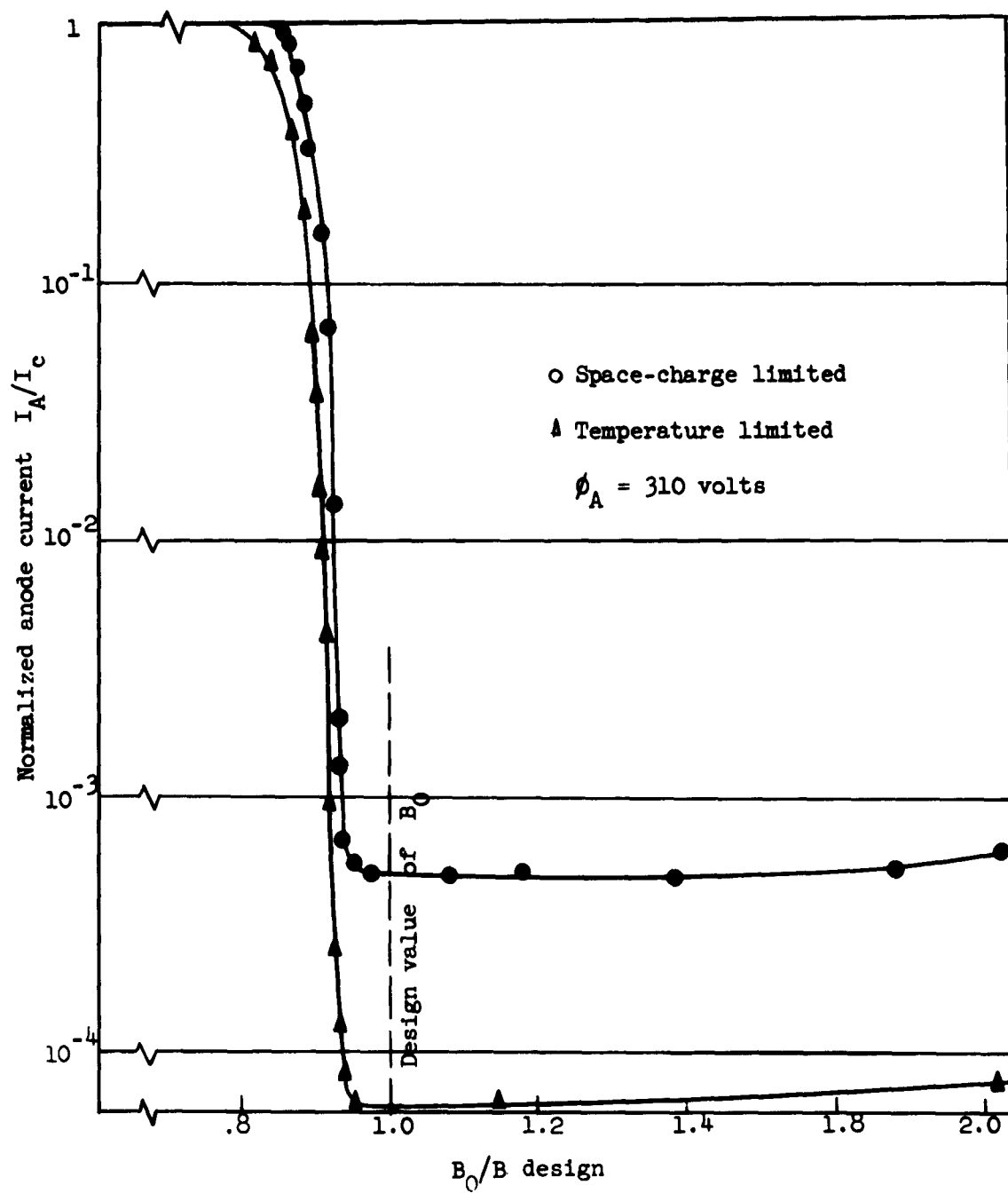


FIG. 5.26--Short gun cutoff data obtained by Anderson.

If the interpretation of Anderson's results is correct, it would seem that similar plateaus should exist for the long gun and perhaps are to be found at somewhat lower values of normalized anode current. The alternative possibilities that no electrons strike the focusing electrodes for values of  $B_0$  larger than the design value or that no secondaries are produced as a result, would seem doubtful in view of the excessive sole current which has been observed in the drift region. As a result of the mechanical structure of the gun, it was not possible to measure current to the focusing electrode directly. However, by measuring  $I_c$  and the currents to the other electrodes it could be seen that the magnitude of such current, if present, was small.

c. Cathode Bias Measurements. The object of this experiment, like that of similar measurements made with the short gun, was to determine the effects on the total beam current and on beam transmission of biasing the cathode at a potential above or below that of the focusing electrodes. The results of such measurements are closely related to the focusing properties of the gun and are of importance as a possible method of beam modulation. These results are therefore included here rather than with the remainder of the transmission measurements in section d.

For these measurements the geometry of the gun with respect to the drift region electrodes was the same as in the experiments described in section d-1. The cathode current as well as the current to all other electrodes was measured as the cathode was biased both positively and negatively with respect to the focusing electrodes. The results are shown in Fig. 5.27. We see that the beam is almost entirely cut off for a bias potential of + 100 volts, approximately 40 per cent of  $\phi_A$ . The ability to achieve such a cutoff is undoubtedly a function of the cathode length. When the cathode was made negative, although the cathode current continued to increase, a sharp drop was noted in the current injected from the gun into the drift region (the sum of the currents to the sole, circuit and collector). This was almost certainly a result of current being collected by the forward focusing electrode. At the same time, current was also collected by the gun anode, probably a result of secondary electrons from the focusing electrode. This behavior is shown for moderate values of negative bias potential.

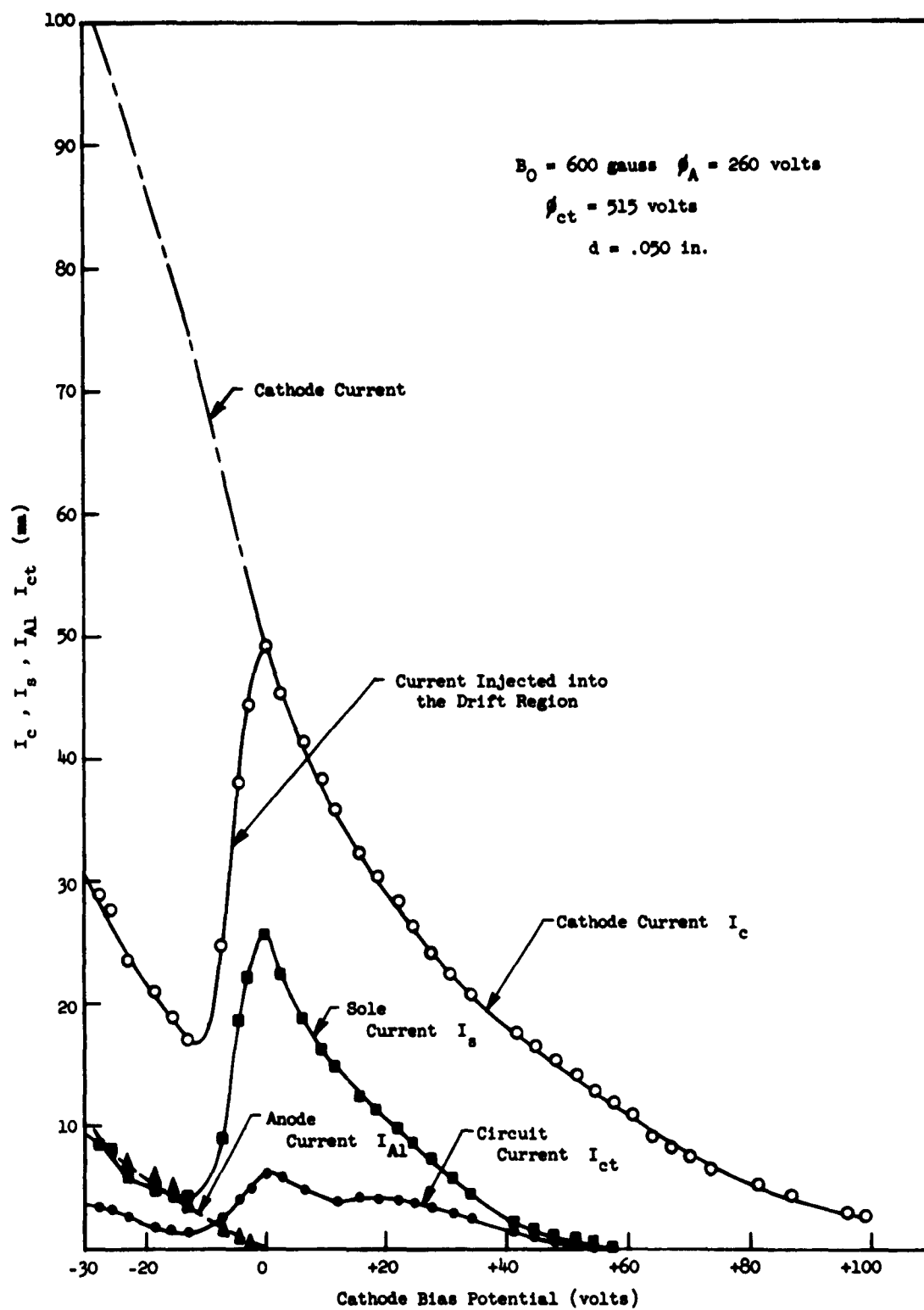


FIG. 5.27--Cathode current and transmission as a function of cathode bias voltage.

d. Transmission Measurements. In the following sections we shall discuss many of our results in terms of the scaling parameter  $(\phi_{ct} - \phi_s)/B_0^2$  which is proportional to the product of the cyclotron wavelength and the sole-circuit spacing. However, since much of the data in the literature, particularly the work of the French, is presented in terms of the parameter  $B_0/B_c$ , where  $B_c$ , the critical magnetic field, is given by  $B_c = 1/d \left[ (\phi_{ct} - \phi_s)/\eta \right]^2$ , we shall also indicate the magnitude of this quantity wherever appropriate. We note that  $B_c$  represents the value of magnetic field at which electrons, leaving the cathode plane of an infinite magnetron diode with zero velocity, will reach the anode with zero normal velocity, assuming that  $(\phi_{ct} - \phi_s)$  represents the potential difference between the cathode and anode. Furthermore, we note that for a constant sole-circuit spacing  $(B_0/B_c)^2$  is proportional to the reciprocal of the scaling parameter.

The geometry for the long gun transmission measurements is shown in Fig. 5.28. During the course of these experiments, the sole-circuit spacing  $d$ , and  $\Delta$ , the distance of the sole below the end of the focusing electrode, were varied. The particular values of these geometrical quantities will be given in the discussion of the individual experiments.

It should be noted that a direct comparison of data presented in terms of the scaling parameter may be made only for data which is obtained with the same value of  $d$ . In comparing data taken under different geometries, a more useful parameter is the cyclotron wavelength  $\lambda_c = -2\pi/\eta d \left[ (\phi_{ct} - \phi_s)/B_0^2 \right]$ . Thus, where appropriate, we shall use both the scaling parameter and the corresponding value of  $\lambda_c$  in evaluating our results.

(d-1). Gross Characteristics of the Sole and Circuit Current. In general, these experiments were considered as preliminary measurements made in order to gain some knowledge as to the general behavior of the system under a fairly wide range of operating parameters. The data which were obtained were found to be scalable and are compared with some similar measurements of Miller which were obtained using conventional short gun optics.

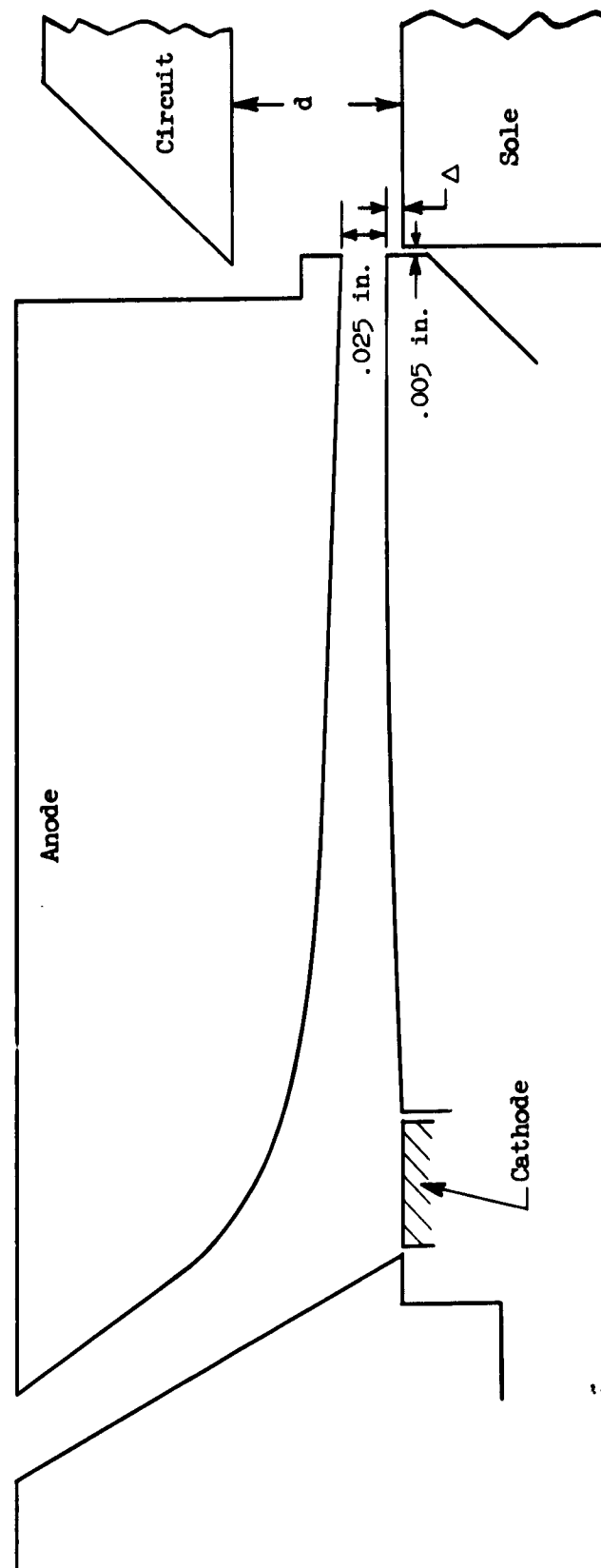


FIG. 5.28--Geometry for the long gun transmission measurements



For these measurements, the values of the geometrical constants  $d$  and  $\Delta$  were .050 in. and zero, respectively. With this geometry, in order to insure approximate field and potential continuity between the gun and drift region, the circuit voltage must be twice the gun voltage, and the sole nominally at the potential of the focusing electrodes.

The experimental procedure was then to measure the total cathode current and the currents to the circuit, sole, and collector

( $I_c$ ,  $I_{ct}$ ,  $I_s$ ,  $I_{co}$ ) for given voltages on the anode, circuit, and sole ( $\phi_A$ ,  $\phi_{ct}$ ,  $\phi_s$ ) and for various values of  $B_0$ . The collector was normally kept at the potential of the circuit. In addition, for this set of measurements,  $\phi_A$  was equal to  $1/2 \phi_{ct}$ .

Miller has reported a similar series of measurements made with a simpler optical system using a form of the French short gun, and has found that  $I_s$ , normalized to  $I_c$ , if plotted as a function of the scaling parameter  $\phi_{ct}/B_0^2$ , is essentially independent of the actual values of voltages and fields. We have plotted our data in a similar manner in Fig. 5.29 which also shows the corresponding values of  $\lambda_c$  in the drift region. The sole potential was zero for all of the data shown. We see that these data are scalable, although for a given value of the scaling parameter the largest value of normalized sole current seems to be associated with the smallest value of  $B_0$ . The other interesting aspect of these data is the very sharp reduction in sole current for values of the scaling parameter greater than about  $10^{-3} \text{ v/gauss}^2$ . However it was found that as  $I_s$  was so reduced,  $I_{ct}$ , the current collected by the circuit, was sharply increased so that for no values of the scaling parameter was the transmission greater than about 70 per cent. These values of circuit current, normalized to the cathode current, are also found to be scalable and are shown in Fig. 5.30.

Figure 5.31 shows values of sole current obtained for two scaled values of negative sole voltage,  $\phi_s/\phi_{ct} = -50$ ,  $-25$ . The data, obtained for zero voltage, are also included for purposes of comparison. Although, for a given value of the scaling parameter,  $I_s$  is seen to decrease with increasing negative sole voltage, it was noted that for values of the scaling parameter at which the circuit was collecting current, the magnitude of this current was essentially independent of the sole voltage.

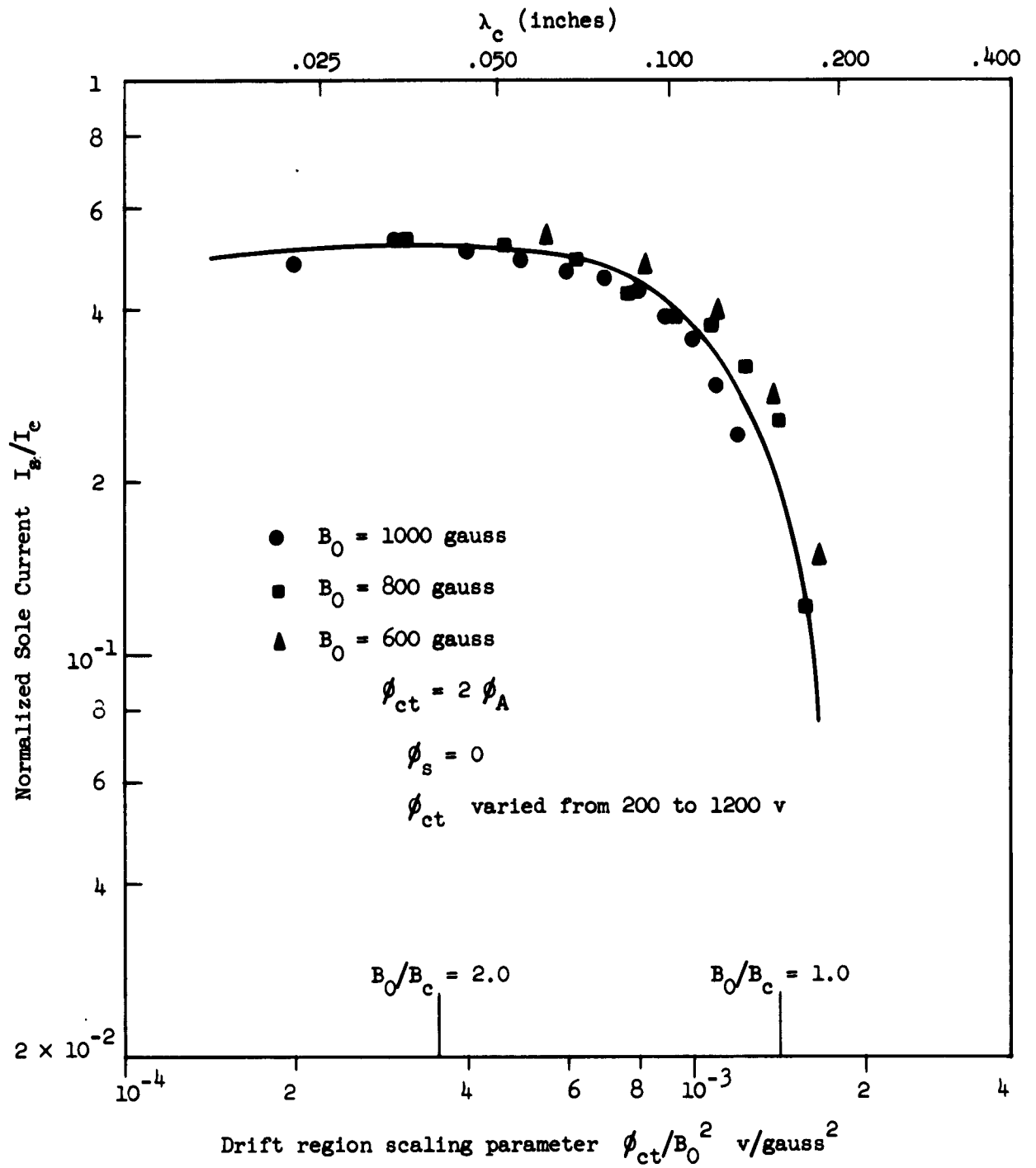


Fig. 5.29--Gross sole current characteristics.

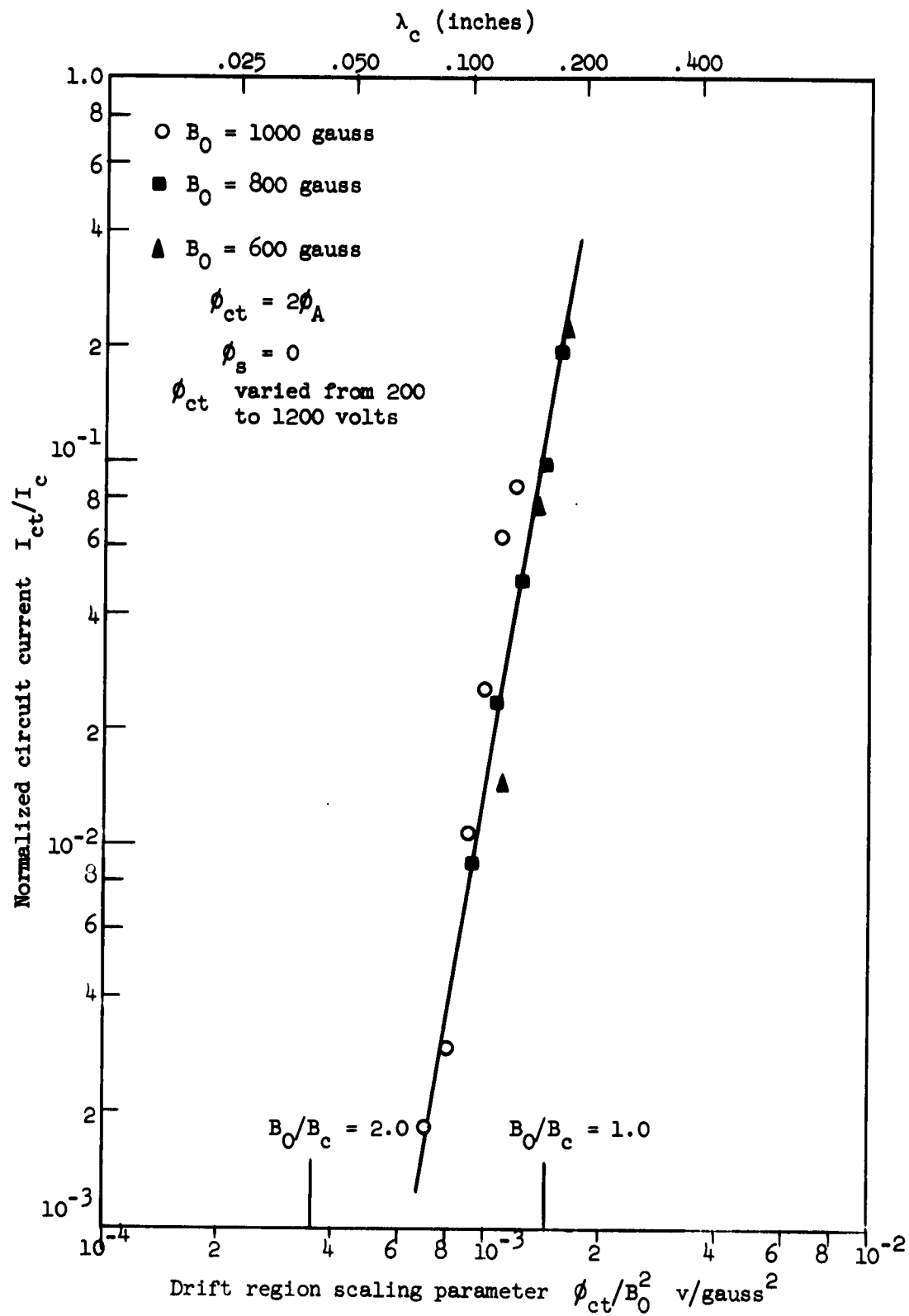


FIG. 5.30--Gross circuit current characteristics.

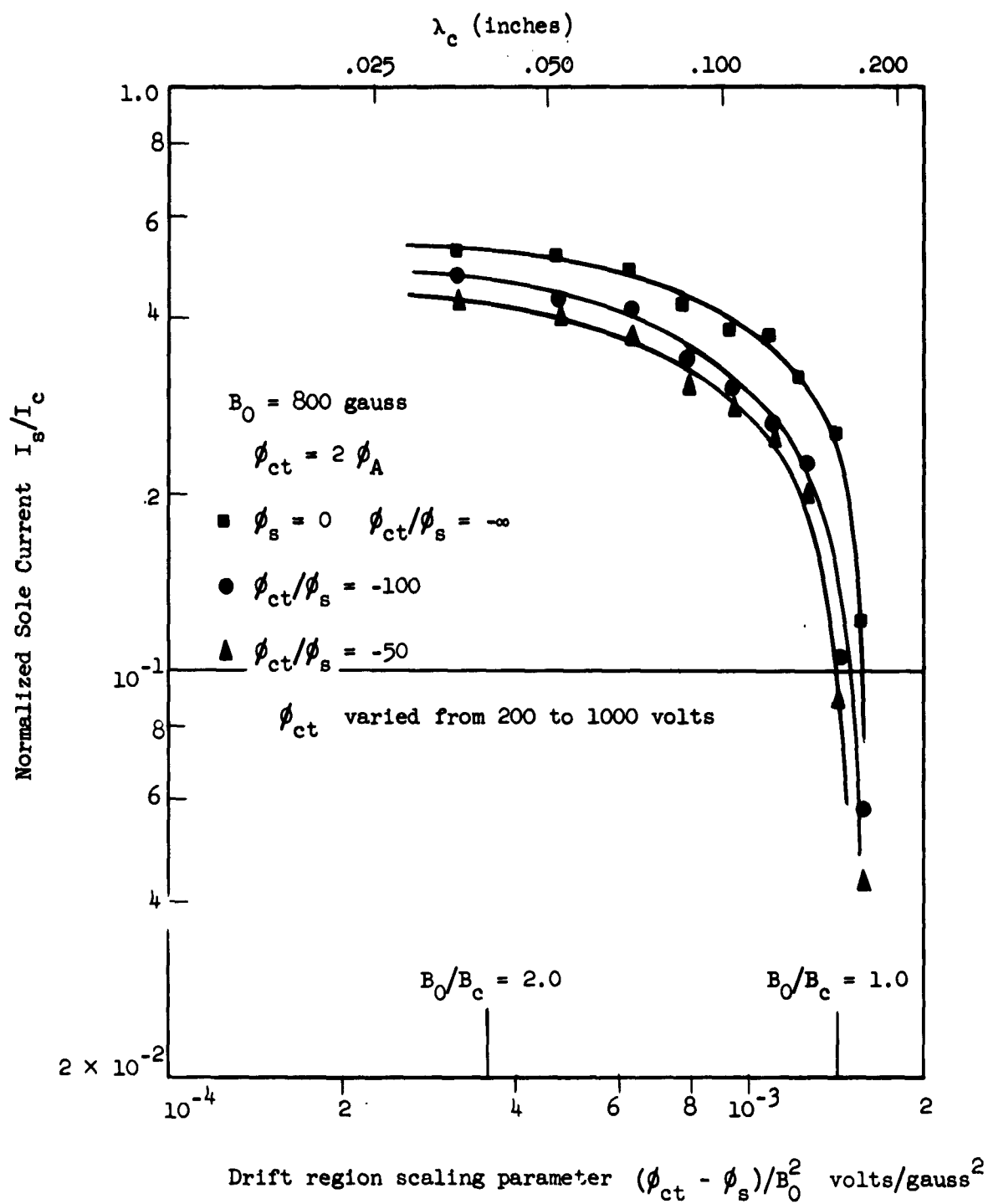


FIG. 5.31--Gross sole current characteristics for various sole potentials

It is instructive to compare our results, using a more sophisticated gun, with Miller's results. In Fig. 5.32 we show Miller's data, along with a sketch of the electrode configuration used in obtaining them. These data are in general agreement with ours except that in Miller's work the abrupt decrease in  $I_s$  appears at a slightly larger value of the cyclotron wavelength. However, under no circumstances does Miller report circuit current. It was speculated (and later confirmed by experiment) that the effect of increasing the sole-circuit spacing in our electrode system would be to eliminate the circuit current without appreciably changing the value of the cyclotron wavelength at which the sole current is cut off.

In regard to these scaling data, it should be noted that, in general, the gun was not operating at the design parameters; thus, in no sense should these data be regarded as representing optimum transmission conditions.

A remark should be made regarding the significance of these results. On the basis of the data shown in Figs. 5.29 and 5.30, it follows that the phenomena responsible for the collection of both sole and circuit currents is primarily a function of the geometry of the beam, as measured by the value of the scaling parameter which is proportional to  $\lambda_c$  in the drift region. In the gun region where the electric field is non-uniform, we have already pointed out that the shape of the gun trajectories is determined by the value of the gun scaling parameter  $\phi_A/B_0^2$ .<sup>(19)</sup> In addition,  $u$ , the gun transit angle, and hence the equivalent number of cyclotron wavelengths of the beam in the gun, is also determined by  $\phi_A/B_0^2$ . In the present series of measurements we have shown that the normalized sole current scales with the total number of cyclotron wavelengths of the beam (including the portion of the beam in the gun). In section d-iv we shall see that normalized sole current scales in much the same manner when only the value of  $\lambda_c$  in the drift region is varied with the gun parameters held fixed, and moreover, that the sole current may be greatly diminished by increasing the value of the drift region scaling parameter sufficiently.

---

<sup>(19)</sup> Note that  $\phi_0$ , the potential associated with the normal component of the thermal velocities at the cathode, does not scale with  $\phi_A/B_0^2$  (see section d-iv).

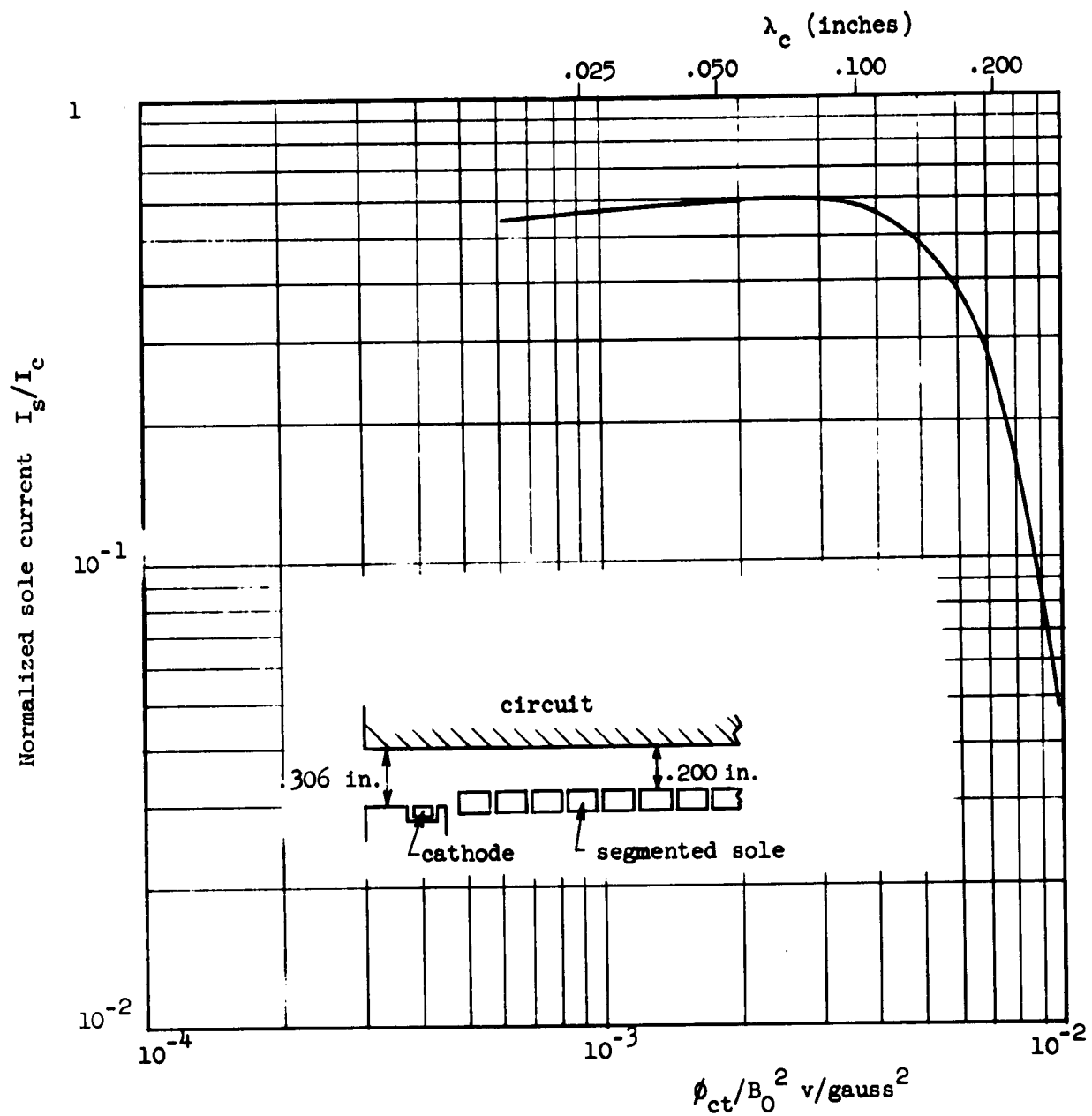


FIG. 5.32--Gross sole current characteristics of Miller:  
 $\phi_s = 0$  ;  $\phi_{ct}$  varied from 500 to 1700v;  $B_0$  varied from  
 250 to 1675 gauss.

(d-ii) The Total Sole Current as a Function of the Cathode Current for Space-Charge-Limited Conditions at the Cathode. The object of this set of experiments was to determine how the sole current varies with the magnitude of the total beam current. Values of sole current were measured as a function of  $I_c$ , which was varied by means of the gun anode potential  $\phi_A$ , under conditions of full space-charge limitation at the cathode. Data were taken for three values of magnetic field. The values of  $\phi_s/B_0^2$  and  $\phi_{ct}/B_0^2$  were always kept constant, so as to maintain a constant value of the scaling parameter in the drift region. The values of  $d$  and  $\Delta$  were .100 in. and .010 in., respectively.

Figure 5.33 shows  $I_s$  plotted as a function of  $I_c$  for the three values of  $B_0$ . From the slope of these curves we find that, for each value of  $B_0$ ,  $I_s$  varies almost exactly as  $I_c^3$  over most of the range. The other interesting aspect of these data is the tendency for  $I_s$  to saturate at large values of  $I_c$ . The points in this region correspond to values of  $\phi_A$  somewhat above the design value where current is beginning to be collected by the gun anode. For the data taken for  $B_0 = 400$  gauss,  $\phi_A$  was purposely increased to the point where relatively large currents were collected by the anode in order to illustrate this effect. For the two points labeled on the graph, increasing  $I_c$  from 40 to 46 ma resulted in an increase in  $I_A$  of 8 to 12 ma, while  $I_s$  increased only from 14 to 14.4 ma. Even if compensation is made for the net current removed from the beam as a result of anode interception, these points are still found to lie well below the extension of the original slope. A possible implication of this result is that the top edge of the beam, the portion intercepted by the anode, contains a greater fraction of the excess energy electrons which give rise to the sole current than does the beam as a whole. We shall say more concerning this observation later.

(d-iii). The Effect of Temperature-Limiting the Cathode on the Magnitude of the Sole Current. In the previous section we have seen that the magnitude of the sole is dependent on the total beam current, and in fact varies approximately as  $I_c$  to the third power when the cathode current is space-charge limited. In this section we shall describe experiments which were performed with the cathode temperature-limited. Under these conditions, a substantial reduction in the magnitude

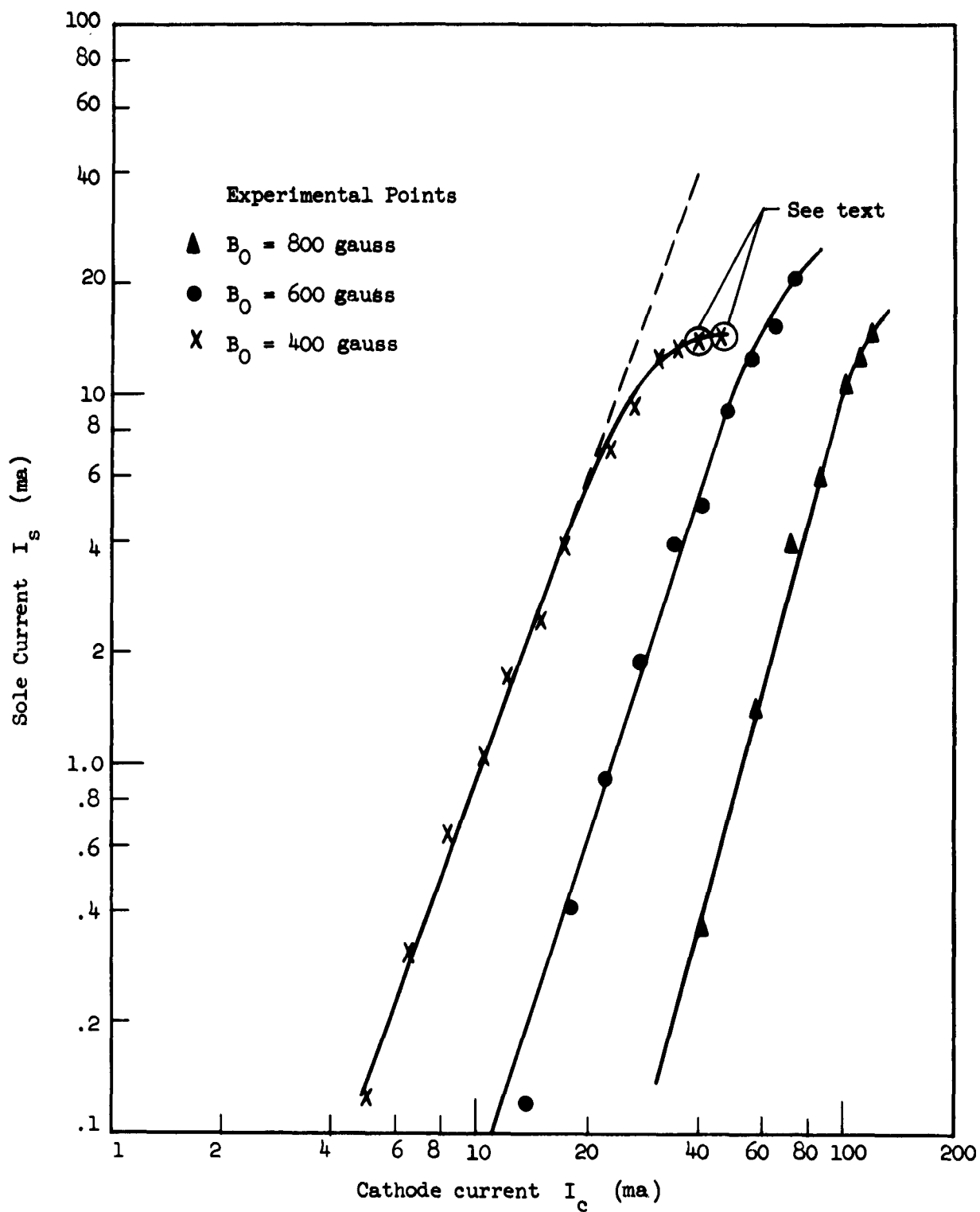


Fig. 5.33--Sole current as a function of cathode current, with the cathode space-charge limited.



of the normalized sole current, as compared to the corresponding values measured with the cathode space-charge-limited, was found.

Figure 5.34 shows the effect of temperature-limiting the cathode on total sole current. For these measurements the gun anode voltage was fixed at 256 volts, the design value for  $B_0 = 600$  gauss. The values of  $d$  and  $\Delta$  were .050 in. and zero, respectively. Values of cathode current and normalized sole current are plotted as functions of the heater current. We note a very abrupt drop-off in normalized sole current at the corresponding knee of the cathode current curve. This result indicates that the magnitude of the sole current is either strongly dependent on the conditions at the cathode, upon the total beam current, or both. We have already noted the dependency of  $I_s$  on the value of  $I_c$ . In order to determine the actual effect of conditions at the cathode it is necessary to compare sole current as a function of cathode current under both space-charge- and temperature-limited conditions at the cathode. The former measurements, where  $I_c$  is determined by the gun anode potential, have been discussed in the previous section. In Fig. 5.35 we show normalized sole current as a function of  $I_c$ , where the latter was varied both by temperature-limiting the cathode and by varying  $\phi_A$ . Potentials on the drift region electrodes, the value of  $B_0$ , and the geometry were the same for both of these sets of data, although not the same as for the data shown in the previous figure. We see that the normalized sole current falls off noticeably faster when  $I_c$  is reduced by temperature-limiting, rather than by reducing the anode potential.

This reduction in sole current resulting from a temperature-limited cathode has been noted previously by Guenard and Huber<sup>13</sup> and by Epsztein and Maillart.<sup>33</sup> A corresponding reduction in crossed-field beam noise has been observed as a result of the same condition by Little, Ruppel and Smith.<sup>14</sup> One point regarding these earlier measurements should be made. In each of the reported experiments, the electrode configuration was basically similar to that used by Miller<sup>8</sup> and illustrated in Fig. 5.32. In each case, the accelerating electrode above the cathode was either an integral part of, or electrically connected to the positive electrode in the drift region. In making their measurements, for a

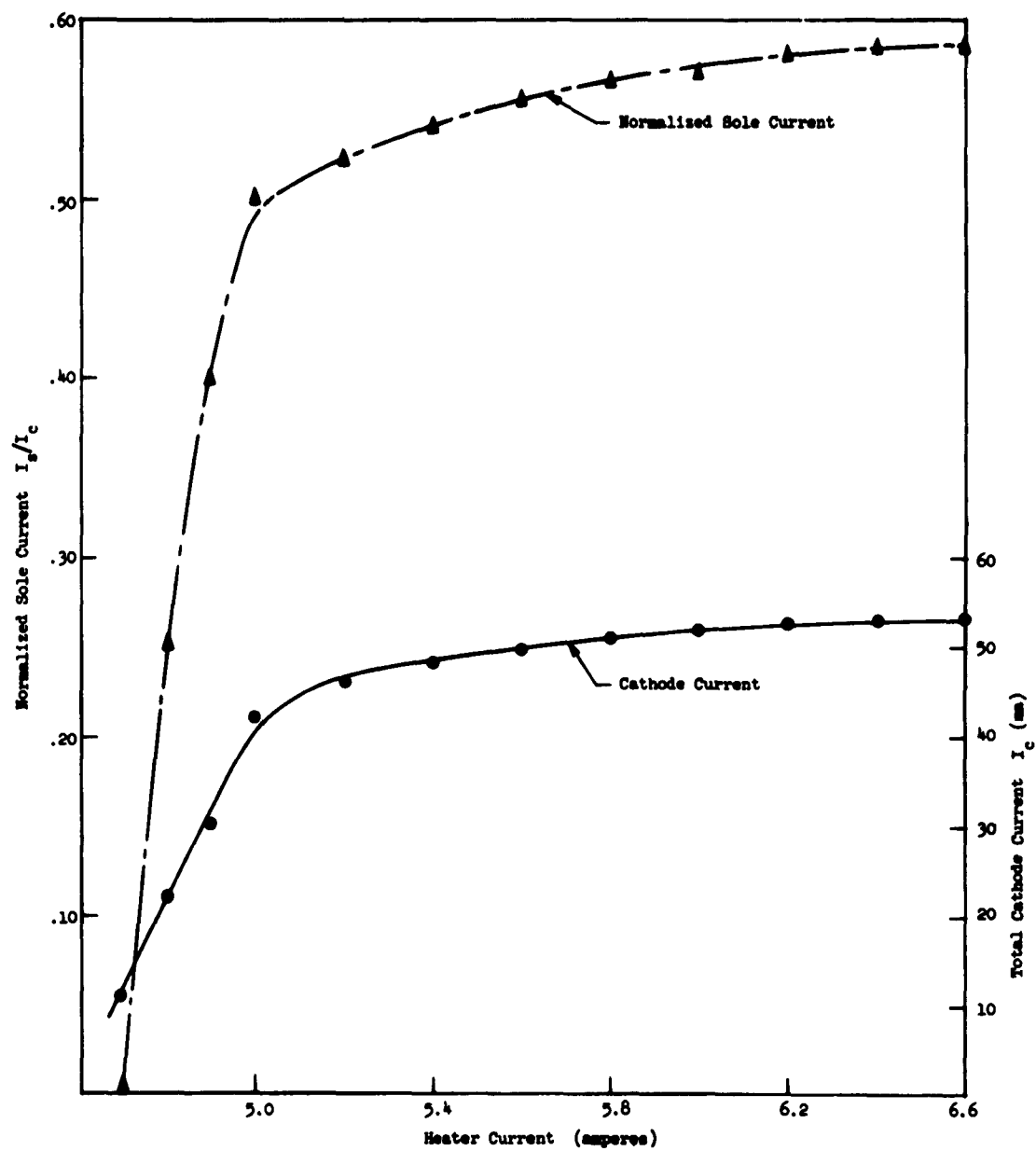


FIG. 5.34--Effect of temperature limiting on the gross sole current.

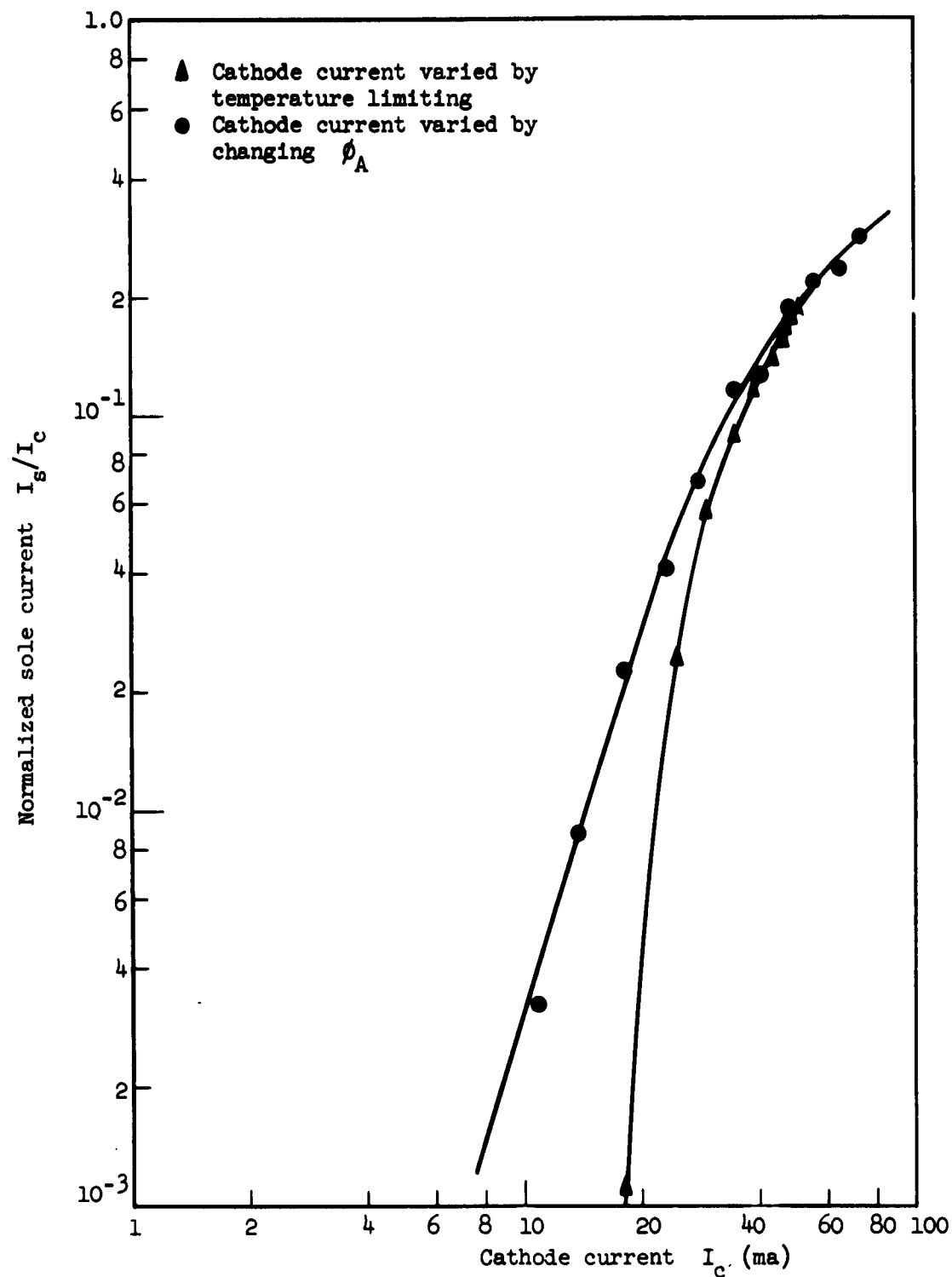


FIG. 5.35--Comparison of normalized sole current as a function of cathode current for temperature and space-charge limiting at the cathode.

given cathode temperature, these investigators increased the accelerator voltage until the cathode became temperature-limited. For further increases in accelerator potential, the cathode current remained essentially constant, and at the same time sole current or noise was found to decrease. However, at the same time, the electric field and hence the scaling parameter, as well as the beam cyclotron wavelength in the gun and the drift region, were also increased. We have seen that on the basis of the space-charge-limited experiments discussed in section d-i (and also those to be discussed in section d-iv) that an increase in the scaling parameter alone might be expected to bring about a reduction in sole current; thus it would seem that two mechanisms were actually responsible for the observations which were reported. It should be mentioned that evidence to this effect is found in the work of Epsztein and Maillart,<sup>33</sup> who noted an irregular decrease in sole current for increasing values of accelerator and circuit voltage corresponding to  $B_0/B_c \approx 2$  even with the cathode space-charge-limited. In the same tube a similar cutoff of sole current was seen with the cathode temperature-limited, but at a higher value of  $B_0/B_c$  (lower anode voltage) than for space-charge-limited emission.

(d-iv). Total Sole Current as a Function of the Scaling Parameter in the Drift Region. The results of the gun cutoff measurements described in section b, as well as visual observations of the beam, indicate that a reasonably well-defined beam was ejected at the exit plane of the long gun. Moreover, as the nature of the gun is such that the cathode is completely shielded from the drift region, the sole and circuit potentials and hence the electric field in this area may be varied without affecting the behavior of the gun. The effect of such variation is to cause field and potential discontinuities at the gun exit, which in turn cause the beam to undulate in the drift region. With the types of field discontinuities encountered during the transmission experiments,<sup>(20)</sup> such undulations were observed usually to have an amplitude of the order of the beam thickness. It is assumed that

---

<sup>(20)</sup> The electric field in the drift region was never less than three-fourths or greater than two and one-half times that supplied by the gun electrodes at the gun exit plane.

such small undulations have little effect on the inherent beam instabilities. This assumption is a seemingly valid one, since our results, obtained with a reasonably straight beam, are found to be in qualitative agreement with the earlier experiments of Aström,<sup>12</sup> which were performed with the trochotron, an M-type device in which the beam is in the form of a curtate cycloid (Fig. 3.1a).

In this section, we shall describe some experiments in which total sole current was measured as a function of the external potentials on the drift region electrodes. On the basis of the apparent dependency of the sole current and noise mechanisms on the mode of current limitation at the cathode, it is reasonably safe to assume that the source of these instabilities is to be found in the gun region, and is quite probably associated with the formation of the potential minimum near the cathode under space-charge-limited conditions. However, a significant result of the present measurements is that it was found possible to greatly diminish the magnitude of the observed sole current, merely by increasing the electric field in the drift region over the value required for field and potential continuity at the gun exit. As mentioned earlier, the amount of undulation introduced onto the beam by the resulting sudden acceleration at the gun exit plane was small. Moreover, on the basis of visual observations, the exit plane discontinuities did not appear to alter the beam thickness (see Fig. 5.49).

In the case of the scaling measurements which were discussed in section d-1, both the gun and circuit voltages were varied so as to insure approximate field and potential continuity between the gun and drift region. As a result, the value of  $\phi_A$  was, for the most part, not correct, and as a consequence the form of the gun trajectories was also perturbed from the design shape. In the present set of measurements the gun voltage was set at the design value for a given value of  $B_0$ . Current to the continuous sole was measured as a function of sole and current voltages. For these measurements, the values of  $d$  and  $\Delta$  were .100 in. and .010 in., respectively. For this geometry, conditions for potential and field continuity at the exit were:  $\phi_S = -.4 \phi_A$ , and  $\phi_{ct} = 3.6 \phi_A$ . The following data were taken: (1). With a constant negative value of  $\phi_S = -.4 \phi_A$ ,  $\phi_{ct}$  was varied, resulting in a

discontinuity both in field and potential at the gun exit plane. (2). The values of  $\phi_s$  and  $\phi_{ct}$  were varied, the ratio  $\phi_{ct}/\phi_s$  being maintained at a value of  $\sim 9$ , thus maintaining continuity in potential, but not electric field at the exit.

The values of normalized sole current as a function of the drift region scaling parameter  $(\phi_{ct} - \phi_s)/B_0^2$  are shown, for both types of measurements and for four values of  $B_0$ , in Figs. 5.36 and 5.37. No significant circuit current was measured, except for very high values of  $\phi_{ct}$ , where its maximum value was less than 1 per cent of  $I_c$ .

Similar data are shown in Figs. 5.38 and 5.39 for temperature-limited conditions at the cathode with  $B_0 = 600$  gauss. Normalized sole current is again plotted as a function of the scaling parameter for two values of  $I_c$  obtained by reducing the heater power. The corresponding space-charge limited curves, as given in the two previous figures, are also shown for comparison.

The most significant aspect of these measurements is the very great reduction in sole current which was achieved by merely increasing the value of the circuit potential, and hence the scaling parameter and consequently decreasing the number of cyclotron wavelengths of the beam in the drift region. We see in addition in Figs. 5.36 and 5.37 that although the experimental points are closely grouped for values of the scaling parameter less than  $3 \times 10^{-3}$  v/gauss<sup>2</sup>, for larger values of this parameter the sole current falls off more rapidly with increasing values of  $B_0$ . In this respect we note that as a result of scaling the gun voltages, the trajectories in the gun have the same shape for each value of  $B_0$ . However,  $\phi_0$ , the initial potential at the cathode, does not scale in the same manner; thus for the data shown in these same figures,  $\phi_0$  varies from a maximum of .144 volts for  $B_0 = 900$  gauss to a minimum of .0285 volts at  $B_0 = 400$  gauss. However, there does not seem to be any particular evidence for correlating this variation with the results of the scaling measurements.

In comparing the space-charge and temperature-limited data we see that normalized sole current falls off more rapidly with increasing values of the scaling parameter as the cathode current is decreased and the gun becomes more completely temperature-limited. In order to see the actual effect of temperature-limiting apart from that due to the

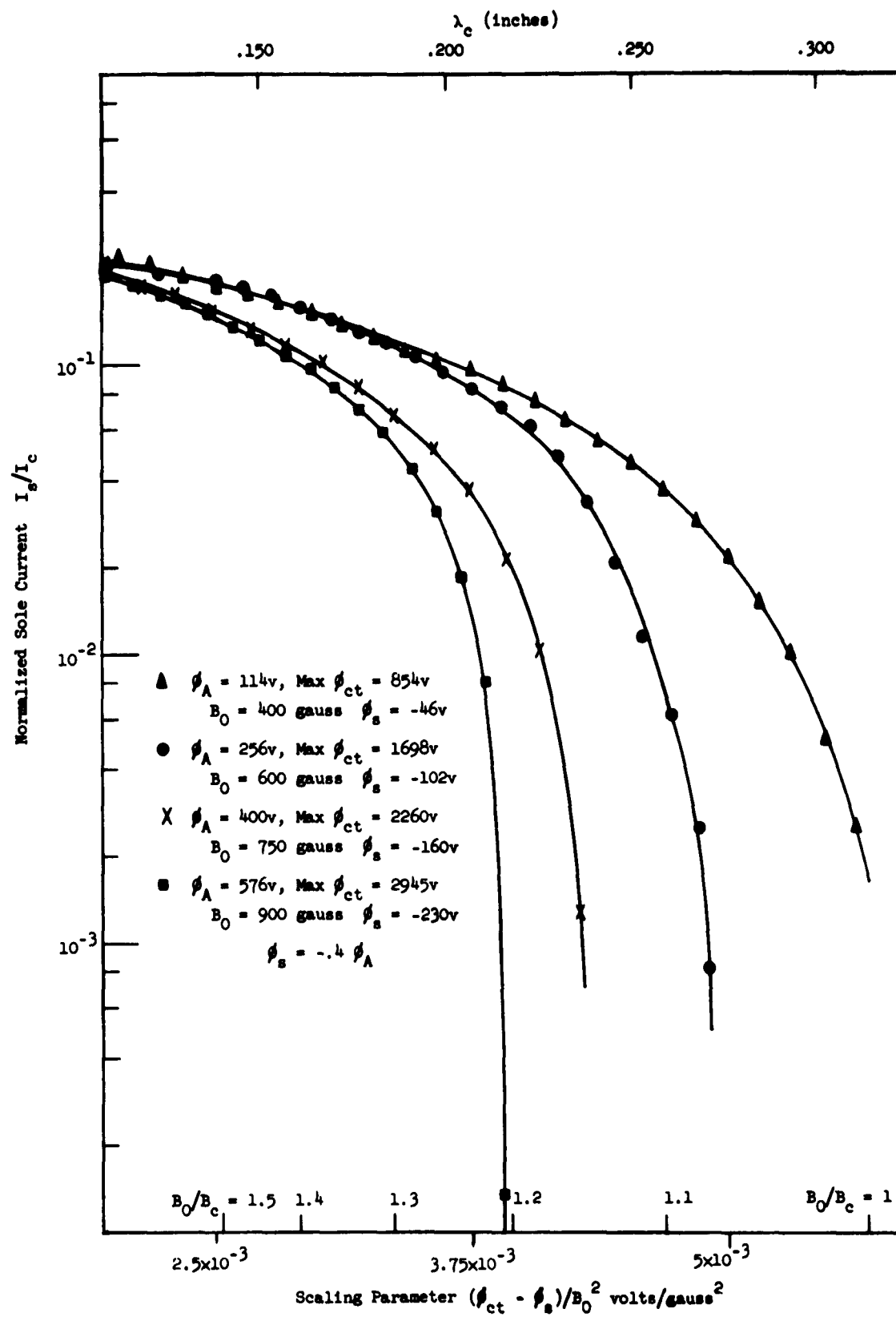


FIG. 5.36--Normalized sole current as a function of the drift region scaling parameter for constant  $\phi$ .

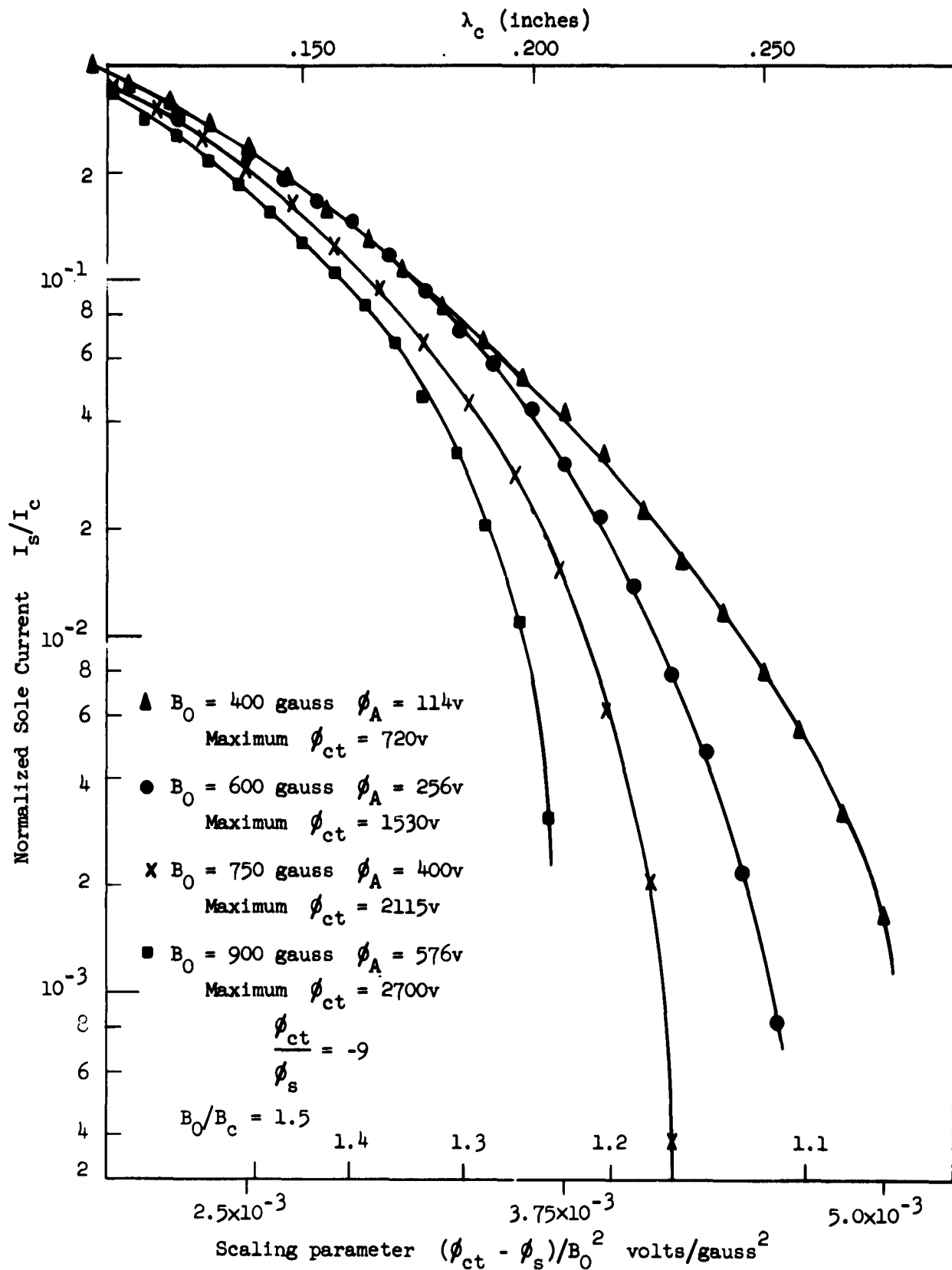


Fig. 5.37--Normalized sole current as a function of the drift region scaling parameter for scaled  $\phi_s$ .



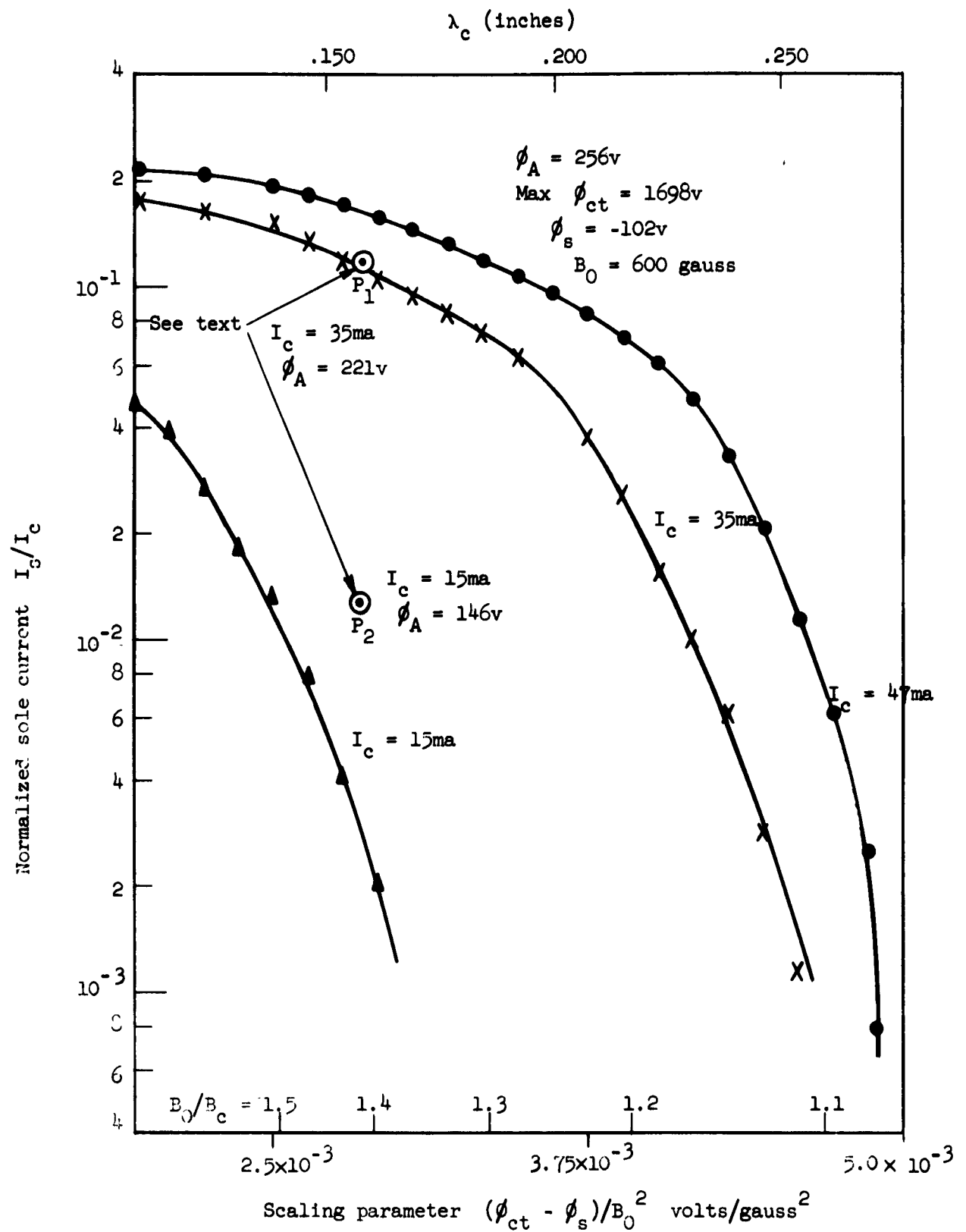


FIG. 5.30--Normalized sole current as a function of the drift region scaling parameter for  $\phi_s = \text{constant}$ , showing the effect of temperature limiting.

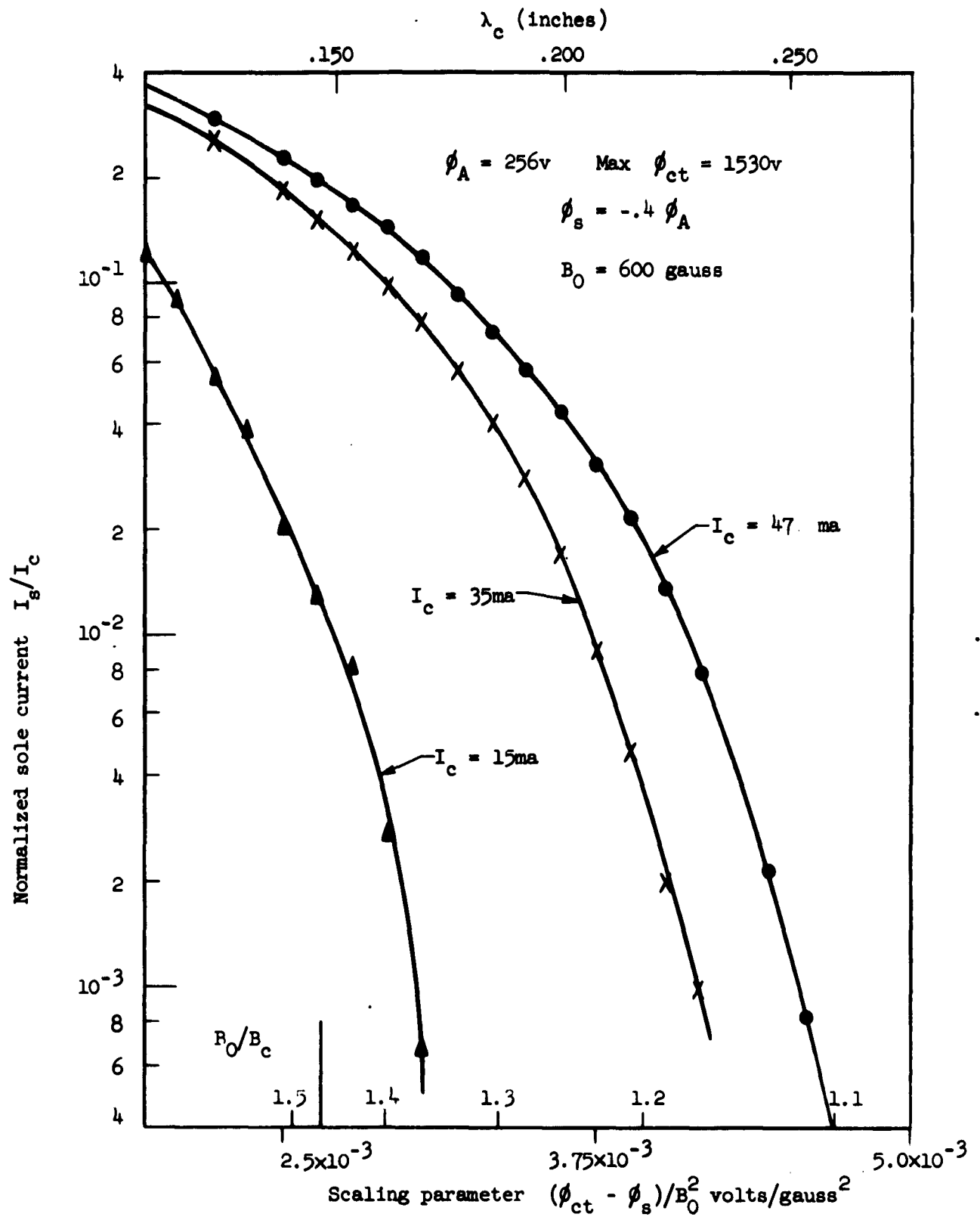


FIG. 5.39--Normalized sole current as a function of the drift region scaling parameter for scaled  $\phi_s$ , showing the effect of temperature limiting.

decrease in  $I_c$ , we show in Fig. 5.38 points  $P_1$  and  $P_2$  which indicate the corresponding sole currents for the same values of  $I_c$  obtained with lower gun voltages with the cathode space-charge limited. Conditions in the drift region for these points are the same as for the temperature-limited data. We see that for  $I_c = 37$  ma, the decrease in normalized sole current is almost entirely due to the decrease in  $I_c$ , while for  $I_c = 15$  ma, a significant reduction in  $I_s/I_c$  is seen as a result of temperature-limiting at the cathode.

(d-v). The Distribution of the Sole Current Along the Length of the Sole. A series of measurements were made using a modified form of the segmented sole structure described earlier. These experiments, for the most part, consisted in measuring the fraction of the total beam current intercepted by each of the sole segments as a function of conditions in the drift region and the mode of current limitation at the cathode. The purpose of such measurements was to determine the location of the parts of the beam characterized by the greatest instabilities (largest sole currents) as a function of these conditions. Some similar measurements have been reported earlier by Åström<sup>12</sup> and Miller,<sup>8</sup> and after presenting our results, we will compare them with this earlier work.

As was mentioned earlier in discussing the details of the beam tester, an alternate sole assembly was constructed so as to be able to measure the distribution of sole current along the sole as a function of the distance from the exit plane of the gun. Because of the very low sole currents measured with the short gun, this structure was not used in the earlier experiments. The assembly was modified for use with the long gun as shown in Fig. 5.2. This modification was made for two reasons: (1) the beam tester had been altered so that it was no longer possible to bring in the twenty-eight leads required if the twenty segments of the sole were to be connected independently, and (2) the .250 in. length of the segments, if each were separated from the adjacent ones, would result in a structure with a periodicity equal to  $\lambda_c$  for the beam under certain experimental conditions. It was felt that this condition should be avoided if possible. The modified structure consisted of seven insulated segments, each composed of approximately three and one-fourth of the short segments, in close physical contact and electrically

connected. The length of one of the modified segments was then approximately .850 in., a value much larger than  $\lambda_c$  under all experimental conditions.

However, anomalous effects were still observed in conjunction with the segmented structure. In comparing measurements of sole current as a function of the drift region scaling parameter (as in Fig. 5.36) for the two structures, under otherwise identical geometries, it was noted that: (1) although the general dependency on the scaling parameter was the same, the sole current was found to decrease much more irregularly with increasing values of the scaling parameter for the segmented sole than for the smooth structure, (2) for equal values of the scaling parameter, somewhat larger values of  $I_s$  were generally measured with the segmented sole, and (3) under certain conditions in the drift region, and only for the segmented sole, the amplitude of the cyclotron undulations on the beam was visually observed to grow or diminish with distance along the beam in the drift region.

This latter phenomenon was particularly apparent in the range of scaling parameters corresponding to  $\lambda_c \simeq .250$  in. For  $\lambda_c$  slightly smaller than this value the undulation amplitude was seen to grow by a factor of 2 to 3 in a distance of several cyclotron wavelengths, while with  $\lambda_c$  slightly larger than .250 in., a beam undulating with an amplitude 2 to 3 times its thickness was rendered almost completely straight in about the same distance. For photographs of these effects the reader is referred to Appendix D. In Appendix D, this behavior is shown to arise from the lens action of very small discontinuities in the drift region electric field, which resulted from the nature of the modified sole segments. Such effects might be expected in any geometry characterized by such periodically perturbed fields, thus for any distribution measurements involving a segmented sole, provided that: (1) the beam is reasonably well focused and rectilinear, and (2) the perturbations occur over a distance small compared to the beam cyclotron wavelength  $\lambda_c$  and have a spatial periodicity approximately equal to  $\lambda_c$ . It is doubtful that condition (1) was sufficiently well satisfied for these effects to be seen in the earlier experiments of Åström and Miller.

Such lens effects, which may be described as dc pumping of a dc cyclotron wave, could in principle be very useful, either for "straightening"

thin undulating beams, or increasing the amplitude of undulation of such beams for applications such as the rippling beam amplifier. Consequently, we have investigated them in detail both experimentally and theoretically in terms of a paraxial analysis. The results of these investigations are summarized in Appendix D.

On the basis of the foregoing observations, the absolute accuracy of the sole current measurements made with the segmented structure is somewhat open to question. However, we have found no reason to suppose that the general behavior of the sole current distribution, as a function of the drift region parameters, or conditions at the cathode, was grossly affected by the detailed structure of the sole (see the remark made in conjunction with the visual observations of the beam below). For a given value of the scaling parameter, the mechanism which gives rise to the excess energy electrons which are intercepted as sole current appears to be largely independent of the dc shape of the beam, i.e., whether it be cycloidal or rectilinear. Consequently, the observed lens effects of the segmented sole are believed not to have greatly altered the results which we shall present.

Figure 5.40 shows the normalized sole current distribution, that is, the total fraction of the cathode current,  $I_{s1}/I_c$ , collected by each of the sole segments for a number of values of sole voltage. The sole segments are numbered in order of increasing distance from the cathode. For these data, the gun was operated at the design conditions for  $B_0 = 800$  gauss and the sole-circuit potential difference was kept constant as the sole potential was varied. The values of  $d$  and  $\Delta$  were .050 in. and zero, respectively.

Figure 5.41 shows the sole current distribution as a function of the scaling parameter in the drift region. In this case the gun parameters were fixed at the design values for  $B_0 = 600$  gauss, the sole potential kept constant at zero and the circuit voltage varied. For these measurements  $d$  was increased to .100 in., while  $\Delta$  was zero.

Figure 5.42 shows the sole current distribution as the transition is made between space-charge and temperature-limited conditions at the cathode. The geometry was the same as for the data shown in Fig. 5.40. The value of  $\phi_A$  in the gun was the design value for  $B_0 = 600$  gauss

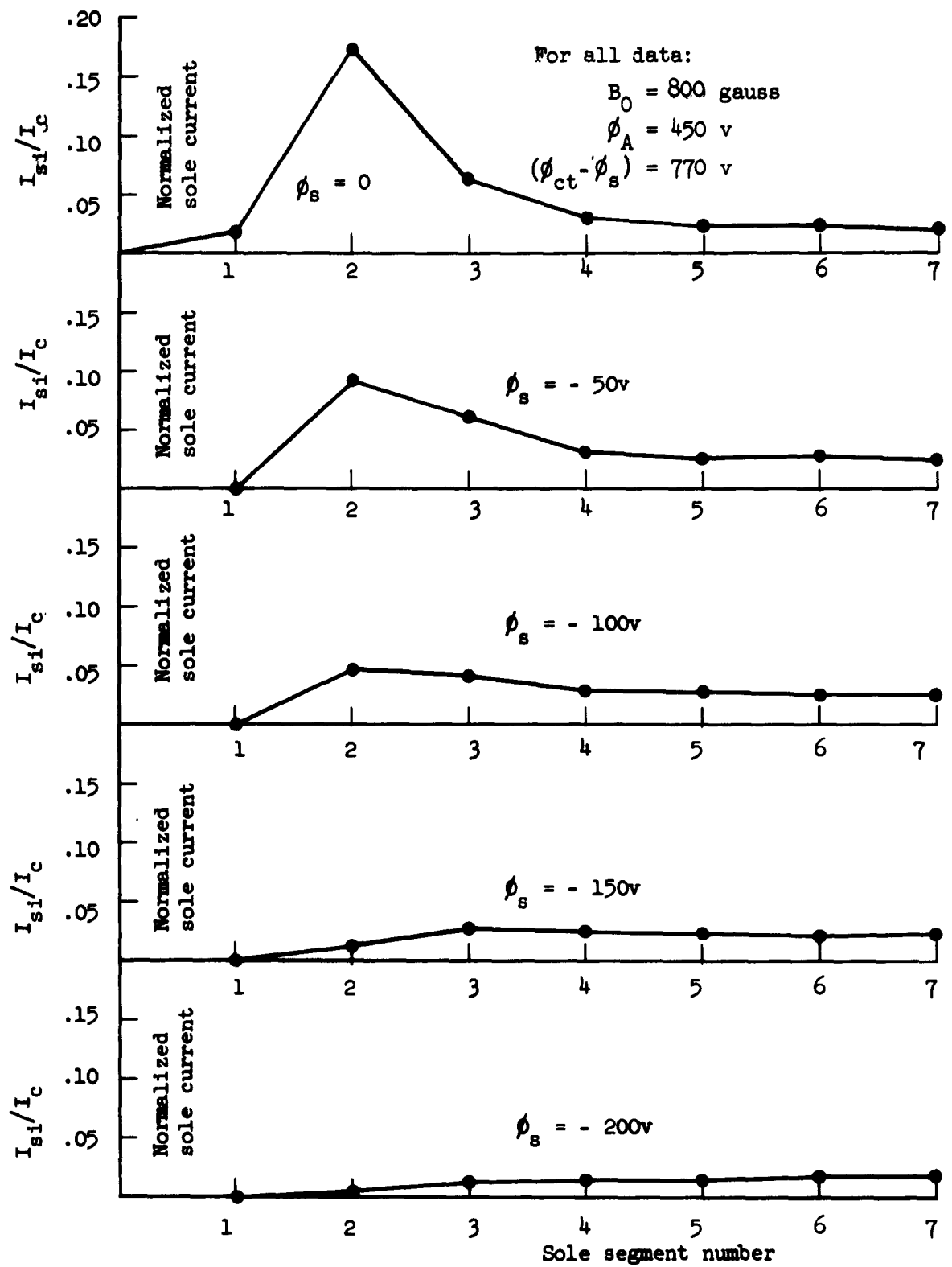


FIG. 5.40--Normalized sole current distribution for various sole potentials.

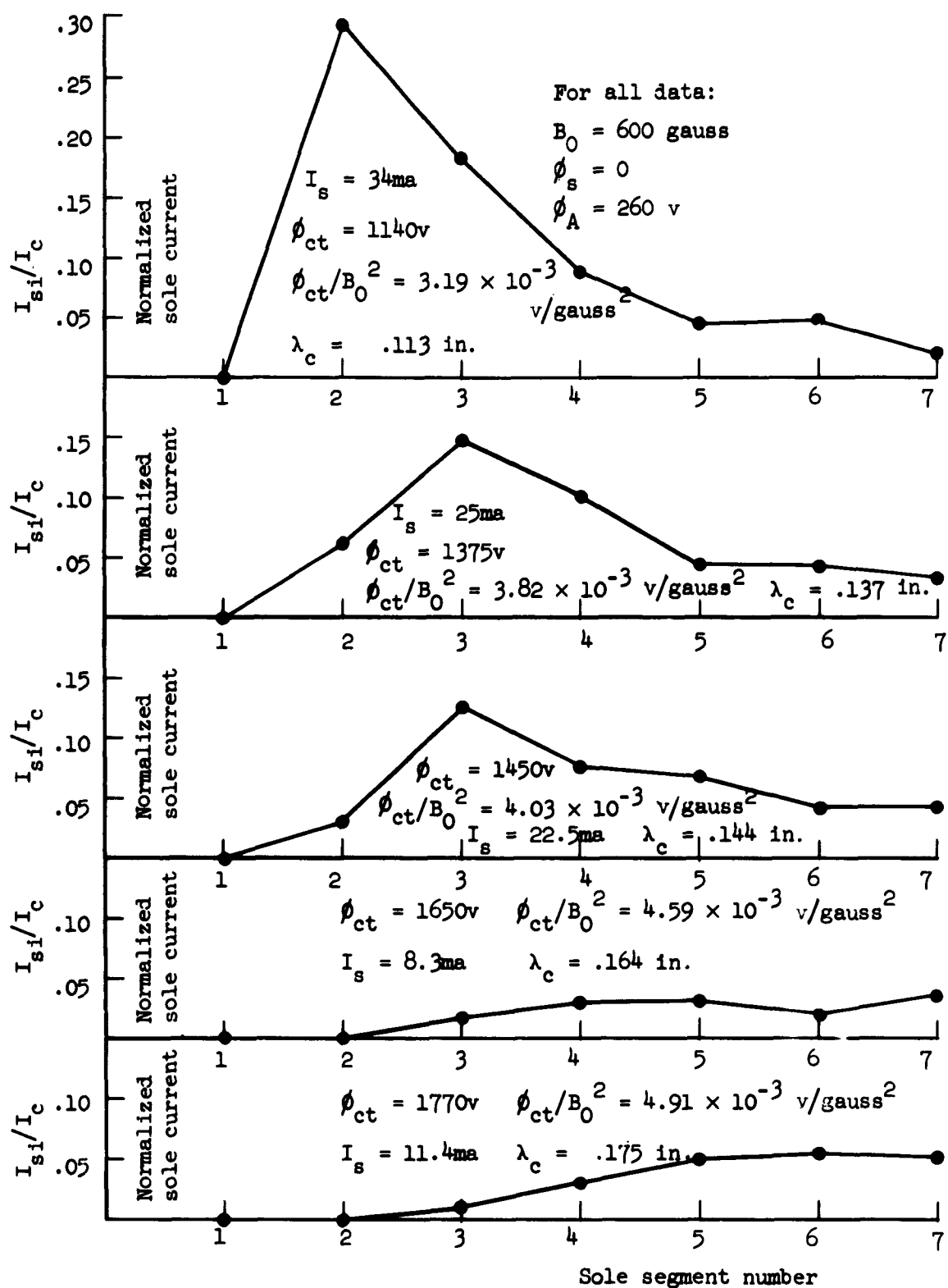


FIG. 5.41--Sole current distribution for various values of the drift region scaling parameter.

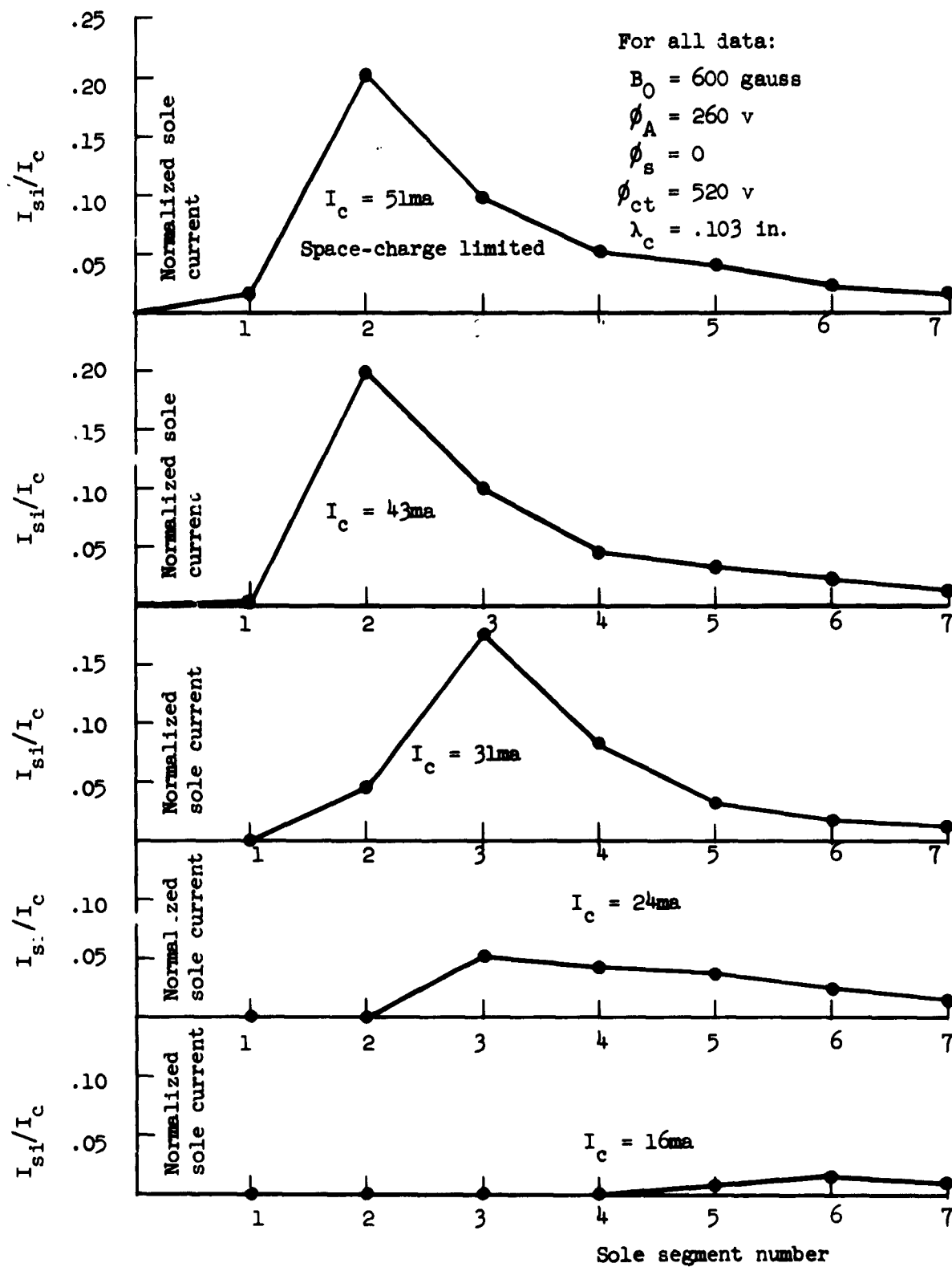


FIG. 5.42--Normalized sole current distribution for various degrees of temperature-limiting.



and  $\phi_{ct}$  was kept constant at  $2\phi_A$ . The distribution of sole current is then shown for decreasing heater power and cathode current.

These data have a number of implications. The results of Fig. 5.41 definitely imply that the mechanism responsible for the excessive sole current exhibits spatial growth along the beam; moreover, the rate of this growth is strongly dependent upon the value of the scaling parameter in the drift region. For low values of the scaling parameter we see definite evidence of saturation in the peaked value of sole current collected by the second and third segments. As the scaling parameter is increased, the growth rate appears to decrease and the position of the segment intercepting the maximum sole current is seen to shift in the direction away from the gun at the same time the total sole current decreases. This same evidence of spatial growth and saturation is seen in the data shown in Fig. 5.39. A rather interesting aspect of these data is that the currents intercepted by all of the segments after the third are for the most part independent of the sole voltage, and are possibly a result of secondary electrons which are emitted from the first few sole segments. The data in Fig. 5.42 show that decreasing the total cathode current by temperature-limiting the cathode has the same general effect on the sole current distribution as increasing the value of the scaling parameter in the drift region. Again, however, we must take care to distinguish between the actual effect on the magnitude of the sole current of either space-charge or temperature-limiting and a similar effect due to a change in beam current. The behavior of the data shown in Fig. 5.42 in all probability is a result of both effects.

We note that the saturation phenomena implied by these current distribution measurements are in agreement with visual observations of the beam. At pressures where the beam was visible, and under conditions where the maximum amount of sole current was measured at the third segment, the beam was observed to rapidly increase in thickness upon leaving the gun. This increase was seen to continue for a distance equal approximately to the location of the third sole segment, at which point the beam thickness was 2 to 3 times the value at that gun exit. Over the remainder of the drift region the beam thickness appeared to remain essentially constant. As the scaling parameter was increased, the

position of maximum beam thickness was seen to shift away from the gun, a result which is in agreement with the distribution measurements. These observations were made for both the continuous and segmented sole structures and for both undulating and nearly rectilinear beams.

It is useful to compare our results with the earlier work previously cited. Figure 5.43 shows a distribution of sole current given by Åström. Here sole current intercepted by a particular element of a segmented sole structure is shown as a function of the distance from the cathode with total cathode current, which was varied by changing the temperature of the cathode. In this figure the electrode configuration of the trochotron is also shown. For these measurements the side plates, used to provide lateral beam confinement parallel to the magnetic field, were electrically connected to the sole; hence the measured sole current includes both sole and sideplate current. In comparing Åström's results with the similar measurement made with the long gun shown in Fig. 5.42, we see that the results of the trochotron measurements are very similar to ours on two counts: (1) the increase to a maximum, then subsequent decrease, of sole current with increasing distance from the gun, and (2) the shift away from the cathode of the part intercepting the maximum sole current, as the cathode current is decreased. In comparing these results, it should be noted that the trochotron cathodes as a rule were sufficiently short so that the entire beam executed a looped trochoidal trajectory. The beam from the long gun, however, was nearly rectilinear in the drift region, and nonundulating in the gun region.

Miller has reported a series of distribution measurements, made with the electrode configuration shown in Fig. 5.32. These measurements were made for numerous values of the scaling parameter. In all his measurements the cathode was space-charge limited with essentially a constant value of cathode current. The essential feature of these measurements is that under almost all circumstances maximum sole current was intercepted by the first few sole segments, and smaller currents were noted for all of the remaining segments. It should be noted that while the electrode system used in these measurements employed a conventional French short gun, much of the data was taken for smaller values of the scaling parameter than the design figure for the gun. Thus,

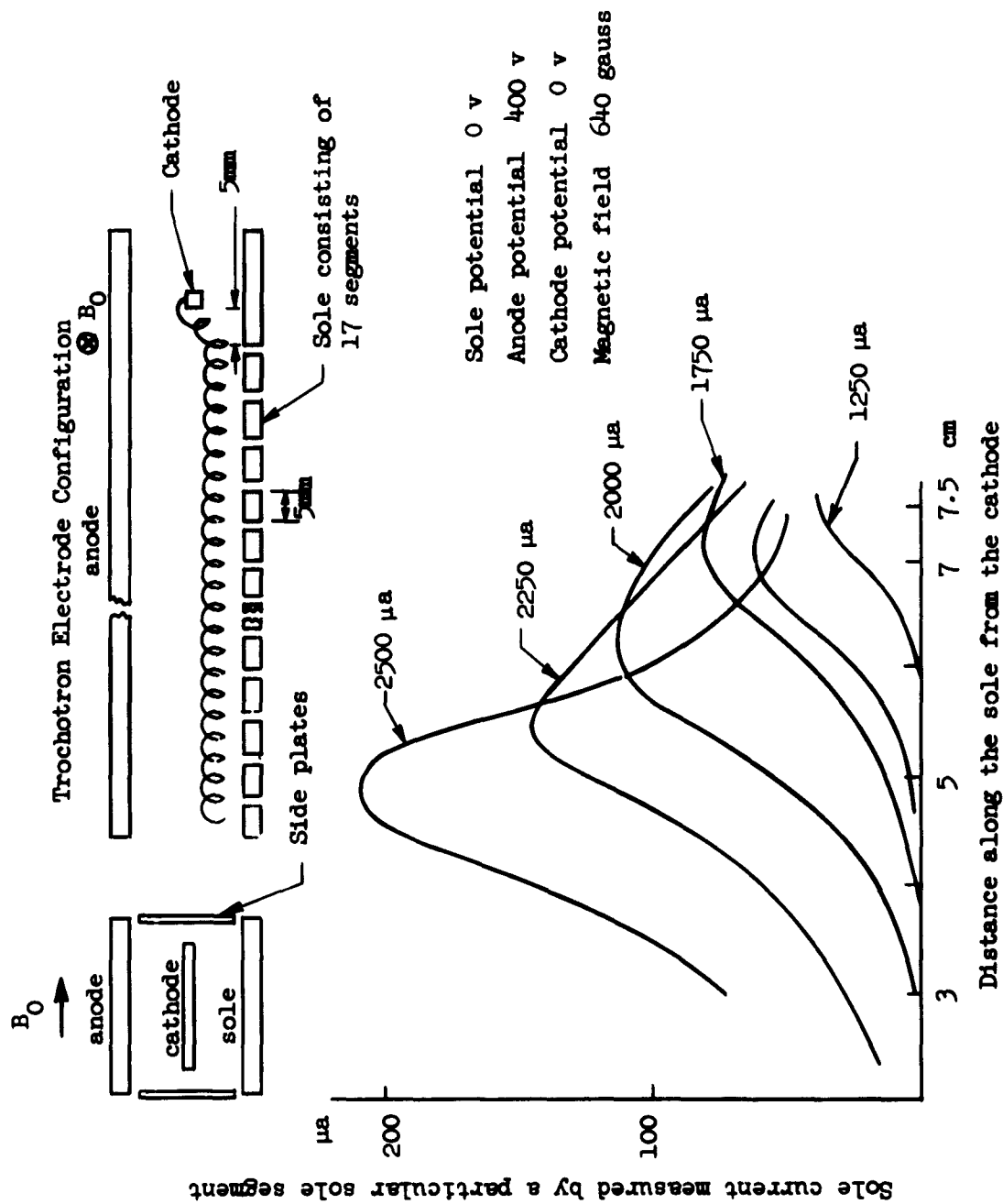


FIG. 5.43--Trochotron sole current distribution obtained by Åström.

the space-charge free trajectories in the gun were not half-cycloidal, but consisted of many very tight cycloidal loops which approximately followed the equipotential lines from the cathode into the drift region. Miller then correlated the high sole current measured at low values of the scaling parameter with possible "electron trapping" in the potential well between the cathode and the sole-circuit space (Fig. 5.32). This observation is in agreement with the measured sole current distribution, since if the energy exchange mechanism responsible for the excessively energetic sole electrons were to occur in this region, it is to be expected that the maximum sole current would be collected in the first portion of the drift region. But in view of the fact that large sole currents have been observed in geometries (including the present long gun) different from Miller's and where no such potential wells exist, it would seem that such a mechanism could at best be only partially responsible for the observed sole current phenomenon, although it may well have accounted for the differences between our results and those of Åström, as compared to Miller's results.

(d-vi). Temperature of the Electrons Collected by the Sole. During the course of these experiments, numerous measurements of sole current as a function of negative sole voltage were made under various conditions in the drift region, and for different geometries. Such data exhibited, in many cases, an approximately Maxwellian velocity distribution, although frequent departures from this dependency were also noted. When the velocity distribution was approximately Maxwellian, equivalent electron temperatures of 10-100 volts ( $\approx 10^{5.9} \text{ K}$ ) were noted. This value is in agreement with the results of previous workers.<sup>8,13</sup> The particular objective of these present measurements was to look for any possible dependency of the temperature of the sole electrons on the conditions which in the previous experiments have been found to influence the magnitude of the sole current.

In Figs. 5.44 and 5.45, results of temperature measurements made with the modified segmented sole are shown. The data, plotted on a semilogarithmic scale, show current intercepted by certain sole segments as a function of the potential applied to these segments. Measurements were made for each segment separately, all other segments being held at

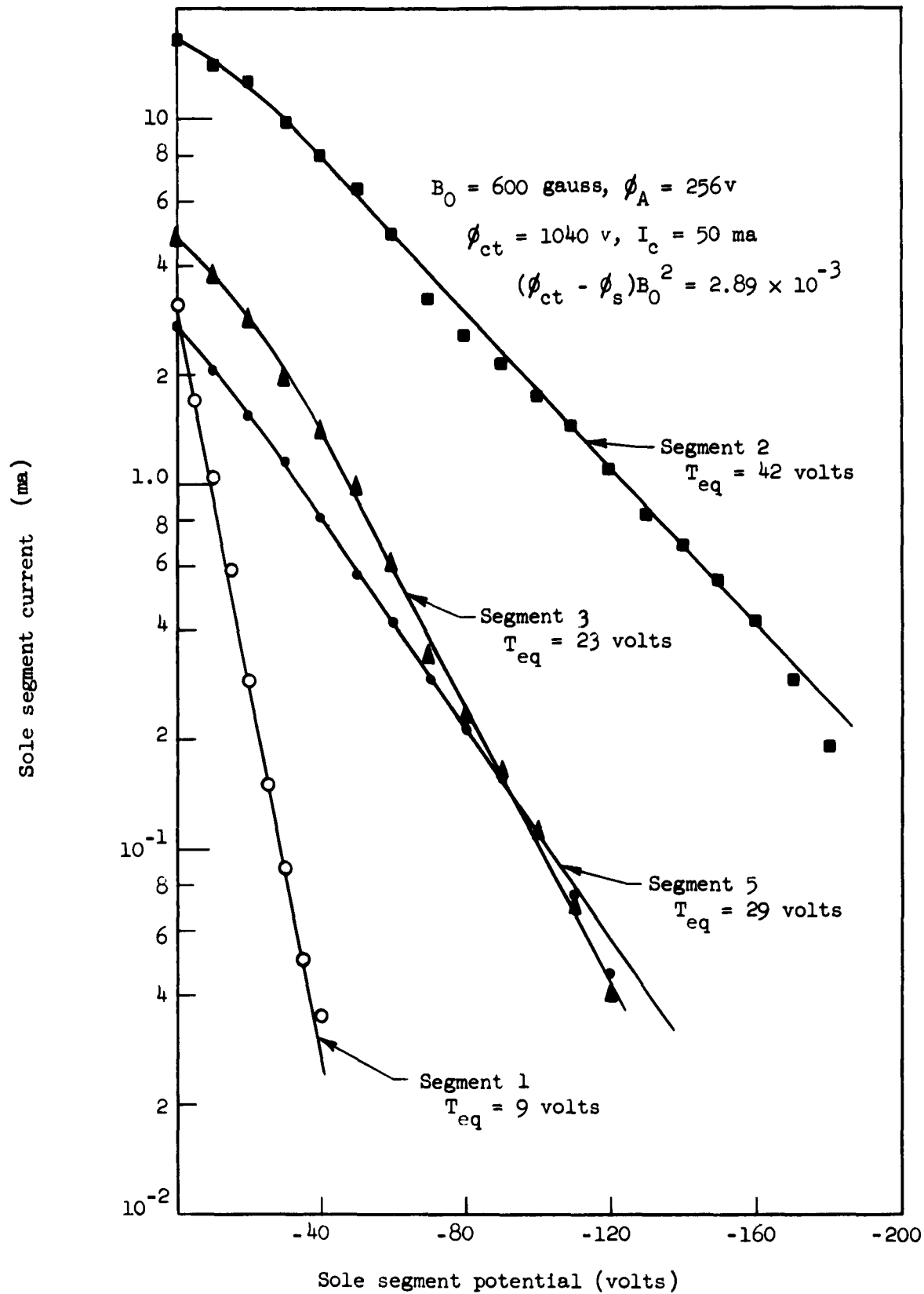


FIG. 5.44--Sole current intercepted by segments 1,2,3 and 5 as a function of their potential.

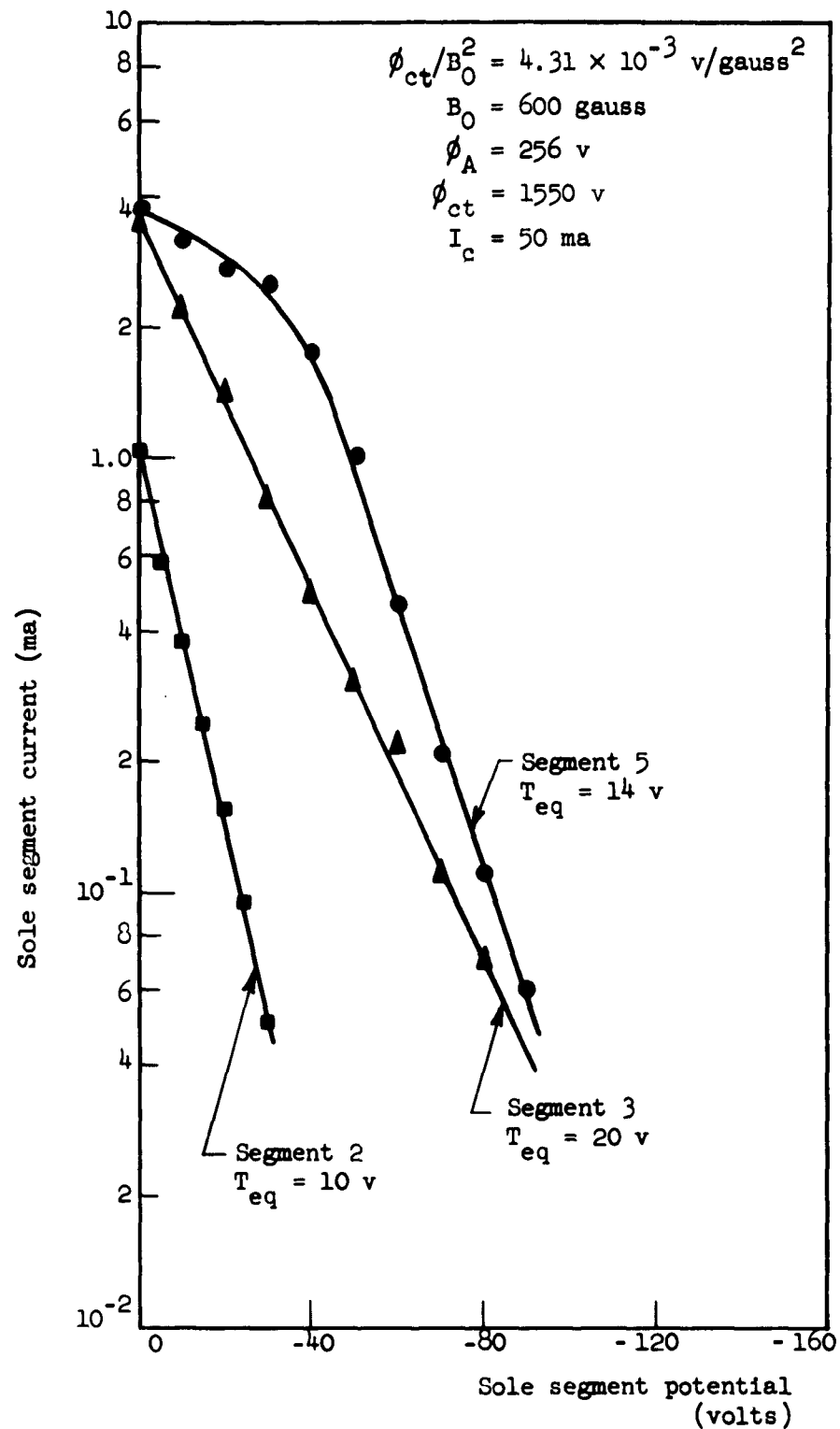


FIG. 5.45--Sole current intercepted by segments 2, 3, and 5 as a function of their potential.

zero potential. For these measurements, the values of  $d$  and  $\Delta$  were .100in. and sole. The two figures show this data for two different values of circuit voltage, the purpose being to illustrate the effect of changing the drift region scaling parameter. We see that these curves are approximately half-Maxwellian. The equivalent electron temperature  $T_{eq}$  obtained from the slope of the curves and expressed in volts is shown for each set of points.

We see in Fig. 5.44 that the saturation phenomena found in the sole current distribution measurements also appear in the temperature measurements. Thus the second sole segment intercepts the highest temperature electrons as well as the greatest fraction of the total sole current. Note particularly the relatively low temperature associated with the first segment. Figure 5.45, when compared with the previous figure, illustrates the effect of increasing the drift region scaling parameter. The temperature associated with the second segment is seen to be greatly reduced, while those of the third and fifth segments have changed considerably less. No current was intercepted by the first segment.

It was generally noted that increasing  $\phi_{ct}$ , and hence the scaling parameter, additionally, did not significantly reduce the temperatures measured with the sole segments farthest from the cathode. Thus with the scaling parameter equal to  $5.55 \times 10^{-3}$  v/gauss<sup>2</sup>, no sole current was intercepted by the first three segments, yet equivalent temperatures of approximately 20 volts were measured at the fifth and sixth segments.

Throughout all such measurements, it was observed that as the scaling parameter is increased, the position of the segment at which the maximum beam temperature is measured tends to shift in a direction away from the gun. Similar behavior was noted earlier in the variation in position of the segment collecting the maximum amount of sole current.

It should be noted that these results must be used with caution, for the same reasons as were given in section d-v in connection with the distribution measurements. Also the error introduced by secondary emission from the sole should again be mentioned.

Temperature measurements were also made for the entire beam, using the continuous sole plate. Typical results are shown in Fig. 5.46.

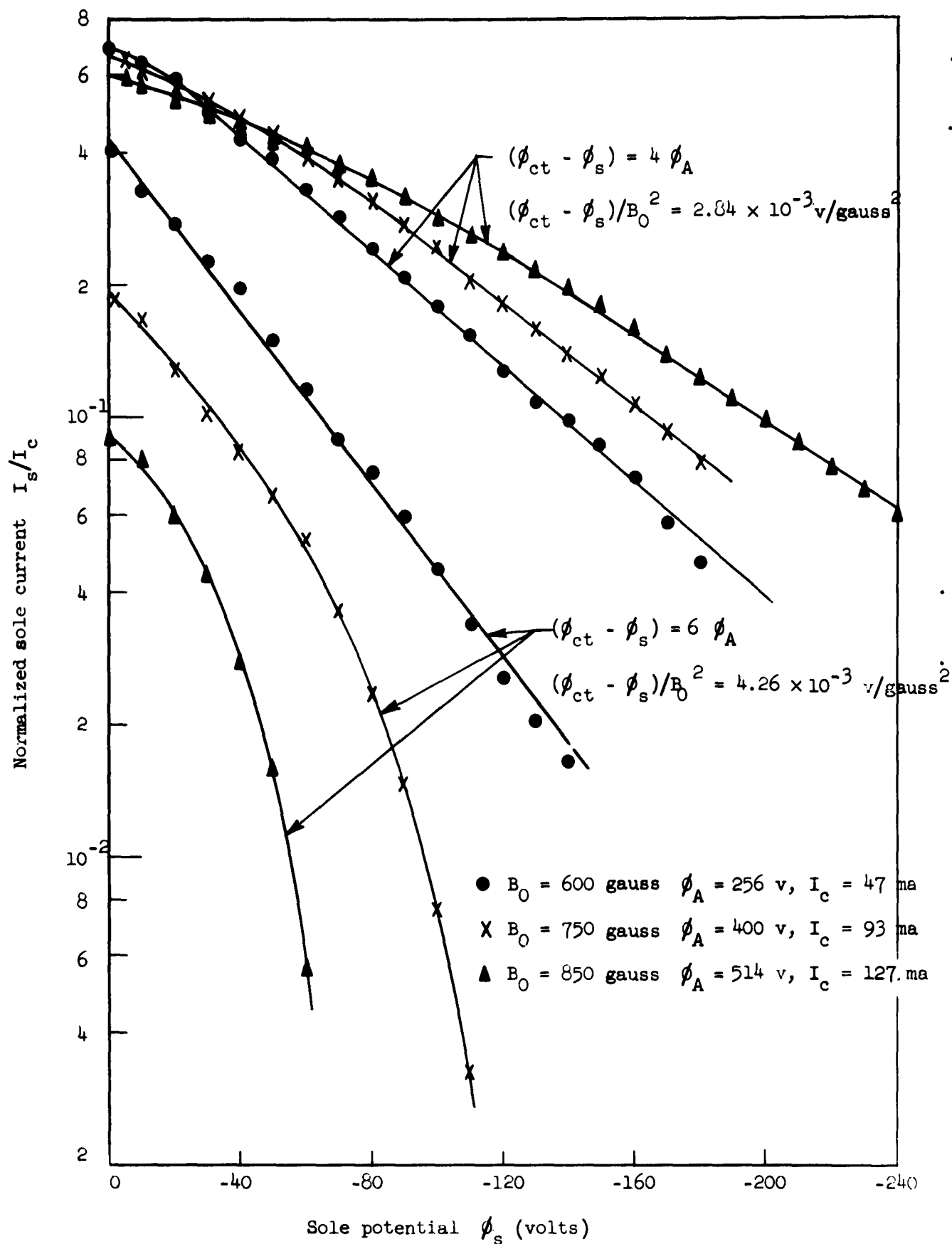


FIG. 5.46--Total sole current as a function of sole potential for the continuous sole.



Here we show current intercepted by the entire sole as a function of negative sole voltage for three values of  $B_0$ , and each of these for two values of the scaling parameter. It should be noted that for a particular set of points,  $\phi_{ct}$  was varied along with  $\phi_s$ , so as to keep  $(\phi_{ct} - \phi_s)$  a constant. For each value of  $B_0$ ,  $\phi_A$  was fixed at the design value.

A number of aspects of these curves are noteworthy. Increasing the scaling parameter has the effect of lowering the measured beam temperature. For all values of  $B_0$  for the smaller of the two values of the scaling parameter, the equivalent beam temperature is of the order of 80 volts, a somewhat larger value than was measured with any particular portion of the segmented sole. An additional observation regarding these data, which has no apparent precedent, is the tendency for the curves to be increasingly non-Maxwellian for increasing values of  $B_0$ . This tendency is seen for both values of the scaling parameter.

Similar measurements made under temperature-limited conditions at the cathode showed no great change in beam temperature, although a decrease in this quantity was noted for a decrease in beam current, either as a result of temperature-limiting or decreasing the potential of the gun anode, all other conditions remaining constant.

e. Visual Observations. Viewed at a pressure of  $8 \times 10^{-6}$  Torr, the beam from the long gun appeared to be considerably thicker at the exit plane than is predicted by the gun theory. Thus, while the design method predicts a beam thickness of approximately .002 in. at the exit plane, a thickness of about .010 in. was measured using a micrometer telescope. As a result of close electrode spacing and reflection of cathode glare, it was not possible to accurately examine the shape of the beam in the gun, but it was determined that with the gun parameters at the design values, the beam was ejected from the gun approximately centered in the space between the focusing electrode and the anode as would be expected from the theory.

The reasons for the apparent increase in beam thickness are numerous. The thickness of the beam as predicted by theory approaches the limit of accuracy of the beam viewing technique ( $\sim .0004$  in. as estimated by Wightman<sup>19</sup>). We would also expect beam spreading as a result of dc

thermal effects at the cathode. Probably the most important contributing factor to the increased thickness, however, is rf growth in the gun. It was noted that the beam thickness increases rapidly in the drift region for small values of the scaling parameter ( $< 3 \times 10^{-3} \text{ v/gauss}^2$ ); and since the gun scaling parameter, although varying as a function of position, is always less than this magnitude, there is every reason to assume that such growth exists in the gun region as well (see section f-1).

In Fig. 5.47 we show beam thickness as measured by means of the micrometer telescope as a function of the distance in the drift region from the gun exit plane. For these measurements, the value of the drift region scaling parameter was  $4.1 \times 10^{-3} \text{ v/gauss}^2$ . In the figure,  $(\delta - \delta_0)$ , the increase in beam thickness over the value at the gun exit, is plotted on a semilogarithmic scale as a function of the distance in inches from the exit plane. We note a slight tendency toward saturation after a distance of about 3 in. Converting the slope of this curve to power gain, we find a growth rate of approximately 500 db/meter, a value, it is interesting to note, which is comparable to the maximum value of diocotron gain in the beam.<sup>5</sup>

A series of photographs of the beam are shown in Figs. 5.48 and 5.49. Figure 5.48 shows the beam with the gun voltage at its design value and with the proper sole and circuit potentials to provide potential and field continuity at the exit plane. We see that the beam is injected so that it undulates slightly in the drift region, although the amplitude of these undulations is less than the beam thickness. The increase in beam thickness and the tendency for the undulations to become blurred out can be seen by following the beam away from the gun, in a direction from left to right in the photograph. The cloudy area on the underside of the beam is thought to be caused by ion current being drawn to the sole. In the original color photographs, this area was much less intense and of a slightly different color than the beam itself. Figure 5.48b shows the beam under the same conditions as for the first photograph except that the negative sole potential is increased by 50 volts. The amplitude of the undulations appearing in (a) is seen to be decreased as a result. It is thought that these undulations are at least partially caused by the small injection angle at the gun exit.

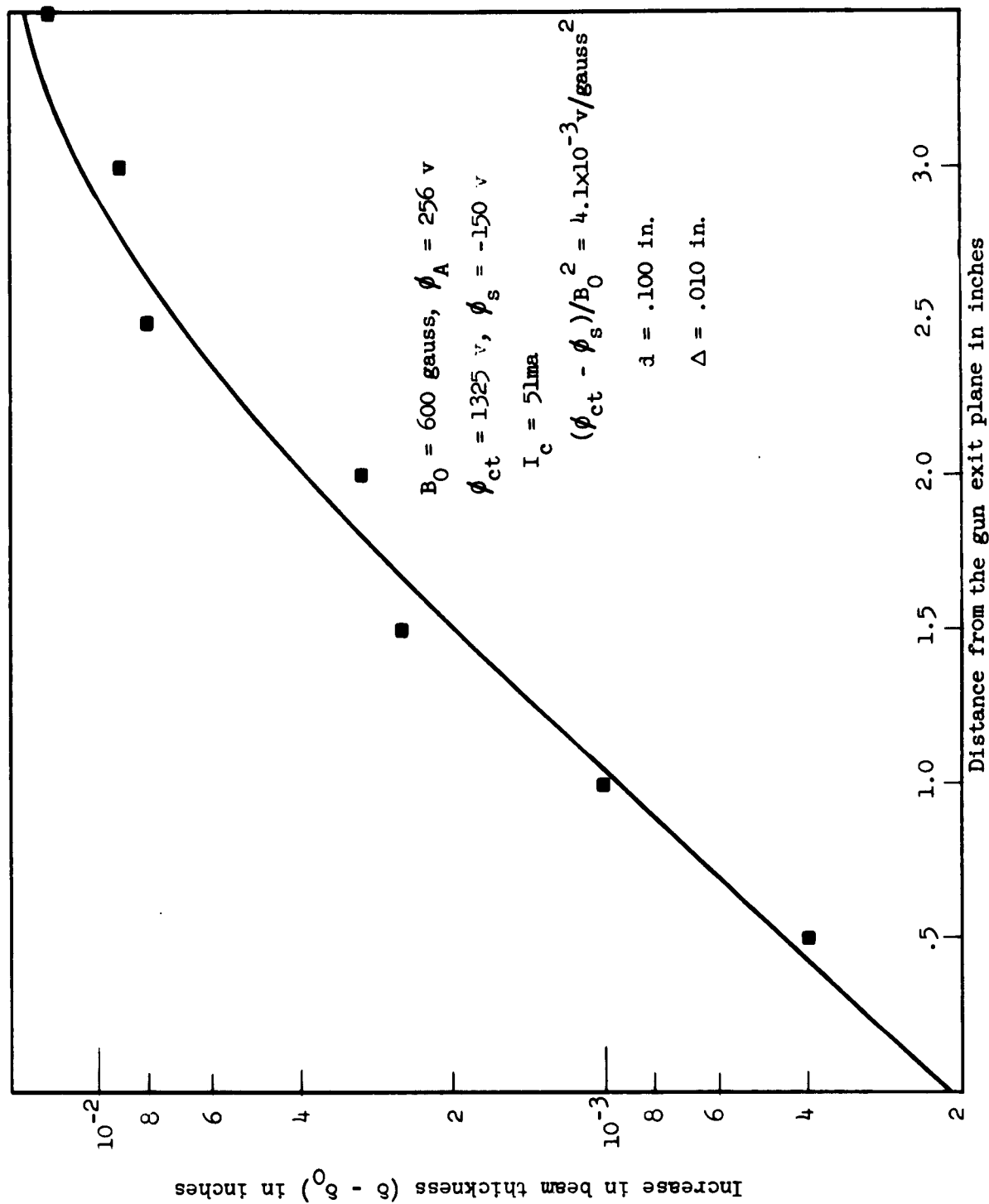


FIG. 5.47--Increase in beam thickness as a function of the distance from the gun exit plane.



(a)

$\phi_A = 256v$	$I_c = 48ma$
$\phi_{ct} = 922v$	$I_s = 6.4ma$
$\phi_s = -110v$	$B_0 = 600 \text{ gauss}$



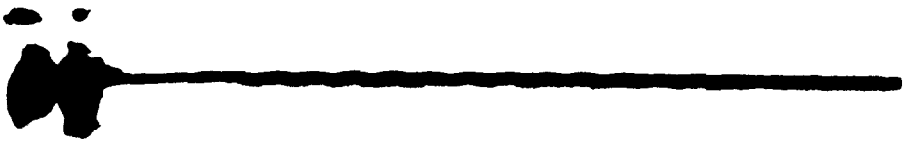
(b)

$\phi_A = 256v$	$I_c = 48ma$
$\phi_{ct} = 922v$	$I_s = 1.8ma$
$\phi_s = -160v$	$B_0 = 600 \text{ gauss}$



(c)

$\phi_A = 220v$	$I_c = 33.8ma$
$\phi_{ct} = 922v$	$I_s = 1.18ma$
$\phi_s = -120v$	$B_0 = 600 \text{ gauss}$



(d)

$\phi_A = 292v$	$I_c = 61ma$
$\phi_{ct} = 922v$	$I_s = 7.4ma$
$\phi_s = -120v$	$B_0 = 600 \text{ gauss}$

FIG. 5.48--Photographs of the beam from the long gun.



(a)

$$(\phi_{ct} - \phi_s)/B_0^2 = 2.22 \times 10^{-3} \text{ v/Gauss}^2$$

$$\lambda_c = .123 \text{ in}$$



(b)

$$(\phi_{ct} - \phi_s)/B_0^2 = 3.89 \times 10^{-3} \text{ v/Gauss}^2$$

$$\lambda_c = .215 \text{ in}$$



(c)

$$(\phi_{ct} - \phi_s)/B_0^2 = 4.44 \times 10^{-3} \text{ v/Gauss}^2$$

$$\lambda_c = .246 \text{ in}$$



(d)

$$(\phi_{ct} - \phi_s)/B_0^2 = 5.00 \times 10^{-3} \text{ v/Gauss}^2$$

$$\lambda_c = .277 \text{ in}$$

FIG. 5.49--Photographs of the beam from the long gun, showing the effect of varying the drift region scaling parameter.

Figures 5.48c and d show the beam with the gun anode potential 14 per cent below and above the design value, respectively. We see that in the former case, the beam in the drift region is actually straighter than for (a). However, the undulation amplitude in (d), while larger than in (a), is still relatively small. Noting that the 14 per cent variation in  $\phi_A$  results in a corresponding 30 per cent change in cathode current, we concluded that varying  $\phi_A$  provides a convenient means of controlling  $I_c$  without greatly altering the shape of the beam.

Figure 5.49 a,b,c,d shows the effect of increasing the scaling parameter on the appearance of the beam. The sole and circuit potentials are increased proportionally in (b) through (d). In addition to the slight decrease in ripple amplitude for the larger scaling parameters, we see that the tendency for the beam to thicken from left to right, which is quite evident in (a) and (b), is almost completely absent in (d) for the largest value of the scaling parameter. At this same time, the sole current is seen to essentially vanish for both (c) and (d). It is thus possible to correlate the measurement of sole current with a visually observed increase in beam thickness as the beam flows through the drift region; moreover, both phenomena are seen to diminish with increasing values of the scaling parameter.

f. Miscellaneous Experiments. Two additional experiments, both involving modification of the basic geometry of the original long gun optics, shown in Fig. 5.28, were performed. The object of these experiments was to investigate the effect on the magnitude of the observed beam instability, as evidenced by the sole current, of variation in the distance over which the beam is accelerated. In the first experiment the slow acceleration of the gun was extended from the gun into the entire drift region by gradually decreasing the sole-circuit spacing with increasing distance from the gun exit. In the second experiment the transit angle, as measured by  $u = \omega_c t$ , of electron trajectories in the gun was reduced by moving the gun exit plane closer to the cathode. In this latter case the beam was accelerated somewhat more rapidly than in the gun as originally designed. The effect of this modification on the beam instability was then investigated.

(1) Adiabatic Acceleration in the Drift Region. In this experiment, the approximate conditions of the long gun were extended by tapering the spacing of the sole and circuit electrodes so as to provide a continually increasing transverse electric field in the drift region.

This experiment was performed because of several earlier observations which tended to indicate a relatively stable beam in the gun where it is slowly accelerated. These observations included: (1) the cutoff measurements of section b and the visual appearance of a sharply defined beam at the gun exit plane, (2) the absence of any substantial current to the forward focusing electrode (equivalent to sole current in the drift region), and (3) the relatively small sole currents measured in the portion of the drift region closest to the gun. On the basis of these observations, it was decided to extend the region of acceleration into the entire drift region as a possible means of achieving greater beam stability.

From the original flow equations for the long gun,

$$X = X_0 + \frac{u^2}{2} \quad (5.5a)$$

$$Y = u \quad (5.5b)$$

$$E_y = u \quad , \quad (5.5c)$$

we see for  $X_0 = 0$  that

$$E_y = \sqrt{2X} \quad . \quad (5.6)$$

From the family of equipotentials shown in Fig. 4.4, we see moreover that for large positive values of  $X$  the electrode curvature becomes very small. Thus it should be possible to approximately "continue" the gun in the drift region by means of a linear variation in the sole-circuit spacing  $d$ , and as a result to provide continuous and gradual acceleration of the beam in the drift region.

The electrode configuration with the appropriate electrode potentials for a given value of magnetic field is shown in Fig. 5.50. The placement and the value of potential applied to the circuit are determined by: (1) the total length of the drift region, (2) the linear normalization

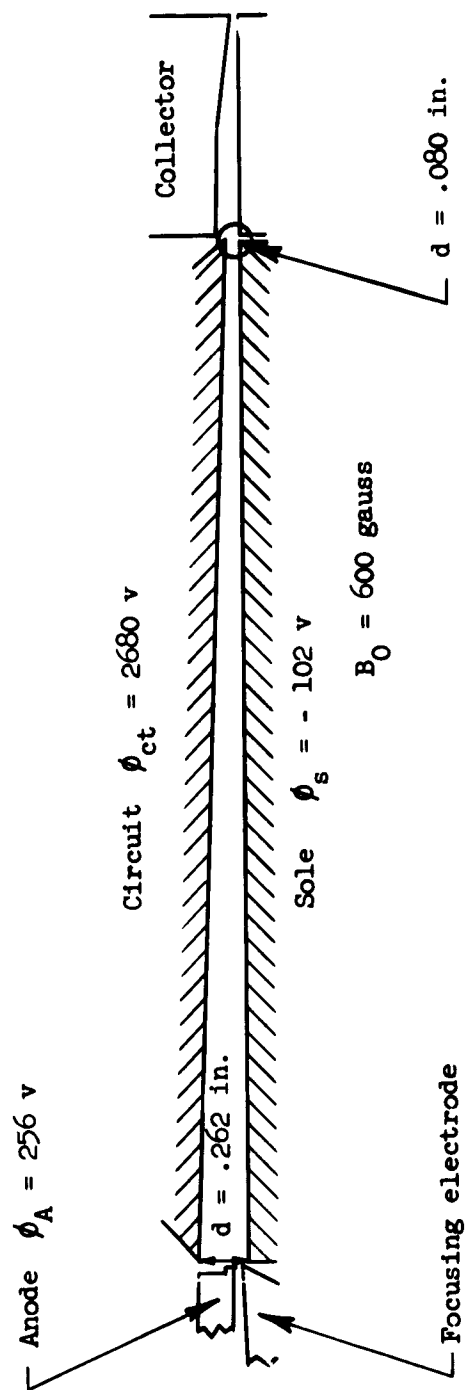


FIG. 5.50--Electrode configuration for extending the long gun.



factor  $\eta J_y / \epsilon_0 \omega_c^3$ , (3) the requirements of field and potential continuity at the gun exit plane, (4) the requirement that the beam not strike the circuit at the collector end of the drift region, and (5) that  $E_y$  shall satisfy Eq. (5.6) at the end of the drift region where  $X$  represents the total normalized distance from the center of the cathode. For this experiment the gun configuration was unchanged.

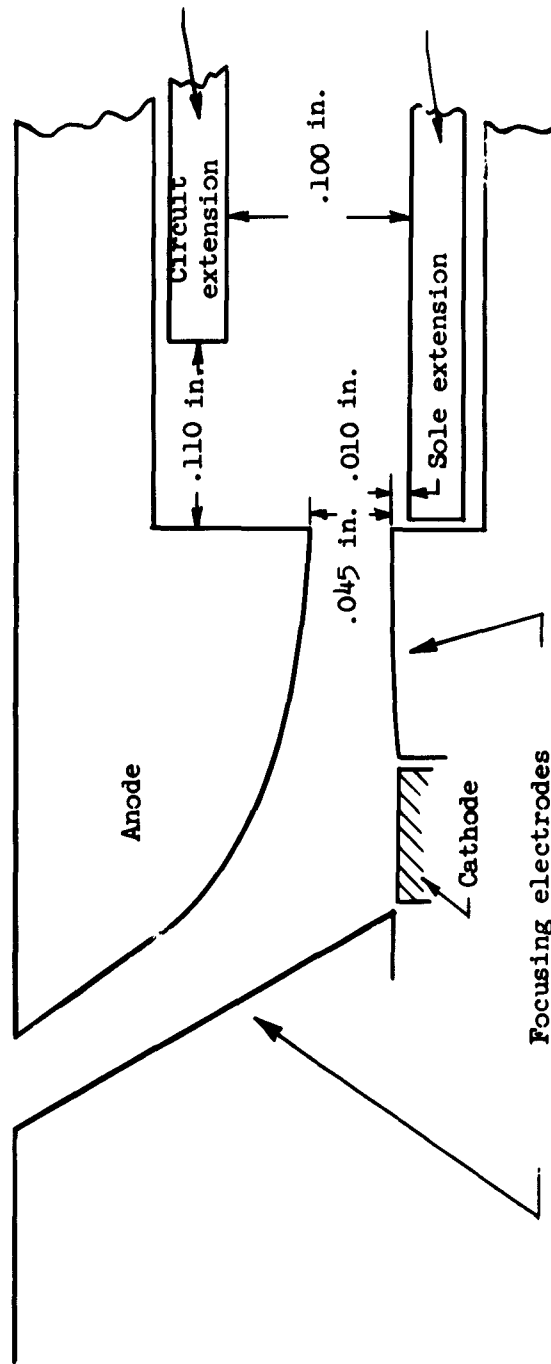
Experimentally, the electrode system appeared to be functioning essentially as designed. The circuit was positioned so as to be just above the top of the beam at the end of the drift region. With the design voltage applied to the circuit no circuit current was seen, but for values of  $\phi_{ct}$  slightly above the design potential, a sizable fraction of the total beam current was intercepted by the circuit, implying that the beam was beginning to graze this electrode.

However, no significant reduction in sole current was obtained with this configuration as compared with the original optical system. Moreover, when the modified configuration was used in conjunction with the segmented sole, no great change in sole current distribution was noted from the earlier results.

These results imply that the crossed-field instability exists and is of the same order of magnitude in accelerated as well as freely drifting electron streams, provided that the acceleration is sufficiently slow or adiabatic. It might be expected therefore that the effects of such instability would build up over the rather long electron transit times associated with the long gun. The object of the following experiment therefore was to investigate the validity of this speculation.

(11). Reduction of the Gun Transit Angle. In this experiment the exit plane of the gun was moved considerably closer to the cathode than originally, and in effect, the transit time in the gun alone was reduced by approximately one-half.

This modification was effected by removing the last portion of the gun electrodes and extending the sole and circuit electrodes into the vacant area. The modified electrode configuration and a comparison of the exit parameters of the modified gun with those of the original design are shown in Fig. 5.51. As shown, a rather long gap (.100 in.) exists between the end of the gun anode and the circuit. The purpose



COMPARISON OF PARAMETERS AT EXIT

	ORIGINAL LONG GUN		MODIFIED LONG GUN	
X upper edge	1000	Normalized units	347	Normalized units
X lower edge	870	Normalized units	217	Normalized units
u upper edge	44.7		26.4	
u lower edge	41.7		20.8	
φ upper edge	227	volts	78.9	volts
φ lower edge	192	volts	49.3	volts
Average exit velocity	8.29	$\times 10^6$ m/sec	4.76	$\times 10^6$ m/sec
Cathode length $l$	.073	in.	.073	in.
Normalized cathode length	130		130	
Average injection angle	1.32°		2.46°	
$\lambda_c$ at exit	.145	in.	.083	in.

FIG. 5.51--Geometry of the modified long gun.

of this gap was to provide a fringing field to accelerate the beam from the exit velocity to the drift region velocity faster, in terms of number of cyclotron wavelengths, than in the original gun, yet not as abruptly as if the gap were not present. We see that the gap is slightly greater than  $\lambda_c$  of the beam at the exit plane. The total acceleration time, expressed in terms of the transit angle from the cathode into the drift region is then roughly about  $10.8 \pi$  as compared to  $14 \pi$  for the original gun.

Experimentally, the results of these modifications were not extremely conclusive, although some evidence was found to indicate a reduction in the effects of the instability. As a result of the electrode configuration at the gun exit, it was not possible to make measurements of sole current which could be compared directly with data obtained with the original long gun, such as that shown in Fig. 5.36. Instead, the following procedure was adopted: With a given value of magnetic field, and for the gun voltage at its design value, the sole and circuit potentials were adjusted to obtain as straight a beam as possible, at the same time maintaining an arbitrarily specified value of normalized sole current. The values of  $\phi_{ct}$  and  $\phi_s$  so obtained were then compared with the corresponding values obtained with the earlier gun, also under linear beam conditions, and for the same value of  $I_s/I_c$ . As a general rule such comparisons showed roughly similar values of  $\phi_{ct}$  but noticeably smaller values of negative sole voltage for the shortened gun. For example, for  $I_s/I_c = 10^{-3}$ , the values of  $\phi_{ct}$  and  $\phi_s$  were found to be 1600 v and - 65 v, respectively. For the original version of the gun the corresponding values were 1560 v and - 180 v. For these conditions, the total number of beam cyclotron wavelengths in the drift region was approximately 23 for the modified gun as compared to 20.5 for the original geometry. We see that for equal values of normalized sole current that almost three times as much negative sole potential was required for the beam from the original gun than from the shortened one, even though the latter beam was more cyclotron wavelengths long. Similar comparisons were noted for smaller values of  $\lambda_c$  and larger sole currents.

On the basis of this experiment, it is not possible to conclude that the long transit time of the trajectories in the gun was alone responsible for the observed beam instabilities, yet the evidence does seem to point in this direction. It is felt that additional and more clearcut experiments of this type are now necessary.

## VI. CONCLUSIONS AND RECOMMENDATIONS FOR FURTHER WORK

In this chapter the significant results of the experiments described in the previous chapter are summarized, and some suggestions for possible further investigations are presented. In discussing the experiments we will consider the two guns which have been studied, both from the point of view of verification of the design theory and in terms of their potential utility in practical devices. In addition we will point out some conclusions which may be drawn from the experiments regarding the problem of crossed field instability and briefly indicate some possible further experiments and theoretical work in this area.

### A. CONCLUSIONS AND RECOMMENDATIONS REGARDING THE GUNS

On the basis of the experiments described in sections (C-3-a) and (D-3-a) of Chapter V we concluded that the present design method is successful insofar as it provides a means of analytically designing convergent crossed-field guns which in practice provide the current predicted by theory. Experimentally, both guns were found to have an order of magnitude convergence of ten to one, a value somewhat smaller than predicted on the basis of the exact space-charge flow solutions.

The short gun which was studied produced a reasonably well-defined beam which was found to be free of excessive space current and which is seemingly a better approximation to planar Brillouin flow than has heretofore been achieved. Anderson<sup>34</sup> has reported noise measurements made with a crossed-field backward wave amplifier incorporating a short gun similar to ours and based on the same design method. His results show noise figures comparable to O-type tubes before noise reduction methods are employed. The short gun as it now stands is thus capable of practical application and represents a significant improvement over previous guns.

As has already been noted, it is possible that the performance of this gun might be further improved by better matching at the exit plane and some additional work in this area might well prove useful. Also a more comprehensive set of noise measurements relating noise to various beam parameters is needed. Finally some attention might be given to the role of thermal velocities at the cathode.

As far as the dc aspects of the long gun are concerned, theory and experiment appear to be in good agreement. As a result of the appearance of the excessive sole current in the beam from this gun, its potential utility is perhaps not so clearly established as is that of the short gun. Yet we have shown experimentally that it is possible to achieve a beam from this gun which is almost completely free from sole current and, as it might be supposed, is relatively noise free as is the short gun beam. Clearly a complete set of noise measurements would also be useful here although since high noise and excessive sole current are probably manifestations of the same phenomenon, the existence of one very likely implies the other. In addition the effect of thermal velocities at the cathode should be considered in more detail than in the present work.

It may well be possible to reduce the effect of the instabilities associated with the long gun by means similar to those described in Chapter V, section (D-3-f-ii). Thus the exact analytic electrode shapes might be used as an initial focusing element to take the beam out of the immediate area of the cathode. A transition region employing much more abrupt acceleration than the analytic electrodes would then be used to increase the beam velocity to the final desired value. Undulations which might be introduced onto the beam in this area could be removed by means described in Appendix D. This could be accomplished in the same transition region. By this means we believe a well-focused and reasonably stable beam could be achieved.

#### B. CONCLUSIONS AND RECOMMENDATIONS REGARDING CROSSED-FIELD INSTABILITIES

On the basis of the measurements described in Chapter V (section D-3-d,f) the following statements can be made regarding crossed-field instabilities as evidenced by excessive sole current:

1. The source of the instability is to be found near the cathode and is probably associated with the formation of a potential minimum as a result of space-charge limiting (Chapter V, parts d-iii, d-iv, d-v, d-vi).<sup>(21)</sup>

2. The instability results from the growth of the above disturbance along the beam. Such growth exists both on the freely drifting portion of the beam (d-v) and on a slowly accelerated stream (f-i). Whether

---

<sup>(21)</sup> These designations refer to subsections of section D-3 in Chapter V which describe the relative experiments.

this growth occurs in the body of the beam or along its boundaries is still open to question. Evidence obtained in (d-11) tends to indicate that a majority of the excess energy electrons in the beam are to be found near the edges, although the increase in beam thickness ( $e$ ) as correlated to the sole current distribution would indicate a growth in the stream body.

3. The total sole current is found to scale with the total number of cyclotron wavelengths in the beam. This observation points up the need in any crossed-field optical system for quick acceleration from the cathode and for keeping the total transit angle  $\omega_c t$  as small as possible. On this basis it is also possible to explain the relative stability of the short gun beam, since the total transit angle from the cathode to the collector in this case was roughly equivalent to that for the gun alone in the long gun optics.

4. The growth of the instability is not critically dependent upon the shape of the beam, i.e., whether for a given value of  $\lambda_c$  it is rectilinear or trochoidal (d-v).

5. Some evidence of growth in electron temperature along the beam was found (d-vi), although these measurements are somewhat open to question.

It may be added that the observed growth along the beam is almost certainly related to slipping stream or diocotron amplification, although in the case of nonlaminar flow the actual mechanism is of necessity more complex than this simple model.

In conclusion, two possible areas of further work should be mentioned:

A theoretical analysis of "diocotron like" growth along an adiabatically accelerated stream, the result of which could be compared with freely drifting diocotron growth rates, would be of considerable interest. This problem could perhaps be attacked using a perturbation method somewhat along the lines of the W.K.B. approximation.

Experimentally, the problem of overcoming the instabilities inherent in the crossed-field beam would seem to be a matter either of reducing the growth rate along the stream or somehow removing the source disturbance close to the cathode. On the basis of the present work, the former

approach has been shown to be a useful one; however, the latter may ultimately provide the more satisfactory solution. One means of achieving this end would be the use of a temperature limited cathode. However, in addition to the undesirable loss of current, in practice it is often difficult to achieve uniform temperature limiting over the entire cathode surface; thus it would be difficult to completely eliminate the effect of the potential minimum without going to very low current densities. One alternative is the shielded gun which has no magnetic field at the potential minimum. Another possibility is a gun with a grid located very close to the cathode in the vicinity of the potential minimum. We suggest that both of these devices are worthy of further investigation.



## APPENDIX A

### A DC SMALL SIGNAL FIELD ANALYSIS OF A THIN UNDULATING CROSSED-FIELD BEAM

Consider a thin undulating crossed field beam in the geometry shown in Fig. A.1. All quantities are assumed to have no explicit time dependence and, moreover, all perturbed quantities are assumed small and only first order effects will be considered. In the unperturbed state the beam is situated in the plane  $y = y_0$ . The undulations are assumed to result from improper injection optics of the type mentioned in Chapter II, although this assumption is in no way essential to the analysis. Finally, all perturbed quantities are assumed to have an  $x$  dependence of the form  $e^{-j\beta x}$ .

In evaluating the space charge fields of the undulating beam we shall follow the method of Buneman.<sup>34</sup> Thus if the coordinates of a small element of the unperturbed beam are given by  $x = x_0$ ,  $y = y_0$ , in the perturbed beam this same element has the coordinates  $x = x_0 + x_1$ ,  $y = y_0 + y_1$ . If the amplitude of the undulation is small so that  $(dy_1)/(dx) \ll 1$ , Buneman shows that the discontinuity in the  $x$  and  $y$  components of electric field across the undulating beam may be written as

$$E_x^- - E_x^+ = \frac{-j\beta y_1 \sigma_0}{\epsilon_0} \quad (\text{A.1a})$$

$$E_y^- - E_y^+ = \frac{-j\beta x_1 \sigma_0}{\epsilon_0}, \quad (\text{A.1b})$$

where the superscripts  $+$  and  $-$  indicate fields above and below the beam, respectively, and where  $\sigma_0$  is the unperturbed surface charge density of the sheet beam.

The ratios of  $E_y^+ : E_x^+$  above and below the beam are determined by the external electrode configuration. The fields in these regions must be derivable from separate scalar potentials which satisfy Laplace's equation and which vanish at the boundary electrodes. We write these potentials above and below the beam as

$$\phi^+ = \phi_1 \sinh \beta(y - d) \quad (\text{A.2a})$$

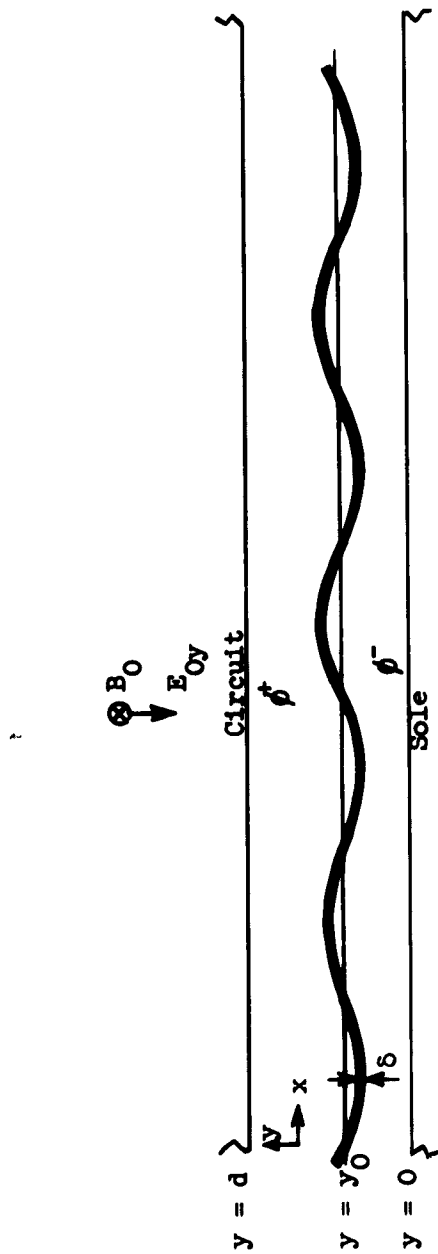


FIG. A.1--Geometry for the thin beam analysis.

and

$$\phi^- = \phi_2 \sinh \beta y , \quad (\text{A.2b})$$

where  $\phi_1$  and  $\phi_2$  include constant terms and the assumed  $x$  dependency. The corresponding components of electric field in these regions are

$$E_x^+ = + j\beta\phi_1 \sinh \beta(y - d) \quad (\text{A.3a})$$

$$E_y^+ = - \beta\phi_1 \cosh \beta(y - d) \quad (\text{A.3b})$$

$$E_x^- = + j\beta\phi_2 \sinh \beta y \quad (\text{A.3c})$$

$$E_y^- = - \beta\phi_2 \cosh \beta y . \quad (\text{A.3d})$$

Inserting these relations evaluated at the beam into Eq. (A.1) and solving for  $\phi_1$  and  $\phi_2$  results in (hereafter the  $e^{-j\beta x}$  dependency will not be explicitly written)

$$\phi_1 = - \frac{\sigma_0}{\epsilon_0 \sinh \beta d} (y_1 \cosh \beta y_0 + jx_1 \sinh \beta y_0) \quad (\text{A.4a})$$

$$\phi_2 = - \frac{\sigma_0}{\epsilon_0 \sinh \beta d} [y_1 \cosh \beta(y_0 - d) + jx_1 \sinh \beta(y_0 - d)] . \quad (\text{A.4b})$$

If the components  $E_x$  and  $E_y$  of the mean field acting on the beam are taken as

$$E_x = \frac{1}{2} (E_x^+ + E_x^-) \quad (\text{A.5a})$$

$$E_y = \frac{1}{2} (E_y^+ + E_y^-) , \quad (\text{A.5b})$$

we obtain, for the mean field components,

$$E_x = - \frac{j\beta\sigma_0}{2\epsilon_0 \sinh \beta d} \left\{ y_1 \sinh \beta(2y_0 - d) + j2x_1 \sinh \beta y_0 \sinh \beta(y_0 - d) \right\} \quad (\text{A.6a})$$

$$E_y = + \frac{\beta\sigma_0}{2\epsilon_0 \sinh \beta d} \left\{ 2y_1 \cosh \beta(y_0 - d) \cosh \beta y_0 + jx_1 \sinh \beta (2y_0 - d) \right\} . \quad (\text{A.6b})$$

For convenience we will write these as

$$E_x = j\beta A y_1 + \beta B x_1 \quad (A.7a)$$

$$E_y = \beta C y_1 + j\beta D x_1, \quad (A.7b)$$

where

$$-D = A = -\frac{\sigma_0}{2\epsilon_0} \frac{\sinh \beta(2y_0 - d)}{\sinh \beta d} \quad (A.8a)$$

$$B = \frac{\sigma_0}{\epsilon_0} \frac{\sinh \beta y_0 \sinh \beta(y_0 - d)}{\sinh \beta d} \quad (A.8b)$$

$$C = \frac{\sigma_0}{\epsilon_0} \frac{\cosh \beta(y_0 - d) \cosh \beta y_0}{\sinh \beta d} \quad (A.8c)$$

The linearized equations for the perturbed motion of the beam may then be written as

$$\left. \begin{aligned} \dot{x}_1 &= +\omega_c \dot{y}_1 + \eta(j\beta A y_1 + \beta B x_1) \\ \dot{y}_1 &= -\omega_c \dot{x}_1 + \eta(\beta C y_1 + j\beta D x_1) \end{aligned} \right\} \quad (A.9a)$$

$$\left. \begin{aligned} \ddot{x}_1 &= +\omega_c \ddot{y}_1 + \eta(j\beta A \dot{y}_1 + \beta B \dot{x}_1) \\ \ddot{y}_1 &= -\omega_c \ddot{x}_1 + \eta(\beta C \dot{y}_1 + j\beta D \dot{x}_1) \end{aligned} \right\} \quad (A.9b)$$

where  $d/dt = -jv_0\beta$ , and where  $v_0$  is the average electronic speed in the beam. The differentiation is thus performed in a coordinate system moving with velocity  $v_0$ . Equations (A.9) may then be written (assuming  $\beta \neq 0$ ),

$$\left. \begin{aligned} (\eta B + v_0^2 \beta)x_1 + j(-\omega_c v_0 + \eta A)y_1 &= 0 \\ j(\omega_c v_0 + \eta D)x_1 + (\eta C + v_0^2 \beta)y_1 &= 0 \end{aligned} \right\} \quad (A.10a)$$

$$\left. \begin{aligned} (\eta B + v_0^2 \beta)x_1 + j(-\omega_c v_0 + \eta A)y_1 &= 0 \\ j(\omega_c v_0 + \eta D)x_1 + (\eta C + v_0^2 \beta)y_1 &= 0 \end{aligned} \right\} \quad (A.10b)$$

The vanishing of the determinant of these two equations gives the dispersion equation for the system

$$\beta^2 + \beta \frac{\eta}{v_0^2} (C + B) + \frac{\eta \beta_c}{v_0^2} (A - D) + \frac{\eta^2}{v_0^4} (AD + BC) - \beta_c^2 = 0 \quad (A.11)$$

Each of the quantities A , B , C , D defined by Eq. (A.8), when multiplied by  $(\eta)/(v_0^2)$  , is proportional to  $\beta_p^2 \delta$  . Since in the thin beam approximation this quantity must be small with respect to  $\beta_c$  , and since the geometrical quantities appearing in Eq. (A.8) are all of order unity, we shall ignore the fourth term of Eq. (A.8) which is of second order. In addition, since

$$-1 \leq \frac{\sinh \beta(2y_0 - d)}{\sinh \beta d} \leq +1 ,$$

it follows that

$$\frac{\eta(D - A)}{v_0^2} \leq \beta_p^2 \delta \ll \beta_c ,$$

and as a result, that the sum of the third and fifth terms of Eq. (A.11) is always negative, and hence that  $\beta$  can assume only real values.<sup>(22)</sup>

Having established the nature of its roots, we shall examine some approximate solutions of Eq. (A.11). If all space-charge terms are neglected, we obtain the roots

$$\beta = \pm \beta_c , \quad (A.12)$$

as expected.

With the first order space-charge terms present, Eq. (A.11) may be written as

$$\beta^2 + \beta \beta_p^2 \delta \frac{\cosh \beta(2y_0 - d)}{\sinh \beta d} + \beta_c \beta_p^2 \delta \frac{\sinh \beta(2y_0 - d)}{\sinh \beta d} - \beta_c^2 = 0 . \quad (A.13)$$

We shall first consider the solutions to this equation for two special geometries:

(1) The sole-circuit separation is small with respect to the beam wavelength. In this case

$$\beta d \ll 1 ,$$

---

<sup>(22)</sup> It may be noted that this result is still valid even though the second order terms are present since both of the products AD and BC are always negative.

and also

$$|\beta(2y_0 - d)| \ll 1 ;$$

hence we may write Eq. (A.13) as

$$\beta^2 + \frac{\beta_p^2 \delta}{d} + \beta_c \beta_p^2 \delta \left( \frac{2y_0}{d} - 1 \right) - \beta_c^2 = 0 . \quad (\text{A.14})$$

Noting that the third term of this expression is much smaller than the second, we find that

$$\beta \approx \pm \left( \beta_c^2 - \frac{\beta_p^2 \delta}{d} \right)^{1/2} . \quad (\text{A.15})$$

(2) The beam is located midway between the sole and circuit. In this case Eq. (A.13) reduces to

$$\beta^2 + \frac{\beta \beta_p^2 \delta}{\sinh \beta d} - \beta_c^2 = 0 \quad (\text{A.16})$$

and

$$\beta \approx - \frac{\beta_p^2 \delta}{2 \sinh \beta_c d} \pm \beta_c , \quad (\text{A.17})$$

where we have replaced  $\beta$  by  $\beta_c$  in the argument of the hyperbolic sin . In the limit of very large sole-circuit separation, such that  $\beta d \gg 1$  , the roots of Eq. (A.17) are then given<sup>(23)</sup> by Eq. (A.12).

In general the solutions of Eq. (A.13) will not differ by more than a small amount from  $\beta = \pm \beta_c$  . As a means of obtaining the approximate roots, we may replace  $\beta$  in the arguments of the hyperbolic sine and cosine functions which occur in Eq. (A.13) by  $\beta_c$  . The roots are then given by

$$\beta \approx - \frac{\beta_p^2 \delta \cosh \beta_c (2y_0 - d)}{2 \sinh \beta_c d} \pm \beta_c \left( 1 - \frac{\beta_p^2 \delta \sinh \beta_c (2y_0 - d)}{2 \beta_c \sinh \beta_c d} \right) = - \beta_q \pm \alpha \beta_c . \quad (\text{A.18})$$

The implications of these results have been discussed in Chapter II.

---

<sup>(23)</sup> The second order terms which were discarded give a very small correction even for large  $d$  ; for infinite  $d$  ,  $\beta = \pm \beta_c (1 + \beta_p^4 \delta^2 / 8 \beta_c^2)$ .

## APPENDIX B

### APPROXIMATE EXPRESSIONS FOR CATHODE CURRENT AS A FUNCTION OF ANODE POTENTIAL AND MAGNETIC FIELD

From Figs. 4.3 and 4.4 we see that, for each of the guns, the individual equipotentials which determine the shape of the anode electrodes are nearly parallel. It is therefore reasonable to assume that a fairly well-focused beam will be ejected by a gun, even though the anode potential is not the exact design value. In this Appendix, we show how it is possible to obtain expressions giving the approximate relationship of cathode current to anode voltage and magnetic field, when either of these latter quantities are varied from the design value.

We first consider the short gun (Fig. B.1). If  $b$  is the distance in the  $x$  direction from the center of the cathode to the exit plane, we may write, from Eq. (4.7), that for the trajectory leaving the center of the cathode

$$b = \frac{\eta J_y}{\epsilon_0 \omega_c^3} \left( \frac{u_b^2}{2} + \cos u_b - 1 \right), \quad (\text{B.1})$$

where  $u_b$  is the transit angle, in the gun, for this trajectory. In addition, the transverse electric field at this trajectory at the exit plane, is

$$E_{oy} = \frac{J_y}{\omega_c \epsilon_0} u_b. \quad (\text{B.2})$$

In order to put these equations into a reasonable analytical form, we make use of the approximation

$$\left( \frac{u_b^2}{2} + \cos u_b - 1 \right) \simeq 2\pi (u_b - \pi) \quad (\text{B.3})$$

for  $u_b \simeq 2\pi$ , which is exact to third-order in  $|u_b - 2\pi|$ . This approximation is valid to within about ten per cent from  $u_b = 3/2 \pi$  to  $3\pi$ . From Eqs. (B.1), (B.2) and (B.3), we obtain the result

$$J_y = \frac{-b \epsilon_0 \omega_c^3}{2\pi^2 \eta} + \omega_c \frac{E_{oy}}{\pi}. \quad (\text{B.4})$$

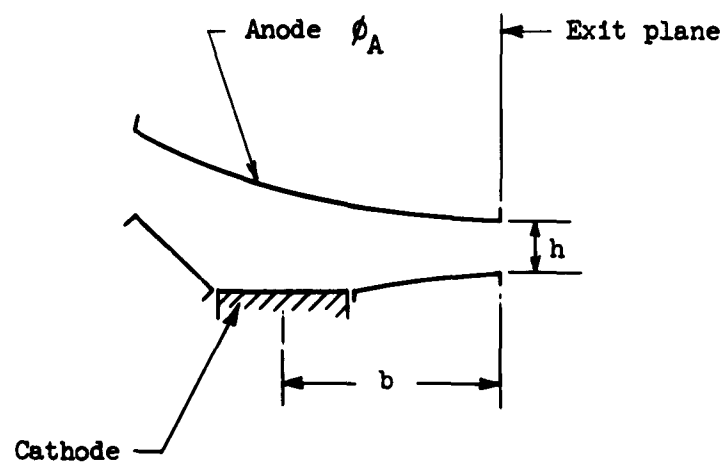


FIG. B.1--Geometry for the calculation of the emission relations.



For the center of the beam, at the exit plane, we may write

$$E_{Oy} \simeq - \frac{\phi_A}{h} , \quad (B.5)$$

where  $h$  is the separation, measured in the  $y$  direction, of the anode and focusing electrode at the exit plane. Note that this approximation neglects the unbalance of space-charge forces due to the different amounts of charge contained in those portions of the beam above and below the center trajectory. In view of the uncertainty as to the precise nature of the beam close to the exit plane, and the small component of the total field due to space charge we shall assume this to be a reasonably valid approximation. Recalling that a negative current density at the cathode corresponds to a positive current, we find that

$$I_c \approx S \left( \frac{\omega_c \phi_A}{\pi h} - \frac{b \epsilon_0 \omega_c^3}{2\pi^2 |\eta|} \right) , \quad (B.6)$$

where  $I_c$  is the total beam current and  $S$  the effective emitting area of the cathode. We choose to write this expression as

$$I_c = -GB_0^3 + HB_0\phi_A , \quad (B.7)$$

where  $G$  and  $H$  are geometrical constants given by the relations

$$G = \frac{Sb\epsilon_0\eta^2}{2\pi^2} \quad (B.8a)$$

and

$$H = \frac{S|\eta|}{\pi h} . \quad (B.8b)$$

For the experimental short gun, these constants have the numerical values:  $G = 3.43 \times 10^{-8}$  amperes/gauss<sup>3</sup>,  $H = 2.64 \times 10^{-6}$  amperes/gauss volt. These values were used in plotting the experimental curves shown in Figs. 5.11 and 5.12.

This same method may be used to obtain a corresponding expression for the long gun. For this simpler case, we find that

$$b = \frac{\eta J_y}{\epsilon_0 \omega_c^3} \frac{u_d^2}{2}, \quad (\text{B.9})$$

and, as before, at the exit plane, it may be shown that

$$E_{Oy} = \frac{J_y}{\omega_c \epsilon_0} u_d. \quad (\text{B.10})$$

Here, no such approximation as Eq. (B.3) is necessary. Combining Eqs. (B.9) and (B.10), we obtain the result

$$J_y = \frac{\eta \epsilon_0 (E_{Oy})^2}{2 \omega_c b}. \quad (\text{B.11})$$

Using Eq. (B.5) for the exit plane field and writing Eq. (B.11) in terms of the total current, we find that

$$I_c = \frac{S \epsilon_0 |\eta| \phi_A^2}{2 \omega_c b h^2}. \quad (\text{B.12})$$

which we write as

$$I_c = M \frac{\phi_A^2}{B}, \quad (\text{B.13})$$

where

$$M = \frac{S \epsilon_0}{2 b h^2}. \quad (\text{B.14})$$

For the experimental long gun, this constant has a value<sup>(24)</sup> of  $4.28 \times 10^{-4}$  amperes gauss/volt<sup>2</sup>. This value was used in plotting Figs. 5.23 and 5.24.

---

<sup>(24)</sup> This value may be compared with  $4.06 \times 10^{-4}$  amperes gauss/volt<sup>2</sup>, the exact design value.

## APPENDIX C

### A METHOD FOR IMPROVING THE LONGITUDINAL HOMOGENEITY OF THE EXPERIMENTAL MAGNET

In this Appendix, a very simple method for improving the uniformity of the magnetic field used in the crossed-field gun experiments is described.

A sketch of the geometry of the magnet pole pieces is shown in Fig. C.1. Before any attempts at improving the field uniformity were made,  $B_0$  (in the z direction) was found to vary as a function of the x-directed distance from the center of the pole faces shown in Fig. C.2. The gun and drift region occupy a length of approximately 7 in., and we see that the unmodified magnet would result in a variation in  $B_0$  of approximately 3 per cent over this distance. However, by the addition of the four shims shown in the sketch, the uniformity of field was substantially improved. The variation in  $B_0$  after these modifications, is also shown in Fig. C.2, and we now note a variation in  $B_0$  of less than 1 per cent over the region of interest.

The optimum shape and position of the shims was determined by trial and error, using thin strips of soft iron to build up the shims to the proper thickness. Upon the satisfactory completion of this work, shims of the proper size were machined from a single piece of material and attached to the pole faces with nonmagnetic clamps.

With regard to field uniformity in the z-direction,  $B_0$  was found to vary about 1 per cent over a distance of 1 in. (the approximate width of beam) located midway between the pole faces. It was assumed that this inhomogeneity was sufficiently small to be ignored.

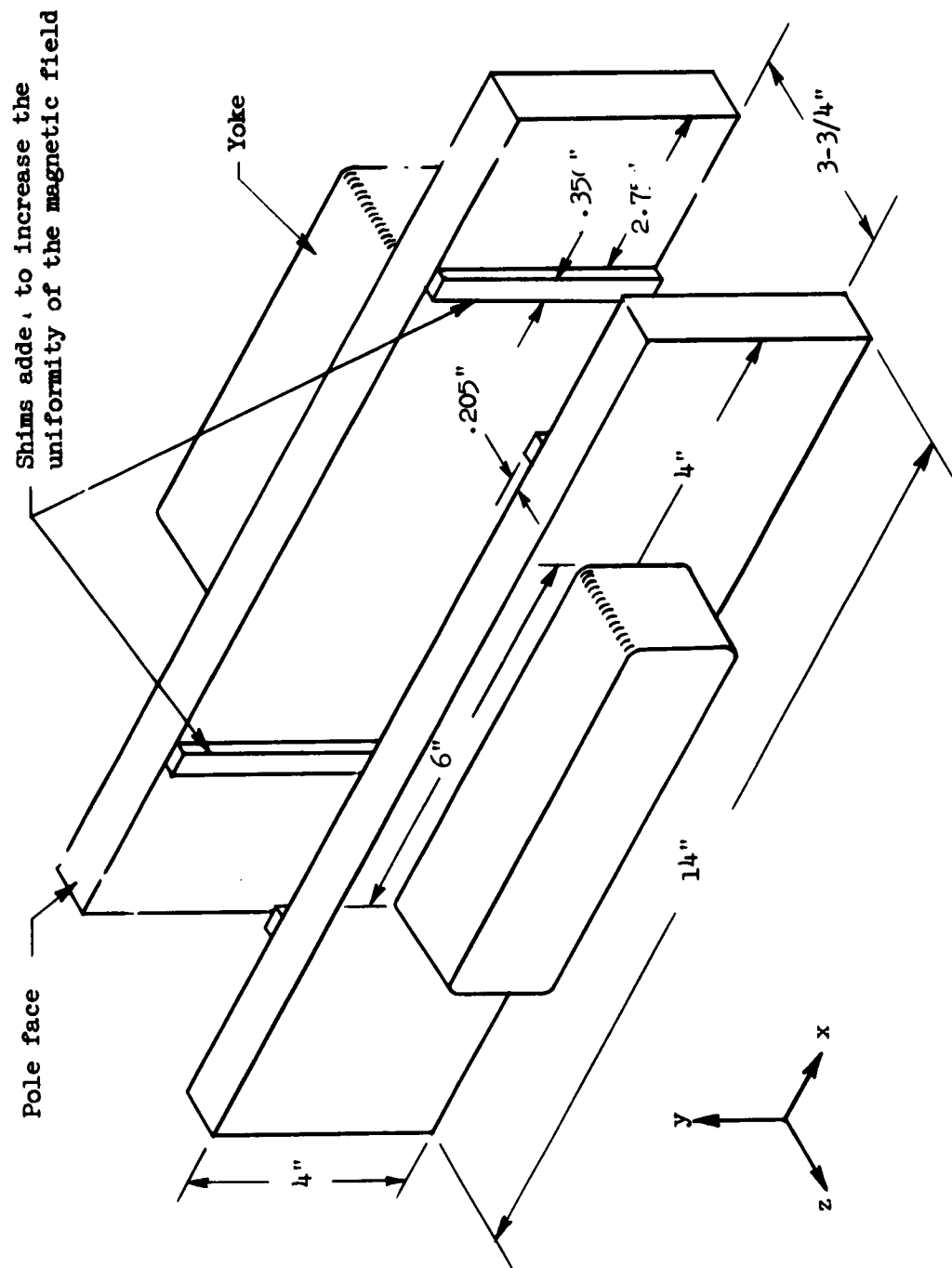


FIG. C.1--Geometry of the magnet pole pieces.

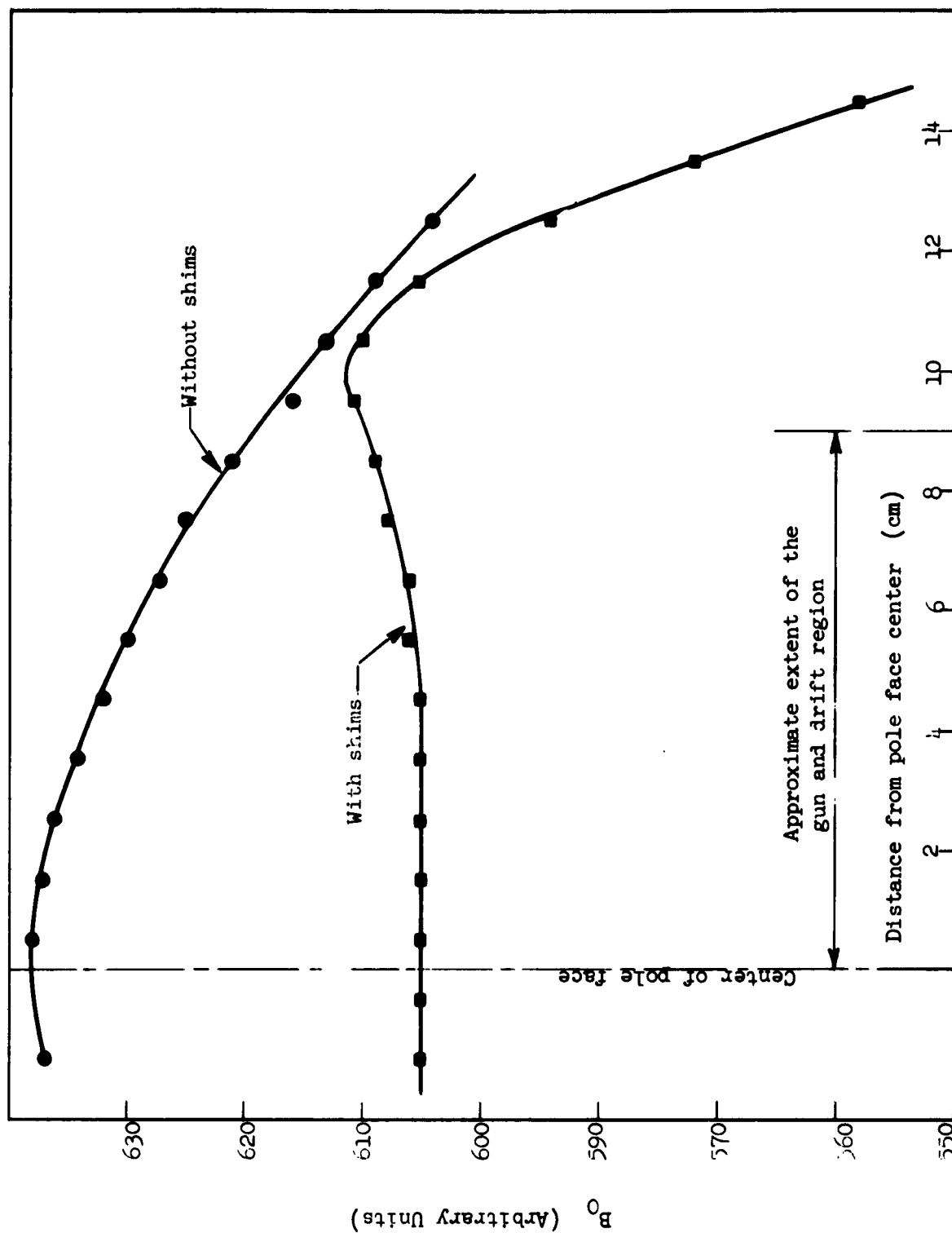


Fig. C.2--Variation in  $B_0$  as a function of longitudinal position with and without the pole piece shims.

## APPENDIX D

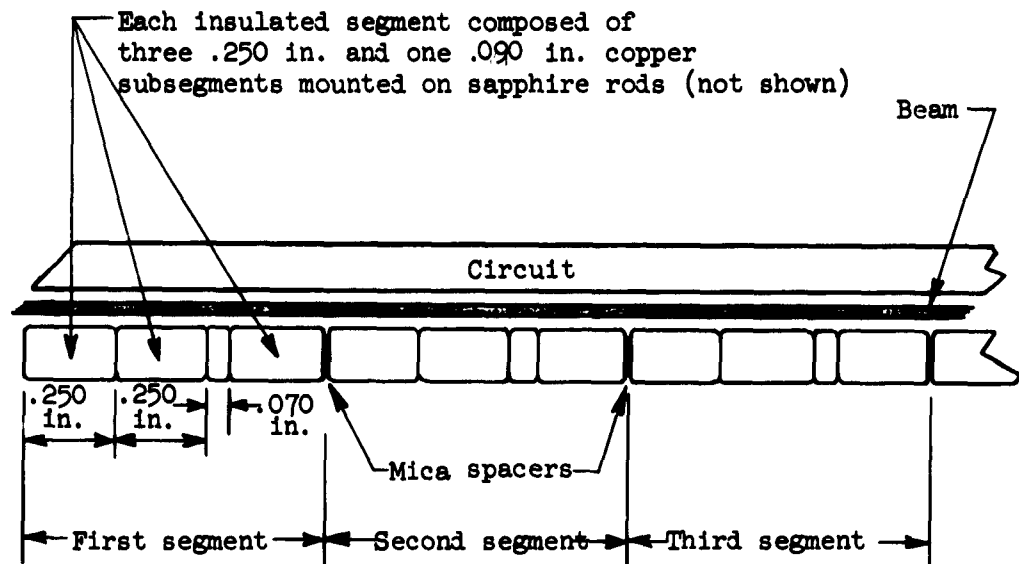
### AMPLIFICATION AND ATTENUATION OF DC CYCLOTRON WAVES BY MEANS OF A PERIODIC PERTURBATION IN TRANSVERSE ELECTRIC FIELD

In this appendix we shall examine the effects on an M-type crossed-field beam of small periodic perturbations in the applied transverse electric field. In making measurements with the segmented sole (Chapter V), under certain conditions growth or decay in the amplitude of cyclotron undulations on the beam was noted. It has been shown that the M-type beam is not subject to dc instabilities as is the hollow beam, consequently such behavior must be the result of the action of external fields on the beam. We will show how these observations may be explained on the basis of a type of dc pumping which results from periodic perturbations in the applied electric field, provided that such perturbations have a periodicity approximately equal to  $\lambda_c$  and occur over a distance small compared to  $\lambda_c$ . With these conditions satisfied it is then possible to either excite or damp out beam undulations, depending on the relative phasing of the applied fields and the beam.

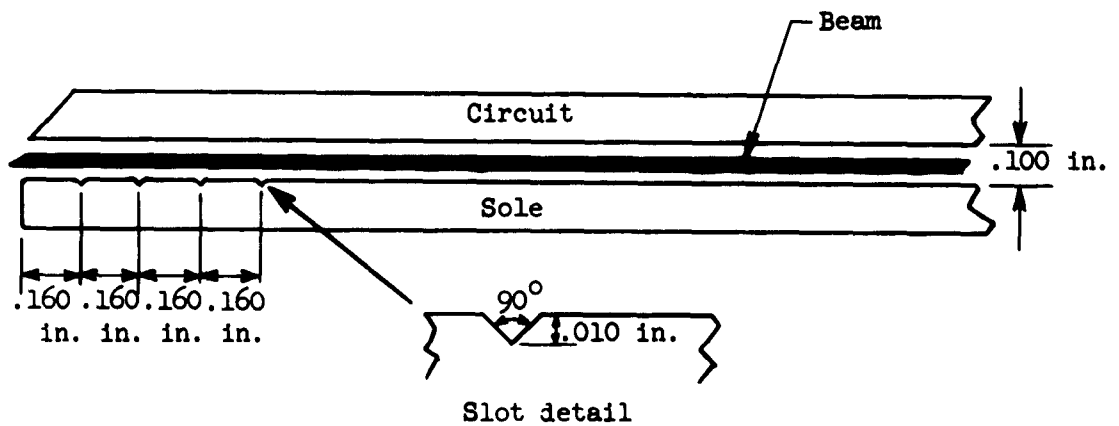
#### 1. Summary of Experiments

The geometry of the segmented sole structure is shown in Fig. D.1a. The details of this structure have already been discussed in conjunction with the long gun experiments in Chapter V. The important point to be noted is that small grooves or slots exist at the sole surface where the short segments which make up the longer insulated segments are in contact. These grooves result from a slight radius ( $\sim .0005"$ ) at the edges of the short segments which were incurred during fabrication. These grooves are clearly seen in the photograph in Fig. 5.2. On the basis of the experiments to be described below, we have concluded that the fields from these small slots are responsible for the anomalous behavior which was observed.

In making the transmission measurements with this structure, anomalies both in sole current and in the visual appearance of the beam were noted when  $\lambda_c$  of the beam was approximately .250 in. With  $\lambda_c$  slightly smaller than this value the amplitude of the cyclotron undulations on the beam was observed to increase with distance along the drift region,



a. Segmented sole structure.



b. Slotted sole.

FIG. D.1--Geometry of the segmented sole and the slotted sole.

while for  $\lambda_c$  slightly larger than .250 in. such undulations decreased in magnitude with increasing distance from the gun. In measuring sole current as a function of the beam cyclotron wavelength, curves similar to those shown in Figs. 5.36 and 5.37 were obtained except that  $I_s$  was found to decrease more irregularly with increasing  $\lambda_c$ , particularly near the value of  $\lambda_c = .250$  in. A peak in sole current was found to correspond to growing cyclotron undulations, and an abrupt decrease in  $I_s$  was noted when  $\lambda_c$  was increased sufficiently to observe damped undulations (this behavior is clearly illustrated in Fig. D.3)

Upon replacing the segmented sole with a continuous plate, none of these phenomena was observed. However, when four grooves were cut onto the first portion of this smooth sole as shown in Fig. D.1b, similar anomalous results were obtained with  $\lambda_c$  of the beam approximately equal to .160 in., the spacing between the slots. Figure D.2 shows two photographs of the beam, illustrating growing and damped cyclotron undulations. These photographs show the sole and circuit electrodes and the position of the four slots in relation to the beam. Note in (a) where the beam undulations exhibit growth that the portions of the beam in the slot fields have negative slope, while in (b) where the undulations are damped out the portions of the beam in the slot fields have positive slope.

Figure D.3 shows a comparison of normalized sole current as a function of the drift region scaling parameter for the slotted and the smooth sole. These data were obtained with otherwise identical geometries, magnetic field and applied voltages. For these data it should be noted that  $\lambda_c = .160$  in. corresponds to a sole-circuit potential difference of 1050 V which is approximately where the points taken with the slotted sole begin to deviate from those obtained with the smooth sole.

From these results we concluded that the small periodic perturbations in the transverse electric field provided by the slots are capable of substantially altering the dc characteristics of the beam. Each of the slot fields acts as a lens which causes the beam to change direction as it passes through the field. In order for the effect to be cumulative over a series of such perturbations, the periodicity of the slots must be sufficiently close to  $\lambda_c$  so that all of the slot fields act on alternate half wavelengths of the beam. We shall now use an approximate





(a). Amplification



(b). Damping

FIG. D.2--Photographs illustrating amplification and damping of dc cyclotron undulations by means of periodic perturbations in the transverse electric field.

paraxial analysis to calculate the amount the beam is deviated in passing through the field of a single slot. For small deviations the effect of several slots can be then obtained approximately by linear superposition. As it is primarily an order of magnitude calculation, this analysis is only intended to show that the fields from such small slots in the sole can account for the observed phenomena.

## 2. Analysis

Next we wish to examine the effect on a thin crossed-field beam of a narrow slot in the sole. Consider the geometry shown in Fig. D.4a. In order to be able to use a simple analytic expression for the slot field and potential we will analyze the configuration shown where the sole is a thin conducting sheet and the slot is of length  $2a$ . The sole circuit spacing  $d$  is assumed to be large compared with both  $a$  and  $\delta$ , the beam thickness, and in addition both  $a$  and  $\delta$  are assumed to be small compared with  $\lambda_c$ .

We may obtain the potential and fields in this configuration by means of a conformal transformation. The imaginary part of the complex potential

$$W = \frac{1}{2} |E_0| (z + \sqrt{z^2 - a^2}) \quad (D.1)$$

gives the potential for the geometry shown in Fig. D.4b in the upper half plane. A sheet conductor is located along the real axis for  $-\infty < x < -a$  and  $a < x < \infty$ . The term  $E_0$  represents a uniform field (in the  $-y$  direction) present when  $a = 0$ . Before deflection the beam is assumed to be a distance  $y_0$  above the plane of the sole. We then have

$$\phi = \frac{|E_0|}{2} \text{Im} (z + \sqrt{z^2 - a^2}) \quad (D.2)$$

and

$$E_y = -\frac{|E_0|}{2} \text{Re} \left( \frac{\partial W}{\partial z} \right) = -\frac{|E_0|}{2} \text{Re} \left( 1 + \frac{z}{\sqrt{z^2 - a^2}} \right) \quad (D.3)$$

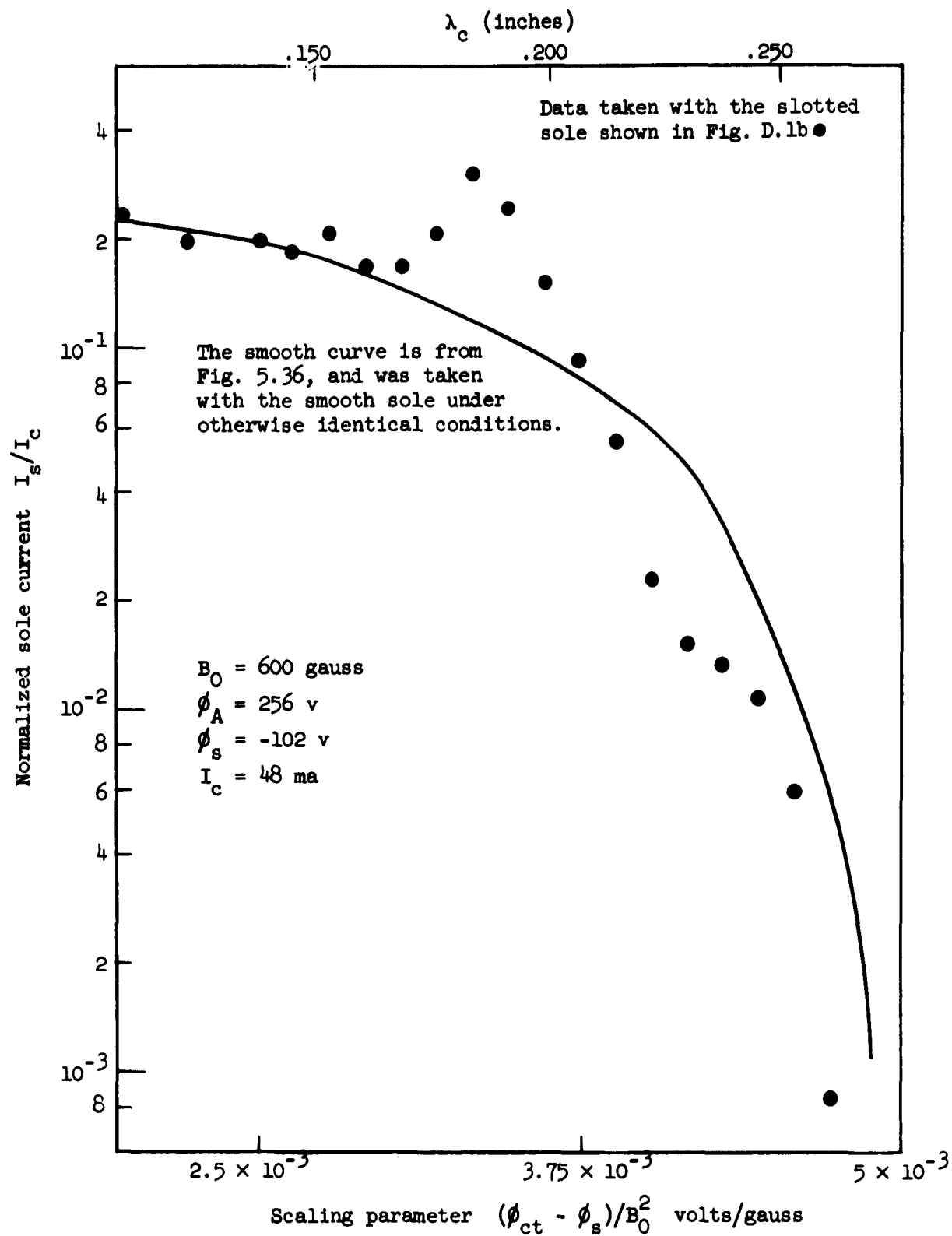
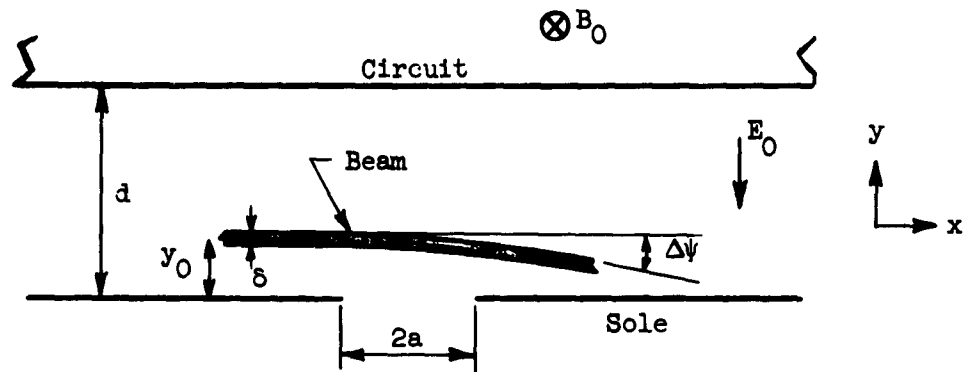
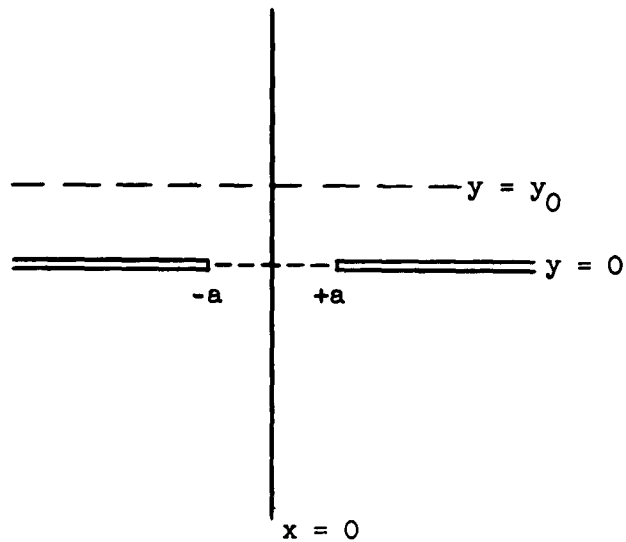


FIG. D.3--Comparison of normalized sole current as a function of the scaling parameter for the smooth and slotted sole plates.



a. Configuration of the paraxial analysis.



b. Geometry for the complex potential of Eq. (D.1).

FIG. D.4--Geometries for the paraxial analysis.

For the field and potentials due to the slot, we may write

$$\phi_1 = \phi - \phi_0 \quad (\text{D.4a})$$

$$E_1 = E_y - E_0, \quad (\text{D.4b})$$

where  $\phi_0$  is the potential for  $a = 0$ . We then have

$$\phi_1 = \frac{|E_0|}{2} \operatorname{Im} (-z + \sqrt{z^2 - a^2}) , \quad (\text{D.5a})$$

and

$$E_1 = -\frac{|E_0|}{2} \operatorname{Re} \left( -1 + \frac{z}{\sqrt{z^2 - a^2}} \right) . \quad (\text{D.5b})$$

The ballistic equations for the beam are

$$\dot{x} = \eta E_x + \omega_c \dot{y}$$

$$\dot{y} = \eta E_y - \omega_c \dot{x} . \quad (\text{D.6a})$$

From conservation of energy we have

$$\dot{x}_0^2 + \dot{y}_0^2 = -2\eta\phi_0 . \quad (\text{D.7})$$

Here  $\dot{x}_0$ ,  $\dot{y}_0$  and  $\phi_0$  are the unperturbed velocity components and beam potential in the absence of the slot. Taking the first order perturbation of this equation to obtain the effect of the slot on the beam, we have (denoting perturbed quantities by subscript 1),

$$2\dot{x}_0\dot{x}_1 + 2\dot{y}_0\dot{y}_1 = -2\eta\phi_1 + 2\eta E_0 y_1 .$$

We shall ignore the second term on the left since  $\dot{y}_0$  is assumed to be small. We then have

$$\dot{x}_1 = -\frac{\eta\phi_1}{\dot{x}_0} + \frac{\eta E_0 y_1}{\dot{x}_0} . \quad (\text{D.8})$$

The y ballistic equation for the perturbed quantities is then

$$\ddot{y}_1 + \omega_c y_1 = \eta E_1 - \frac{\omega_c^2}{|E_0|} \phi_1, \quad (D.9)$$

which may be written as

$$\dot{x}_0 \frac{d\dot{y}_1}{dx} + \omega_c y_1 = \eta E_1 - \frac{\omega_c^2}{|E_0|} \phi_1. \quad (D.10)$$

From this equation we may find the integrated value of  $\dot{y}_1$  in going through the slot field. By integrating Eq. (D.10) along the contour  $y = y_0$  we have

$$\dot{x}_0 \int \frac{d\dot{y}_1}{dx} dx + \omega_c \int y_1 dx = \eta \int E_1 dx - \frac{\omega_c^2}{|E_0|} \int \phi_1 dx.$$

We furthermore assume that  $y_1 = \text{constant} = 0$  in the region in which the beam is influenced by the slot. We then obtain, for  $\Delta\dot{y}_1$ , the change in transverse velocity of the beam caused by the slot

$$\Delta\dot{y}_1 = \frac{\eta}{\dot{x}_0} \int E_1 dx - \frac{\omega_c^2}{\dot{x}_0 |E_0|} \int \phi_1 dx. \quad (D.11)$$

We next examine the two integrals  $\int E_1 dx$  and  $\int \phi_1 dx$  along  $y = y_0$ , where the limits of integration are  $\pm \infty$ . The contribution of the first of these integrals is zero, for if  $W_1 = \psi_1 + j\phi_1$ , then  $E_1 = \partial\phi_1/\partial y = \partial\psi_1/\partial x$  as a result of the Cauchy-Rieman equations. Then along the contour  $y = y_0$ , we find

$$\int_{-\infty}^{\infty} \frac{\partial\phi_1}{\partial y} dx = \int_{-\infty}^{\infty} \frac{\partial\psi_1}{\partial x} dx = 0 \quad (D.12)$$

since both real and imaginary parts of  $W_1$  vanish on  $y = y_0$  for sufficiently large positive and negative values of  $x$ . But since  $\int_{-\infty}^{\infty} E_1 dx = 0$ , it follows that  $\int_{-\infty}^{\infty} \phi_1 dx$  must be independent of the value<sup>(25)</sup>

---

<sup>(25)</sup> Note that this result implies that the deviation of the beam is independent of the distance of the beam from the slot as long as  $y_0 \ll \lambda_c$ .

of  $y_0$ , thus we may integrate along the contour  $y = 0$  from  $-a$  to  $+a$ . We then obtain

$$\int_{-a}^a \phi_1 dx = \frac{|E_0|}{2} \operatorname{Im} \int_{-a}^a (-x + \sqrt{x^2 - a^2}) dx, \quad (D.13)$$

which evaluates to

$$\int_{-a}^a \phi_1 dx = + \frac{|E_0| \pi a^2}{4}. \quad (D.14)$$

We then have

$$\Delta \dot{y} = - \frac{\omega_c^2 \pi a^2}{4 \dot{x}_0}. \quad (D.15)$$

The beam is therefore deflected through an angle  $\Delta \psi$  which is given by the expression

$$\Delta \psi = \frac{\Delta \dot{y}}{\dot{x}_0} = - \frac{\omega_c^2 \pi a^2}{4 \dot{x}_0^2}. \quad (D.16)$$

To first order, the amplitude of the beam cyclotron undulations is changed by an amount  $2\Delta r$ , where  $\Delta r$  is given by

$$\Delta r = \frac{\dot{x}_0 \Delta \psi}{\omega_c} = \frac{\omega_c \pi a^2}{4 \dot{x}_0}. \quad (D.17)$$

The sign of  $\Delta r$  depends on the phasing of the slot with respect to the beam. The effect of the slot field is always to turn the beam towards the sole, thus if a slot acts on an element of beam with positive slope, the magnitude of the slope is decreased and  $\Delta r$  is negative; however, if the beam has a negative slope at the slot the magnitude of the slope is increased and  $\Delta r$  is positive.

We may evaluate  $\Delta r$  from the following set of typical experimental conditions:

$$\begin{aligned}\omega_c &= 1.06 \times 10^{10} \\ a &= 2.54 \times 10^{-4} \text{ m} \\ \dot{x}_0 &= 7.9 \times 10^6 \text{ m sec}^{-1} \quad .\end{aligned}$$

Then we have  $2\Delta r = 1.36 \times 10^{-4} \text{ m} = .0054 \text{ in.}$

These parameters are approximately 1/10 of the photograph shown in (D.2a). From a direct measurement from the photograph, noting that the sole circuit spacing is .100 in., we find that the effect of the four slots is to increase the amplitude of the beam cyclotron undulation by roughly .020 in., thus despite the approximations in the analysis, the results are seen to be in reasonable agreement with the observations.



# LIST OF REFERENCES

1. E. Benham, "Electronic Theory and the Magnetron Oscillator," Proc. Phys. Soc. (London) 47, 1-53 (January 1935).
2. L. Brillouin, "Electronic Theory of the Plane Magnetron," Advances in Electronics 3, 85-141 (1951).
3. P. T. Kirstein, "On the Determination of the Electrodes Required to Produce a Given Electric Field Distribution Along a Prescribed Curve," Proc. IRE 46, 1716-1722 (October 1958).
4. R. J. Loman, "Exact Electrode System for the Formation of an Electron Beam," Brit. J. Elect. and Contr. 3, 367-374 (September 1957).
5. R. W. Gould, "A Field Analysis of the M-Type Backward Wave Oscillator," Technical Report No. 3, Electron Tube and Microwave Laboratory, California Institute of Technology, Pasadena, California (September 1955).
6. G. G. MacFarlane and H. G. Hay, "Wave Propagation in a Slipping Stream of Electrons: Small Amplitude Theory," Proc. Phys. Soc. 63, Sect. 6-B, 407-427 (1950).
7. J. C. Slater, Microwave Electronics, (Van Nostrand, New York, 1950).
8. M. H. Miller, "Study of High Temperature Electrons Originating in Streams Flowing in Crossed dc Electric and Magnetic Fields," Technical Report No. 26, Electron Tube Laboratory, University of Michigan Research Institute, University of Michigan, Ann Arbor, Michigan (July 1958).
9. W. E. Waters, "Paraxial Properties of Crossed-Field Electron Sheet Beams," Microwave Laboratory Report No. 603, Stanford University, Stanford, California (May 1959).
10. L. Brillouin, "A Theorem of Larmor and Its Importance for Electrons in Magnetic Fields," Phys. Rev., Series 2, 67, 260-266 (April 1945).
11. J. R. Pierce, "Instability of Hollow Beams," IRE Trans. PGED ED-3, 183-189 (October 1956).
12. H. Alfven, L. Lindberg, K. G. Malfors, T. Wallmark, and E. Åström, "Theory and Application of Trochotrons," Trans. Roy. Inst. Techn. (Stockholm), No. 22 (1948).
13. P. Guénard and H. Huber, "Étude expérimentale de l'interaction par ondes de charge d'espace au sein d'un faisceau électronique se déplaçant dans des champs électrique et magnétique croisés," Annales de Radio-electricité 7, 252-273 (October 1952).

14. R. P. Little, H. M. Ruppel, and S. T. Smith, "Beam Noise in Crossed Electric and Magnetic Fields," J. Appl. Phys. 29, 1376-1377 (September 1958).
15. J. Dain and I. A. D. Lewis, "Adiabatic Theory of an Electron Gun for Crossed-Field Devices," Proc. Phys. Soc. 67, Sect. B, 449-455 (1956).
16. M. H. Miller and R. W. Larson, Report No. 2854, 3-P, University of Michigan Research Institute, University of Michigan, Ann Arbor, Michigan (June 1958).
17. O. Doehler, "Static Characteristics of Injection Crossed-Field Tubes," in Crossed Field Microwave Devices, Vol. I, ed. by E. Okress, (Academic Press, New York, 1961).
18. B. Epsztein, "Effets de la Charge D'espace sur les Faisceaux Electroniques Minces," Ph.D. Thesis, University of Paris (1957).
19. B. Wightman, "An Investigation of the Magnetron Amplifier," Technical Report No. 52, Stanford Electronics Laboratories, Stanford University, Stanford, California (February 1959).
20. T. Van Duzer, "Noise in Crossed Field Beams," Institute of Engineering Research Report Series No. 60, Issue No. 280, University of California, Berkeley, California (May 1960).
21. R. H. Bartram and M. C. Pease, "Theory of a Space-Charge Limited Crossed-Field Gun," Sylvania Technologist 11, No. 2 (1958).
22. H. Poritsky and R. P. Jerrard, "An Integrable Case of Electron Motion in Electric and Magnetic Fields," J. Appl. Phys. 23, 928-930 (August 1952).
23. O. L. Hoch and D. A. Watkins, "A Gun and Focusing System for Crossed-Field Traveling Wave Tubes," IRE Trans. PGED ED-6, 18-27 (January 1959).
24. J. R. Pierce, Theory and Design of Electron Beams, (Van Nostrand, New York, 1954).
25. J. R. Pierce, "Rectilinear Flow in Electron Beams," J. Appl. Phys. 11, 548-554 (1940).
26. G. S. Kino, "A New Type of Crossed-Field Gun," IRE Trans. PGED ED-7, 179-185 (July 1960).

27. G. S. Kino, "A New Type of Crossed-Field Electron Gun," in Crossed Field Microwave Devices, Vol. I, ed. by E. Okress, (Academic Press, New York, 1961).
28. G. A. Haas and J. T. Jensen, "Use of Oxide Cathodes in Demountable Vacuum Systems," R.S.I., 28, 1007-1010 (December 1957).
29. O. Buneman, "Generation and Amplification of Waves in Dense Charged Beams Under Crossed Fields," Nature 165, 474-76 (March 1950).
30. H. Heffner and T. Unotoro, "Growing Waves in Electron Streams in Crossed Electric and Magnetic Fields," Technical Report No. 14, Stanford Electronics Laboratories, Stanford University, Stanford, California (February 1957).
31. J. R. Anderson, "Experimental Investigation of Large-Signal Traveling-Wave Magnetron Theory," Institute of Engineering Research Report Series No. 60, Issue No. 314, University of California, Berkeley, California (September 1960).
32. I. Langmuir and H. Mott-Smith, "Studies of Electric Discharges in Gases at Low Pressure: Part I," Gen. Elec. Rev. 27, 449-455 (July 1924).
33. B. Epsztein and D. Maillart, "Research and Development, Crossed E-H Field Microwave Tubes," QK603 Final Engineering Report, Raytheon Mfg. Co., Waltham, Massachusetts, (July 1958).
34. J. R. Anderson, "Noise Measurements in an M-type Backward Wave Amplifier," Proc. IRE 48, 946-947 (May 1960).
35. O. Buneman, "Ribbon Beams," Brit. J. Elect. and Contr. 3, 507-508 (November 1957).

# DISTRIBUTION LIST

Contract AF 19(604)-1930

<u>Code</u>	<u>Organization</u>	<u>No. of copies</u>
AF 5	AFMTC (AFMTC Tech Library - MU-135) Patrick AFB, Florida	1
AF 18	AUL Maxwell AFB, Alabama	1
AF 43	ASD (ASAPRD-Dist) Wright-Patterson AFB, Ohio	1
AF 91	AFOSR (SRGL) Washington 25, D. C.	1
AF 124	RADC (RAYLD) Griffiss AFB, New York Attn: Documents Library	1
AF 139	AF Missile Development Center (MDGRT) Holloman AFB, New Mexico	1
AF 318	ARL (Technical Library) Building 450 Wright-Patterson AFB, Ohio	1
AR 5	Commanding General USASRDL Ft. Monmouth, N. J. Attn: Tech. Doc. Ctr. SIGRA/SL-ADT	1
Ar 9	Department of the Army Office of the Chief Signal Officer Washington 25, D. C. SIGRD-4a-2	1
Ar 50	Commanding Officer Attn: ORDTL-012 Diamond Ordnance Fuze Laboratories Washington 25, D. C.	1
Ar 67	Army Rocket and Guided Missile Agency Redstone Arsenal, Ala. Attn: ORDXR-OTL, Technical Library	1
G 2	ASTIA (TIPAA) Arlington Hall Station Arlington 12, Virginia	10
G 68	National Aeronautics and Space Agency 1520 H. Street, N. W. Washington 25, D. C. Attn: Library	1

<u>Code</u>	<u>Organization</u>	<u>No. of Copies</u>
G 109	Director Langley Research Center National Aeronautics and Space Administration Langley Field, Virginia	1
M 6	AFCRL, OAR (CRIPA - Stop 39) L. G. Hanscom Field Bedford, Massachusetts	10
M 78	AFCRL, OAR (CRT, Dr. A. M. Gerlach) L. G. Hanscom Field Bedford, Massachusetts	1
N 1	Director, Avionics Division (AV) Bureau of Aeronautics Department of the Navy Washington 25, D. C.	2
N 29	Director (Code 2027) U. S. Naval Research Laboratory Washington 25, D. C.	2
I 292	Director, USAF Project RAND The Rand Corporation 1700 Main Street, Santa Monica, California Thru: A. F. Liaison Office	1
AF 127	Boston Office-Patents & Royalties Division (Hq AFLC) Building 133, 424 Trapelo Road Waltham 54, Massachusetts	1
AF 253	Technical Information Office European Office, Aerospace Research Shell Building, 47 Cantersteen Brussels, Belgium	1
Ar 107	U.S. Army Aviation Human Research Unit U.S. Continental Army Command P.O. Box 438, Fort Rucker, Alabama Attn: Maj. Arne H. Eliasson	1
G 8	Library Boulder Laboratories National Bureau of Standards Boulder, Colorado	2
M 63	Institute of the Aerospace Sciences, Inc. 2 East 64th Street New York 21, New York Attn: Librarian	1
N 73	Office of Naval Research Branch Office, London Navy 100, Box 39 F. P. O. New York, N. Y.	10

<u>Code</u>	<u>Organization</u>	<u>No. of Copies</u>
U 32	Massachusetts Institute of Technology Research Laboratory of Electronics Building 26, Room 327, Cambridge 39, Massachusetts Attn: John H. Hewitt	1
U 431	Alderman Library University of Virginia Charlottesville, Virginia	1
	Dr. Glen Wade, Spencer Laboratories Burlington, Mass.	1
	Mr. Charles Turner 528 Kenton Road, Kenton, Harrow Middlesex, England	1
	Electronics Laboratories General Electric Company Electronics Park Syracuse, New York Attn: Mr. Henry Grimm	1
	Dr. Yen, Department of Electrical Engineering University of Toronto Toronto 5, Ontario, Canada	1
	Matthew A. Allen, Microwave Associates, Inc. Burlington, Massachusetts	1
AF 247	WADD (WCLKTR) Wright-Patterson AFB, Ohio	1
AF 329	Hq. ARDC (RDR-62) Reference 4619-Ca Andrews AFB, Washington 25, D.C.	2
Ar 103	Commanding Officer U.S. Army Signal Research & Development Lab. Fort Monmouth, New Jersey Attn: SIGFM/El-PRG	1
G 112	Oak Ridge National Laboratory P.O. Box X Oak Ridge, Tennessee Attn: Central Research Laboratory	1
1 774	Lenkurt Electric Company, Inc. 1105 Country Road San Carlos, California Attn: D. Mawdsley, Mail Stop 85	1
I 775	Radio Research Laboratories Kokubunki, P. O. Tokyo, Japan	1
I 925	Hughes Aircraft Company P. O. Box 278 Newport Beach, California Attn: Miss Eileen D. Andjulis Assistant Librarian	1

<u>Code</u>	<u>Organization</u>	<u>No. of Copies</u>
I 943	General Telephone & Electronics Laboratories, Inc. 1015 Corporation Way Palo Alto, California Attn: Librarian	1
I 944	Bomac Laboratories, Inc. Salem Road Beverly, Massachusetts Attn: Mr. Arthur McCoubrey, Manager Research and Development	1
I 954	S. F. D. Laboratories, Inc. 800 Rahway Avenue Union, New Jersey Attn: R. Ullrich, Librarian	1
I 988	Institute of Defense Analysis Research and Engineering Support Division 1825 Connecticut Avenue, N.W. Washington 9, D. C. Attn: Technical Information Office	1
U 10	Cornell University School of Electrical Engineering Ithaca, New York Attn: Prof. B. C. Dalman	1
U 238	University of Southern California University Park Los Angeles 7, California Attn: Z. A. Kaprielian Associate Professor of Electrical Engineering	1
U 290	Dr. A. L. Cullen Department of Electrical Engineering University of Sheffield Sheffield 1, England	1
U 358	University of Arizona Tucson 25, Arizona Attn: Prof. Donald C. Stinson Electrical Engineering Department	1
U 359	The University of British Columbia Department of Electrical Engineering Vancouver 8, B. C. Canada Attn: G. B. Walker Microwave Laboratory	1
U 391	University of Illinois Electrical Engineering Research Laboratory Urbana, Illinois Attn: Professor P. D. Coleman Ultramicrowave Group	1

<u>Code</u>	<u>Organization</u>	<u>No. of Copies</u>
U 430	Chalmers University of Technology Gibraltargatan 5 G Gothenburg, Sweden Attn: Mr. H. Wilhelmsson Research Laboratory of Electronics	1
G 70	Advisory Group on Electron Devices (AGED) Office of the Director of Defense Res and Eng. 346 Broadway, 8th Floor New York 13, New York	2
N 160	U. S. Naval Research Laboratory Washington 25, D. C. Attn: Mr. F. J. Liberatore, Code 7420	1
I 13	Bell Telephone Laboratories, Inc. Whippany Laboratory Whippany, New Jersey Attn: Technical Information Library	2
I 53	Hughes Aircraft Company Florence Avenue and Teale Street Culver City, California Attn: Documents Section Research and Development Library	1
I 96	Sandia Corporation Sandia Base, P.O. Box 5800 Albuquerque, New Mexico Attn: Mrs. B. R. Allen, Librarian	1
I 237	Technical Library G. E. TWT Product Section 601 California Avenue Palo Alto, California Attn: Verna Van Velzer, Librarian	1
I 260	Sylvania Elec. Prod. Inc. Electronic Defense Laboratory P. O. Box 205, Mountain View, California Attn: Library	1
I 266	ITT Federal Laboratories Technical Library 500 Washington Avenue Nutley 10, New Jersey	1
I 297	Sperry Gyroscope Company Division of Sperry Rand Corporation Great Neck, N. Y. Attn: Mrs. Florence W. Turnbull Engineering Librarian	1
I 305	General Electric Company Power Tube Dept. Electric Components Division Building 269, Room 205 One River Road Schenectady, 5, New York	1



<u>Code</u>	<u>Organization</u>	<u>No. of Copies</u>
I 306	General Telephone and Electronics Laboratories, Inc. Bayside Laboratories Bayside 6, New York Attn: Mr. D. Lazare Manager, Project Adm.	1
I 309	Litton Industries, Inc. 960 Industrial Road San Carlos, California Attn: Document Custodian, Engr. Dept.	1
I 310	Varian Associates 611 Hansen Way Palo Alto, California Attn: Dr. Richard B. Nelson	1
I 312	STL Technical Library Document Acquisitions Space Technology Laboratories, Inc. P.O. Box 95001 Los Angeles 45, California	1
I 366	Radio Corporation of America Defense Electronic Products Camden, New Jersey Attn: Mr. S. Schach, Building 10-5 Standards Engineering, Section 577	1
I 367	Stanford Research Institute Document Center Menlo Park, California Attn: Acquisitions	1
I 382	RCA Laboratories David Sarnoff Research Center Princeton, New Jersey Attn: Dr. Harwick Johnson	1
I 384	Bell Telephone Laboratories Murray Hill Laboratory Murray Hill, New Jersey Attn: Dr. J. R. Pierce	2
I 435	General Electric Company P.O. Box 1088 Schenectady, New York Attn: Mr. E. D. McArthur, Manager Superpower Microwave Tube Laboratory	1
I 450	Bell Telephone Laboratories, Inc. Murray Hill, New Jersey Attn: J.W. Fitzwilliam, Director Electron Tube Development	1
I 547	The Rand Corporation 1700 Main Street Santa Monica, California Attn: Technical Librarian	1

<u>Code</u>	<u>Organization</u>	<u>No. of Copies</u>
I 562	Philips Laboratories A Division of North American Philips Company, Inc. Irvington on Hudson, New York Attn: William P. Arnett Security Officer	1
I 577	Raytheon Manufacturing Company 520 Winter Street Waltham, Mass. Attn: Mr. O.T. Fundingsland	1
I 594	Research Technology Associates, Inc. 100 Ladge Drive Electronic Park at Avon Avon, Mass. Attn: J. Babakian	1
I 595	Gianninni Research Santa Ana, California Attn: J.K. Hagele Technical Librarian	1
I 666	Ramo-Wooldridge A Division of Thompson Ramo-Wooldridge Inc 8433 Fallbrook Avenue Ganoga Park, California Attn: Technical Information Services	1
I 756	Varian Associates 611 Hansen Way Attn: Mr. C. W. McClelland Technical Publications Manager	1
I 759	Stanford Research Institute Menlo Park, California Attn: Mr. C. J. Cook	1
I 760	General Atomic, Div. of General Dynamics Corporation P.O. Box 608, San Diego, California Attn: Mr. M. Rosenbluth	1
I 761	Linfield Research Institute McMinnville, Oregon Attn: Dr. W.P. Dyke, Director	1
I 762	Columbia Radiation Laboratory 538 West 120th Street New York 27, New York	1
I 763	Sperry Gyroscope Company Engineering Library Mail Station C-39 Great Neck, Long Island, New York	1
I 764	Watkins-Johnson Company 3333 Hillview Avenue Palo Alto, California Attn: Dr. H. R. Johnson	1

<u>Code</u>	<u>Organization</u>	<u>No. of Copies</u>
I 765	Westinghouse Electric Corporation Friendship International Airport Box 746, Baltimore 3, Maryland Attn: G. Ross Kilgore, Manager Applied Research Department Baltimore Laboratory	1
I 766	Services Electronic Research Laboratories Baldock, Herts, England Attn: Dr. Boot	1
I 767	Standard Telephone Laboratories Harlow, Essex, England Attn: Dr. E. A. Ash	1
I 768	Eitel-McCullough, Inc. 798 San Mateo Avenue San Bruno, California Attn: Librarian	1
I 769	Hewlett-Packard Company 275 Page Mill Road Palo Alto, California	1
I 770	Hughes Aircraft Company Research and Development Laboratories Culver City, California Attn: L.M. Field	1
I 999	Raytheon Company Box 171, Wayland, Massachusetts Attn: E. Rolfe	1
I 771	Advanced Kinetics Inc. P.O. Box 1803 Newport Beach, California Attn: Dr. R. Wanick	1
I 772	RCA Laboratories Princeton, New Jersey Attn: Harwell Johnson	1
I 844	Bomac Laboratories, Inc. 8 Salem Road Beverly, Massachusetts Attn: Dr. Arthur McCoubrey, Manager Research and Development	1
U 2	California Institute of Technology Jet Propulsion Laboratory Pasadena 4, California Attn: Documents Library	1
U 21	The Johns Hopkins University Department of Physics Homewood Campus Baltimore 18, Maryland Attn: Dr. Donald E. Kerr	1

<u>Code</u>	<u>Organization</u>	<u>No. of Copies</u>
U 26	Massachusetts Institute of Technology Lincoln Laboratory P.O. Box 73 Lexington 73, Mass. Attn: Mary A. Granese, Librarian	1
U 40	New York University Department of Physics College of Arts and Science Washington Square, New York 3, N.Y. Attn: Professor J. H. Rohrbaugh	1
U 42	The Ohio State University 2024 Neil Avenue Columbus 10, Ohio Attn: Prof. E. M. Boone Department of Electrical Engineering	1
U 59	Library Georgia Technology Research Institute, Engineering Experiment Station 722 Cherry Street, N.W. Atlanta, Georgia Attn: Mrs. J.H. Crosland, Librarian	1
U 79	University of Michigan Engineering Research Institute Radiation Laboratory Attn: Prof. K.M. Siegel 912 N. Main Street Ann Arbor, Michigan	1
U 100	University of California Electronics Research Lab. 332 Cory Hall, Berkeley 4, California Attn: J.R. Whinnery	1
U 102	Harvard University Technical Reports Collection Gordon McKay Library 303A Pierce Hall Oxford Street Cambridge 38, Mass. Attn: Librarian	1
U 107	University of Michigan Electronic Defense Group Engineering Research Institute Ann Arbor, Michigan Attn: J.A. Boyd, Supervisor	1
U 114	University of California 390 Cory Hall Berkeley 4, California Attn: Dr. Charles Susskind	1

<u>Code</u>	<u>Organization</u>	<u>No. of Copies</u>
U 150	University of Washington Department of Electrical Engineering Seattle 5, Washington Attn: Mr. A.E. Harrison	1
U 168	The George Washington University Department of Electrical Engineering School of Engineering Washington 6, D.C. Attn: Dr. N.T. Grisamore, Exec. Officer	1
U 169	Illinois Institute of Technology 3301 S. Dearbon Street Chicago 16, Illinois Attn: Dr. George I. Cohn	1
U 209	New York University College of Engineering 346 Broadway New York, N.Y. Attn: Mr. L.S. Schwartz, Research Division	1
U 228	University of Kansas Electrical Engineering Department Lawrence, Kansas Attn: Dr. H. Unz	1
U 237	Polytechnic Institute of Brooklyn Microwave Research Institute 55 Johnson Street Brooklyn, New York Attn: Dr. N. Marcuvitz	1
U 240	Illinois Institute of Technology Technology Center Department of Electrical Engineering Chicago 16, Illinois Attn: Paul C. Yuen Electronics Research Laboratory	1
U 284	Dr. J.T. Senise Instituto Tecnológico de Aeronautica São José dos Campos São Paulo, Brazil	1
U 288	Polytechnic Institute of Brooklyn Microwave Research Institute 55 Johnson Street Brooklyn 1, New York	1
U 292	University of Maryland College Park, Maryland Attn: Dr. J.M. Burgers	1
U 294	University of Illinois Electrical Engineering Research Laboratory Urbana, Illinois Attn: Dr. A.A. Dougal	1

<u>Code</u>	<u>Organization</u>	<u>No. of Copies</u>
U 308	Brandeis University Waltham, Mass. Attn: Dr. E.P. Gross	1
U 320	California Institute of Technology 1201 East California Street Pasadena, California Attn: Prof. R.W. Gould	1
U 321	University of California Radiation Laboratory Livermore, California Attn: N. Christofilos	1
U 322	University of California Radiation Laboratory Livermore, California Attn: S.A. Colgate	1
U 323	University of California Radiation Laboratory Livermore, California	1
U 324	Princeton University Princeton, New Jersey Attn: L. Spitzer Project Matterhorn	1
U 325	Massachusetts Institute of Technology 77 Massachusetts Avenue Cambridge, Mass. Attn: W.P. Allis	1
U 326	University of California Electrical Engineering Department Berkeley 4, California Attn: Prof. J.R. Singer	1
U 327	University of California Radiation Laboratory Berkeley, California Attn: Dr. R.K. Wakerling Information Division, Building 50, Room 128	1
U 328	University of Chicago Institute of Air Weapons Research Museum of Science and Industry Chicago 37, Illinois Attn: Mrs. Norma Miller, Technical Librarian	1
U 329	University of Florida Department of Electrical Engineering Gainesville, Florida Attn: Prof. W.E. Lear	1
U 330	University of Illinois Control Systems Laboratories Urbana, Illinois Attn: Prof. Daniel Alpert	1

<u>Code</u>	<u>Organization</u>	<u>No. of Copies</u>
U 331	University of Illinois Department of Electrical Engineering Urbana, Illinois Attn: Prof. L. Goldstein	1
U 332	University of Illinois Department of Physics Urbana, Illinois Attn: Dr. John Bardeen	1
U 333	John Hopkins University Radiation Laboratory Baltimore 2, Maryland Attn: J.M. Minkowski	1
U 334	Iowa State University Physics Department Iowa City, Iowa Attn: Professor Frank MacDonald	1
U 335	University of Colorado Department of Electrical Engineering Boulder, Colorado Attn: Professor W.G. Worcester	1
U 337	McMurray College Department of Physics Abilene, Texas Attn: Dr. Virgil E. Bottom	1
U 338	University of Michigan 3506 East Engineering Building Ann Arbor, Michigan Attn: Electron Tube Laboratory	1
U 339	University of Minnesota Institute of Technology Department of Electrical Engineering Minneapolis, Minnesota Attn: Prof. A. van der Ziel	1
U 340	Ohio University College of Applied Science Athens, Ohio Attn: D.B. Green	1
U 341	Oregon State College Department of Electrical Engineering Corvallis, Oregon Attn: H.J. Oorthuys	1
U 342	Princeton University Department of Electrical Engineering Princeton, New Jersey	1
U 343	Purdue University Research Library Lafayette, Indiana Attn: Electrical Engineering Department	1

<u>Code</u>	<u>Organization</u>	<u>No. of Copies</u>
U 344	Rensselaer Poltechnic Institute Office of the Librarian Troy, New York	1
U 345	Scientific Attache Swedish Embassy 2249 R Street, N.W. Washington 8, D.C.	1
U 346	Rutgers University Physics Department Newark 2, New Jersey Attn: Dr. Charles Pine	1
U 347	University of Texas Military Physics Research Laboratory Box 8036, University Station Austin, Texas	1
U 348	University of Utah Electrical Engineering Department Salt Lake City, Utah Attn: Richard W. Grow	1
U 350	University of Puerto Rico College of Agriculture and Mechanical Arts Mayaguez, Puerto Rico Attn: Dr. Braulio Dueno	1
U 351	The Royal Institute of Technology Stockholm 70, Sweden Attn: Dr. B. Agdur	1
U 352	Drexel Institute of Technology Department of Electrical Engineering Philadelphia 4, Pennsylvania Attn: F. B. Haynes	1
U 353	Forsvarets Forskningsinstitut Avdeling for Radar Bergen, Norway Attn: WADD (WCOSR, Mr. Knutson) Wright-Patterson AFB, Ohio	1
U 354	Massachusetts Institute of Technology Research Laboratory of Electronics Cambridge 39, Mass. Attn: L. D. Smullin	1
U 355	Massachusetts Institute of Technology Research Laboratory of Electronics Cambridge 39, Mass. Attn: S.C. Brown	1
U 356	University of Chicago Midway Laboratories 6220 S. Drexel Avenue Chicago, Illinois Attn: P.J. Dickerman	1



<u>Code</u>	<u>Organization</u>	<u>No. of Copies</u>
U 436	University of Mississippi University, Mississippi Attn: Mr. Thomas Tullus	1
	Hq. AFRL, Office of Aerospace Research (CRRC) L. G. Hanscom Field Bedford, Mass.	4